

# Oxidative Stress on Human Cells in the Presence of Nano-Sized Titanium Dioxide

THÈSE N° 4906 (2010)

PRÉSENTÉE LE 10 DÉCEMBRE 2010

À LA FACULTÉ SCIENCES DE BASE

LABORATOIRE DE PHYSIQUE DE LA MATIÈRE COMPLEXE

PROGRAMME DOCTORAL EN PHYSIQUE

ÉCOLE POLYTECHNIQUE FÉDÉRALE DE LAUSANNE

POUR L'OBTENTION DU GRADE DE DOCTEUR ÈS SCIENCES

PAR

Katarzyna PIERZCHAŁA

acceptée sur proposition du jury:

Prof. O. Schneider, président du jury

Dr A. Sienkiewicz, Prof. L. Forro, directeurs de thèse

Prof. T. Kohn, rapporteur

Prof. M. Lekka, rapporteur

Prof. V. Slaveykova-Startcheva, rapporteur



ÉCOLE POLYTECHNIQUE  
FÉDÉRALE DE LAUSANNE

Suisse  
2010



***To my relatives***



*“The important thing is not to stop questioning. Curiosity has its own reason for existing. One cannot help but be in awe when he contemplates the mysteries of eternity, of life, of the marvelous structure of reality. It is enough if one tries merely to comprehend a little of this mystery every day. Never lose a holy curiosity.”*

**Albert Einstein**



# Abstract

Nanosized TiO<sub>2</sub> (nanoTiO<sub>2</sub>) is one of the most widely used nanomaterials, with applications ranging from paints, self-cleaning coatings, pharmaceuticals, to food and cosmetics. In spite of this massive use of nanoTiO<sub>2</sub>, its biological activity and toxicity remains subject of the intense debate. In particular, there is still considerable uncertainty in the current understanding of the relationship between physico-chemical parameters of nanoTiO<sub>2</sub>, such as crystalline phase, size, aspect ratio, surface properties, surface defects and surface chemistry and its potential toxicological effects. Motivated by this general problem, this thesis provides a multidisciplinary experimental insight into to the toxicity and photo-toxicity of various forms of nanoTiO<sub>2</sub>.

Firstly, since all of the widely accepted models of nanoTiO<sub>2</sub> toxicity involve reactive oxygen species (ROS), electron spin resonance (ESR) in combination with spin-trapping was used to measure ROS formation efficiency for the two most industrially important polymorphs of TiO<sub>2</sub>, anatase and rutile. The study was performed in an unprecedentedly broad range of particle sizes: 3.8 nm to 150 nm and 5 nm to 215 nm, for anatase and rutile nanoTiO<sub>2</sub>, respectively. Moreover, the photocatalytic and toxic properties of custom-made anatase-based TiO<sub>2</sub> nanowires (with a diameter of 35 nm and a length of 0.5-1 μm) were characterized for the first time. For pure anatase nanoTiO<sub>2</sub>, the maximum ROS generation efficacy was found for nanoparticle sizes in the range of 25 – 30 nm. The ROS generation efficacy of the custom-made TiO<sub>2</sub> nanowires was *ca.* 30% lower, being close to that of the commercial anatase nanoTiO<sub>2</sub> with primary grain sizes of 5.3 nm.

Secondly, this thesis addressed challenging, complex and still poorly understood processes occurring when nanoTiO<sub>2</sub> particles are brought into contact with living cells. In particular, the comparative nanotoxicity study towards human melanoma Lu1205 and WM793 cell lines was performed for three selected nanomaterials: the custom-made anatase-based TiO<sub>2</sub> nanowires, the commercial anatase nanoTiO<sub>2</sub> with a primary particle size of 5.3 nm and similar *in vitro* ROS formation efficacy, and the industrial photocatalytic standard, P25 Degussa (a formulation consisting of 80% anatase and 20% rutile, with primary grain sizes of 25 nm). This comparative nanotoxicity study was performed using very low concentrations of nanoTiO<sub>2</sub> (2 – 2.5 μg/mL), considerably lower than that applied in the majority of previous *ex vivo* cell culture studies.

A wide palette of spectroscopic and microscopic methods was applied to verify the cellular response to the presence of selected nanoTiO<sub>2</sub>-based particles, both in the dark and under illumination with UV-A light of low intensity ( $\lambda = 365 \text{ nm}$ ,  $1 \text{ mW/cm}^2$ ). In particular, to detect intracellular ROS in cells incubated with the selected nanoTiO<sub>2</sub>, ESR spin-trapping with an intracellular spin-trap (ACP) and histochemical detection with a ROS-sensitive dye (NBT) were used. These studies were completed by optical microscopy visualization of ROS-induced changes in cell morphology and actin filament organization (FITC-phalloidin staining). Moreover, atomic force microscopy (AFM) was used to follow the changes in the cell topology and elastic properties (AFM force spectroscopy) of cells incubated with nanoTiO<sub>2</sub> and exposed to photo-oxidative stress under UV-A illumination.

All of these techniques revealed, either directly or indirectly, deleterious effects induced by incubation of living cells with nanoTiO<sub>2</sub> and by photo-oxidative stress under illumination with UV-A. Primarily, optical microscopy visualization of selectively stained actin stress fibers and AFM topography images pointed to a rapid disorganization of the actin cortex for cells exposed to photo-oxidative stress in the presence of nanoTiO<sub>2</sub>. These results corroborated the changes in the cell shape and elasticity measured by AFM. The cell elasticity measurements, quantitatively described in terms of local Young's modulus values, pointed to an internal remodeling of the cytoskeleton in cells exposed to the presence of nanoTiO<sub>2</sub> and photo-oxidative stress.

The custom made anatase-based TiO<sub>2</sub> nanowires revealed generally stronger cytotoxic effects than the anatase nanoTiO<sub>2</sub> with a particle size of 5.3 nm, despite having similar photocatalytic properties *in vitro*. These observations were confirmed by AFM measurements of the cellular elasticity, histochemical detection with a ROS-sensitive dye (NBT) and by intracellular detection of ROS with ESR spin-trapping. The latter technique provided also a new important observation pointing to the enhanced ROS formation in cells incubated with nanoTiO<sub>2</sub> in the dark.

Overall, the findings stemming from cell toxicity studies were much more complex than those obtained from measurements of ROS generation efficacy in the presence of nanoTiO<sub>2</sub> *in vitro*. In contrast to a marked evolution of ROS generation efficacy as a function of the primary grain size *in vitro*, the cellular work pointed to the lack of direct and simple correlations between the physical parameters of nanoTiO<sub>2</sub>, such as particles size, their aspect ratio, and aggregation state, and cell toxicity.



**Keywords:** Electron Spin Resonance, spin trapping, Atomic Force Microscopy, Oxidative Stress, Reactive Oxygen Species, cell, protein staining, histopathological staining, nano-engineered materials, nanotoxicity, titanium dioxide (TiO<sub>2</sub>).

# Version Abrégée

De nos jours, le dioxyde de titane nanocristallin ( $\text{nanoTiO}_2$ ) est l'un des matériaux nanoscopiques le plus répandu, trouvant de nombreuses applications dans les domaines des surfaces autonettoyantes, des cellules solaires à colorants, dans les industries pharmaceutique, alimentaire et cosmétique. Malgré les nombreuses applications industrielles du  $\text{nanoTiO}_2$  et son inévitable présence dans l'environnement, ses effets sur le corps humain demeurent un sujet très débattu et nécessitent de nombreuses clarifications. De plus, il reste de nombreuses inconnues concernant la relation entre la toxicité *in vivo* et les paramètres physico-chimiques du  $\text{nanoTiO}_2$ , comme sa phase cristalline, sa taille, son rayon hydrodynamique, ses états actifs de surface, son efficacité photo-catalytique globale *in vitro*. Motivée par cet enjeu général, cette thèse fournit un aperçu expérimental et multidisciplinaire au problème de la toxicité et photo-toxicité du  $\text{nanoTiO}_2$ .

Cette thèse se concentre, premièrement, sur la vérification de l'efficacité de la génération des espèces réactives oxygénées (ROS, *Reactive Oxygen Species* en anglais) *in vitro*, car tous les modèles de toxicité communément acceptés du  $\text{nanoTiO}_2$  impliquent des ROS. A cette fin, la résonance paramagnétique électronique (RPE) en combinaison avec le piégeage de spin a été appliquée et a révélé que l'efficacité de la génération ROS est fortement dépendante de la phase cristalline et de la taille des particules. La recherche a été menée pour les deux plus importants polymorphes du  $\text{TiO}_2$ , l'anatase et le rutile, avec une fourchette de tailles primaires de particules d'une étendue sans précédent, allant de 3.8 nm à 150 nm pour l'anatase et de 5 nm à 215 nm pour le rutile, respectivement. De plus, les propriétés photocatalytiques et toxiques de nano-filaments basés sur de l'anatase (35 nm de diamètre et 0.5 à 1  $\mu\text{m}$  de long) ont été caractérisées pour la première fois. Pour les échantillons de  $\text{nanoTiO}_2$  anatase pur, le maximum de l'efficacité de la génération ROS a été obtenu pour des particules de taille de 25 nm à 30 nm. L'efficacité de la génération ROS des nano-fils de  $\text{TiO}_2$  s'est révélée de 30% plus basse et correspondait à celle du  $\text{nanoTiO}_2$  anatase commercial de taille de 5.3 nm.

Deuxièmement, cette thèse tente d'étudier les processus complexes, difficiles mais motivants et peu compris qui se passent lorsque des particules de  $\text{TiO}_2$  sont mises en contact avec des cellules vivantes. En partant des efficacités de la formation ROS obtenues, le choix des matériaux  $\text{nanoTiO}_2$  a été fait pour vérifier *ex vivo* la toxicité

contre les mélanomes humains Lu1205 et WM793 issus de culture cellulaire. En particulier, pour effectuer l'étude comparative de la toxicité des nano-fils basés sur de l'anatase contre des cellules vivantes, du nanoTiO<sub>2</sub> anatase commercial avec des tailles primaires de 5.3 nm a été choisi, car il possédait une efficacité similaire de formation ROS *in vitro*. L'action toxique de ces deux matériaux a également été comparée avec la toxicité du standard industriel photocatalytique, P25 Degussa (80% de TiO<sub>2</sub> anatase et 20% de TiO<sub>2</sub> rutile) avec un diamètre de 25 nm. Cette étude de nano-toxicité a été menée en utilisant de très faibles concentrations de nanoTiO<sub>2</sub>, de 2 à 2.5 µg/ml, nettement inférieures à la majorité des précédentes études sur des cultures cellulaires *ex vivo*.

Une large palette de méthodes spectroscopiques et microscopiques a été utilisée pour vérifier la réponse cellulaire au stress dû à la présence de nanoTiO<sub>2</sub> dans l'obscurité ou avec une illumination UV-A de basse intensité ( $\lambda = 365$  nm, 1 mW/cm<sup>2</sup>). En particulier, afin de détecter ROS intracellulaires dans des cellules incubées avec les trois types de nanoTiO<sub>2</sub> sélectionnés, la RPE combinée avec le piégeage de spin par l'intermédiaire des pièges de spin intracellulaires et une détection histochimique avec un colorant (NBT), sensible aux ROS, ont été utilisés. Ces études ont été complétées par de l'imagerie microscopique optique des changements induits dans la morphologie cellulaire et des filaments d'actine (marquage par la phalloïdine-FITC), par de la microscopie par force atomique (AFM) pour suivre les changements de la topologie et par de la spectroscopie de force AFM pour mesurer les propriétés élastiques des cellules incubées avec du nanoTiO<sub>2</sub> et exposées au stress photo-oxydant par illumination UV-A.

Toutes ces techniques ont révélé, directement ou indirectement, les effets délétères induits par l'incubation de cellules vivantes avec du nanoTiO<sub>2</sub> et par le stress photo-oxydant d'une illumination UV-A. En particulier, l'imagerie par la microscopie optique des filaments d'actine sélectivement marqués et les images topographiques AFM ont montré une rapide désorganisation du cortex d'actine pour les cellules exposées à un stress photo-oxydant en présence de nanoTiO<sub>2</sub>. Ces résultats sont corroborés avec les mesures AFM de la morphologie de l'élasticité de la cellule. Les mesures d'élasticité cellulaire, décrits quantitativement en termes de valeurs locales du module de Young, ont montré une réorganisation interne du cytosquelette dans les cellules exposées à la présence de nanoTiO<sub>2</sub> et de stress photo-oxydant.

Les nano-fils de TiO<sub>2</sub> anatase synthétisés dans notre laboratoire, avec des propriétés photocatalytiques *in vitro* similaires aux particules de nanoTiO<sub>2</sub> anatase de

taille 5.3 nm, ont généralement révélé de plus grand effets cytotoxiques. Ces observations ont été confirmées par des mesures AFM de l'élasticité cellulaire, par détection histochimique avec un colorant (NBT) sensible aux ROS et par la détection RPE intracellulaire des ROS. Cette dernière technique a fourni un nouveau résultat qui montre l'augmentation de ROS dans les cellules incubées avec du nanoTiO<sub>2</sub> sans lumière.

De manière générale, les résultats des études de toxicité *ex vivo* étaient bien plus complexes que ceux obtenus par mesure de l'efficacité de la génération ROS en la présence de nanoTiO<sub>2</sub> *in vitro*. Contrairement à la variation marquée de l'efficacité de la génération ROS en fonction de la taille primaire des particules *in vitro*, l'étude *ex vivo* (sur les cellules) a montré le manque de corrélations simples et directes entre les paramètres physiques du nanoTiO<sub>2</sub>, tels que la taille des particules, leurs formes ou l'état d'agrégation, et la toxicité cellulaire.

**Mots-clés :** résonance paramagnétique électronique, piégeage de spin, microscope à force atomique, stress oxydatif, espèces réactives oxygénées, cellules, marquage de protéines, marquage histopathologique, nanomatériaux, nanotoxicité, dioxyde de titane (TiO<sub>2</sub>).

# Acknowledgements

My PhD years in Lausanne were sometimes hard, but there are several people who contributed to also making it a happy and joyful period in my life. I am greatly indebted to the friends and colleagues who crossed I crossed paths with, in many different ways.

At the official level, I would like to acknowledge Swiss National Science Foundation (project No. 205320-112164 “Biomolecules under stress: ESR in vitro study”) for providing funds for this work and my stay in Switzerland.

I would like to express my deep and sincere gratitude to my supervisor, Dr. Hab. Andrzej Sienkiewicz, for the trust he has placed in me from the onset of this Doctoral work. As much as his contagious passion for Physics and Science in general, I appreciate his being available at all times, his enthusiasm and his kindness. His can-do attitude has been a challenging and motivating driving force.

Special thanks also go to Professor László Forró, my thesis Co-director, for giving me the opportunity to carry out fruitful and thorough scientific work in an environment abundant with expertise and willingness to help.

Thanks to Dr. Hab. Małgorzata Lekka for introducing me to the world of Atomic Force Microscopy and its bio-applications, for her useful suggestions both in the experimental work and in interpretation of the results, for her constant support, and for her guidance not only in the realms of science and academics, but also in personal matters.

I thank Andrzej Kulik who generously gave his time and attention to proofreading this manuscript, as well as advising me on AFM experiments.

My thanks also go to Anna Kusmartseva, Zlatko Micković and Marijana Mionić, with whom I had the pleasure of sharing offices during last 4 years. In addition of always being ready to help, they also provided a friendly, fun atmosphere, and many suggestions and intelligent comments.

I am also grateful to Richard Gaal, for his scientific and technical advice on a number of subjects.

Many thanks to all the technicians in the group, who were always patient and willing to help, even when I arrived in the last minute, with complicated requests.

I would also like to acknowledge Monique Bettinger and Evelyn Ludi, the best secretaries on the Earth.

I further wish to acknowledge my badminton mates Aurore, John, and Markus - I hope our Tuesday evening tradition will continue. A special thanks to Aurore, my friend, for all the affection, love, and support you shone on me.

I want to thank Gerit and Andrzej, Karolina and Mariusz, Anita and Michał, Marcin, Agnieszka and Piotr for being my second family here in Switzerland.

My days at EPFL and experience in Lausanne have been enriched by many extraordinary people. Anna, I am indebted to you for your goodness, open heart, for being my wonderful friend, and for sharing so much and always being there for me. I am also thankful to Sipi, my dancing partner for two years, for adding color to my life. To Gøran, for correcting this work and being a perfect friend. To Bastien and Mireille for translating my abstract to French on such a short deadline. My gratitude extends to my colleagues, both past and present members of the group who became valuable friends, for the collegial atmosphere, their assistance, and our memorable times at the workplace as much as outside EPFL. Big thanks to you: Luka, Dejan, Martial, Claudia, Ana, Arnaud, Pablo, Camilo, Johanna, Tamas, Bibe, Guido, Branimir, Kyumin, Vincent, Silvia, Julian, Christian and Areta.

Many thanks to all my friends in Poland: to Aleksandra and Łukasz, Agata and Dawid, Magdalena and Piotr.

It is very hard to express in words my gratitude to my parents, Jolanta and Tadeusz, and grandparents, Kazimiera and Leon. They were geographically far away, but always here with me. Your presence, wisdom and unconditional love followed me like a shadow in easy days, and supported me like a solid rock during hard times.

Last, but definitely not least, my deepest thank to you, Tomasz, my soulmate and best friend, for holding my hand tight and leading me where I couldn't see, for your care and infinite patience during the last period of my doctorate. Even when apart, you always succeeded in showing me your trust, support throughout my life, thoughtfulness and love.

# Contents

<b>List of Abbreviations</b> .....	<b>4</b>
<b>List of Symbols</b> .....	<b>6</b>
<b>I. Introduction</b> .....	<b>7</b>
<b>II. Health effects of Titanium Dioxide</b> .....	<b>12</b>
II.1. The main health hazards associated with breathing in titanium dioxide .....	13
II.2. Potential hazard of titanium dioxide on skin .....	17
II.3. Titanium dioxide in circulatory system – toxicity and tissue distribution .....	22
II.4. Oral administration of TiO <sub>2</sub> – acute toxicity and biodistribution .....	25
<b>III. The cell</b> .....	<b>29</b>
III.1. Basic biology of cells .....	30
III.2. The biology of cancer .....	35
III.2.1. Description of cancer .....	35
III.2.2. Basic Facts about cancer .....	37
III.2.3. Causes of cancer .....	39
III.2.4. Cellular responses and oncogenic consequences associated with ultraviolet radiation .....	40
III.2.5. Melanoma cell lines .....	41
III.2.6. Choice of cell lines in this study .....	43
III.3. Mechanical properties of cells .....	44
III.3.1. Experimental techniques in cell mechanics .....	45
<b>IV. Principle action of photosensitizers</b> .....	<b>49</b>
IV.1. Reactive oxygen species .....	50
IV.2. Photo-generation of Reactive Oxygen Species .....	54
IV.3. Nanoparticles and nano-filaments of TiO <sub>2</sub> - semiconductor-based photosensitizers in aqueous solutions .....	58
IV.3.1. Mechanism of ROS generation by TiO <sub>2</sub> .....	60

<b>V. Sample characterization techniques</b> .....	<b>62</b>
<b>V.1. ESR - electron spin resonance: a tool for detection of ROS</b>	
<i>in vitro</i> and <i>ex vivo</i> .....	<b>63</b>
V.1.1 Introduction and principles of EPR spectroscopy .....	64
V.1.2. Detection of reactive oxygen species	
by electron spin resonance .....	67
V.1.2.1. Photocatalytic properties of TiO <sub>2</sub> nanoparticles	
and nanowires .....	70
V.1.2.2. EPR <i>ex vivo</i> detection of ROS caused by TiO <sub>2</sub>	
nanoparticles and nanowires .....	73
<b>V.2. Atomic force microscopy: a tool for detection of ROS-induced</b>	
<b>damages to living cells</b> .....	<b>73</b>
V.2.1. Introduction and principles of AFM .....	74
V.2.1.1. Contact Mode .....	78
V.2.2. Elastic properties of living cells - determination of the Young's	
modulus - force spectroscopy mode .....	79
V.2.2.1. Force Curves on Soft Samples .....	81
V.2.2.2. The Young's modulus of cells .....	82
V.2.3. Experimental conditions for cells elasticity	
and topography measurements .....	83
V.2.3.1. AFM imaging of cells .....	83
V.2.4. <i>Single-cell-level</i> AFM study of cellular response to ROS formed	
in the presence of TiO <sub>2</sub> nanoparticles and nanowires .....	85
<b>V.3. Techniques used for TiO<sub>2</sub> characterization</b> .....	<b>86</b>
V.3.1. Transmission electron microscopy .....	86
V.3.2. X-ray powder diffraction .....	87
V.3.3. Dynamic light scattering .....	87
<b>V.4. Techniques used for cells characterization</b> .....	<b>87</b>
V.4.1. Visualization of actin filaments .....	88



V.4.2. Cell viability assay . . . . .	88
V.4.3. Cell morphology . . . . .	91
V.4.4 .NBT staining. . . . .	91
<b>VI. Experimental results . . . . .</b>	<b>92</b>
VI.1. Characterization of TiO <sub>2</sub> nanoparticles and nanofilaments . . . . .	93
VI.1.1. ROS generation by TiO <sub>2</sub> -based nanoparticles . . . . .	94
VI.1.2. ROS generation by TiO <sub>2</sub> - anatase based nanowires . . . . .	101
VI.2. ESR <i>ex vivo</i> detection of ROS generation in cells in the presence of nanoTiO <sub>2</sub> . . . . .	109
VI.3. Detection of intracellular ROS - NBT staining . . . . .	112
VI.4. Cell viability. . . . .	116
VI.5. Morphology of melanoma cells exposed to photo-oxidative stress. . . . .	118
VI.5.1. Cell cytoskeleton studies using fluorescence microscopy . . . . .	121
VI.5.2 High resolution AFM imaging of cells. . . . .	126
VI.6. AFM - determination of the Young's modulus . . . . .	133
<b>Discussion. . . . .</b>	<b>137</b>
<b>Concluding remarks and outlook . . . . .</b>	<b>144</b>
<b>References . . . . .</b>	<b>147</b>
<b>List of Figures . . . . .</b>	<b>165</b>
<b>List of Tables . . . . .</b>	<b>176</b>
<b>Curriculum Vitae . . . . .</b>	<b>177</b>

# List of Abbreviations

1D	One-Dimensional
2D	Two-Dimensional
3D	Three-Dimensional
ABP	Actin Binding Protein
ACP	Acetoxy-3-carboxy-2, 2, 5, 5 tetramethylpyrrolidine
AFM	Atomic Force Microscopy or Atomic Force Microscope
AOP	Advanced Oxidation Processes
ATP	Adenosine triphosphate
CM	Contact Mode Atomic Force Microscopy
CNS	Central Nerve System
CNT	Carbon Nanotube
CPD	Cyclobutane Pyrimidine Dimer
DNA	Deoxyribonucleic acid
DMPO	5, 5-Dimethyl-1-pyrroline N-oxide
ER	Endoplasmic Reticulum
ESR	Electron Spin Resonance
FBS	Fetal Bovine Serum
FFM	Friction Force microscopy
HBSS	Hanks Balanced Salt Solution
IC	Internal Conversion
ISC	Inter System Crossing
LFM	Lateral Force microscopy
MM	Metastatic Melanoma
MTC	Magnetic Twisting Cytometry
MWCNT	Multi Wall Carbon Nanotube
NADPH	Nicotinamide adenine dinucleotide phosphate
NBT	Nitro Blue Tetrazolium
NPs	Nanoparticles
NWs	Nanowires
OS	Oxidative Stress
PBS	Phosphate Buffered Saline

PDT	Photodynamic Therapy
PI	Propidium Iodide
PS	Photosensitizer
RET	Resonant Energy Transfer
RGB	Radial Growth Phase
ROS	Reactive Oxygen Species
RPMI 1640	Cell Medium-developed at Roswell Park Memorial Institute
SEM	Scanning Electron Microscopy or Scanning Electron Microscope
SPM	Scanning Probe Microscopy or Scanning Probe Microscope
STM	Scanning Tunneling Microscopy
SWCNT	Single-Wall Carbon Nanotube
TEM	Transmission Electron Microscopy or Transmission Electron Microscope
TEMPOL	4-hydroxy-2, 2, 6, 6-tetramethylpiperidine 1-oxyl
UFP	Ultra Fine Particles
UVA	Ultraviolet Radiation, where $\lambda = 320 - 400$ nm
UVB	Ultraviolet Radiation, where $\lambda = 280 - 320$ nm
VGB	Vertical Growth Phase
XRD	X-ray Diffraction

# List of Symbols

$\alpha$	Half-opening angle of the conical tip
$\beta$	Tip cone half-angle
$\delta$	Tip-sample contact deformation
$\gamma$	Gyromagnetic ratio
${}^1\Delta_g$	First singlet excited state of molecular oxygen
$B_0$	Magnetic field
$c$	Speed of light
$e$	Elementary charge $e = 1.6022 \times 10^{-19} [C]$
$E$	Young's Modulus
$E_g$	Energy band gap
$g_e$	<i>g-factor</i> , a free electron its value $g_e = 2.00232$
$h$	Planck's constant $h = 6.6261 \times 10^{-34} [J \cdot s]$
$k$	Cantilever spring constant
$\lambda$	Wavelength
$m_e$	Electron rest mass $m_e = 9.1094 \times 10^{-31} \text{ kg}$
$n$	Refracting index
$\mu_B$	Bohr magneton $\mu_B = 9.274 \times 10^{-28} [J \cdot G^{-1}]$
$O_2^{\bullet-}$	Superoxide anion radical
$OH^{\bullet}$	Hydroxyl radical
$R$	Radius of curvature of the paraboloidal indenter
$S_z$	$z$ -component of the spin angular momentum operator
$\nu_c$	Cell Poisson ratio
$\omega$	Larmor frequency
$z$	Cantilever deflection. Positive for upward deflection (away from the sample) and negative for downward deflection (towards the sample)
$Z$	$Z$ scanner displacement

# I. Introduction

**Nanoscience** and **nanotechnology** are emerging interdisciplinary fields that have experienced a boom during the past decade. They have already impacted materials technology, electronics, optics, medicine, as well as energy and aerospace industries. Nanoscience, which is aimed at investigating and manipulating atoms, molecules and particles at the nanometer scale, is driven by the fact that the properties of bulk materials dramatically change when their size is reduced to the nanometer range. A nanometer is one billionth of a meter,  $10^{-9}$  m, about the size of ten atoms in a row. In comparison, the average diameter of an influenza virus is 100 nm and the thickness of a human hair is about 100,000 nm [see Fig. 1].

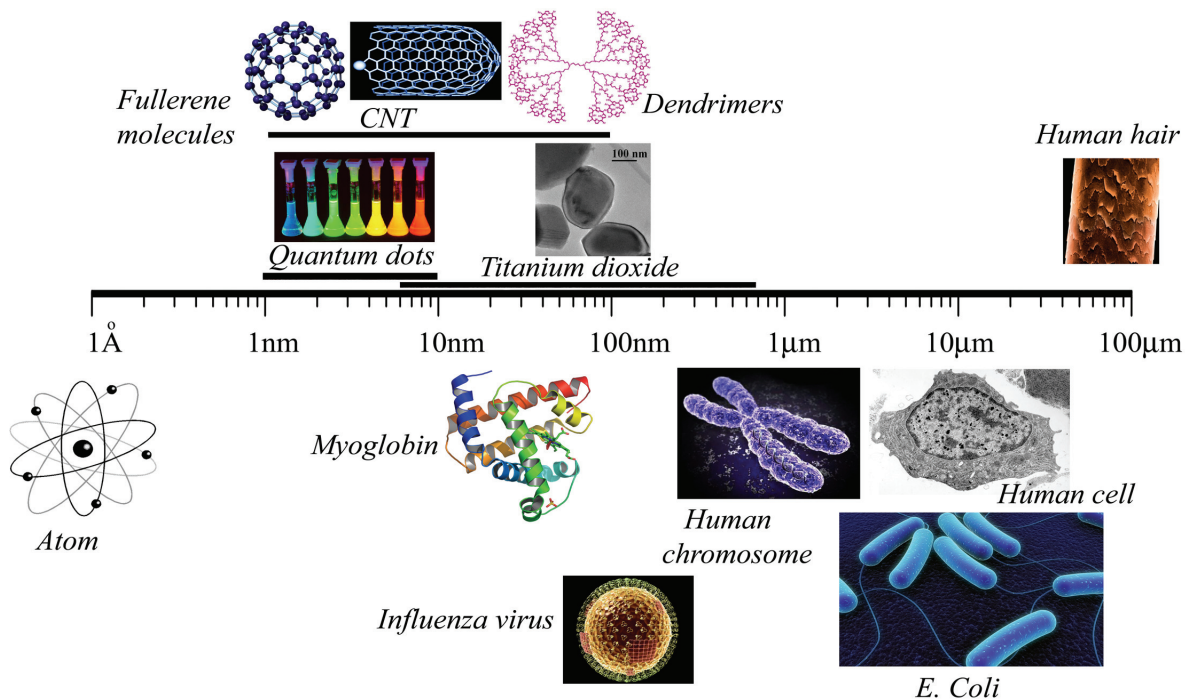


**Figure 1.** The size of various familiar objects on a logarithmic scale.

To understand processes occurring at the nanoscale, nanoscience exploits traditional branches of physics, chemistry and materials science. In a sense, nanoscience also provides a natural link between these ‘traditional sciences’ and ‘life sciences’, since nanometer-length scales are also characteristic for the basic building blocks and molecular machines in living organisms.

One of the most widely discussed but least understood issues in nanoscience concerns the biochemical processes which occur when nano-sized objects are brought into contact with biological targets. In this context, nanotoxicology is emerging as an important sub-discipline of nanoscience and nanotechnology (Donaldson and Tran, 2002; Donaldson et al., 2004). Nanotoxicology refers to the study of interactions of nanoengineered materials with biological systems, with an emphasis on elucidating the relationship between the physical and chemical properties of nanostructures with toxic biological responses. It has been suggested that the particle's physical and chemical parameters, including particle size and composition, particle surface, hydrodynamic radius, surface chemistry, play a decisive role (Jiang et al. 2008)

The effect of nanoparticles (NPs) on the human body is of increasing concern as the particles are found in an ever-expanding variety of goods. Human are exposed to NPs through inhalation, ingestion, dermal contact and injection. The small size of the nanoparticles facilitates their uptake into cells as well as allowing transcytosis of epithelial cells into blood and lymph circulation systems and from there to sensitive target sites, where they then persist.

Nowadays, nanosized crystalline titanium oxide (nanoTiO<sub>2</sub>), being one of the top fifty chemicals produced world-wide, is also one of the most widespread nanomaterials. Due to its excellent photo-catalytic properties, nanoTiO<sub>2</sub> is now the industry-leading nanomaterial, and has found numerous applications. These range from self cleaning coatings, advanced oxidation processes (AOPs), to dye-sensitized solar cells (DSSC). Micronized TiO<sub>2</sub>, a commonly employed as a white pigment and opacifier, is as a key ingredient for providing whiteness and opacity to products such as paints, paper, inks, food, several pharmaceuticals, and plastics. Since the discovery of TiO<sub>2</sub>-mediated photolysis of water by Fujishima and Honda in the seventies, both micronized and nanoTiO<sub>2</sub> have been intensively investigated as photocatalytic materials (Fujishima and Honda, 1972; Fujishima et al., 2000). In particular, nanoTiO<sub>2</sub> has found applications as a very efficient photocatalyst for environmental purification, such as decomposition of organic compounds in polluted air and waste waters (Mills and Wang, 1999a; Sopyan et al., 1996; Tachikawa et al., 2007), and inactivation of pathogens. It has been demonstrated that the photocatalytic activity of nanoTiO<sub>2</sub> can be tailored by judicious use of surface activation and doping with various impurities (Lin et al., 1998; Ruiz and et al., 2002; Thevenot and et al., 2008; Rengifo et al., 2010).

Overall, nanoTiO<sub>2</sub>-containing systems are attracting increasing attention as potent photo-sensitizers, and are finding numerous applications in bio-oxidative processes. One potential implementation is in photodynamic therapy (PDT), which is based on a selective '*light-plus-drug*' dye-sensitized photo-oxidation of biological matter in the target tissue (Brown et al., 2000). They are also finding applications in the emerging technologies of smart self-cleaning surfaces as well as environmental applications for air- and waste-water treatments. Moreover, nanoTiO<sub>2</sub> is used as an additive in UV-blocking cosmetics (UV filters) (Konstantinou et al., 2004).

In spite of the large number of studies aimed at establishing the biological activity of nanoTiO<sub>2</sub>, its toxicity is a subject of intense debate (Morganti, 2010). Furthermore, there is still uncertainty in the current understanding of the relationship between physico-chemical parameters such as crystalline phase, size, surface properties, surface defects and surface chemistry, and potential toxicological effects of nanoTiO<sub>2</sub>.

Regarding the potential toxicity of nanoTiO<sub>2</sub>, different studies have shown that there is a risk of translocation of nanoTiO<sub>2</sub> along axons and dendrites of neurons, as well as access to the central nervous system and ganglia (Ophus et al., 1979; Hoffmann et al., 1995; Oberdörster et al., 2004; Oberdörster et al., 2005). As membrane-bound layers of aggregates or single particles, nanoparticles can enter not only the cells, but also mitochondria and nuclei. Therefore, these particles can interact with cytoplasmic proteins such as actin filaments - cytoskeletal proteins that are essential in eukaryotic cells for a variety of functions such as cellular transport or cell motility - and affect their crucial functions.

The percutaneous absorption of titanium in the epidermis and dermis were observed by applying sunscreens containing micron- and nanosized TiO<sub>2</sub> to subjects daily for 2-4 weeks (Tan et al., 1996). The distribution of nanoTiO<sub>2</sub> within the different layers of human skin has been demonstrated (Puccetti et al., 1997), and it has been shown that sunlight-illuminated nanoTiO<sub>2</sub> internalized in cells can cause DNA damages (Dunford et al., 1997).

The skin and the lungs are examples of organs which are continuously exposed to environmental particles. Several studies have already reported phagocytosis of particles by lung epithelial cells (Oberdörster et al., 1992; Geiser et al., 2008). It is believed that nanoTiO<sub>2</sub> particles are not removed from the cells, rather persisting within them, and that their concentration increases with time. This is especially important, as the internal surface area of the lungs is vast (alveoli and airways represent approximately 140 m<sup>2</sup>)

(Gehr et al., 1978), thus facilitating efficient access of particles to the lung tissue. Analytical transmission electron microscopy of different cell culture lines showed single TiO<sub>2</sub> particles, small free aggregates and membrane-bound layer aggregates in the cytoplasm after exposure to nanoTiO<sub>2</sub> (Long, 2007; Li et al., 2008). In another study, nanoTiO<sub>2</sub> particles with diameters in the range 20–30 nm, were detected as free single particles in cytoplasm. Exposure to these nanoparticles leads to their accumulation in cells in different organs, where vital structures such as microtubules can interact with them (Stearns et al., 2001; Mühlfeld et al., 2007; Rothen-Rutishauser et al., 2007; Gheshlaghi et al., 2008).

In contrast with the large number of studies related to the toxicity in the absence of light, the problem of light-induced toxicity of different nanoTiO<sub>2</sub> polymorphs and morphologies, including nano-filamentous TiO<sub>2</sub>, has been addressed less frequently (Almquist Biswas, 2002). Although many studies have been done on nanoTiO<sub>2</sub> toxicity in animal models and cell cultures (Cai et al., 1991; Cai et al., 1992; Rahman et al., 2002, Zhang et al., 2004), there is little data on the interaction of this material with subcellular structures. Evidence of oxidative stress responses after nanoTiO<sub>2</sub> endocytosis indicates that research on possible cellular interactions between such particles and cellular structures such as actin filaments is urgently needed.

Despite intensive research efforts, there is still much controversy concerning the relationship between the physico-chemical parameters of nanoTiO<sub>2</sub>, including the crystalline phase, particle size, hydrodynamic radius, surface active states, and the overall *in vitro* photocatalytic efficiency, and the toxicity of this nanomaterial *in vivo*.

Therefore, this thesis addresses the problem of toxicity and photo-toxicity of various forms of nanoTiO<sub>2</sub> towards living human cells. In particular, the thesis focuses on the cellular toxicity of particulate nanoTiO<sub>2</sub> and TiO<sub>2</sub>-based nanowires. Similarly to nanoTiO<sub>2</sub>, the latter material, due to its nanoscale dimensions and high aspect ratio, has generated a lot of interest for possible applications in photovoltaic devices (like in *so-called* Graetzel cells), bio-sensing, bio-compatible scaffolds for tissue engineering, medical implants, etc.

It is becoming evident that the interactions of nanoTiO<sub>2</sub> with cells are cell type-dependent. Since malignant cells are easy to culture, as well as tumors (cancerous or otherwise) being interesting targets for *in vivo* applications of nanoparticles, two malignant human melanoma cell lines, metastatic Lu1205 and non-metastatic malignant WM793, were chosen for this study.



The response of Lu1205 and WM793 cells exposed to low concentrations of custom made TiO<sub>2</sub> nanowires (TiO<sub>2</sub> NWs) and to commercially available particulate nanoTiO<sub>2</sub> photo-catalysts (AMT100 and Degussa P25, composed of 80% anatase and 20% rutile crystal structure) were performed. Studies were carried out in the dark and compared to those performed under the illumination with UV-A light of low intensity (1 mW/cm<sup>2</sup>).

The induced ROS generation of free radicals caused significant reorganization of actin filaments, which was visualized using fluorescent staining and quantify by measuring the elastic properties of cells with atomic force microscopy (AFM). AFM was used to follow both the changes in the cell topology and cell elasticity. This latter approach, *i.e.* AFM force spectroscopy, made it possible to measure the local Young's modulus of living cells. It was found that both custom made TiO<sub>2</sub> NWs and nanoparticles caused marked reorganization of actin filaments in both studied cell lines.

The overall goal of the work shown in this thesis was to study mechanisms involved in formation of reactive oxygen species (ROS) in the presence of nano-structured materials, as well as to detect and monitor the ROS-induced deleterious action on bio-molecular targets. The understanding of these processes is of utmost importance, since the rapidly developing field of nanotechnology is likely to become an important source of environmental nanoparticles which can be absorbed by plants, animals and humans through inhalation, ingestion, skin uptake, and/or injection. Clearly, there is growing concern about the adverse aspects of nano-engineered materials on human health and the environment (Nel et al., 2006).

## **II. Health effects of titanium dioxide**

A nanoparticle is far smaller than the diameter of a common cell, and thus has an opportunity to enter the human body during production, transportation, storage and consumption. The potential impacts and influence of TiO<sub>2</sub> on human health and the environment have attracted great attention from scientists, industry and governments (Colvin, 2003; Donaldson et al., 2004; Nel et al., 2006; Oberdörster et al., 2005). For more than 10 years, a growing number of epidemiological studies suggest and provide consistent evidence for the link between adverse health effects and increased concentration of ambient fine and ultrafine particles in the body (Dockery DW et al., 1993).

## II.1. The main health hazards associated with breathing in titanium dioxide

A high concentration of titanium dioxide dust in the air may cause coughing or irritation revealed by increased neutrophil and phagocyte count in the bronchoalveolar lavage fluid (BAL fluid) of rats and mice after exposure. Lactate dehydrogenase leakage in the lungs is also observed (Geiser et al., 2008). Results reported by Oberdörster (Oberdörster et al., 1992) show that ultrafine  $\text{TiO}_2$  particles have a significantly greater pulmonary inflammatory potency than larger  $\text{TiO}_2$  particles, and that this response is accompanied by an increased interstitial access of these particles (Bermudez et al., 2002, 2004; Oberdörster et al., 1992). In the study performed by Geiser on “The Role of Macrophages in the Clearance of Inhaled Ultrafine Titanium Dioxide Particles”, there are evidences showing that lung surface macrophages do not efficiently phagocytose these ultrafine particles but take them up in a rather sporadic and unspecific way [Fig.1] (Geiser et al., 2008). Several internalized nano $\text{TiO}_2$  particles (up to 5) were found in individual BAL-macrophages in this study.

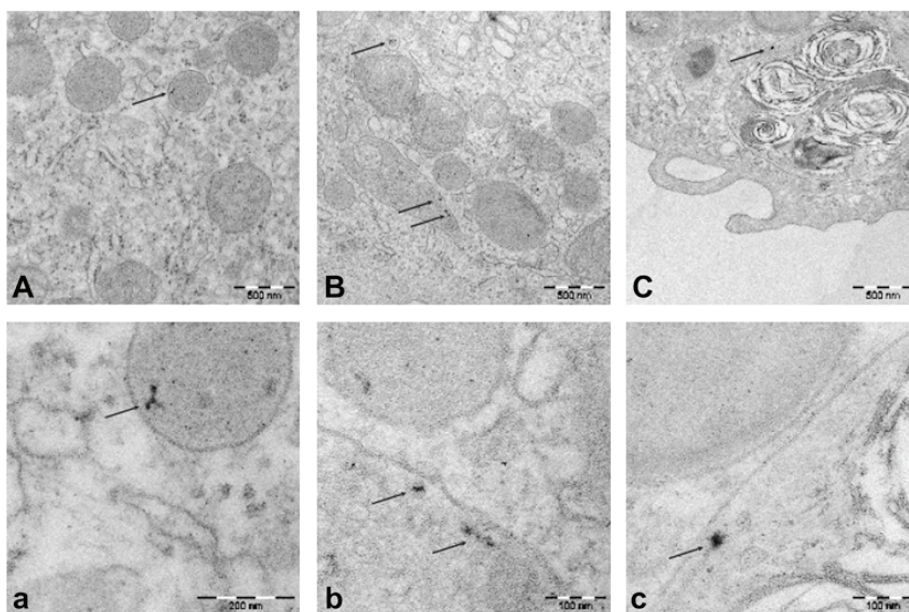


**Figure 1.** Localization of ultrafine  $\text{TiO}_2$  particles in ultrathin sections of BAL-macrophages. Micrographs with uppercase letters show the cellular localization of the particles at a magnification of 36,300 while those with lowercase letters show the individual particles at a magnification of 325,000. (A, a). Ultrafine  $\text{TiO}_2$  particle contained in a vesicle with gray, homogenous matter. (B, b) Multiple ultrafine particles in one macrophage profile; (b) shows the two particles located in the elongated vesicle. (C, c) Particle located in a phagolysosome containing surfactant. (Taken from Geiser et al., 2008)

Inhalation of ultra fine particles (UFP) is the most common route to exposure. Nanoparticles can then be translocated into the central nervous system (CNS) *via* the olfactory pathway. For example, Oberdörster showed that there was an increase in the concentration of ultrafine elemental  $^{13}\text{C}$  particles (36 nm) in the olfactory bulb (Oberdörster et al., 2004).

The UFP deposition is dependent on the particle size. Above 50% of inhaled UFP (~ 20 nm) can be deposited in the nasopharyngeal region during nasal breathing. The preliminary results of Oberdörster show that around 20% of the UFP (~ 5-10 nm) deposited on the olfactory mucosa of the rat can be translocated to the olfactory bulb. Such neuronal translocation constitutes an additional not generally recognized clearance pathway for inhaled solid UFP [Fig.2].

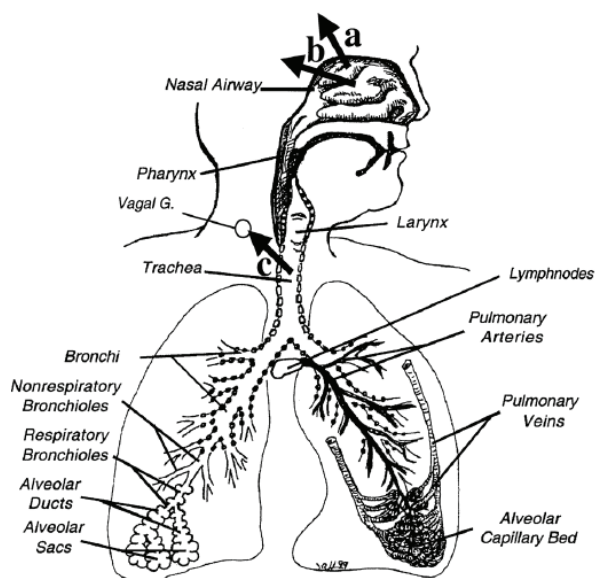


**Figure 2.** Suggested neuronal translocation pathways in humans for solid nanosized particles and for soluble components of larger particles. These include uptake into nerve endings embedded in mucosa of nasal (a, olfactory; b, trigeminal nerves) and tracheobronchial (c, afferent vagal nerves) region. The biological/toxicological importance of these pathways and their contribution to particle clearance vis-a-vis the classical clearance pathways of mucociliary and phagocytic cell transport, dissolution, diffusion, and protein binding remain to be determined. Taken from Oberdörster et al., 2004.

Wang (Wang et al. 2007, 2008) has reported distributions of nanoTiO<sub>2</sub> in the brain sections using the microbeam mapping technique of Synchrotron Radiation X-Ray Fluorescence Spectroscopy (SR-XRF). They found that nanoTiO<sub>2</sub> was mainly accumulated in the cerebral cortex, thalamus and hippocampus [Fig.3, Fig.4, (Wang et al. 2007, 2008)].

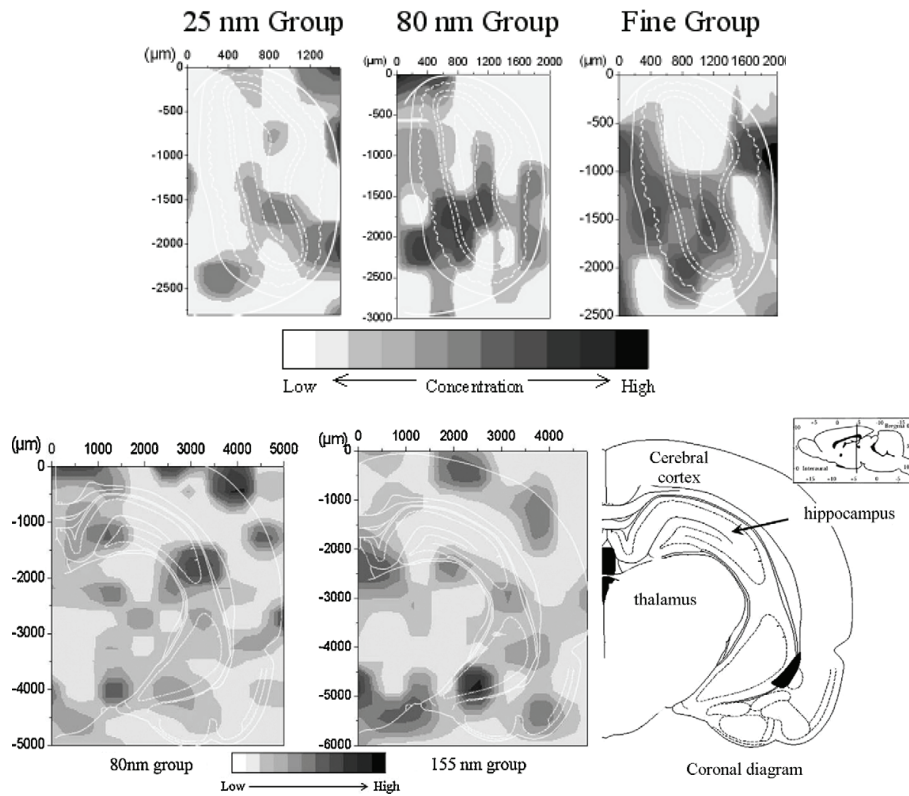


**Figure 3.** Distribution of titanium in olfactory bulb of mice in the different experimental groups analyzed by SR-XRF (Taken from Wang et al., 2007, 2008). The greyscale shows the nanoparticle concentration, from white (no particles observed) to black (high concentration of nanoparticles).

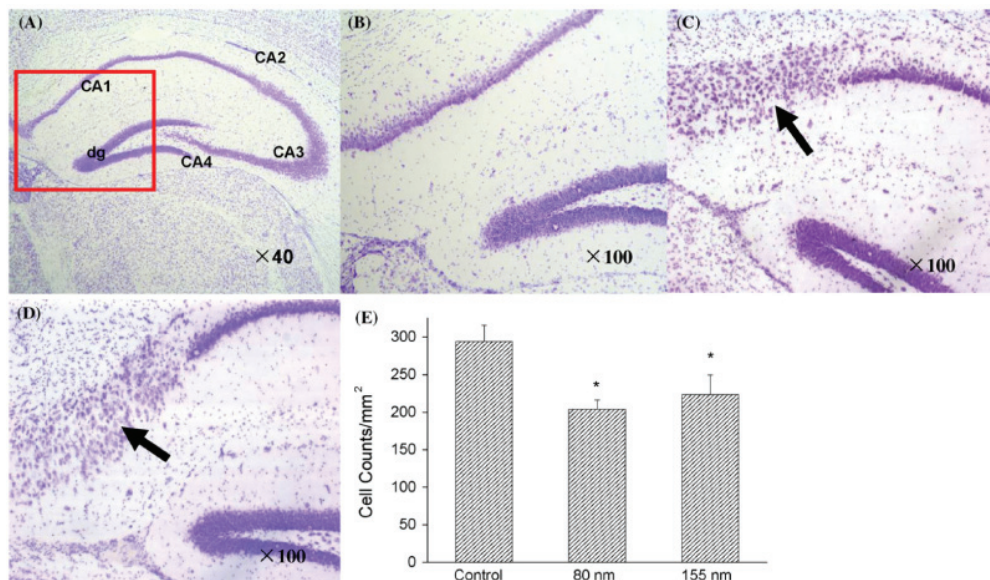


**Figure 4.** Morphological changes of neurons in the Nissl stained brain tissue sections of (A&B) control group, (C) 80 nm group and (D) 155 nm group. Note that apparently scattered Nissl body, large cell somata (arrows) and an irregular appearance were found especially in the CA1 region of hippocampus in the exposed mice. Image magnification: 100× (B–D); 40× (A). E represents the comparison of cell numbers in the CA1 region of the hippocampus (number/mm<sup>2</sup>)

of mice 30 days after treatment with different TiO<sub>2</sub> nanoparticles. (Taken from Wang et al., 2007, 2008)

The TiO<sub>2</sub> nanoparticles may produce ROS and induce oxidative stress due to their high reactivity. When TiO<sub>2</sub> is translocated into the brain, macrophages such as monocytes, neutrophils and microglia can release oxygen radicals which react with these particles in the brain (Colton and Gilbert, 1987), as well as phagocytizing. The synthesis of some enzymes can be influenced and the balance of the oxidative/antioxidative system can be disrupted, resulting in lipid peroxidation and protein oxidation (Wang et al., 2008). Nanoparticles (TiO<sub>2</sub> or gold) are no longer freely distributed in the cytoplasm after being internalized by cells, but they are preferentially located in mitochondria (De Lorenzo, 1970).

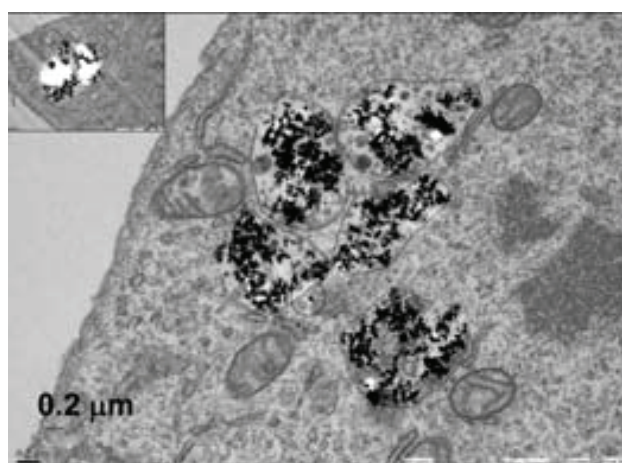


**Figure 5.** TEM of P25 (20 ppm, 3 hr) treated N27 neurons showed numerous membrane-bound aggregates. An amorphous substance was seen within the vacuoles (insert). In addition, individual nanosize P25 particles (circle) were noted throughout the cytoplasm. Mitochondria in nearby proximity showed no evidence of disruption or swelling. (Taken from Long, 2007)

When the mitochondria are invaded by these nanoparticles (Long et al., 2006), they possibly produce ROS and interfere with antioxidant defenses. Toxicity analysis performed by Long (2007) indicated cell internalization of nanoTiO<sub>2</sub> after three hours [Fig.5], leading to strong up-regulated pathways primarily associated with inflammatory, cell cycling and pro-apoptotic activities.

## II.2. Potential hazard of titanium dioxide on skin

The application of sunscreens to protect against UV induced skin damages, such as sunburn, cancer, premature aging and photoallergies, is generally recommended. Physical sunscreens, such as titanium dioxide ( $\text{TiO}_2$ ) and zinc oxide ( $\text{ZnO}$ ), that do not undergo any chemical decomposition when they are exposed to UV radiation, have been introduced as supposedly safer alternatives to chemical agents. They can also offer a wider spectrum of photoprotection than many chemical sunscreens (Anderson et al., 1997). Nanoparticles of  $\text{TiO}_2$  and  $\text{ZnO}$  are transparent in formulations spread on the skin surface. This transparency provides the cosmetic acceptability which is not achievable with larger-particle formulations. The potential of solid nanoparticles to penetrate the stratum corneum [Fig. 6] and diffuse into underlying structures lies at the centre of the debate concerning their safety for topical use. Dermal administered nanoparticles are known to localize to regional lymph nodes, potentially *via* skin macrophages and Langerhans cells [Fig. 7] (Kim et al., 2004).

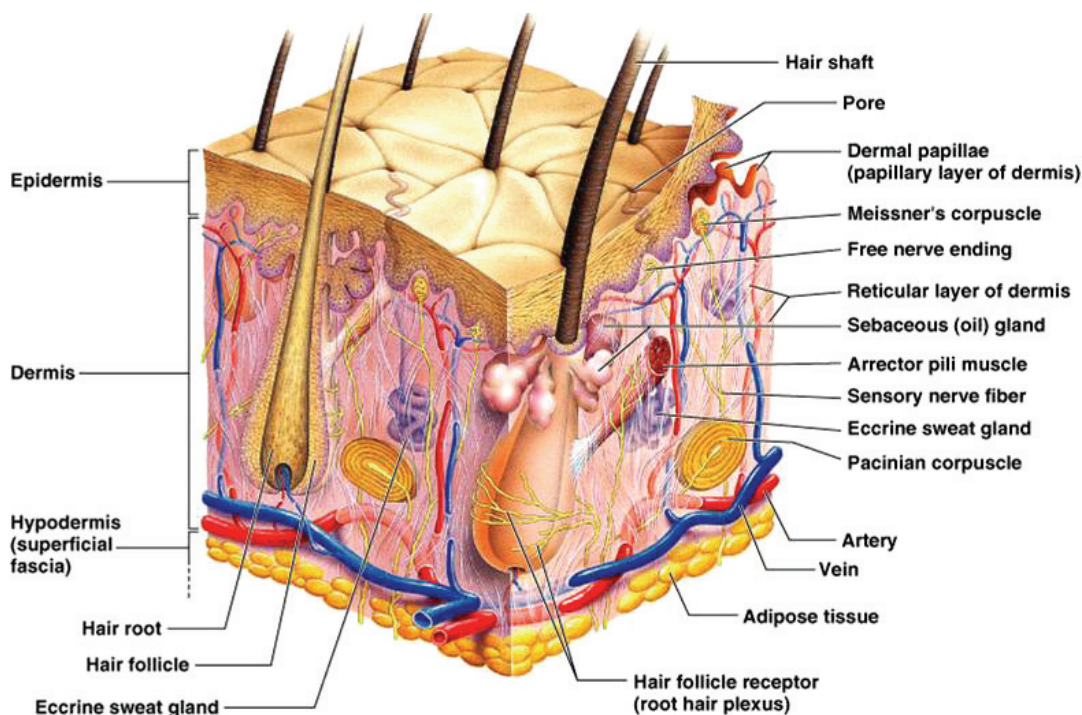


**Figure 6.** The structure of skin.

(Taken from <http://faculty.irsc.edu/FACULTY/TFischer/AP1/skin.jpg>)

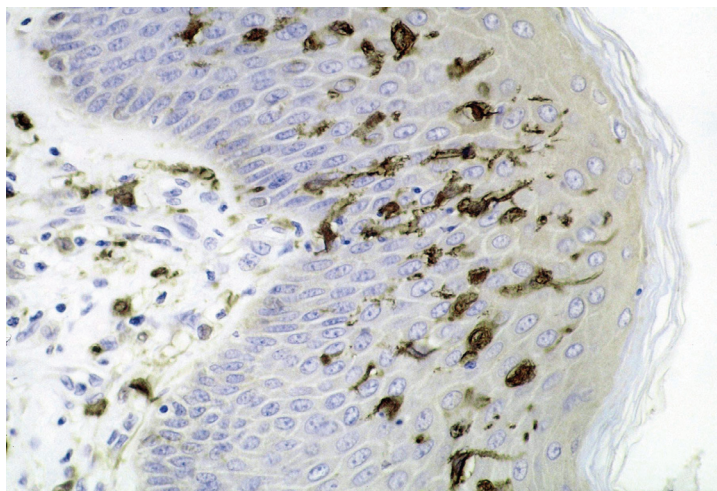


**Figure 7.** Section of skin showing large numbers of dendritic (Langerhans) cells in the epidermis. *M. ulcerans* infection, S100 immunoperoxidase stain. (Taken from Kim et al.,2004)

Studies performed by Wu et al. (Wu et al. 2009) show that topical administration of titanium dioxide NPs of different sizes for 30 days on porcine skin results in nanoTiO<sub>2</sub> being detectable in the stratum corneum, stratum granulosum, and the prickle cell layer, but not in the dermis. It has been shown that the ability of TiO<sub>2</sub> nanoparticles to penetrate skin is dependent on their size. Only nanoparticles with a diameter of 4 nm reached the deeper layer of the epidermis (the basal cell layer). The authors observe also some pathological changes in cellular structures.

To evaluate the potential toxicity of nanoTiO<sub>2</sub> particles after a relatively long-term dermal exposure, Wu et al. (Wu et al., 2009) examined several of the main rat organs including the skin, liver, spleen, and heart, in search of potential pathological changes. After 8 weeks of exposure to TiO<sub>2</sub> nanoparticles, skin sections from all treated groups showed excessive keratinization, and also other pathological changes such as thinner dermis and epidermis with wrinkles. Two other groups of rats treated either with anatase nanoparticles of 10 nm diameter, or 26 nm P25 Degussa particles (20% rutile, 80% anatase), showed more severe pathological changes in comparison with the control group. They also showed differences with respect to the group treated with micrometer-size TiO<sub>2</sub>. In the liver, histopathological changes were identified as focal necrosis (for TiO<sub>2</sub> particles with diameter of 25 nm and 60 nm, also for P25 Degussa) and liquefaction necrosis (10 nm sized TiO<sub>2</sub>) [**Fig. 8**].



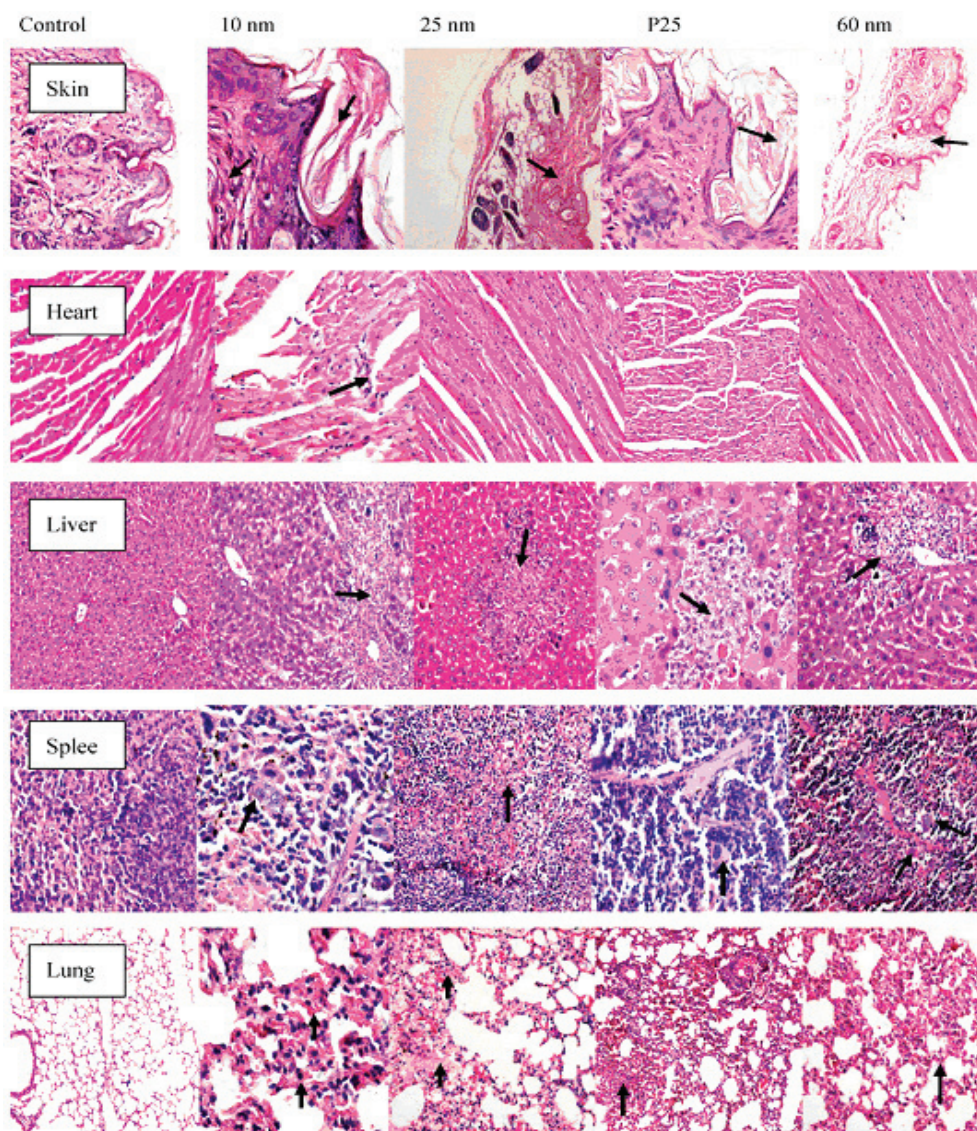


**Figure 8.** Histopathological evaluation of the organ of hairless mice after dermal exposure to different sized  $\text{TiO}_2$  nanoparticles for 60 days. Samples were stained with hematoxylin and eosin (H&E) and observed at  $100\times$ . The arrows points at pathological changes in various tissue sections (Taken from Wu et al., 2009). The marked histopathological changes corresponding to focal necrosis are visible for the tissues exposed to 25 and 60 nm particles, and for P25 Degussa. In contrast, liquefaction necrosis was observed for 10 nm sized  $\text{TiO}_2$ .

In the heart, lymphatic infiltration was found in the form of traces of white blood cells only in the group treated with particles of 10 nm size. This revealed that even though the heart is one of the most important organs, it was not significantly damaged by the accumulated  $\text{TiO}_2$  nanoparticles, except those of 10 nm size. In the spleen and lung tissues, minor lesions were observed as increased proliferation of local macrophages and small alveolar thickness, respectively. Moreover, it was shown that  $\text{TiO}_2$  micro-sized particles did not induce obvious pathologic lesions since the tissue morphologies from

these mice were similar to those of normal mice in the control group. In the brain, no abnormal histopathological lesion was observed; in the kidney, saccus lymphaticus (subcutaneous) histopathological lesions were found in all treatment groups.

Luke et al. (Luke et al., 2008) present the importance of the skin condition on the penetration of nanoparticles. They show that Quantum Dots (QDs, with diameter ~ 30 nm) pass between the corneocytes of the stratum corneum and penetrate deep in the epidermis and dermis [**Fig.9** and **10**] of an in vivo model with exacerbation of UV radiation penetration.

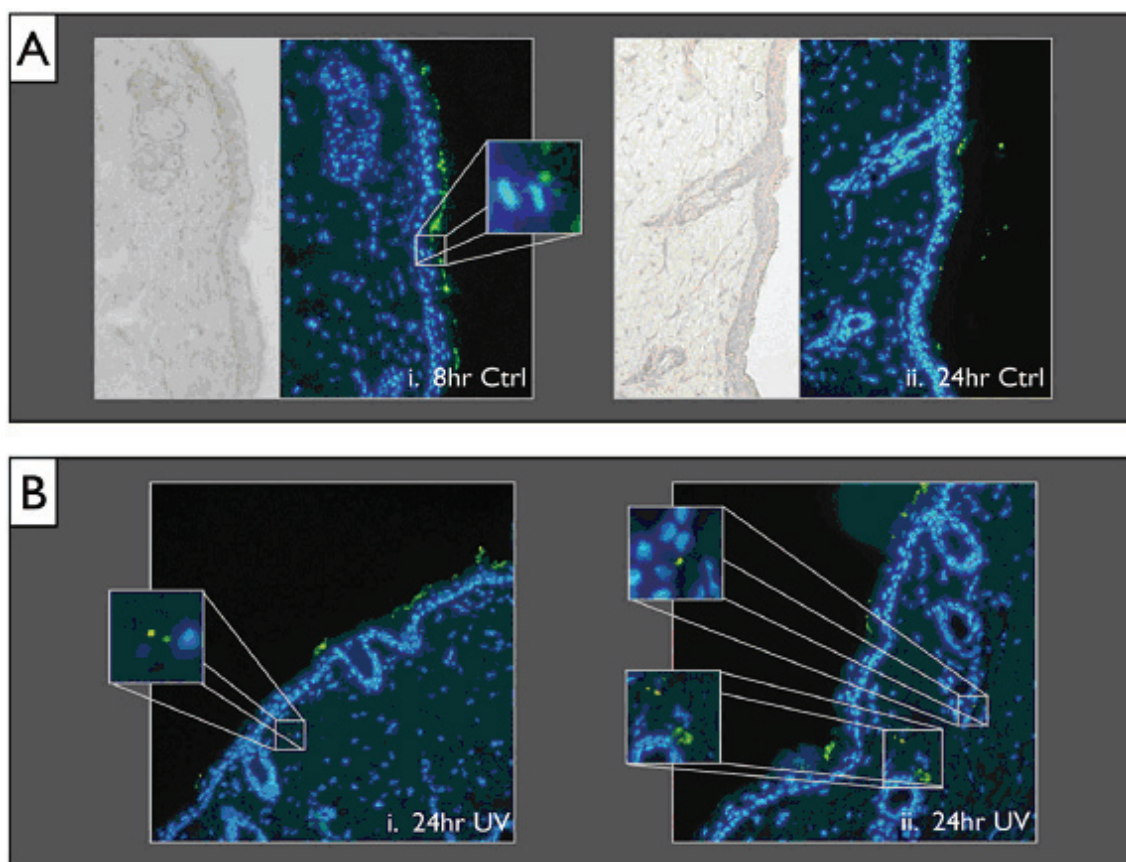


**Figure 9.** (A) Overview (20 $\times$  magnification) of the 8 h control (i) and 24 h control (ii). Perinuclear localization highlighted by magnified inset. Minimal presence of QD can be seen even in the lower stratum corneum layers. (B) Example slices of the 24 h UV radiation exposed mouse skin with high penetration areas in the dermis highlighted by magnified insets. (Taken from Luke et al., 2008)

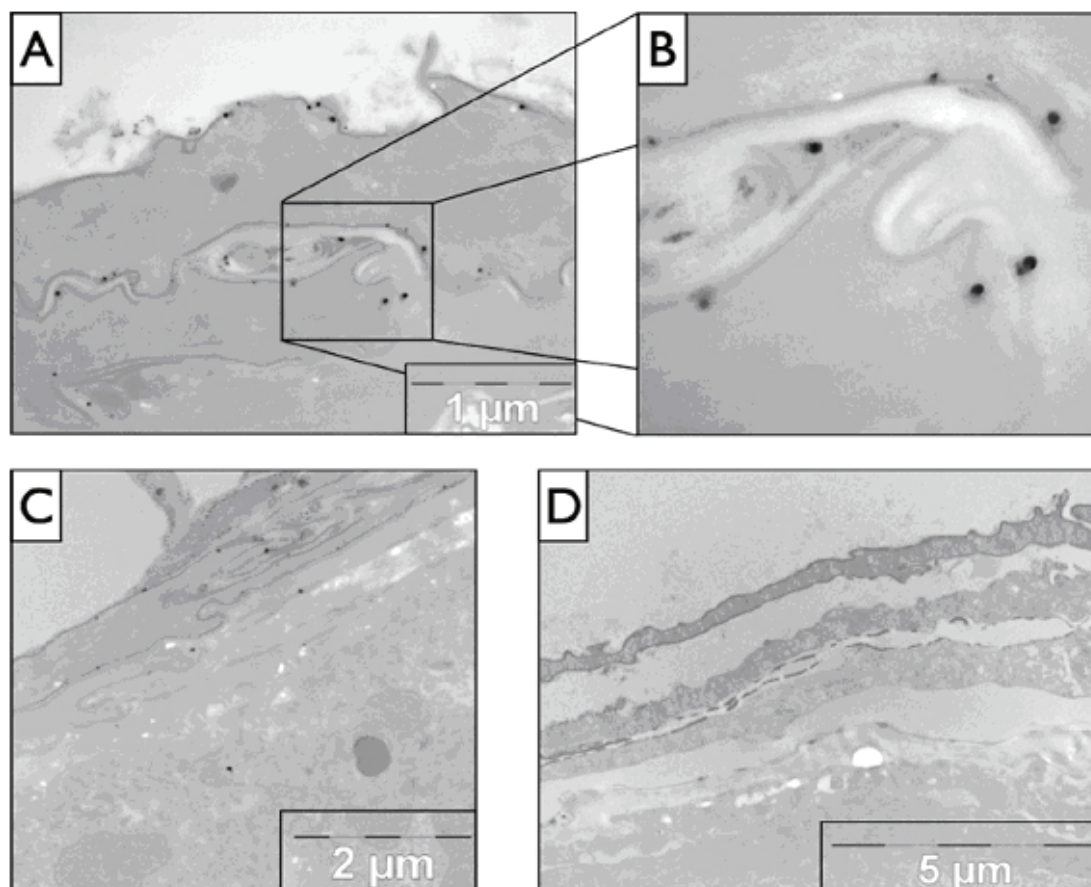


**Figure 10.** TEM images of 24 h UV radiation exposed mouse skin sections. (A) The penetration pathway through the skin can be clearly seen and is shown in more detail in B with the large dark spots being the NP's. (C) Another section of skin demonstrating the penetration pathway and with an example silver enhanced QD present in the epidermal layer. (D) The negative control (no QD, glycerol only) of silver enhanced mouse skin 24 h UV radiation exposure. (Taken from Luke et al., 2008)

They also suggested that UV radiation induced an outside-in barrier defect, likely due to a loss of epidermal calcium gradient and resultant stratum corneum lipid disruption, as well as through loosening of cell-cell junctions that down-regulate following an acute UV radiation exposure. The minimal QD penetration that was observed on barrier intact (non-UV radiation exposed) skin supports the preponderance of current literature which suggests that  $\text{TiO}_2$  and  $\text{ZnO}$  nanoparticles used in commercial sunscreens exhibit limited penetration in layers below the lower stratum corneum.

This is an important discovery for nanoparticle safety, since consumers often apply sunscreens containing metal oxide nanoparticles of similar size (~20- 30 nm).

### II.3. Titanium dioxide in circulatory system – toxicity and tissue distribution

The understanding of the kinetics, distribution, and toxicity of intravenously administered nanoTiO<sub>2</sub> particles in a situation of 100% bioavailability is also very important. In particular, Scown et al. (Scown et al., 2009) performed short-term injection studies on rainbow trout, revealing that intravenously injected nanoTiO<sub>2</sub> particles accumulated in the kidney and liver. Trace metal analysis of the trout tissues showed that 10–19% of injected titanium accumulated in the trout kidneys, equivalent to a nanoTiO<sub>2</sub> concentration in the kidneys of 22.81 µg/g ± 1.23 µg/g (mean ± standard error (SE)) and very low concentration in blood [Fig.11]. Long-term accumulation of nanoTiO<sub>2</sub> particles was observed in liver and kidney during a period of 90 days. In contrast, there were no detectable levels of TiO<sub>2</sub> in plasma, brain and gills.

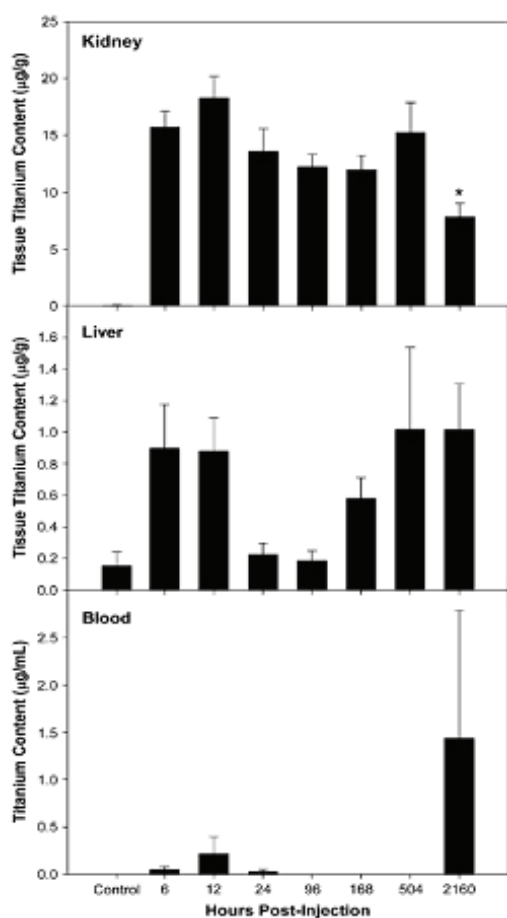


**Figure 11.** Titanium levels in the kidney, liver, and blood of trout at sampling time points from 6 h to 90 days after intravenous injection of nanoTiO<sub>2</sub> (34.2 nm). Data are means ± SE. \*Significantly different from 6, 12, and 504 h. (Taken from Scown et al., 2009) Long-term accumulation of nanoTiO<sub>2</sub> over a period of 90 days was observed in liver and kidney.

TEM examination of the kidney tissue showed the presence of aggregates of nanoparticles in cells surrounding the kidney tubules [Fig.12].

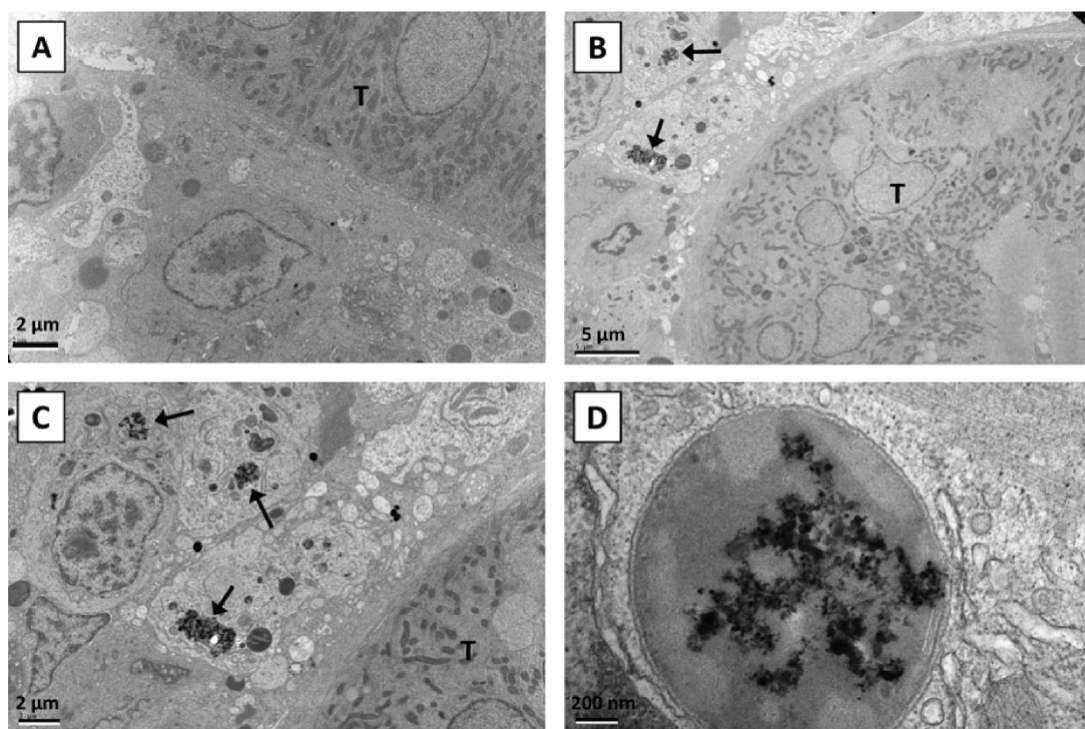


**Figure 12.** TEM images of kidney tissues dissected from rainbow trout 3 weeks after intravenous injection of 1 ml of trout perfusion ringer (A) or 100  $\mu\text{g}$   $\text{TiO}_2$  nanoparticles (34.2 nm) in 1 ml of trout ringer (B–D). (B, C) Clusters of nanoparticles, indicated by arrows, are visible in tissue surrounding the kidney tubule T. (D) A cluster of nanoparticles in a membrane-bound vesicle. (Taken from Scown et al., 2009)

Measurements performed *in vitro* on animal and human blood by several groups also shows an adverse effect on blood cells. Li et al. (Li et. al, 2008) showed that nano $\text{TiO}_2$  has seriously deleterious effect on erythrocyte in a dose-dependent way. Firstly, the nano $\text{TiO}_2$  particles were adsorbed to the erythrocyte membrane due to their high surface-volume ratio [Fig.13]. Once the majority of the surface area was covered by nano $\text{TiO}_2$ , erythrocyte showed a tendency to agglutinate, resulting in membrane deformation [Fig.14], which decreases the repulsion among erythrocytes. This observation was confirmed by the change of the erythrocyte's shape from bi-concave to the modified one with aggravated hemoagglutination (Li et al., 2008).

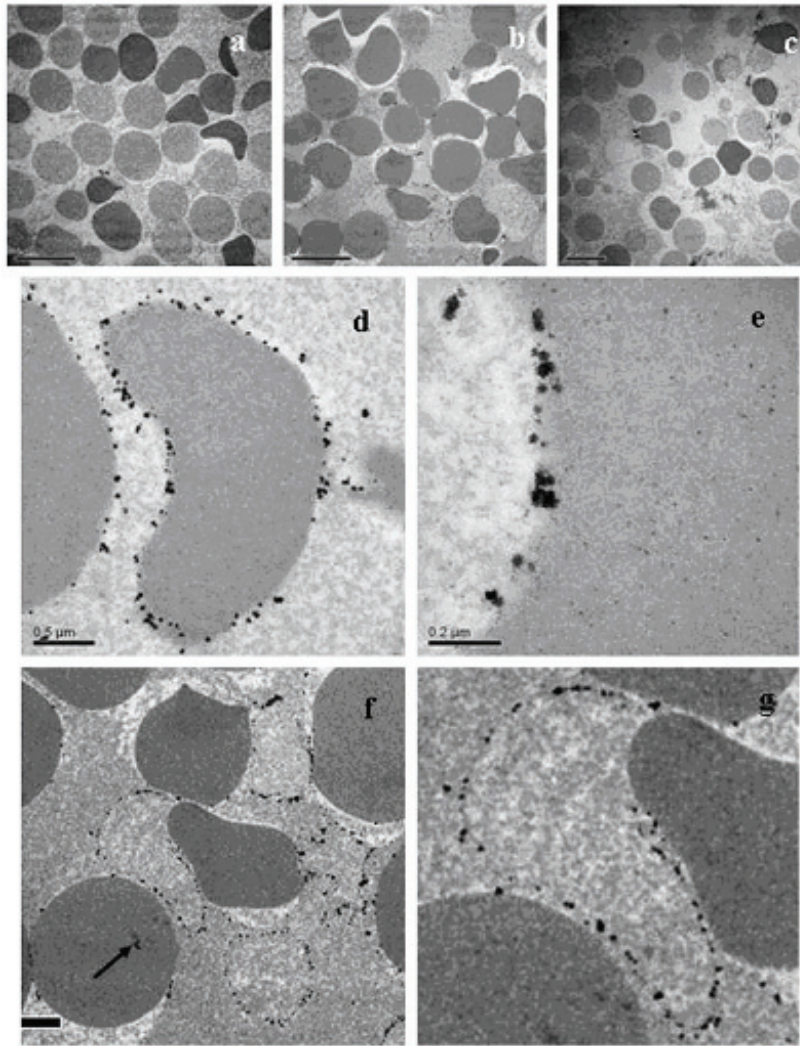


**Figure 13.** Ultra-thin section of erythrocyte under exposure to nanoTiO<sub>2</sub> analyzed by TEM. (a) Erythrocyte + PBS, (b) erythrocyte + nanoTiO<sub>2</sub> (100 µg/ml, 20 nm in diameter), (c) erythrocyte + microTiO<sub>2</sub> (100 µg/ml, 200 nm in diameter), (d, e, f, and g) erythrocyte + nanoTiO<sub>2</sub> (100 µg/ml) at higher magnification. NanoTiO<sub>2</sub> aggregate was found to be attached along the membrane of erythrocyte (Fig. 13b), with only a few within the erythrocyte (black arrow, Fig. 13f). MicroTiO<sub>2</sub> can be seen as small dark spots close to the erythrocyte membranes (Fig. 13c). At higher magnification, the nanoTiO<sub>2</sub> was seen to insert into the membrane (Fig. 13e). Ghost cells (Fig. 13f, g) were found in erythrocytes exposed to nanoTiO<sub>2</sub>. (Taken from Li et al., 2008)

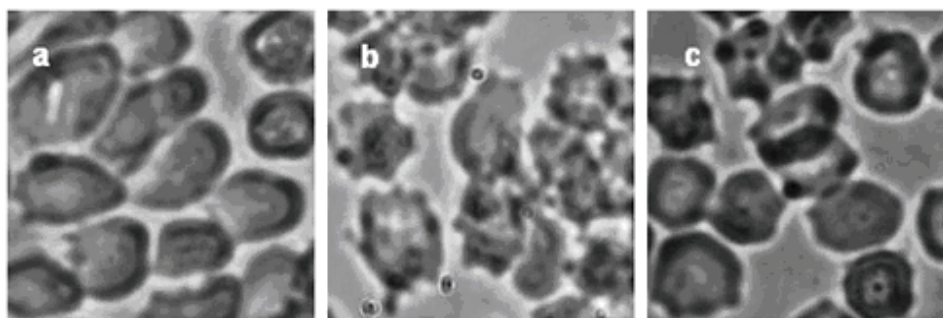


**Figure 14.** Erythrocyte morphology after exposure to TiO<sub>2</sub> particles. (a) erythrocyte + PBS, (b) erythrocyte + nanoTiO<sub>2</sub> (100µg/ml, 20 nm in diameter), (c) erythrocyte+microTiO<sub>2</sub> (100µg/ml, 200 nm in diameter). NanoTiO<sub>2</sub> attachment-deformed erythrocytes with surface herniations (Fig. 14b). The effect is more pronounced than for microTiO<sub>2</sub> (Fig. 14c). (Taken from Li et al., 2008)

## **II.4. Oral administration of TiO<sub>2</sub> – acute toxicity and biodistribution**

Another potential exposure route can be linked with oral ingestion: TiO<sub>2</sub> particles are used as food additives in sugar products such as candy, icing, chewing gum, toothpaste. They are also used in low-or no-fat products, such as coffee creamer, salad dressings, cheese, whey, etc. The quantity of titanium dioxide in these products should not exceed 1% by weight of the food according to the Federal Regulations of the US Government.

Most studies on the toxicity of TiO<sub>2</sub> particles in mammals were focused on dermal exposure to or inhalation of TiO<sub>2</sub> nanoparticles. In contrast, there is much less information on the impacts of oral exposure to nanoTiO<sub>2</sub>, neither on its quantitative distribution *in vivo*. Wang et al. investigated the characteristic changes in tissue weight, histopathology, the biochemical parameters of the blood, and the distribution of titanium dioxide nanoparticles (25 and 80 nm) in tissues after administration *via* the gastrointestinal tract in mice (Wang et al., 2007). Blood samples were collected from the eye vein. Serum was harvested by centrifuging blood at 2500 rpm for 10 minutes, and red cells were kept for analyzing titanium content. The tissues and organs, such as the heart, liver, spleen, kidneys, lung, brain, and testicle (ovary), were excised and weighed accurately. In the study, liver function was evaluated with serum levels of total bilirubin levels (TBIL), alkaline phosphatase (ALP), alanine aminotransferase (ALT) and aspartate aminotransferase (AST). Nephrotoxicity was determined by uric acid (UA), blood urea nitrogen (BUN) and creatinine (Cr). The enzymes creatine kinase (CK), lactate dehydrogenase (LDH) and alpha-hydroxybutyrate dehydrogenase (HBDH) were assayed to evaluate cardiac damage. It is well known that both LDH and alpha-HBDH are common markers of cardiovascular damage or liver diseases. Generally, a high LDH level shows myocardial lesion when combined with CK and alpha-HBDH, and hepatocellular damage is expressed when combined with AST and ALT enzymes

In their experiment, Wang et al. (2007) showed that nanoTiO<sub>2</sub> particles induce more severe myocardial damage than fine particles. They also performed histopathological assays to check the changes of the brain, kidneys, liver and stomach [Fig.15-18]. The liver, as the main detoxification tissue, is activated to eliminate the side

effects induced by mass ingested TiO<sub>2</sub> particles. Some of these particles should also be excreted by the kidneys. Wang et al. (2007) observed in their work that the small size and difficult clearance of 80 nm TiO<sub>2</sub> particles resulted in long-time retention of nanoparticles in vivo and induced damage of liver and kidneys after oral exposure to 5 g/kg TiO<sub>2</sub> particles. In particular, in the liver tissue, the measured accumulation of 80 nm sized TiO<sub>2</sub> particles was ca. 30 times higher than that of 155-nm sized particles [Fig.15-18].

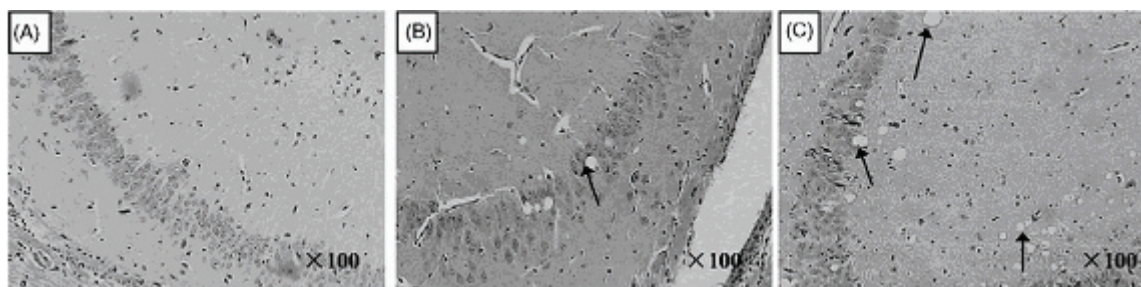


**Figure 15.** Histopathology of brain tissue (100×) in female mice 2 weeks post-exposure to different sized TiO<sub>2</sub> particles by a single oral administration of control group (only exposure to 0.5% HPMC) (A), 80 nm group (B), and fine (155 nm) group (C). Arrows indicate the fatty degeneration of hippocampus in the brain tissue. (Taken from Wang et al., 2007)

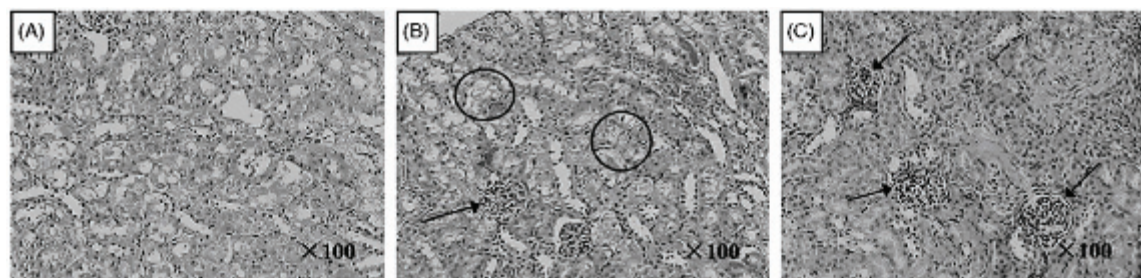


**Figure 16.** Histopathology of kidney tissue (100×) in female mice 2 weeks post-exposure to different sized TiO<sub>2</sub> particles by a single oral administration of control group (only exposure to 0.5% HPMC) (A), 80 nm group (B), and fine (155 nm) group (C). Circles indicate the proteinic liquid in the renal tubule; arrows indicate the swelling in the renal glomerulus. (Taken from Wang et al., 2007)



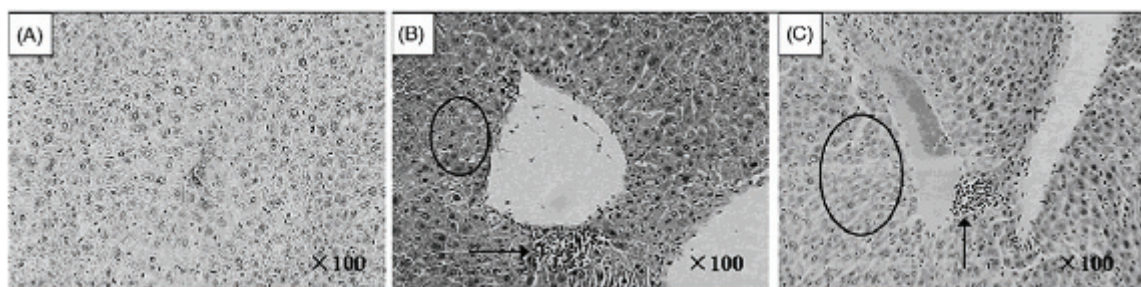


**Figure 17.** Histopathology of liver tissue (100×) in female mice 2 weeks post-exposure to different sized TiO<sub>2</sub> particles by a single oral administration of control group (only exposure to 0.5% HPMC) (A), 80 nm group (B), and fine (155 nm) group (C). Circles indicate the hydropic degeneration around the central vein; Arrows indicate the spotty necrosis of hepatocytes. (Taken from Wang et al., 2007)

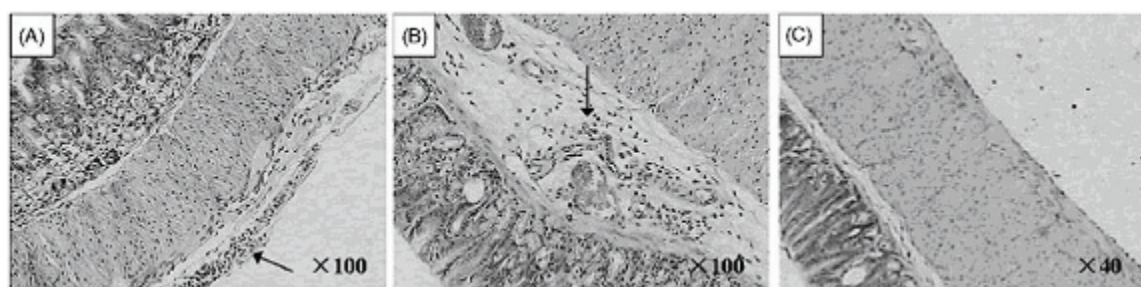


**Figure 18.** Histopathology of stomach tissue (100× for A and B; 40× for C) in female mice 2 weeks post-exposure to different sized TiO<sub>2</sub> particles by a single oral administration of control group (only exposure to 0.5% HPMC) (A), 80 nm group (B), and fine (155 nm) group (C). Arrows indicate the inflammation cells. (Taken from Wang et al., 2007)

Moreover, the epidemiological study reported that a papillary adenocarcinoma was located in the lung of a 53-year-old male, who was engaged in packing titanium dioxide for about 13 years. Titanium dioxide was diffusely deposited in the lung and was engulfed by macrophages in the interstitium and alveolar spaces. Slight fibrosis of the interstitium around bronchioles and vessels was also observed (Yamadori et al., 1986). In animal studies, exposure of rats to titanium dioxide for 2 years by inhalation revealed a dose-dependent accumulation of TiO<sub>2</sub> dust in cells, a foamy macrophage response, type II pneumocyte hyperplasia, alveolar proteinosis, alveolar bronchiolarization, cholesterol granulomas, focal pleurisy, bronchioloalveolar adenomas and cystic keratinizing squamous cell carcinomas (Borm et al., 2004).

In brief, the above-cited literature data point to a high potential toxicity of nano- and micro-sized TiO<sub>2</sub>. Adverse effects of the exposure to TiO<sub>2</sub> particles were found for a

wide spectrum of human and animal cells and tissues. Although these numerous studies testify the toxicity of nano- and micro-sized TiO<sub>2</sub>, much less is known about the detailed mechanisms of the deleterious action of these materials. Therefore, one of the goals of this thesis was to pinpoint the primary processes and early damages occurring when TiO<sub>2</sub> nanoparticles are brought into contact with living cells.

### **III. The cell**

All living creatures are made of cells – small membrane-bounded compartments filled with a concentrated aqueous solution of chemicals. The simplest forms of life are solitary cells that propagate by dividing in two. Higher organisms, such as ourselves, are built of groups of cells which perform specialized functions and are linked by intricate systems of communication. The fact that the cell is the fundamental unit of biological organization originated in seventeenth century with the microscopic observations of Hooke and Leeuwenhoek (Enc. Brit. 2010). Cells are small and complex units, which are able to consume energy from their environments and use it to create ordered structures. They can also harness energy and materials from the environment to create new cells. It is difficult to see the structure of cells, hard to discover their molecular composition, and harder to find how their various components function.

### III.1. Basic biology of cells

Eukaryotic (animal) cells [Fig. 1] are typically 10 to 100  $\mu\text{m}$  in diameter (Campbell Neil A., 1991). At their core is a *nucleus* (“*caryon*” in Greek), which contains most of the cell’s DNA, enclosed by a double layer membrane, the so-called nuclear envelope. The entire region between the nucleus and the membrane bounding the cell is called the *cytoplasm*. It consists of a semifluid medium called the *cytosol*, in which are suspended organelles of specialized form and function. Internal membranes in a eukaryotic cell serve as partitions, dividing the cell into compartments, which allows different processes to go on simultaneously.

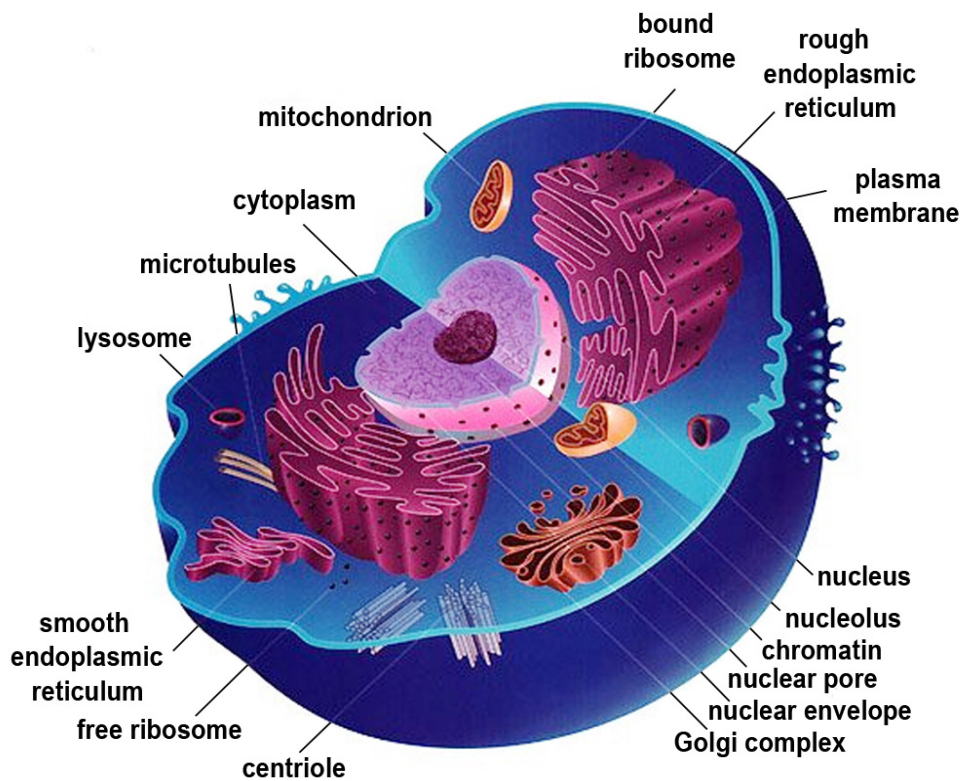


**Figure 1.** Eukaryotic (animal) cell. (Adapted from: [http://www.malebolge.net16.net/science10/animal\\_cell.gif](http://www.malebolge.net16.net/science10/animal_cell.gif))

Biological membranes consist of a double layer of lipids, in which diverse proteins are embedded. A scheme of the plasma membrane is presented in **Figure 2**.

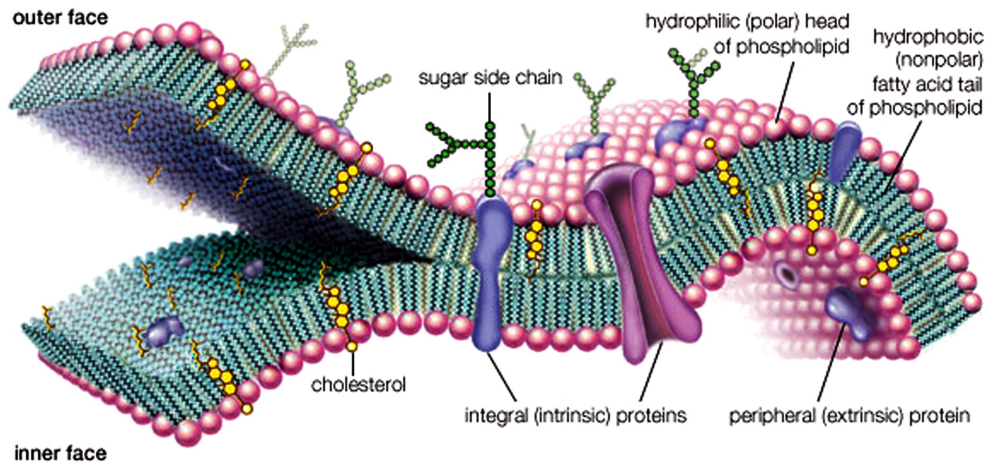


**Figure 2.** Plasma membrane – a continuous sheet of bilayer of phospholipid molecules, about 4 - 5 nm thick, with various proteins embedded.  
(Taken from: <http://www.britannica.com/EBchecked/topic-art/463558/45550/A-molecular-view-of-the-cell-membrane-Intrinsic-proteins-penetrate>)

Biological lipids are a chemically diverse group of compounds. One of the main types are phospholipids [Fig. 3], which are amphipathic – one end of the molecule is hydrophobic whereas the other hydrophilic. Their hydrophobic interaction with other lipid molecules and hydrophilic one with water defines their packing into sheets called membrane bilayers.

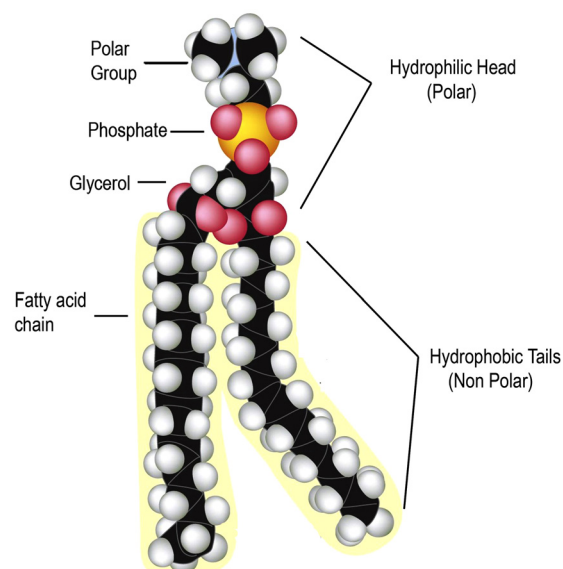


**Figure 3.** Phospholipid molecule (Bruce Alberts et al., 1994).

The typical cell is composed of several organelles. The structure and function for the most important ones are presented below.

The *nucleus* [Fig. 4] is the most conspicuous organelle in the cell with an approximate diameter of 5  $\mu\text{m}$ . It contains most of the genes that control the cell (some genes are located in the mitochondria). The *nuclear envelope* (double-layer membrane) encloses the nucleus, separating its contents from the cytoplasm. The entire chromosomal DNA is held in the nucleus, packed into chromatin fibers. The nuclear contents communicate with the cytosol by means of openings in the nuclear envelope called *nuclear pores*. The most visible structure in the nucleus is the *nucleolus*, which functions in the synthesis of *ribosomes*. In ribosomes, the cell assembles proteins according to genetic instructions. The ribosome is generally considered the cell's smallest organelle. It is not enclosed by a membrane and exists in two forms, i.e. free and bound ribosomes. *Free* ribosomes are suspended in the cytosol while *bound* ribosomes are attached to the *endoplasmic reticulum* (ER) (Bruce Alberts et al., 1994). The ER consists of a network (Latin *reticuli*) of membranous tubules and sacs called *cisternae* (Latin *cisterna* - box) and is continuous with the nuclear envelope. It specializes in the synthesis and transport of lipids and membrane proteins.

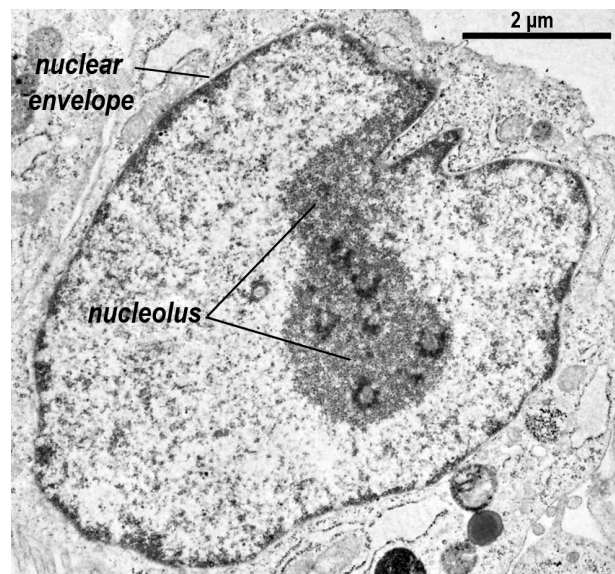


**Figure 4.** Electron micrograph of a thin section of the nucleus of a human cell, showing the nuclear envelope and nucleolus. (Taken from E.G. Jordan and J. McGovern)

Transport vesicles, which leave the ER, travel to the *Golgi apparatus* (*Golgi complex*), where the products of the ER are modified, stored, and then sent to other destinations. The Golgi apparatus is composed of numerous sets of smooth *cisternae*, which are coated with lipid membranes. Each disc-shaped *cisternae* forms a structure that resembles a stack of plates, called a *Golgi stack*.

A *lysosome* is a membrane-bound vesicle of hydrolytic enzymes (~ pH 5) that are involved in intracellular digestion (hydrolysis of proteins, polysaccharides, fats, and nucleic acid). The hydrolytic enzymes and lysosomal membrane are made by the ER and then transferred to a Golgi complex for further processing.

The *peroxisome – microbody* is a specialized metabolic compartment bounded by a single membrane. It contains oxidative enzymes that generate and destroy hydrogen peroxide.

The *mitochondrion* is enclosed in an envelope of bilayer phospholipid membrane with an embedded collection of unique proteins. Mitochondria are the power centers of the cell, providing adenosine triphosphate (ATP), a source of chemical energy. The cell uses this energy for several processes including movement, signaling, cellular differentiation, cell death, and control of the cell cycle and cell growth (McBride et al., 2006).

The *cytoskeleton* gives mechanical support to the cell and helps to maintain cell shape [**Fig. 5**]. The cytoskeleton also organizes other constituents of the cell, enabling the cell to change its shape. Like a scaffold, the cytoskeleton can be dismantled in one part of the cell and reassembled in a new location. It is also associated with cell motility: the locomotion of the cell itself and the movement of the various organelles within it.

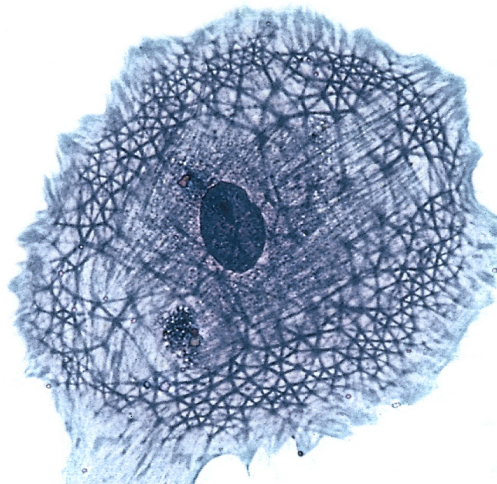


**Figure 5.** The cytoskeleton – a complex network of intermediate filaments, actin, and microtubules, all of them stained with Coomassie Blue. (Taken from Weinberg, 2007)

The cytoskeleton is constructed from at least three types of fibrous biopolymer [**Fig. 6**], which effectively act as structural elements in the cell's cytoskeleton. These components, i.e. microfilaments, intermediate filaments and microtubules, play a major role in the

mechanics of the cell (K.D. Costa, 2003). *Microtubules* [Fig. 6A] are the thickest of the three types of these fibers. They are straight, hollow rods, having ~25 nm diameter, and 200 nm to 25  $\mu\text{m}$  length. The wall of the hollow tube is constructed from globular proteins ( $\alpha$  and  $\beta$  tubulin). A microtubule can elongate by the addition of tubulin on one end of the tubule and can be disassembled and used to build microtubules elsewhere in the cell (Campbell Neil A., 1991).

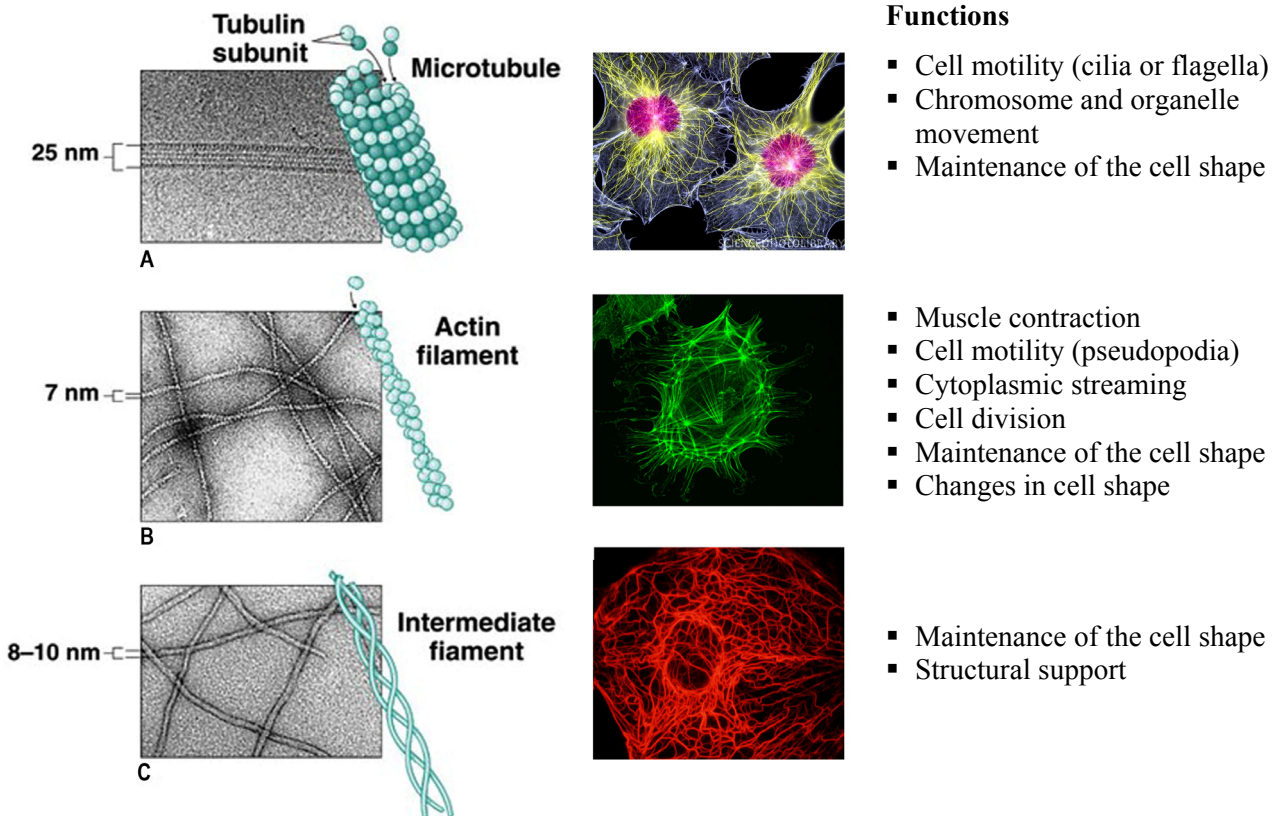


**Figure 6.** The structure and function of the cytoskeleton.

*Microfilaments* [Fig.6B], also called *actin filaments*, are the thinnest. Actin filaments are solid two stranded helical rods about 5-9 nm in diameter built of actin, a globular protein. In cells, there are large numbers of actin-binding proteins, which can trigger or inhibit the formation of filaments, disassemble filaments, or determine the architecture of the network. Prominent examples of actin-binding proteins are  $\alpha$ -actinin (bundler), gelsolin (severs filaments, binds to monomers), filamin (cross-links filaments), myosin (slides along filaments), myosin II (cross-links filaments), and spectrin (attaches filaments to the plasma membrane) (Hartwig and Kwiatkowski, 1991). Actin filaments may organize 2D networks and 3D gels. Actin filaments are dispersed throughout the



cell, but their highest concentration is in *cortex*, just beneath the plasma membrane. *Intermediate filaments* [Fig.6C] are ropelike filaments with a diameter about 8-12 nm and comprise a diverse class of cytoskeletal elements, with a heterogeneous protein composition differing from one type of cell to another (Bruce Alberts et al., 1994).

## **III.2. The biology of cancer**

### ***Definition of Cancer***

Cancer is an abnormal growth of cells caused by multiple changes in gene expression leading to a dysregulated balance of cell proliferation and cell death, ultimately evolving into a population of cells that can invade tissues and metastasize to distant sites, causing significant morbidity and, if untreated, death of the host (Ruddon, 2007).

### **III.2.1. Description of Cancer**

Cancer is a group of diseases which occur in multicellular organisms. At the cellular level, the most important characteristics of cancer cells versus normal cells are alterations in the expression of multiple genes, leading to dysregulation of the normal program for cell proliferation, differentiation and homeostasis. This results in an imbalance of cell replication and cell death that favors growth of a tumor cell population.

The characteristic differences between a malignant cancer and benign tumor is the ability of the former to invade locally, enter the bloodstream or spread to regional lymph nodes (Fisher et al., 1966; Fidler, 2003), and form secondary tumor or metastases at distant organs in the body [Fig. 7]. Thus, a tumor is counted as a cancer only if it is malignant (Ruddon, 2007; Campbell, 1991). Tumor cells can spread by direct extension into a body cavity, such as the pleural or peritoneal space, or the cerebrospinal fluid. In these cases, tumor cells released into the body space can seed out onto tissue surfaces and develop. Examples of this are lung cancers that enter the pleural cavity, ovarian cancers that shed cells into the peritoneal cavity, and brain tumors that shed cells into cerebrospinal fluid.

The mechanisms for invasion of tumor cells through tissue barriers and into blood and lymphatic vessels are not well understood, but they appear to involve both mechanical and enzymatic processes.

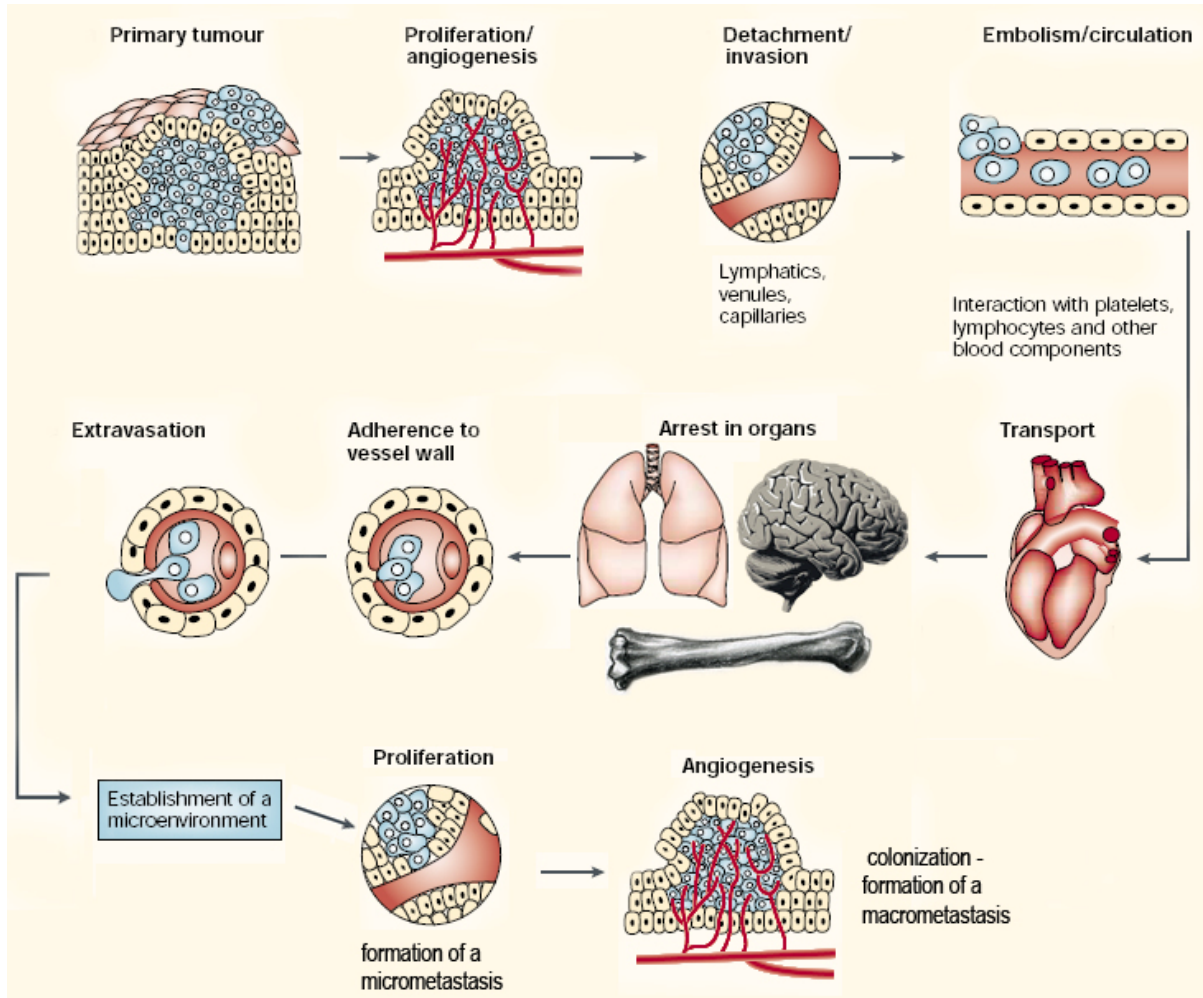


**Figure 7.** The main steps in formation of metastasis – the metastasis cascade. (Adapted from Fidler, 2003)

Clinically, various cancers appear with different phenotypic characteristics. Cancers are classified according to the tissue and cell type from which they arise. Cancers arising from epithelial cells are termed *carcinomas*, and those which arise from connective tissue or muscle cells are termed *sarcomas*. Cancers which do not fit in either of these two broad categories include the various *leukemias* derived from hemopoietic cells and cancers of the nervous system.

### III.2.2. Basic Facts about Cancer

Cancer is a complex family of diseases. Carcinogenesis, which is a series of events that turn a normal cell into a cancerous one, is a multistep process. Some of the more than 100 types of human cancer have a high proportion of tumors which are caused by random, unavoidable accidents of nature and thus occur with comparable frequencies in various human populations. In addition, the environment in which people live may contribute enormously to disease incidence rates.

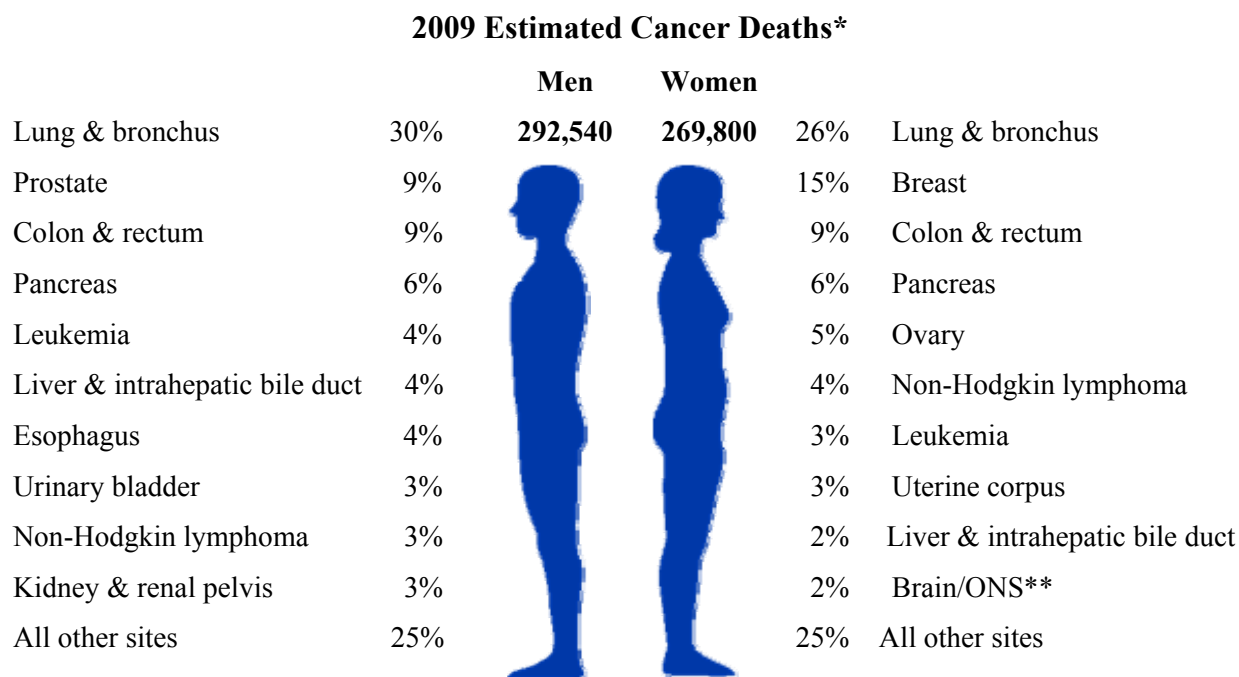
**Table 1.** US Mortality Data in 2006. (Source: National Center for Health Statistics, Centers for Disease Control and Prevention, 2009)

<b>Rank</b>	<b>Cause of Death</b>	<b>No. of deaths</b>	<b>% all deaths</b>
1.	Heart Diseases	631,636	26.0
<b>2.</b>	<b>Cancer</b>	<b>559,888</b>	<b>23.1</b>
3.	Cerebrovascular diseases	137,119	5.7
4.	Chronic lower respiratory diseases	124,583	5.1
5.	Accidents (unintentional injuries)	121,599	5.0
6.	Diabetes mellitus	72,449	3.0
7.	Alzheimer disease	72,432	3.0
8.	Influenza & pneumonia	56,326	2.3
9.	Nephritis*	45,344	1.9
10.	Septicemia	34,234	1.4

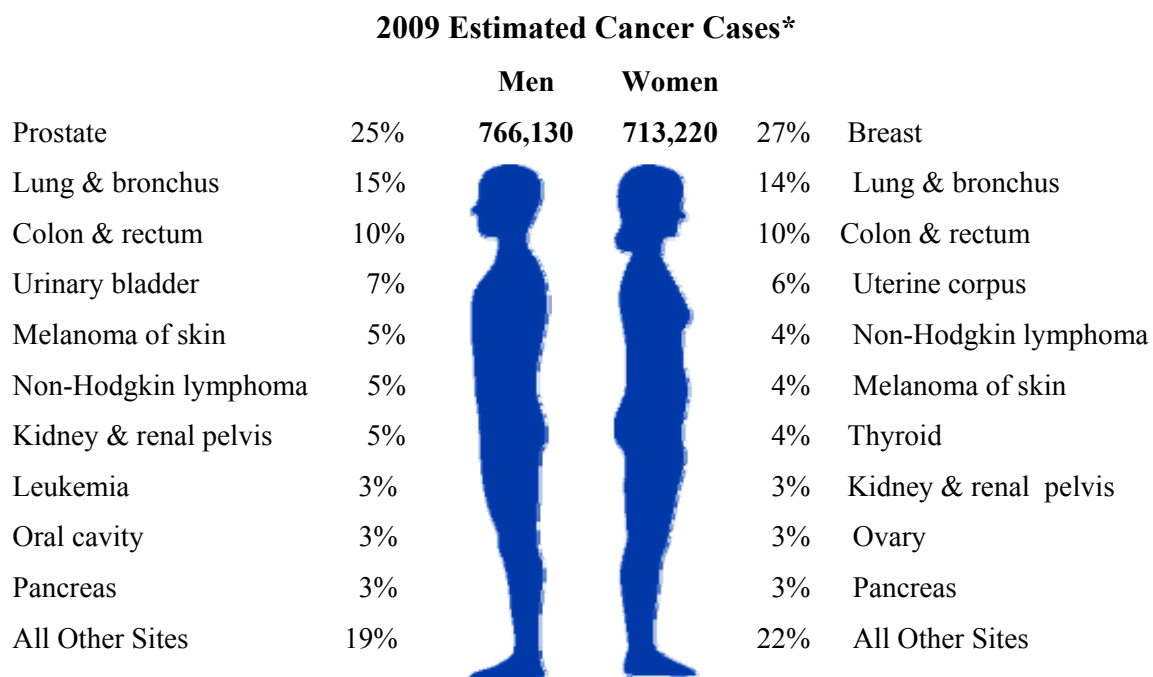
\* Includes nephrotic syndrome and nephrosis.

Cancer is one of the leading causes of death in the Western world. In the United States and a number of European countries, cancer is the second-leading killer after cardiovascular disease [Table 1], although in the US, since 1999, cancer has surpassed heart disease as the number one cause of death in people younger than 85.

**Table 2.** Ten leading cancer types for estimated new cancer cases and deaths, grouped by sex, in United States in 2009 (Source: American Cancer Society, 2009).



\*\*ONS=Other nervous system.



\*Excludes basal and squamous cell skin cancers and in situ carcinomas except urinary bladder.

The highest mortality rates are seen with lung, colorectal, breast, and prostate cancers [Table 2]. Melanoma is a type of skin cancer that is one of the most aggressive and proliferating cancers, which can spread to other organs, such as liver, lungs, lymph nodes, gastro-intestinal tract, etc., where it can be fatal.

### III.2.3. Causes of Cancer

One of the most important questions concerning cancer is: “*what causes the cellular alternations that produce a cancer?*” The nature of cancer suggests that it is a disease of chaos, a breakdown of existing biological order within the body. About  $10^{16}$  cell divisions which take place in a human body in the course of lifetime and even in an environment free of mutagens, mutation will occur spontaneously at an estimated rate about  $10^{-6}$  mutation per gene per cell division, which means almost  $10^7$  events per second (Weinberg, 2007) – a value set by the fundamental limitation on the accuracy of DNA replication and repair (Cairns, 1975). Evidently a single mutation is not enough to convert a typical cell into a cancer.

The evidence that many types of cancer might be associated with specific exposures or lifestyles was reported for the first time in 1567 when Paracelsus described a “*wasting disease of miners*”, and proposed that exposure to something in the mined ores caused the diseased condition (Ruddon, 2007). Later, in the eighteenth century, the first direct observation associating chemicals with cancer was made by John Hill, a British physician, who in 1761 noted the connection between the excessive use of tobacco snuff and development of nasal cancer. Fourteen years later, in 1775, Percivall Pott, a surgeon in London, concluded that the high incidence of cancer of the nasal cavity and skin cancer of the scrotum in adolescent men who had worked as chimney sweeps was due to chronic exposure to soot. In 1838 an Italian physician reported that breast cancer rates in the nunneries were six times higher than among women in the general population who had given birth multiple times (Karp, 1997; Weinberg, 2007).

More recently, it has been shown that chemicals and irradiation (ionizing and ultraviolet) affect DNA and can be mutagenic in certain conditions. The standard concept of how cancer starts is that a malignant tumor arises from a single cell transformed by a chemical carcinogen, oncogenic virus, radiation damage, endogenous genetic damage caused by oxidative insult to DNA, chronic infection with bacteria (e.g. *Helicobacter pylori*) or hormonal imbalance (Luch, 2005).

### **III.2.4. Cellular responses and oncogenic consequences associated with ultraviolet radiation**

UV rays are directly mutagenic and carcinogenic for the human skin: the incidence of squamous cell skin carcinoma doubles with each 10° decline in latitude, reaching its peak at the equator, where the cumulative UV exposure is highest. Irradiation with UV-B ( $\lambda = 280 - 320$  nm), which is strongly absorbed by DNA, mostly produces cyclobutane pyrimidine dimers (CPDs). UV-A radiation ( $\lambda = 320 - 400$  nm) is poorly absorbed by DNA, and produces predominantly oxidative lesions by photosensitization mechanisms. The resulting DNA damage is converted to mutation during cellular repair processes (Merlino, 2003). Both UV-A and UV-B generate different types of DNA damage and induce diverse DNA repair mechanisms.

For most cancers, the relevant environmental carcinogens have not been identified. One major exception is cutaneous malignant melanoma, for which the primary environmental agent is solar ultraviolet radiation (Merlino, 2003). The irradiation mainly activates tyrosine kinases receptors, but also other cell surface receptors. It enhances phosphorylation by ligand-independent mechanisms *via* inhibition of protein tyrosine phosphatase activity. Ligand-dependent activation of cell surface receptors can arise by activation of autocrine or paracrine release of growth factors from keratinocytes, melanocytes, or neighboring fibroblasts.

Strongly oxidative agents, also called reactive oxygen species (ROS) may be formed either during normal metabolic processes in cells, or as a consequence of a irradiation. These include superoxide  $O_2^{\bullet-}$  and hydroxyl  $OH^{\bullet}$  radicals, singlet oxygen ( $^1\Delta_g$ ), and hydrogen peroxide  $H_2O_2$ . They are capable of damaging DNA and inducing mutagenesis. The skin shields itself from UV-B radiation using the melanin pigment that is donated by melanocytes to keratinocytes located in the basal region of the epidermis (Ruddon, 2007) [Fig. 8]. The ambushing of ROS is the job of a variety of enzymes, including superoxide dismutase and catalase. They collaborate to detoxify ROS to unreactive forms of oxygen. The ROS may be also intercepted by a series of free radical scavengers, including vitamin C,  $\alpha$ -tocopherol (vitamin E), bilirubin, and urate.

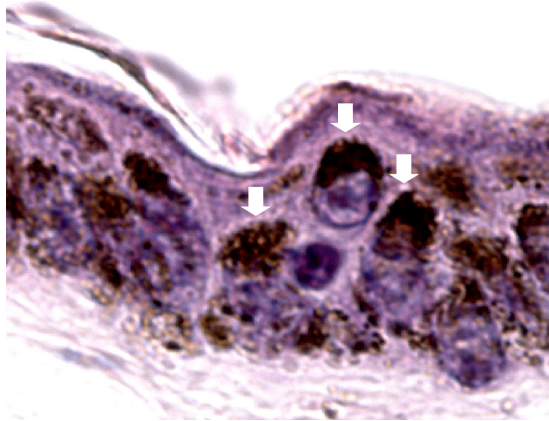


**Figure 8.** Physical shielding of keratinocyte nuclei from UV radiation. The white arrows indicate agglomerations of melanin on the surface of keratinocytes. (Taken from Weinberg, 2007)

Apoptosis (programmed cell death) often occurs in response to DNA damage and other forms of stress. Acquisition of the ability to prevent this programmed cell death is a key event in tumor progression. Normal melanocytes are relatively resistant to cell death caused by UV radiation (Gilchrest et al., 1999). Similarly, melanoma cells tend to be resistant to chemotherapy-induced apoptosis (Hersey and Zhang, 2001).

The p53 protein (a tumor suppressor protein) is involved in regulation of the repair of both UV-B and UV-A-initiated DNA damage. Soengas et al. reported that metastatic melanoma cells can escape p53-dependent apoptosis through a deficiency in apoptotic-protease activating-factor-1, thereby producing a chemoresistant phenotype (Soengas et al. 2001). The p16<sup>INK4a</sup> and p14<sup>ARF</sup> proteins regulate the retinoblastoma protein (pRB-tumor suppressor protein) and p53, respectively, and these in turn link pathways that control the cell cycle, senescence and apoptosis (Chin et al., 1998).

### III.2.5. Melanoma cell lines

Melanoma is known as the most lethal form of skin cancer because it accounts for 77% of all deaths from skin cancer. Studies have shown that melanoma can easily spread from the primary tumor. The cancer cells first pass through the lymph channel nearest the melanoma, and proceed from there to almost any organ of the body. This, indeed, represents a wider variety of attacked areas than for any other cancer [Table 3]. Metastases in the brain usually occur in the late stage of the disease and carry the worst prognosis, with an average survival rate of only 4 months. Melanoma may also recur.

**Table 3** shows the organs towards which melanoma is most likely to travel once it spreads.

**Table 3.** Locations of melanoma secondary sites. (Source: Meyers ML, Balch CM. “Diagnosis and Treatment of Metastatic Melanoma.” Cutaneous Melanoma. Balch CM, Houghton AN, Sober AJ, Soong S-J (Eds): St. Louis: Quality Medical Publishing, Inc. 1998:329).

<b>Organ</b>	<b>Likelihood of Spreading to Organ</b>
Other areas of the skin, fat and muscle	65 - 70%
Lungs and area between the lungs	70 - 87%
Liver and gallbladder	54 - 77%
Brain	36 - 54%
Bone	23 - 49%
Gastrointestinal tract	26 - 58%
Heart	40 - 45%
Pancreas	38 - 53%
Adrenal glands	36 - 54%
Kidneys	35 - 48%
Thyroid	25 - 39%
Lymph Nodes	70 - 75%
Spleen	30%

A milestone in the study of the progress of cancer was the development of a cell culture beyond the primary one, which resulted in a so-called “cell line”. The importance of cell lines lies in their ability to provide a renewable source of cell material for repeated studies. In principle, cancer cell line models should reflect the properties of their original cancers (Masters, 2000; Clark, 1991; Herlyn et al 1985).

The easy accessibility and long-term clinical and histopathological observation of cutaneous melanoma has led to the definition of 5 major steps of tumor progression in the human melanocytic system. The lesions representing each step are: (i) common acquired nevus, (ii) dysplastic nevus, (iii) radial growth phase (RGP) primary melanoma, (iv) vertical growth phase (VGP) primary melanoma, and (v) metastatic melanoma (MM).



### **III.2.6. Choice of cell lines in this study**

Overall, there have been relatively few studies involving nanoTiO<sub>2</sub> particle–cell interactions. In the limited number of published results, cancer cells were used as targets for investigating the potential toxicity of nanoTiO<sub>2</sub>. The interest in using cancer cells has mostly been driven by three factors: (i) nanoTiO<sub>2</sub> particles are considered as potential anti-cancer drugs in photodynamic treatment (PDT), (ii) cancer cells can be used as representatives of tissues where they form metastases, and (iii) in the laboratory conditions the culture of cancer cells is easier than that of primary cells. In particular, the nanoTiO<sub>2</sub> mediated and UV light-induced toxicity was used to eradicate cancer cells via PDT treatment in several studies (Huang et al., 1997; Zhang et al., 2004).

In this thesis, melanoma cell lines were selected as cellular models of adverse effects of nanoTiO<sub>2</sub>. The human melanoma cell lines were kindly provided by Prof. Piotr Laidler, Chair of Medical Biochemistry, Jagiellonian University Medical College, Kraków, Poland. The original specimens were collected at the Department of Surgical Pathology at the Hospital of the University of Pennsylvania (Masters and Palsson, 1999).

Two melanoma cell lines were used: the WM793B and Lu1205 cell line. The WM793B line was established from skin taken from the primary melanoma of a vertical growth phase (VGP) lesion from the sternum of a patient on 01/07/83. The Lu1205 cell line was directly derived from lung melanoma metastases of WM793 (VGP) after subcutaneous injection into immunodeficient mice (Herlyn et al., 1990). The Lu1205 cells were collected from the lungs, where they formed a tumor. These cells are highly invasive and can exhibit spontaneous metastasis to lungs and liver (Herlyn et al., 1991). In general, cultured melanoma cells maintain their properties in a stable manner, which is indicated by chromosomal analyses at the time of isolation of the cells, after 12 passages, and prolonged culture (more than 6 months) (Masters and Palsson, 1999).

### **III.3. Mechanical properties of cells**

Living cells in the human body are constantly subjected to mechanical stimulations throughout their lifetime. The stresses and strains can arise from both the external environmental and internal physiological conditions. Depending on the magnitude, direction and distribution of these mechanical stimuli, cells can respond in a variety of ways. For example, within the body, fluid shear of endothelial cells activate hormone release and intracellular calcium signaling, as well as stiffening of the cells by rearrangement of the cytoskeleton (Sato et al., 1987; Kuchan and Frangos, 1993; Jen et al., 2000). The cellular mechanics is fundamental to cell shape, motility, division, tissue organization, and other biologically important properties and processes (Alberts et al., 1994; Howard, 2001; Boal, 2002).



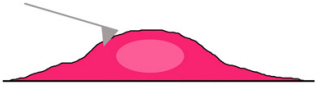
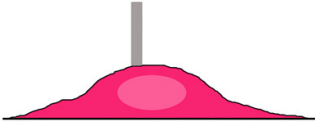
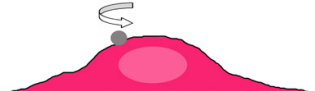

The mechanical properties of many cell types have been studied extensively (Elson, 1988; Evans, 1989; Pollard et al., 2000, 2003). Although the molecular underpinnings of cell mechanics are not fully understood, it is clear that the cytoskeleton plays a central role. For example, pharmacological disruption of actin fibers causes a significant change in cell mechanics (Rotsch and Radmacher, 2000; Yamada et al., 2000; Wakatsuki et al., 2001). Likewise, genetic disruption of cytoskeletal proteins has significant mechanical consequences (Janssen et al., 1996; Weber et al., 1999). Studies have also shown that many biological processes, such as growth, differentiation, migration, and even apoptosis are influenced by changes in cell shape and structural integrity. In fact, any change in the structural and mechanical properties can result in the breakdown of these physiological functions and may possibly lead to diseases (Boudreau and Bissell, 1998; Huang and Ingber, 1999).

### III.3.1. Experimental techniques in cell mechanics

With recent advances in nanotechnology, various innovative experimental techniques have been developed to probe mechanical properties of single cells all the way down to the nanometer scale.

Crick and Hughes were among the first researchers to quantitatively study the mechanical properties of cells using magnetic tweezers (Crick and Hughes, 1950). Mitchison and Swann (Mitchison and Swann, 1954) first developed the micropipette aspiration technique to measure the elastic properties of sea urchin eggs, and this method was later used by Band and Burton (Band and Burton, 1964) to measure the mechanical properties of the red blood cell membrane. The more recent experimental techniques developed include cell poker (Petersen et al., 1982), particle tracking (Geerts et al., 1987), magnetic twisting cytometry (MTC) (Wang et al., 1993), oscillatory magnetic twisting cytometry (Maksym et al., 2000), atomic force microscopy (AFM) (Wesenhorn et al., 1993 ;Hoh and Schoenenberger, 1994) microplate manipulation (Thoumine and Ott, 1997), cytoindenter (Shin and Athanasiou, 1999), electrical cell–substrate impedance sensing coupled with magnetic bead pulling (Lo et al., 1998), optical tweezers or laser traps (Henon et al., 1999) and tensile tester (Miyazaki et al., 2000). The force applied to the cell can either be concentrated (e.g. AFM) or distributed (e.g. microplate manipulation), either intracellular (e.g. particle tracking using optical or magnetic tweezers) or applied to the cell surface (e.g. MTC) in both transient (e.g. micropipette aspiration) or dynamic (e.g. oscillatory MTC) ways. These different techniques tend to elicit different mechanical responses of the cell, which leads to a wide variety of mechanical models as shown schematically in **Table 4**.

**Table 4.** Experimental techniques and mechanical models of a cell.

Experimental techniques	Mechanical models
 micropipette aspiration	<ul style="list-style-type: none"> <li>- solid model</li> <li>- cortical shell-liquid core model</li> </ul>
 optical tweezers / optical trap	<ul style="list-style-type: none"> <li>- cortical shell-liquid core model</li> </ul>
 AFM indentation	<ul style="list-style-type: none"> <li>- power-law structural damping model</li> <li>- solid model</li> </ul>
 cytoindenter	<ul style="list-style-type: none"> <li>- solid model</li> <li>- biphasic model</li> </ul>
 magnetic twisting cytometry	<ul style="list-style-type: none"> <li>- solid model</li> <li>- power-law structural damping model</li> </ul>
 fluid shear flow	<ul style="list-style-type: none"> <li>- solid model</li> </ul>

The *cortical shell–liquid core model* is a continuum model, which simplifies the cell as a cortical shell, composed of membrane, actin cytoskeleton and associated cross-linking proteins, and a liquid core that consists of viscous cytoplasm (Evans and Yeung, 1989). However, the cortical shell–liquid core model has limitations since it does not readily account for adhesive forces and does not extend to chondrocytes and endothelial cells, which behave more like solid materials (Hochmuth, 2000). The most striking feature of the *solid models*, compared with the cortical shell–liquid core models, is that the whole cell is usually assumed as homogeneous, without considering the distinct cortical layer (cortical shell–liquid core models). The solid models include the incompressible elastic solid or the viscoelastic solid. The experimental basis for the solid models is that equilibrium can usually be achieved after certain amount of loading. The *Power-law*

*structural damping model* has been suggested to behave like soft glassy materials close to glass transition (Sollich, 1998; Fabry et al., 2001). This indicates that the cytoskeleton might be a scale-free network, in that it possesses no internal scale that can typify the number of interactions (Jeong et al., 2000; Fabry et al., 2003). Therefore, it will exhibit a continuous spectrum of relaxation times. The cortical shell–liquid core models, power-law structural damping model and solid models all treat the cell as an effective single-phase material. However the cytoplasm is known to consist of both the solid polymeric content and interstitial fluid (Leterrier, 2001). Therefore, it is more appropriate to treat the two phases separately, thus leading to the biphasic model. This model has been widely used to study musculoskeletal cell mechanics, especially in single chondrocytes and their interaction with the extracellular cartilage matrix (Guilak et al., 1999; Shieh and Athanasiou, 2002, 2003).

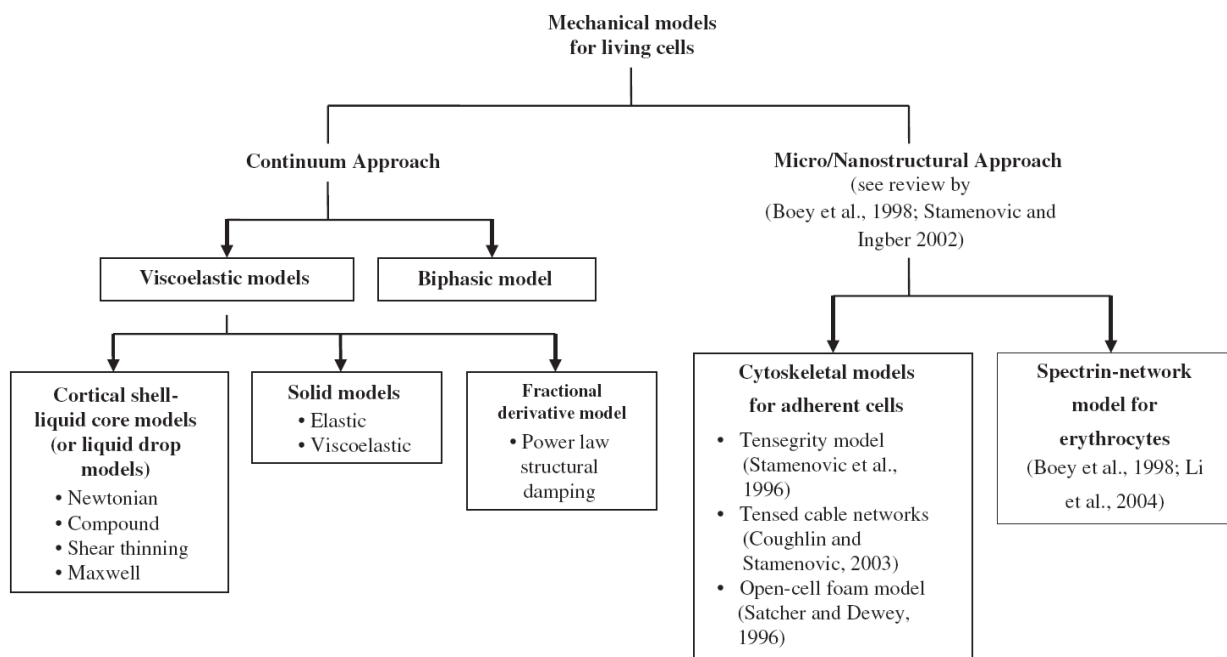


**Figure 9.** An overview of the mechanical models for living cells (Taken from Lim, Zhou, Quek, 2006).

An overview of the mechanical models developed by various researchers is shown in **Figure 9**. Generally, these models are derived using either the micro/nanostructural approach or the continuum approach.

In this work, atomic force microscopy was chosen to study the mechanical response of cells exposed to the presence of nanoTiO<sub>2</sub>. AFM, unlike other high-

resolution microscopic techniques, gives not only the topography (Langer et al., 2000) but also allows to investigate mechanical properties of cells, like elasticity and adhesion under almost any physiological conditions. AFM can also be used to study the mechanical response of living cells to different external stressors. In particular, the cell deformability was evaluated based on the cell stiffness, which in turn reports on the changes in the cytoskeleton (Radmacher, 1997; Lekka et al., 2001). Increasing evidence exists that structural changes in cells can be translated into variations in their Young's moduli and can be measured by AFM. For this purpose, AFM was used to monitor the evolution of mechanical properties of single living cells under oxidative stress by measurement of their local Young's modulus.

## **IV. Principle of action of photosensitizers**

Photosensitization is a reaction to light that is mediated by a light-absorbing molecule, which is not the ultimate target. Photosensitization can involve reactions within living cells or tissues, or they can occur in pure chemical systems.

Recall that the *First Law of Photochemistry* states that light (photons) must be absorbed to have an effect. In some cases, the molecule that absorbs a photon is altered chemically, but does not change any other molecule in the system. In other cases, the molecule that absorbs the photon ultimately alters another molecule in the system. In the latter process (photosensitization), the molecule that absorbs the photon is called the photosensitizer (PS), and the altered molecule is the acceptor or substrate. Both a photosensitizer and light are required for photosensitization. Photosensitizers are not usually consumed during photosensitization reactions. They return to their original state once the photosensitization reaction is complete. Photosensitizers can be photo-bleached, a chemical reaction following the absorption of light that produces a different molecular form, which does not absorb light, but this process typically *competes* with the photosensitization reaction.

## IV.1. Reactive oxygen species

Reactive oxygen species (ROS) are chemically-reactive molecules containing oxygen. They are highly reactive, some due to the presence of unpaired valence shell electrons. In living cells, such oxidation products are formed during normal metabolic processes and have important roles in cell signaling. Cells contain a variety of biomolecules, which are potential targets for oxidation by various types of ROS, like the hydroxyl radical ( $\text{OH}^\bullet$ ) and superoxide anion ( $\text{O}_2^{\bullet-}$ ), and molecules like hydrogen peroxide ( $\text{H}_2\text{O}_2$ ), hypochlorous acid ( $\text{HClO}$ ) as well as singlet oxygen ( $^1\Delta_g$ ) - an electronically excited state of molecular oxygen ( $^3\Sigma_g$ ). Additional environmental stresses (e.g. UV or heat exposure) can dramatically increase ROS levels. This can result in significant damage to cell structures that cumulate into a situation known as oxidative stress (OS). In living cells, OS occurs when the level of pro-oxidants, i.e. ROS exceeds the ability of the cell to respond through its antioxidant defense. Proteins comprise about 70% of the dry weight of cells and, because of their abundance, are major targets for OS-induced damages (Davies, 2005).

**Singlet oxygen ( $^1\Delta_g$ )** is the common name used for the diamagnetic form of molecular dioxygen ( $\text{O}_2$ ), which is less stable than the ground state triplet oxygen ( $^3\Sigma_g$ ), possessing two unpaired electrons (Khan and Kasha, 1963) [Fig. 1]. With two singlet states lying close above its triplet ground state, the  $\text{O}_2$  molecule possesses a unique configuration, which gives rise to a very rich and easily accessible chemistry, and also to a number of important photophysical interactions. The energy difference between ground state dioxygen and electronically excited singlet oxygen is of 0.98 eV (94.3 kJ/mol) and corresponds to the radiative transition (phosphorescence) in the near-infrared at  $\sim 1270$  nm. In the isolated oxygen molecule, this transition is strictly forbidden by spin, symmetry and parity selection rules, making it one of nature's most forbidden transitions. In other words, direct excitation of ground state oxygen by light to form singlet oxygen is very improbable. As a consequence, singlet oxygen in the gas phase is extremely long lived (72 minutes). Interaction with solvents, however, reduces the lifetime to microseconds or even nanoseconds.



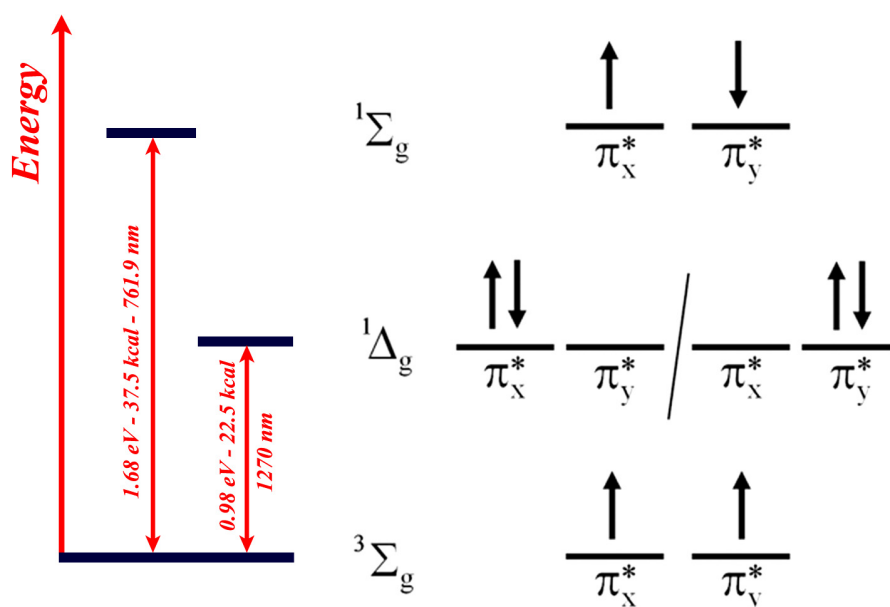


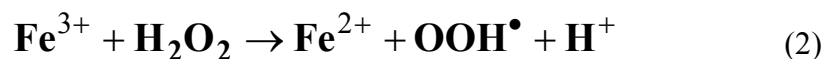
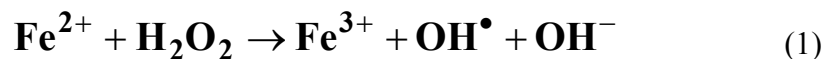
**Figure 1.** Excitation energy and orbital occupancy of the lowest singlet excited states of molecular oxygen ( $1\Delta_g$  and  $1\Sigma_g$ ).

Thus, in aqueous media,  $1\Delta_g$  can affect chemical reactions relatively far on a molecular scale from the place of its creation. The mean path of singlet oxygen in water is  $3.3 \mu\text{m}$  (Moan and Boye, 1981). In contrast, in the crowded environment of living cells, singlet oxygen has a very short lifetime  $\tau_{\Delta} = 0.04 \mu\text{s}$ , resulting in a rather small diffusion length of  $20 \text{ nm}$  (Niedre et al., 2002).

**Superoxide radical ( $\text{O}_2^{\bullet-}$ )** is the anion product of the one-electron reduction of  $\text{O}_2$ , which occurs widely in nature. With one unpaired electron, the superoxide radical, like dioxygen, is paramagnetic. Biologically, superoxide is quite toxic and is deployed by the immune system to kill invading microorganisms. In phagocytes, superoxide is produced in large quantities by the family of enzymes (NADPH oxidases) for use in oxygen-dependent killing mechanisms of invading pathogens. Superoxide is also deleteriously produced as a byproduct of mitochondrial respiration, most notably by Complex I - NADH dehydrogenase - an enzyme located in the inner mitochondrial membrane, which catalyzes the transfer of electrons from NADH to coenzyme Q (CoQ), and by Complex III - coenzyme Q: cytochrome-*c* oxidoreductase, the third complex in the electron transport chain, which plays a critical role in biochemical generation of ATP (oxidative phosphorylation). Several other enzymes also participate, for example xanthine oxidase.



The main deleterious action comes from its ability to generate hydroxyl and peroxide radicals as a result of reaction with iron (dissolved or clustered). This is called the Fenton reaction (Nieto-Juarez, 2010) [Eq.1 and 2].



While iron is an essential element for most life on the Earth including human beings, it may also be an important cytotoxin. Iron (II) is oxidized by hydrogen peroxide to iron (III), a hydroxyl radical and a hydroxyl anion. Iron (III) is then reduced back to iron (II), a peroxide radical and a proton, also by hydrogen peroxide (disproportionation - dismutation).

**Hydroxyl radical (OH<sup>•</sup>)** has a very short *in vivo* half-life of approx. 10<sup>-9</sup> sec. and a high reactivity (Sies, 1993). The hydroxyl radical, unlike superoxide that can be detoxified by superoxide dismutase (SOD), cannot be eliminated by an enzymatic reaction. In the presence of hydrogen peroxide, metallic cations like Fe<sup>2+</sup> are oxidized to Fe<sup>3+</sup>, which results in generation of highly reactive hydroxyl radicals and hydroxyl anions [Eq. 1] (Wardman et al., 1996). The iron-catalyzed decomposition of H<sub>2</sub>O<sub>2</sub> is a highly frequent reaction in biological systems and the source of various harmful effects. It can damage several types of macromolecules: carbohydrates, nucleic acids mutations, lipids and amino acids oxidation (Stadtman, 1990).

## IV.2. Photo-generation of reactive oxygen species

Photosensitized oxidations have been of interest to chemists and biologists since Raab's discovery (Raab, 1900) showing that microorganisms can be killed by light in the presence of oxygen and sensitizing dyes. A "photodynamic reaction" describes a photochemical process involving the absorption of light by a photosensitizer (examples of such photosensitizers are Rose Bengal, Methylene blue, fluorescein, etc.) and the subsequent generation of reactive oxygen species. The interaction of light with chemical agents present in the skin and eyes often results in the photodynamic generation of ROS in both human and animal subjects. These conditions cause pathological effects (referred to as "photodynamic action") that encompass induction of mutations, cell damage, cancer, and cell death, which are consequences of the photooxidation of sensitive cell constituents. Photosensitization may take the form of phototoxicity or photoallergy.

In brief, photosensitization is the process of initiating a reaction through the use of a substance capable of absorbing light, a photosensitizer (PS), and transferring the energy to the desired reactants. The mechanism is similar for quite a number of molecular photosensitizers that might be encountered in liquid or solid phases, where their presence is a prerequisite for triggering the photosensitization processes. PS molecules act as light-harvesting antennas.

Systems under study are illuminated with light of appropriate energy,  $h\nu$  (or specific wavelength  $\lambda$ ), which corresponds to the characteristic absorption bands of PS. This activates the photosensitizer and results in generation of reactive oxygen species (ROS) in its immediate vicinity (Dolmans et al., 2003). Higher excited singlet states ( $^1S_n^*$ ) of PS are short-lived and decay within a few tenths of a nanosecond to the lowest excited state *via* internal conversion (IC). Afterwards the inter system crossing mechanism (ISC) yields the excited triplet state ( $^3S^*$ ) of the PS molecule. Although the lowest excited singlet state ( $^1S_1^*$ ) might give rise to a radiative decay of its energy excess *via* fluorescence, it is customarily accepted that the major deactivation channel for  $^1S_1^*$  occurs mostly through the ISC mechanism, which effectively populates  $^3S^*$  states.

Depending on PS and its environment, the lifetime of  $^3S^*$  states might be in the range from a few microseconds to milliseconds which can favor the energetically rich excited triplet states of PS to react with other molecules in their neighborhood [Fig. 4]. The long-lived excited triplet states of photosensitizers can give rise to two major types of photophysical processes, defined as Type I and Type II mechanisms.

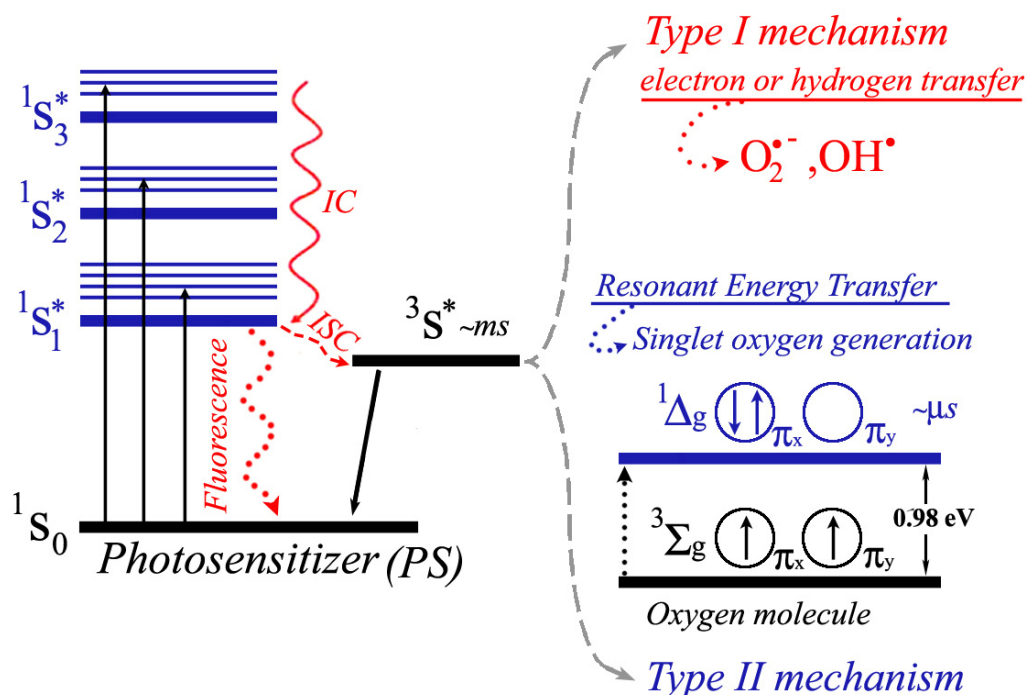
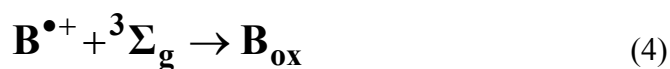


**Figure 4.** Jablonski-Kasha diagram showing ROS generation via Type I or II photoreaction mechanisms. The light-induced excitation populates the short-lived singlet excited states ( $^1S_n^*$ ) of the PS. The process then proceeds by a rapid internal conversion (IC) to the lowest singlet excited state ( $^1S_1^*$ ). Then, the majority of the captured energy of  $^1S_1^*$  is transferred via an efficient inter system crossing mechanism (ISC) to a long-lived excited triplet state ( $^3S^*$ ). Subsequently, for Type I processes, electron or hydrogen transfer leads to free radical generation, whereas for type II processes, molecular oxygen in its triplet ground state ( $^3\Sigma_g$ ) effectively quenches the PS triplet state ( $^3S^*$ ), through a resonant energy transfer (RET), which results in singlet oxygen ( $^1\Delta_g$ ) generation.

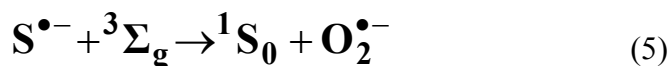
**Type I mechanism.** A consequence of electron or hydrogen transfer is the formation of free radicals like hydroxyl radicals ( $\text{OH}^\bullet$ ) or the superoxide radical anion ( $\text{O}_2^{\bullet-}$ ). It is a radical- or redox-type reaction in which a PS, excited to its triplet state  $^3\text{S}^*$ , can react directly with a neighboring organic biomolecule “B” through electron or hydrogen exchange leading to an oxidized substrate following the common equations:



followed by:



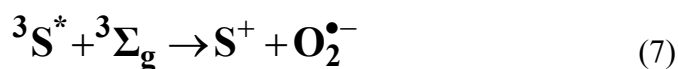
or



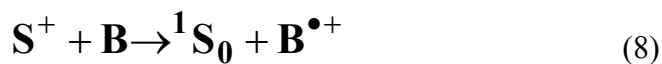
and



where  $\text{B}_{\text{ox}}$  is the oxidized substrate. Thus, both pathways result in the oxidization of “B”. An alternative Type I pathway reaction is:



that can either lead to **Eq.6** or be followed by:



which can then be followed by **Eq.4**.

**Type II mechanism** - collisions between molecular oxygen in its ground state ( $^3\Sigma_g$ ) and the photosensitizer in its photoactive triplet excited state ( $^3S^*$ ) result in the process of resonant energy transfer (RET). The energy captured by the PS is then transferred to dioxygen, thus leading to formation of singlet excited state of the oxygen molecule ( $^1\Delta_g$ ), which is the most common pathway of bio-oxidization:



### **IV.3. Nanoparticles and nano-filaments of TiO<sub>2</sub> - semiconductor-based photosensitizers in aqueous solutions**

Nanostructures of titanium dioxide (TiO<sub>2</sub>) have been of considerable scientific interest for more than thirty years, because of their superior performance in a range of advanced photochemical applications (Fujishima and Honda, 1971). Titanium dioxide is a well known white pigment and opacifier, which is commonly employed as a key ingredient to provide whiteness and opacity to products such as paints, coatings, paper, inks, and plastics. TiO<sub>2</sub> is also used in pharmaceuticals as a coloring agent for capsules, films, tablets and coated pills, medical sticky tapes and toothpastes. Various forms of micron-sized and nano-sized TiO<sub>2</sub> have found applications in the food industry as colorants for sugar-containing products, chewing gums, dairy products whiteners, ingredients of salad dressings, cheese and whey, as well as in cosmetics for water-dispersible/water-based foundations and sunscreens.

It has been found that the size, crystalline phase (anatase or rutile), and the shape of individual nanocrystals are critical parameters in determining their photocatalytic efficiency (Testino et al., 2007; Mogyorósi et al., 2008) and in their overall suitability for particular applications (Rajh et al., 1999). The two most commercially important polymorphs of TiO<sub>2</sub> are rutile and anatase. It is well-known that rutile is the thermodynamically stable phase of TiO<sub>2</sub> under ambient conditions at the macroscale (Muscat et al., 2002) and that anatase is the thermodynamically stable phase at the nanoscale (Levchenko et al., 2006). Both rutile and anatase crystallize in the tetragonal crystal system (space group P4<sub>2</sub>/mnm) with six-coordinated titanium atom (TiO<sub>6</sub>). In both structures, TiO<sub>6</sub> octahedra share edges and corners. However, in anatase, there are zig-zag chains of TiO<sub>6</sub> octahedra, whereas the more tightly packed rutile has straight chains of TiO<sub>6</sub> octahedra [Fig. 4a and b].



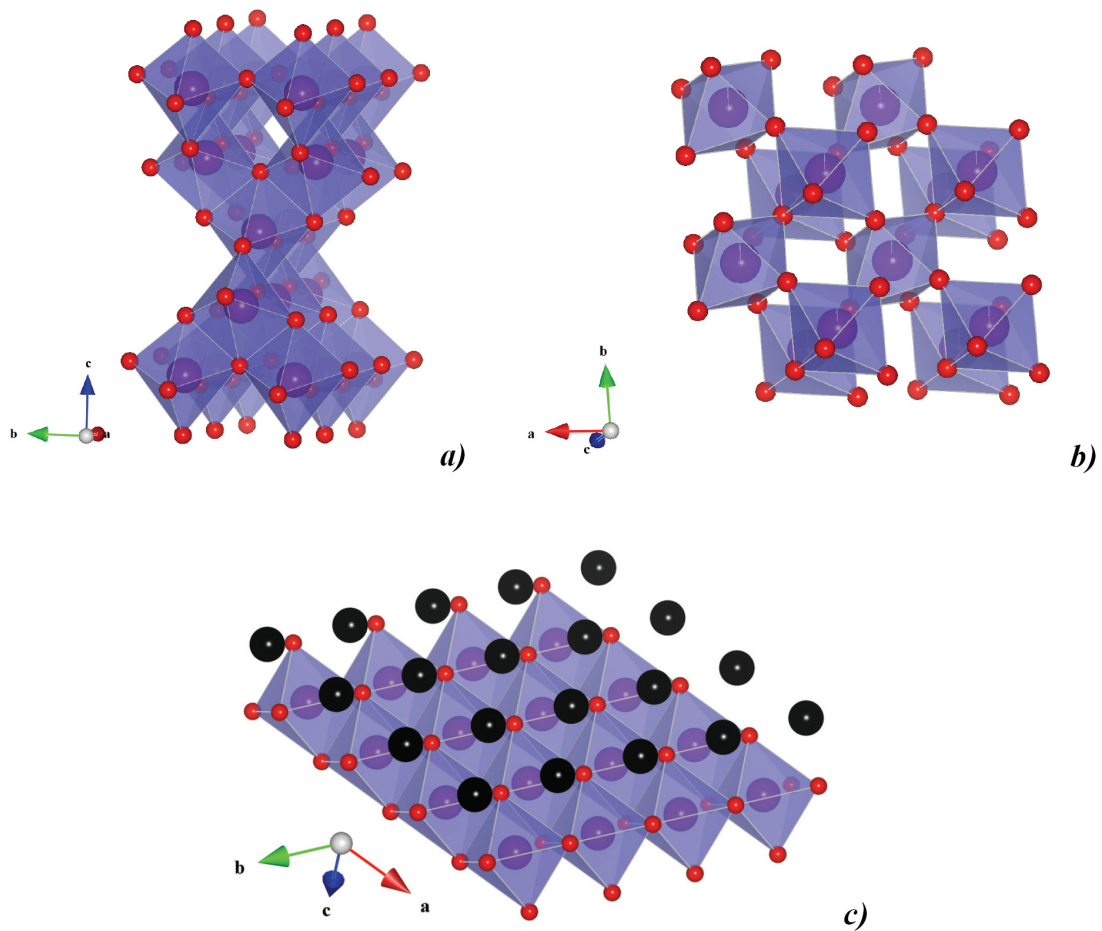


**Figure 4.** Crystal structure of anatase (a), and rutile (b), anatase nanoTiO<sub>2</sub>-based custom-made nanowires (c). (Made using the free software VESTA - 3D visualization program).

These crystallographic differences are reflected in the optical band gap ( $E_g$ ) and refractive indexes ( $n$ ) for both materials, being 3.2 eV and 2.49, and 3.0 eV and 2.9 for anatase and rutile, respectively. It is customarily believed that anatase possesses superior photo-catalytic properties as compared to rutile (Chen et al., 2007).

Titania nanowires [**Fig. 4c**] are especially interesting, as they combine the high aspect ratio and high specific surface area with versatile chemistry, thus opening new avenues for numerous applications as sensitive and selective chemical or biological sensors, which could potentially be massively multiplexed in devices of small size (Kolmakov and Moskovits, 2004; Liao et al., 2008; Mor et al., 2004). The importance of TiO<sub>2</sub> nanotubes and nanowires in the field of bio-mimetic materials and implants technology is becoming increasingly recognized (Park et al., 2007).

### IV.3.1. Mechanism of ROS generation by TiO<sub>2</sub>

The energy of UV photons typically exceed the band gap of both forms of TiO<sub>2</sub>: for example, in the case of anatase, the band gap of 3.2 eV corresponds to a photon with a wavelength of less than ~385 nm, (UV-A range). Hence, this process gives rise to an active electron/hole pair ( $e_{cb}^-/h_{vb}^+$ ) [Fig. 5] (Duonghong et al., 1982).

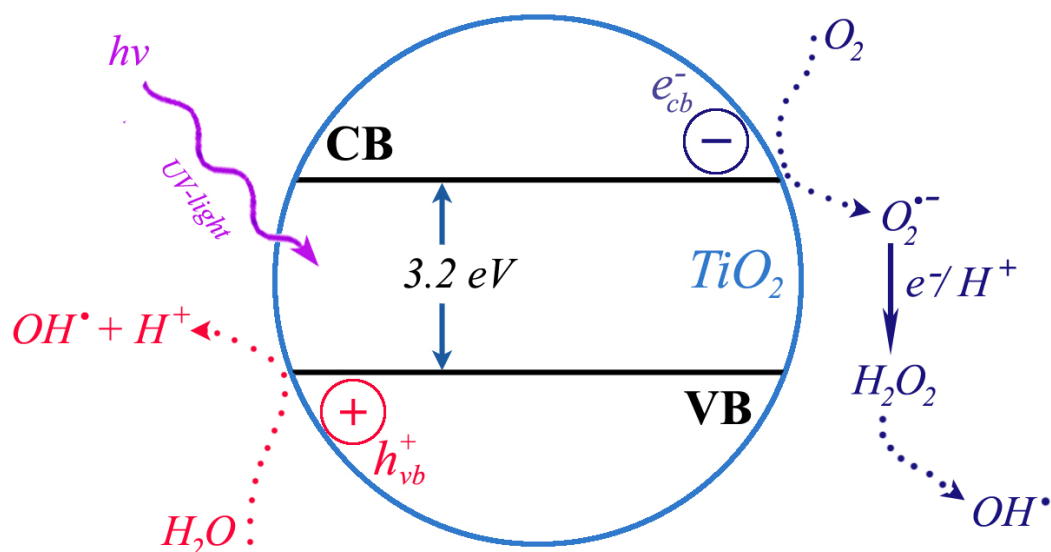
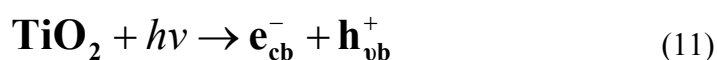


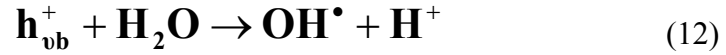
**Figure 5.** Schematic representation of the mechanisms involved in the generation of an electron/hole pair ( $e_{cb}^-/h_{vb}^+$ ) and primary radicals formation for a TiO<sub>2</sub> anatase particle upon UV irradiation.

The photogenerated conduction band electron may act as a reducing agent and the simultaneously formed valence hole which can act as an effective oxidizing agent. Both can cause the generation of reactive oxygen species and other free radicals. Numerous studies have demonstrated that under illumination with UV light, nanoTiO<sub>2</sub> causes severe oxidative damage to living cells (Cai et al., 1991; Saito et al., 1992; Sakai et al., 1994).

The fundamental reactions of the process, which take place, are the following:



where the valence band hole,  $h_{vb}^+$ , reacts with hydroxyl anions ( $OH^-$ ) giving hydroxyl radicals,  $OH^\bullet$  [Eq.12], whereas the conduction band electron,  $e_{cb}^-$ , leads to generation of superoxide anions,  $O_2^{\bullet-}$  [Eq.13].



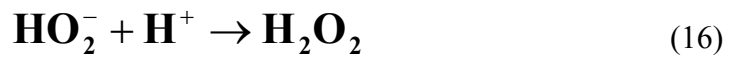
The hole/electron recombination is a very fast process ( $\sim$  ns) and produces heat:



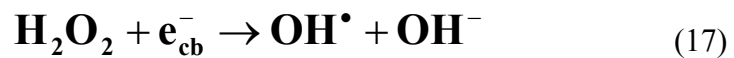
The primary products of photooxidation and photoreduction,  $OH^\bullet$  and  $O_2^{\bullet-}$  radicals, can react further with electrons and holes, which are still being photoproduced, e.g.:



The thus formed peroxide ion,  $HO_2^-$  can combine with a proton.



The product, hydrogen peroxide,  $H_2O_2$ , can undergo a further reaction:



The photo-produced radicals, usually the primary products, can react further, thus leading to a cascade of secondary oxidative processes.

## **V. Sample characterization techniques**

## **V.1. ESR - electron spin resonance: a tool for detection of ROS *in vitro* and *ex vivo***

The principle of Electron Spin Resonance (ESR) was first successfully applied to a system containing unpaired electronic spins in 1944 by Evgeny K. Zavoisky in Kazan (Zavoisky, 1945 a and b).

The technique was further developed just after the World War II, and was originally used to study transitions in paramagnetic metal complexes (Abragam and Bleaney, 1973). Since these pioneering times, ESR has continued to be an increasingly attractive radio-spectroscopic technique, applicable to almost all fields of pure and applied sciences, including physics, chemistry, material sciences, biology, and medicine. It has been used to reveal the magnetic nature, concentration, dynamics, reactivity and underlying reaction mechanisms of paramagnetic species.

In the mid fifties, nearly simultaneously in the United States and the Soviet Union, ESR spectroscopy was first used for the investigation of tissues and fluids in human and animals. At that time, owing to the low sensitivity of ESR spectrometers, the method of tissue lyophilic drying was used for sample preparation. The development of low-temperature registration of biological tissues in the early seventies extended the scope of application of ESR spectroscopy in biochemistry and medicine. By the present time, both high sensitivity and precision have been achieved, which allows investigation of even native water-containing tissues. Therefore, ESR spectroscopy has found applications in biochemistry and medicine, in part for studying malignant tumors. The synthesis and introduction of spin labels, probes and traps made it possible to discover many mechanisms of pathologic states. During the last years the possibility of using ESR spectroscopy *in vivo*, including ESR imaging (ESRI), has been intensively examined (Eaton S. and Eaton G., 1998; Swartz and Berliner, 1998).

### V.1.1. Introduction and principles of ESR spectroscopy

Two terms are typically used in the literature to describe electron resonance technique: electron paramagnetic resonance (EPR) and electron spin resonance (ESR). In this thesis we will use the latter.

ESR spectroscopy has been exploited as a very sensitive and informative technique for the investigation of different kinds of paramagnetic species in solid or liquid states. The technique is widely used in many fields of contemporary science, ranging from physics and chemistry to biology and medicine (Galimzyanovich et al., 2002). ESR is a branch of radio-spectroscopy that relies on the behavior of an unpaired electron in a magnetic field. It is mainly applied in studies of paramagnetic, ferromagnetic and antiferromagnetic spin systems. When a single unpaired electron is placed in an external magnetic field  $\mathbf{B}$ , its magnetic moment will align either *parallel* or *antiparallel* to the field, with the corresponding electron spin states being:  $M_S = \pm 1/2$  [Fig. 1].

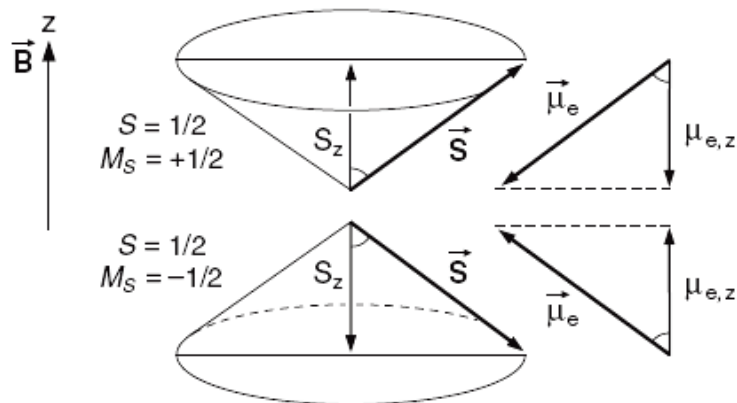


**Figure 1.** Precession of the spin vector  $\vec{S}$  about the magnetic field  $\vec{B}$  in the  $z$  direction.

The degeneracy of the electron spin energy levels is lifted by the field, and an energy gap is created between the energy levels [Fig. 2a]. This phenomenon is known as the *Zeeman effect*, named after the Dutch physicist Pieter Zeeman, who was awarded the Nobel Prize in Physics in 1902 for its discovery.

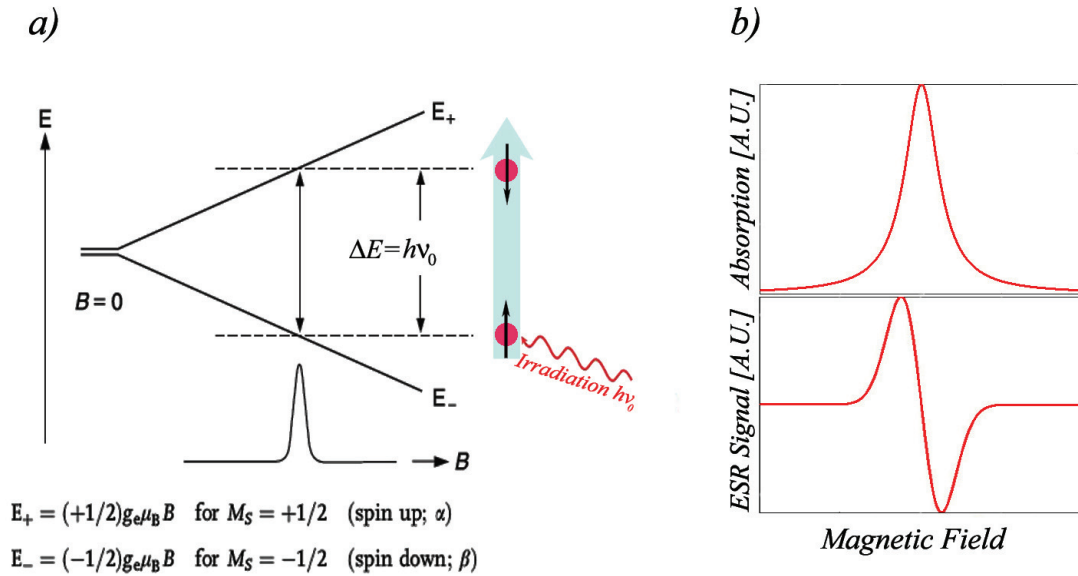


**Figure 2.** Electron-Zeeman splitting as a function of the strength,  $B$ , of the magnetic field and the resonance condition (a), the application of a low-amplitude magnetic field modulation and *lock-in* detection converts the absorption curve into a first derivative (b).

Quantum mechanically, the problem of a single electron in an applied magnetic field is described by the spin Hamiltonian:

$$\hat{H}_s = g\mu_B \mathbf{B} \hat{S}_z \quad (1)$$

where  $g$  is the  $g$ -value (or  $g$ -factor, for a free electron its value  $g_e = 2.00232$ ),  $\mu_B$  is the Bohr magneton ( $9.274 \times 10^{-28} JG^{-1}$ ),  $B$  is the magnetic field strength in Gauss, and  $S_z$  is the  $z$ -component of the spin angular momentum operator (the magnetic field defines the  $z$ -direction). The electron spin energy levels can be easily found by application of  $\hat{H}$  to the electron spin eigenfunctions corresponding to  $M_S = \pm 1/2$ :

$$\hat{H}_s \left| \pm \frac{1}{2} \right\rangle = \pm \frac{1}{2} g\mu_B \mathbf{B} \left| \pm \frac{1}{2} \right\rangle = E_{\pm} \left| \pm \frac{1}{2} \right\rangle \quad (2)$$

The energy difference between the two levels is:

$$\Delta E = E_+ - E_- = g\mu_B \mathbf{B} \quad (3)$$

and a transition between the two levels can be induced by absorption of a photon with energy  $h\nu = \Delta E$  [Fig.2a]. In wave numbers, the difference is expressed as follows:

$$\tilde{\nu} = \lambda^{-1} = \nu / c = (g_e \mu_B / hc) \mathbf{B} \quad (4)$$

where  $g_e \mu_B / hc = 0.9348 \times 10^{-4} \text{ cm}^{-1} \text{ G}^{-1}$ .

For such a spin system in an external magnetic field, the electron spin momentum will precess around the magnetic field with the Larmor frequency  $\omega = -\gamma B_0$ , where  $\gamma = \frac{-eg_e}{2m}$  is the gyromagnetic ratio. For the most frequently used magnetic field strength (0.3 T), the Larmor frequency is in the microwave range ( $\sim 9$  GHz, X-band).

The interaction of an unpaired electron with the magnetic field is just one of the ways in which the interaction of the spin with its surroundings can manifest itself in an ESR spectrum. This case usually gives well-characterized spectra in the form of a single ESR line [Fig.2b]. However, there are other types of magnetic interactions, often of lower energy, which produce additional features in the ESR spectra called *hyperfine* and *fine structure*. These arise from coupling to the nuclear spins of nearby nuclei, spin orbit coupling, and the crystal field, for example.

In the ESR experiment, the absorption of microwave energy is measured as a function of the applied field  $\mathbf{B}$ . The typically observed ESR lines fall into the category of Gaussians, Lorentzians or a combination of these. Electron spin resonance absorption for a single spin is shown in **Figure 2b**. The intensity of the line can be used to determine the concentration of a paramagnetic species. The numerical result of the double integration of the ESR spectrum is directly proportional to the number of paramagnetic centers in the sample. Such analytical applications usually require a standard solution of the reference paramagnetic species to establish a calibrated intensity scale.



## V.1.2. Detection of reactive oxygen species by electron spin resonance

The ROS at ambient conditions are not directly detectable *via* ESR because of their short lifetime and low concentrations. Therefore, an indirect method is required. One of them is *spin trapping*, an analytical technique employed in the detection and identification of short-lived free radicals. In brief, a transient short-lived radical may interact with a diamagnetic reagent (spin trap) in certain reactions in solution to form a more persistent radical. The key reaction is usually one of attachment: the diamagnetic reagent is said to be a spin trap and the persistent product radical is then the spin adduct. The ESR technique offers an ideal method for the study of formation of ROS, which are photo-synthesized in the presence of light-excited nanoparticles (Hirakawa et al., 2001).

One of the most often used spin traps for ROS detection is 5,5-dimethyl-1-pyrroline-N-oxide (DMPO). In certain studies, a stable free radical, 4-hydroxy-2,2,6,6-tetramethylpiperidine-1-oxyl (TEMPOL) is used to detect the presence of ROS. In such a case, TEMPOL serves as a target for ROS. TEMPOL is a well-known free radical which, besides applications in ESR, is also used in other spectroscopic techniques as a long-lived nitroxide radical (UV-VIS and ESRI). The two aforementioned agents are mostly used in ESR detection of ROS *in vitro*. For ROS detection *ex vivo* in living cells, a common spin trap is 1-acetoxy-3-carbamoyl-2,2,5,5 tetramethyl-pyrrolidine (ACP).

We will now consider these three formulations in more detail:

**DMPO** is sensitive to  $\text{OH}^\bullet$  and  $\text{O}_2^{\bullet-}$  radicals. **Figure 3** presents the reactive scheme of formation of the paramagnetic product of DMPO-OH, upon scavenging hydroxyl radical ( $\text{OH}^\bullet$ ) with the diamagnetic DMPO spin trap.

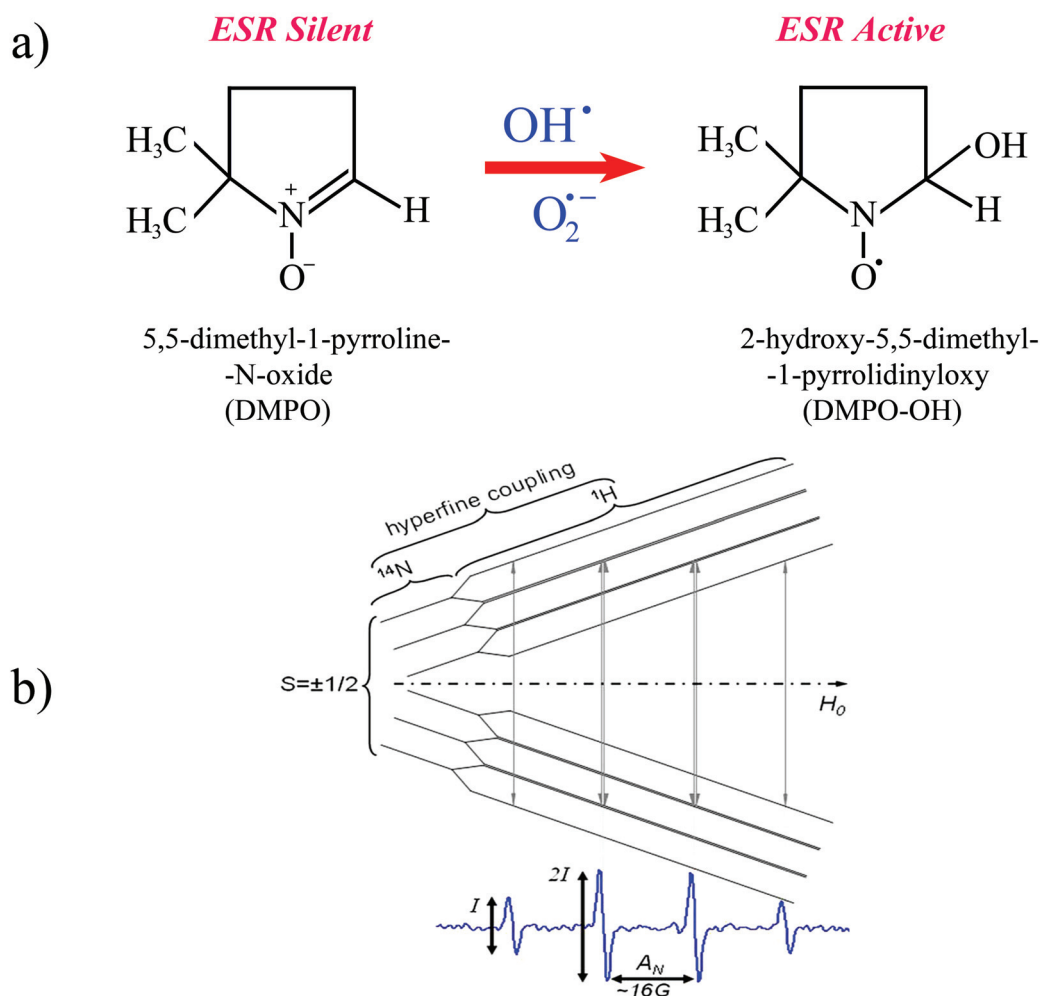


**Figure 3.** Mechanism of DMPO-OH generation resulting from the DMPO spin-trapping of hydroxyl and superoxide radicals (a), splitting diagram and corresponding ESR spectrum ( $d\chi''/dH$ ) of the resonant transitions of the DMPO-OH spin-adduct in  $H_2O$  at ambient conditions (b).

**TEMPOL** reacts with  $^1\Delta_g$ ,  $OH^{\bullet}$  and  $O_2^{\bullet-}$  radicals. **Figure 4** presents the reactive scheme of decomposition of the paramagnetic spin label TEMPOL to diamagnetic hydroxyl amine. Since TEMPOL reacts with  $^1\Delta_g$  as well as  $OH^{\bullet}$  and  $O_2^{\bullet-}$  radicals [see **Fig. 4a**], it can be used as a molecular target for ROS generated in the presence of  $nanoTiO_2$ , thus to characterize the photocatalytic properties of this material.

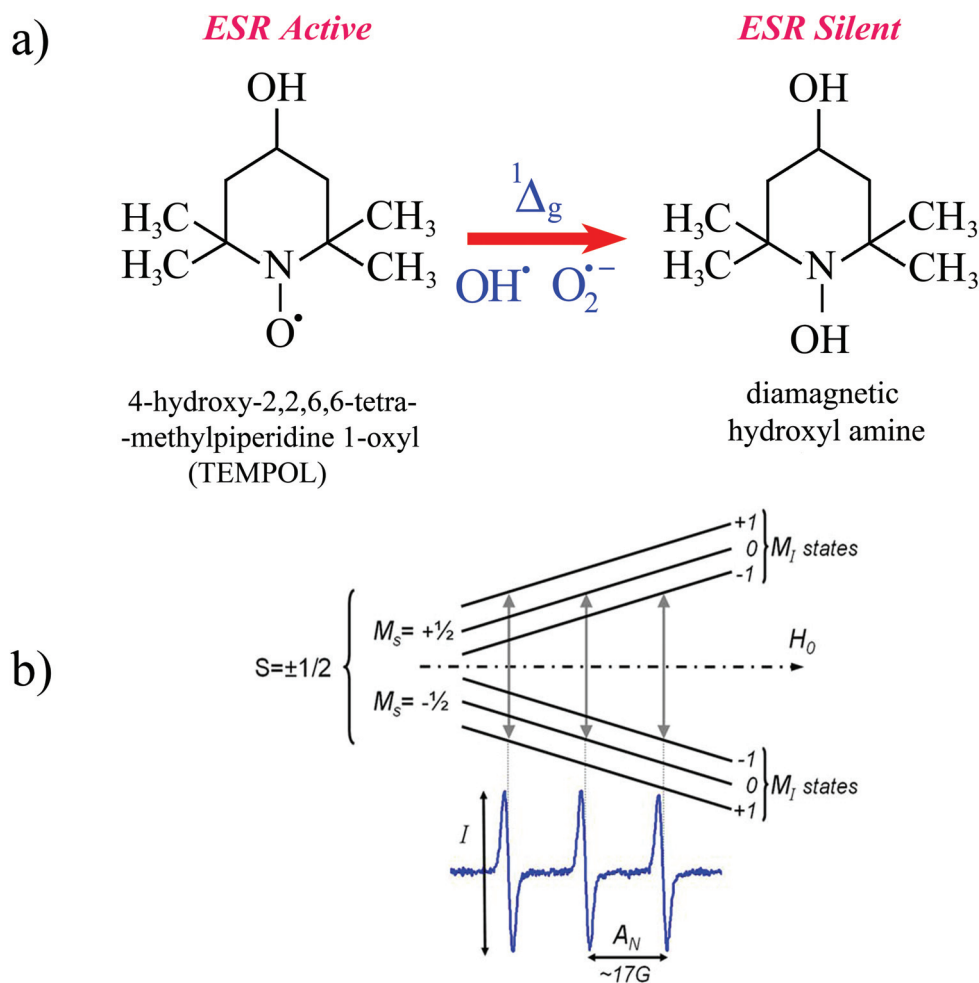


**Figure 4.** Reactive mechanism of TEMPOL degradation to the diamagnetic hydroxyl amine (a), splitting diagram and corresponding ESR spectrum ( $d\chi''/dH$ ) of the resonant transitions of a  $\sim 0.2$  mM TEMPOL solution in  $H_2O$  at ambient conditions (b).

**ACP** (called also as acyl-protected hydroxylamine probe) is a unique probe for *in vivo* measurements of ROS. **Figure 5** presents its mechanism of action. ACP is hydrolyzed by cellular esterases (carboxyesterases) to a hydroxyl amine form (1-hydroxy-3-carbamoyl-2,2,5,5-tetramethylpyrrolidine, CP-H). Under oxidative conditions, in the presence of the superoxide anion radical ( $O_2^{\bullet-}$ ), CP-H is oxidized to 3-carbamoyl-2,2,5,5-tetramethylpyrrolidine-N-oxyl (carbamoyl PROXYL-CP), giving rise to the ESR-detectable nitroxyl radical.

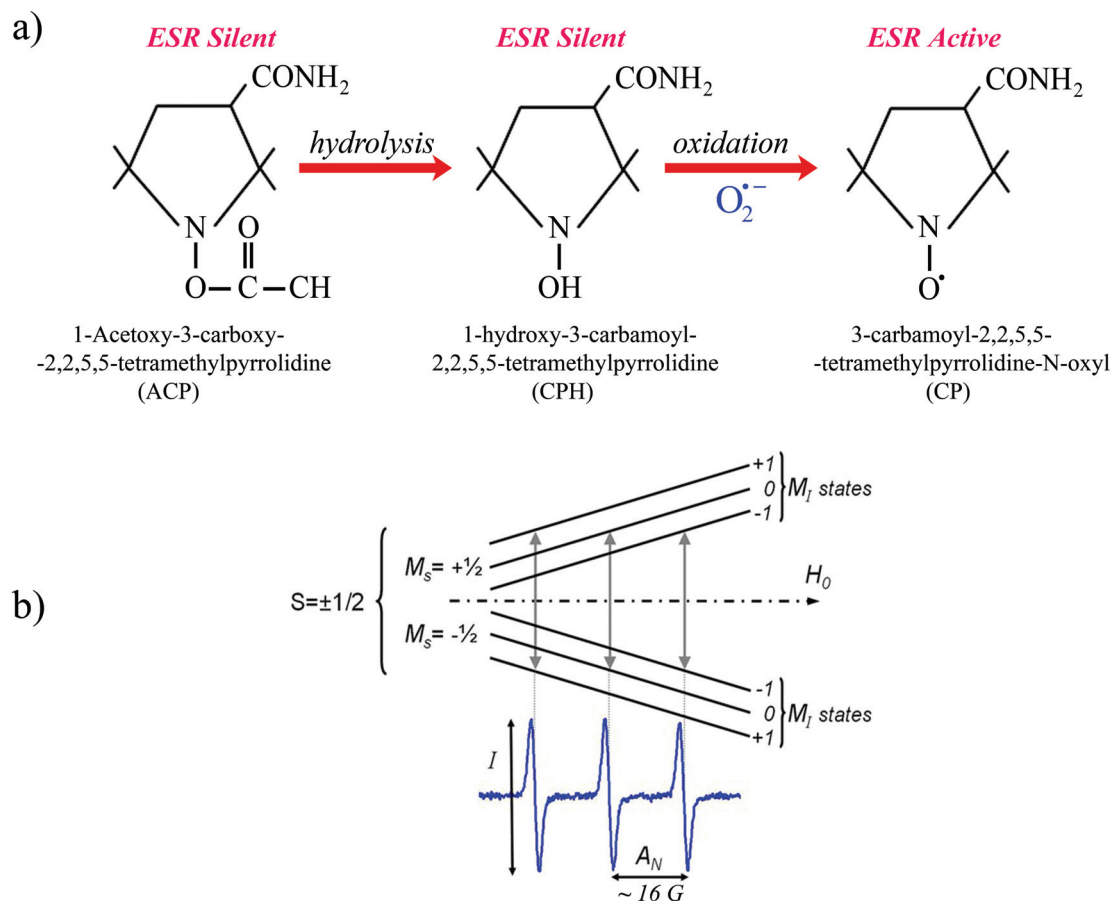


**Figure 5.** Metabolism of ACP in living cells (a), splitting diagram and corresponding ESR spectrum ( $d\chi''/dH$ ) of the resonant transitions of a  $\sim 0.26$  nM CP in HBSS medium at ambient conditions (b).

ACP was designed to prevent the autoxidation of hydroxylamine in the extracellular milieu and to make possible intracellular ROS detection (Itoh, O. et al., 2000). Therefore ACP, which is ‘de-protected’ by the cellular cytosolic esterases, can be used to detect cytoplasmic  $\text{O}_2^{\bullet-}$  generation. In contrast, it is not sensitive to the generation of  $\text{O}_2^{\bullet-}$  within intracellular organelles.

### **V.1.2.1. Photocatalytic properties of TiO<sub>2</sub> nanoparticles and nanowires**

The sample preparation for the ESR experiments consisted of two steps: (i) preparation of aqueous solutions of selected spin traps and (ii) preparation of suspensions containing nanoTiO<sub>2</sub>.

The standard commercially available spin trap, 5,5'-dimethylpyrroline-1-oxide (DMPO), from Sigma, was used for ESR detection of hydroxyl and superoxide radicals. Before its application, DMPO was carefully purified by filtration on charcoal. The commercially available stable nitroxide radical, 4-hydroxy-2,2,6,6-tetramethylpiperidine 1-oxyl (TEMPOL), from Sigma, was also used to verify photocatalytic properties of studied TiO<sub>2</sub> nanoparticles. TEMPOL was used as received. The obtained stock solutions in ultrapure water of 0.5 M DMPO and of 50 mM TEMPOL, were stored at and -20° C and 4° C, respectively.

Aqueous suspensions of the same concentration (32 mg per 90 mL of phosphate-buffered saline (PBS), from Sigma-Aldrich) were prepared for the various types of nanoTiO<sub>2</sub>. Prior to further measurements, the suspensions of nanoTiO<sub>2</sub> were homogenized in an ultrasound bath for 40 minutes.

Before the ESR measurements, 900 µL aliquots of nanoTiO<sub>2</sub> suspension were mixed either with 100 µL of the stock solution of DMPO or with 100 µL of TEMPOL. The resulting final concentrations of DMPO and TEMPOL were 50 mM and 50 µM, respectively. Subsequently, the 1 mL aliquots of prepared suspensions containing either DMPO or TEMPOL and nanoTiO<sub>2</sub> were transferred into small Pyrex beakers (5 mL volume, 20 mm OD and 30 mm height) and exposed to UV-A illumination (wavelength ~ 365 nm) using a UV spot light source, Lightingcure™ (model LC-8, from Hamamatsu Photonics, France) [Fig. 6]. The Lightingcure™ source incorporates a 200 W Mercury-Xenon lamp (model L7212-01) and a quartz fiber light guide, which is optimized for high transmittance in the UV spectral region. The light guide termination was positioned at 0.5 cm distance over the open face of the beaker, thus yielding illumination power density of 10 mW/cm<sup>2</sup>. The actual quantity of UV-A light illuminating the aqueous suspension of nanoTiO<sub>2</sub> was measured with a UV-meter (model C6080, Hamamatsu Photonic, France).

To avoid sedimentation during illumination, the suspensions of nanoTiO<sub>2</sub> were constantly agitated with the use of a small magnetic stirrer. Immediately after exposure to UV-A, aliquots of ca. 7  $\mu$ L of the illuminated suspensions were transferred into 0.7 mm ID and 0.87 mm OD quartz capillary tubes (VitroCom, USA, sample height of 25 mm) and sealed on both ends with Cha-Seal™ tube sealing compound (Medex International, Inc., USA).

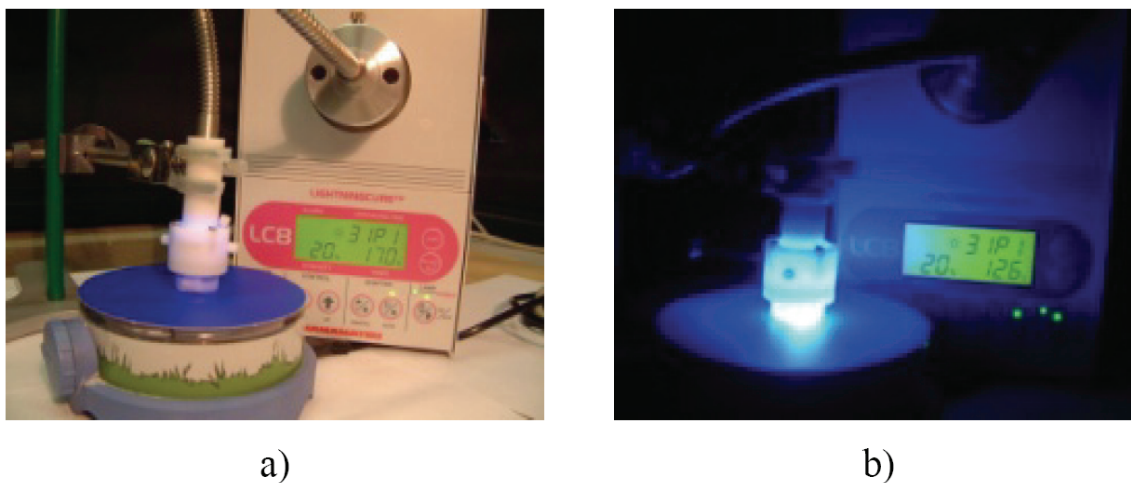


**Figure 6.** The UV-A light generator consisting of the Hamamatsu Lightingcure lamp, quartz light-guide and Delrin-made adapter, which accommodates the light-guide and a 5-mL glass beaker. This setup enables one to mix the aqueous suspensions during illumination as well as to exchange gases (e.g., N<sub>2</sub> and O<sub>2</sub>). Before illumination (a), and during illumination of TiO<sub>2</sub> (b).

ESR experiments were carried out at room temperature using an ESP300E spectrometer (Bruker BioSpin GmbH), equipped with a standard rectangular mode TE<sub>102</sub> cavity. For each experimental point of ROS detection with DMPO or TEMPOL, five-scan field-swept ESR spectra were recorded. The typical instrumental settings were: microwave frequency  $\sim$  9.38 GHz, microwave power 10 mW for DMPO and 2 mW for TEMPOL, sweep width 120 G, modulation frequency 100 kHz, modulation amplitude 0.4 G for DMPO and 0.5 G for TEMPOL, receiver gain  $4 \times 10^4$ , time constant 40.9 ms, conversion time 81 ms, and time per single scan 81 seconds.

### **V.1.2.2. ESR *ex vivo* detection of ROS caused by TiO<sub>2</sub> nanoparticles and nanowires**

For ESR experiments, the studied melanoma cells (WM793 and Lu1205) were grown in 25 cm<sup>2</sup> TC flasks (Sarstedt) at 37°C in 95% humidified air containing 5% CO<sub>2</sub>, in an incubator (Innova, model CO-170, New Brunswick, USA). The applied culture medium was RPMI 1640 (pH 7.4, Sigma), which was supplemented with 10% of Fetal Bovine Serum (FBS, Sigma) and 1% of antibiotics (50.5 units/ml penicillin, 50.5 µg/ml streptomycin and 101 µg/ml neomycin, Sigma). With the use of a cell scraper (Sarstedt) the cells were detached and centrifuged at 2000 RPM for 2 min. Next, they were re-suspended in Hanks Balanced Salt Solution (HBSS, pH 7.4, Sigma) buffer at the concentration of  $\sim 2.0 \times 10^7$  cells/mL and immediately transferred into the Eppendorf tube. Afterwards, the control cells were incubated with 10 mM ACP spin trap (Noxygen Science Transfer & Diagnostics GmbH) for 90 min at 37°C. Next, the oxidative stress was applied. Cells were exposed to the presence of nanoTiO<sub>2</sub> particles at the final concentration of 2.0 µg/mL. The custom-made anatase-based TiO<sub>2</sub> nanowires, commercial nanoparticulate TiO<sub>2</sub> (AMT100, Tayca), and the formulation P25 Degussa (Degussa), were used. These nanoTiO<sub>2</sub> materials were suspended in the culture medium prior to adding them to the cell cultures. 10 µL of the stock suspension of nanoTiO<sub>2</sub> (concentration of 200 µg/mL) were added to 890 µL of the cell suspension in HBSS. Finally, the suspended cells were incubated for 30 min in the dark at 37°C. Afterwards 100 µL of 100 mM concentration of ACP spin trap were added (the final concentration of ACP trap was of 10 mM) and cells were incubated for the next 90 min at 37°C. Immediately after exposure to nanoparticles in the dark, aliquots of ca. 50 µL of cell suspensions were transferred into seven 0.7 mm ID and 0.87 mm OD quartz capillary tubes (VitroCom, USA, sample height of 25 mm;  $\sim 7$  µL of cells suspension for each capillary) and sealed on both ends with Cha-Seal<sup>TM</sup> tube sealing compound (Medex International, Inc., USA).

ESR experiments were carried out at room temperature using an ESP300E spectrometer (Bruker BioSpin GmbH), equipped with a standard rectangular mode TE<sub>102</sub> cavity. Routinely, for each experimental point of ROS detection with ACP, five-scan field-swept ESR spectra were recorded. The typical instrumental setting were:

microwave frequency  $\sim 9.38$  GHz, microwave power 10 mW, sweep width 120 G, modulation frequency 100 kHz, modulation amplitude 0.5 G, receiver gain  $4 \times 10^4$ , time constant 40.9 ms, conversion time 81 ms, and time per single scan 81 seconds.

Finally, it should be noted that the ESR signal intensity depends not only on the amount of generated ROS but also on the concentration of ACP spin trap.

### **V.2. Atomic force microscopy: a tool for detection of ROS-induced damages to living cells**

Scanning probe microscopes are able to create detailed 3D images of specimen surfaces with atomic resolution. The atomic force microscope (AFM) (Binnig et al., 1986) is undoubtedly the most widely used of the local probe devices. It gives access to a wide range of surface properties, including mechanical, electrical, magnetic, and other properties, with very high spatial resolution. Furthermore, it can operate in air, vacuum, or liquid media (Gould et al., 1990). The AFM has emerged in recent years as a powerful tool, especially for the study of structure, dynamics and function of living cells under nearly physiological conditions with ultrahigh resolution and in real time. Nanometer-scale morphological studies revealing details of living cells, which were previously impossible due to the resolution limits of the light microscope, are now possible using the AFM. The essential difference between the physicochemical and the biological applications of the AFM is the constraint imposed by the softness and the fragility of the samples.

The advantage of using the AFM for imaging of cell structures over scanning and transmission electron microscopies (SEM and TEM) is based on the possibility of visualizing structures that are unidentifiable by SEM and TEM techniques. The second advantage of AFM is its capability to study alterations of single cells with the special and temporal resolutions much higher than any biochemical method.



## V.2.1. Introduction and principles of AFM

The atomic force microscope has been designed as a surface metrology instrument, intended to study nanometer-scale features of flat surfaces. The principle of operation is very simple: the force resulting from the tip–surface interaction is measured by detection of the deflection of a delicate cantilever located in the proximity of the surface. The cantilever, which has a tip at its end, is placed almost parallel to the surface and then moved over it, thus performing a raster scan [Fig. 7].

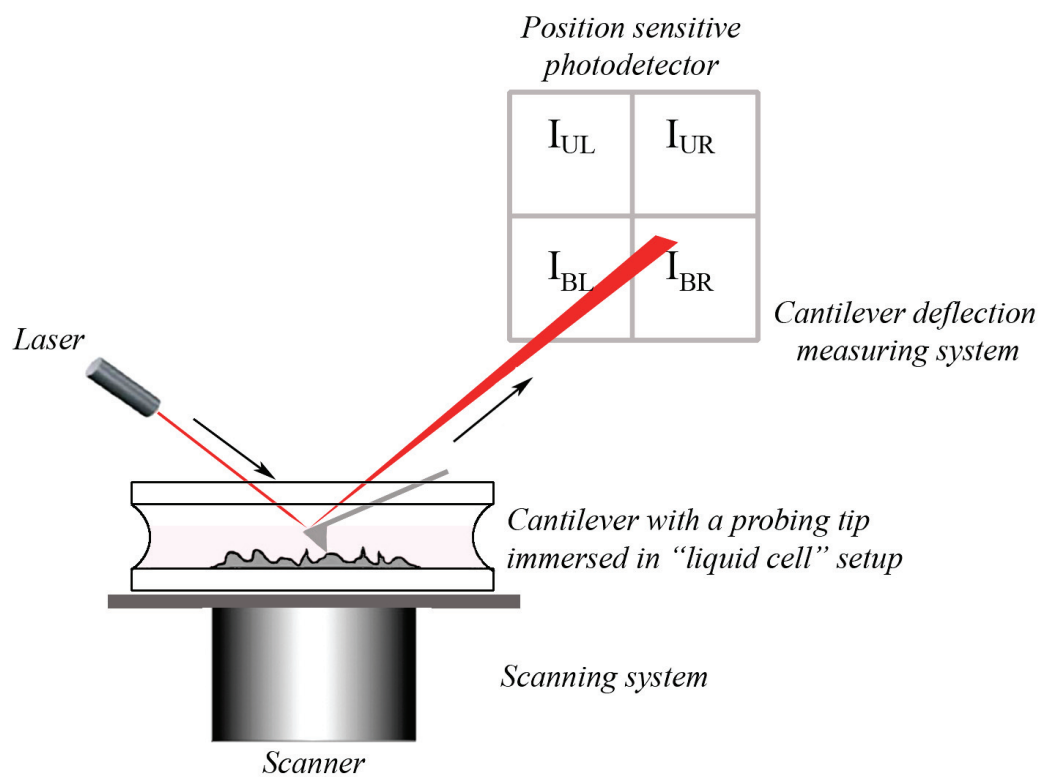


**Figure 7.** Schematic diagram of the atomic force microscope.

In general, the AFM system (commercial or custom-made) consists of three basic elements: (i) the cantilever which probes the sample, (ii) a detection system for the cantilever deflection, and (iii) the moving and scanning system.

**Cantilever** - usually cantilevers are microfabricated from silicon (Si) or silicon nitride ( $\text{Si}_3\text{N}_4$ ) [Fig. 8].

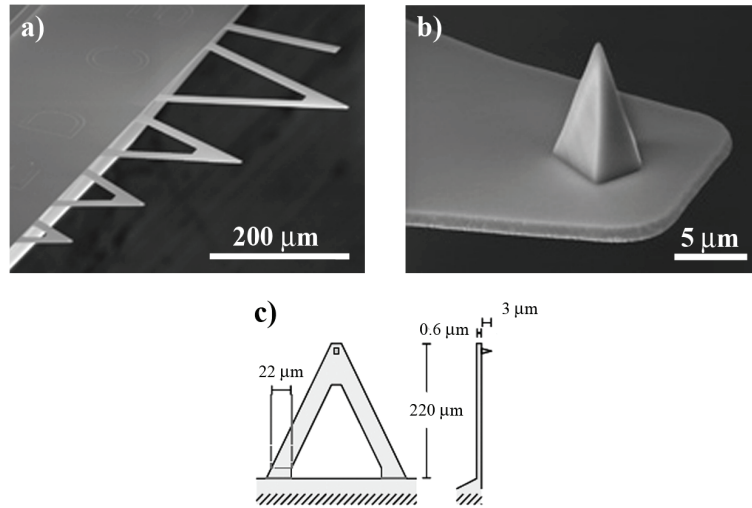


**Figure 8.** Scanning electron microscope images of different cantilevers (a) microfabricated at the edge of a chip. Probing tips (b) are placed at the free ends and have shape of four-sided pyramid. (c) Scheme presenting the dimensions for a cantilever, Veeco Microlever D. (Adapted from Veeco Instruments)

Cantilevers consist of a very delicate spring, either rectangular or triangular, with a probing tip mounted at its free end. The cantilever may be considered as a spring that is characterized by the spring constant  $k$ . The deflection,  $z$ , caused by forces acting on the tip, is converted into force  $F$  according to Hooke's law:

$$\mathbf{F} = -\mathbf{k} \cdot \mathbf{z} \quad (5)$$

The probing tip has the shape of a four-sided pyramid [Fig. 8c] with a height in the range of few microns ( $\sim 3$  microns). The end of the tip is rounded and its radius varies typically from 2 nm to 50 nm [Table 1].

**Table 1.** Typical cantilever characteristics

Shape	Rectangular or V-shaped
Length	50–250 $\mu\text{m}$
Stiffness	0.01–100 N/m
Resonance frequency	10–500 kHz
Radius of curvature of tip apex	2–50 nm
Tip shape	Conical or pyramidal

As the spatial resolution is related to the radius of the tip apex, one seeks to miniaturize the dimensions of the cantilever beam and the tip.

**Detection system for the cantilever deflection.** The most common detection system for cantilever deflection is optical. It consists of a laser and a position sensitive detector (a photodiode). In this system, the laser beam is focused at the end of a cantilever and then, after reflection, is recorded by the photodiode, whose active area is divided into four quadrants: two upper and two lower ones [Fig. 8]. The corresponding currents are  $I_{UL}$ ,  $I_{UR}$ ,  $I_{BL}$  and  $I_{BR}$ . When there is no detectable interaction, which corresponds to lack of measurable force, causing cantilever deflection, the laser beam is focused at the center of the photodetector. Thus, the signal difference between the upper and bottom (and also between left and right) quadrants is zero. The force acting perpendicularly to the investigated surfaces causes vertical movement of the laser beam, while the force acting in parallel to the surface shifts the laser beam horizontally. The corresponding equations are:

$$\mathbf{F}_{\perp} = (\mathbf{I}_{UL} + \mathbf{I}_{UR}) - (\mathbf{I}_{BL} + \mathbf{I}_{BR}) \quad (6)$$

$$\mathbf{F}_{\parallel} = (\mathbf{I}_{UL} + \mathbf{I}_{BL}) - (\mathbf{I}_{UR} + \mathbf{I}_{BR}) \quad (7)$$

Forces acting between the probing tip and the cell surface can have several different origins. In general, the tip-sample interaction can be described by a Lennard-Jones potential [Fig. 9], in which the interaction is attractive at large distances (typically, beyond a few tenths of a nanometer) due to van der Waals forces, capillary forces, some electrostatic or electromagnetic forces, and other types of adhesive forces. On the other hand, at very short range, the resulting repulsive force consists mainly of Pauli, ionic or steric repulsion due to the impenetrability of the electron clouds associated with the two surfaces.

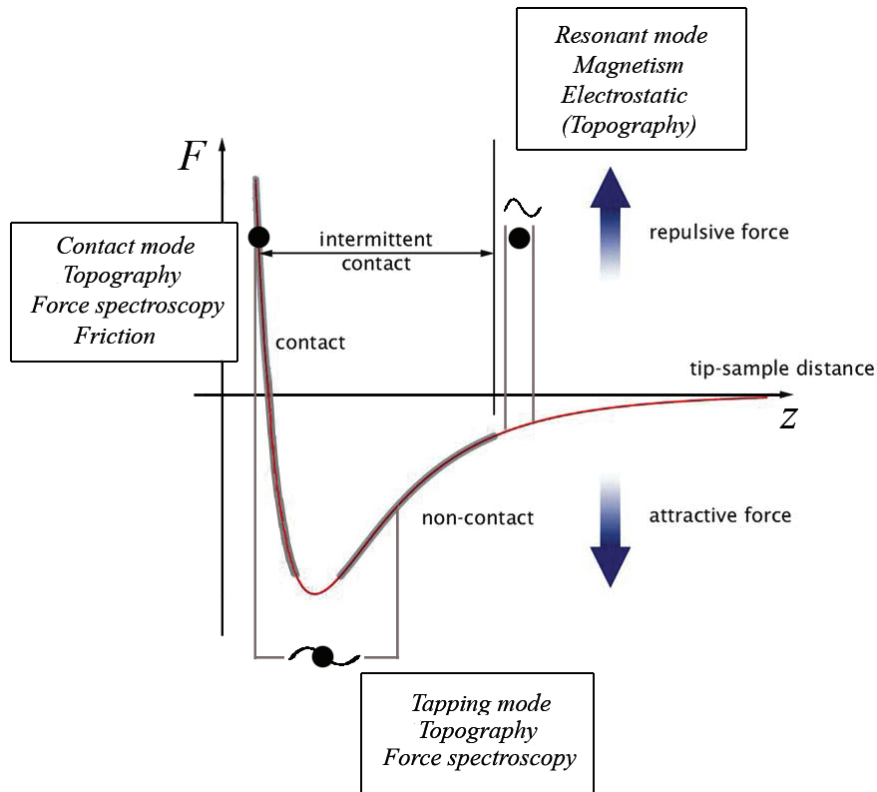


**Figure 9.** Lennard-Jones potential describing the dependence of interatomic forces on tip-sample distance and the resulting modes of AFM operation. Three AFM operating modes are located by black dots in the diagram showing the interaction force between tip and sample. In the tapping and resonant modes, the cantilever vibrates close to its resonance frequency, whereas the contact mode is quasi-static.

Depending on the distance between the tip and sample surfaces, and the resulting forces, different modes of AFM operation can be construed as presented in **Figure 9**. Since in this work only the contact mode was used, it is the only mode which will be described below.

### V.2.1.1. Contact mode

The first version of the AFM worked only in contact mode (CM). In this mode, the AFM operates in the repulsive limit of the Lennard-Jones potential, where clouds of electrons from the tip and surface cannot overlap. In this sense, the tip can be said to actually touch the surface. Usually, during AFM operation, the cantilever deflection is kept constant through a feedback loop controlling the  $z$  scanner position, and the surface

topography is calculated from the output of the feedback loop, namely the voltage applied to the  $z$  scanner. As the  $z$  scanners in commercial AFMs can usually cover ranges as large as 25  $\mu\text{m}$ , we can analyze samples with features taller than the optical lever detection range by using the feedback control.

Imaging of soft samples, like living cells, is limited by several factors. One of them is the presence of the lateral force. Its magnitude can be quantified using **Equation 7**. For hard, non-deformable surfaces, the lateral force is used to estimate the tip-sample friction or at least to compare different surfaces (Meyer et al., 1992). This mode of microscope operation is called lateral force microscopy (LFM) or friction force microscopy (FFM). For soft samples, such as biological specimens, the lateral force can cause a substantial sample deformation and make imaging difficult. Another parameter influencing strongly the imaging in contact mode is the magnitude of the applied load force, acting perpendicularly between the tip and the surface. The range of typical forces applied in CM varies from 10 pN to 10 nN depending on imaging conditions. A higher load force leads to the deformation of a soft sample and thus non-accurate imaging whereas its lower value would compromise high-resolution imaging. Nevertheless, the contact mode of the AFM can be adapted to allow visualization of the surface of living matter, like proteins or cells, in a non-destructive manner.

### **V.2.2. Elastic properties of living cells - determination of the Young's modulus - force spectroscopy mode**

The popularity of the *force spectroscopy* mode of AFM operation in biology related studies stems from the fact that this mode of operation allows for following changes accruing during various biological processes *in situ* in a quantitative manner. It is made possible by the excellent force sensitivity of the AFM, high precision in positioning the tip relative to the sample in all three dimensions, and the possibility of operation in liquids, especially in environments mimicking physiological conditions (Drake et al., 1989). This type of AFM measurement requires recording of so-called *force curves*, which show the dependence of the deflection of the cantilever (converted

into force) on the relative scanner position (which usually converted into tip-sample distance).

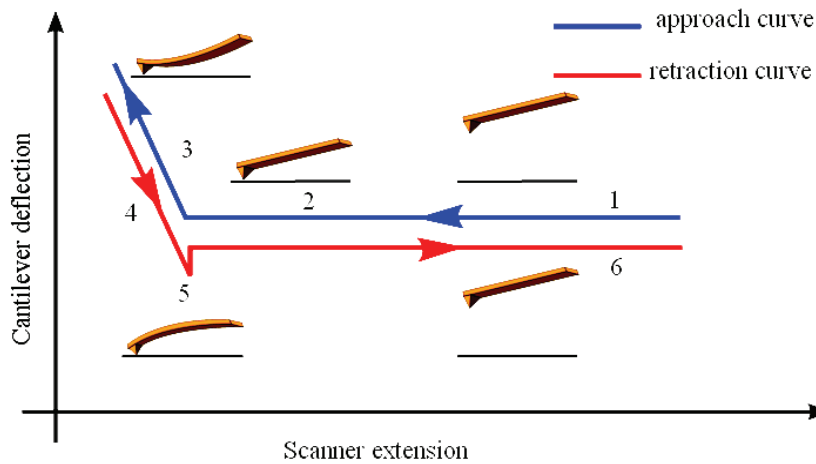


**Figure 10.** Force curve between the end of the AFM tip and the hard surface.

The *force-distance curve* consists of two parts: the first recorded during the approach of the cantilever to the sample surface (an approach curve is shown in **Fig. 10** as a blue line) and the second collected during withdrawal of the cantilever (a retraction curve, the red line in **Fig. 10**). When the cantilever is far away from the surface, the deflection is close to zero, since there is no detectable interaction. When the tip, mounted at the end of the cantilever, touches the surface, the cantilever starts to deflect, and the deflection magnitude increases until a certain maximum value. The deflection decreases when the cantilever is withdrawn from the surface. If there are any adhesive forces acting between the probing tip and the surface, the moment when cantilever detaches from the surface is represented by a jump, followed by horizontal line, thus denoting no measurable interaction force. The character (shape) of the force curve depends strongly on physical and chemical properties of the two interacting surfaces.

### V.2.2.1. Force curves on soft samples

In AFM, the elasticity measurement is realized by moving the  $z$ -scanner perpendicularly to the investigated surface and recording the deflection of the cantilever (Weisenhorn et al., 1993). Scanning function is disabled. The deflection is usually plotted as a function of the relative scanner position. When indentation occurs on a stiff, non-deformable sample, the deflection (after touching the surface) increases proportionally to the scanner position [Fig. 11, blue line].

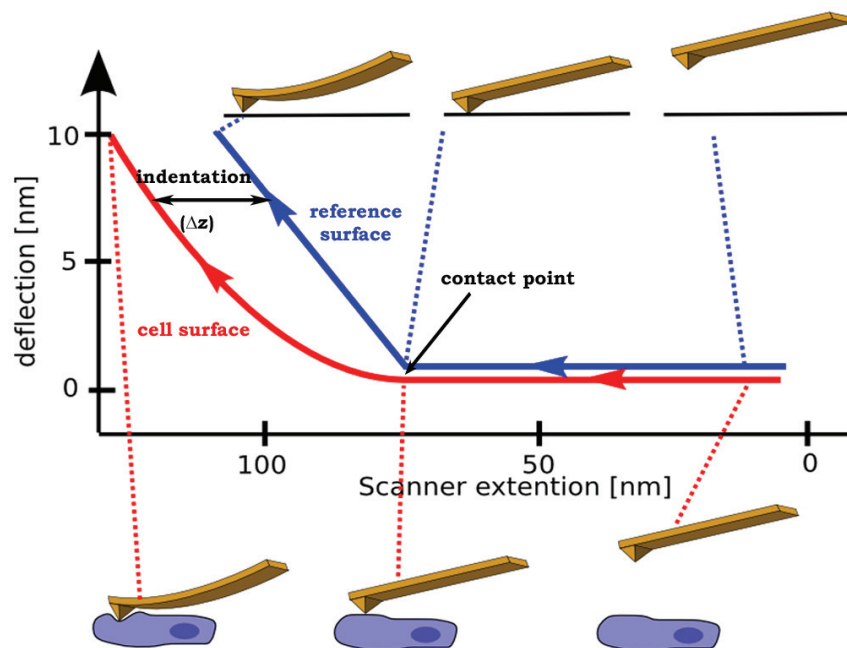


**Figure 11.** The concept of the elasticity measurement in an AFM experiment. The blue line corresponds to the force curve acquired for the stiff substrate, whereas the red line corresponds to the soft specimen.

For soft samples, the applied force may deform (compress) the sample surface. This is represented by the non-linear shape of the curve after contact with the surface [Fig. 9, red line]. This is because the cantilever deflection is smaller than the movement of the scanner. By subtracting two curves recorded on hard and soft samples, the relation between the applied force and the indentation depth can be obtained.

### V.2.2.2. The Young's modulus of cells

The most common physical parameter describing the elastic properties of a system is the Young's modulus. Its value is determined using a physical model based on continuum mechanics, and is derived from the work of Heinrich Hertz (Hertz, 1882). The model was later extended by Sneddon, who considered different shapes of the indenting probe (Sneddon, 1965). Since the number of atoms participating in contact between the probing tip and the sample surface is rather large ( $\gg 100$ ), a classical theory of elasticity can be applied. Usually, the shape of the AFM tip is approximated either by a conical or paraboloidal indenter. As a consequence, two equations describing the relation between the force,  $F$ , and indentation,  $\delta$ , are written down as:

$$\mathbf{F}_{\text{cone}} = \frac{2\mathbf{E}_{\text{cell}}}{\pi(1-\nu^2)} \cdot \delta^2 \cdot \tan(\alpha) \quad (8)$$

$$\mathbf{F}_{\text{paraboloid}} = \frac{4\mathbf{E}_{\text{cell}}}{3(1-\nu^2)} \cdot \delta^{1.5} \cdot \sqrt{\mathbf{R}} \quad (9)$$

where  $\mathbf{E}_{\text{cell}}$  is the Young's modulus,  $\nu$  is the Poisson coefficient,  $\alpha$  is the half-opening angle of the cone, and  $\mathbf{R}$  is the radius of curvature of the paraboloidal indenter. The determination of the Young's modulus requires also an assumption of the Poisson coefficient,  $\nu$ . For cells, its value is usually set to 0.5, corresponding to an assumption that cells are incompressible (Treloar, 1975).

The mechanical response of a cell recorded during an AFM indentation experiment is composed of partial mechanical responses originating from different cellular structures interacting with the indenting tip. First, on its way towards the cell, the tip meets the glycocalix, next the cellular membrane, and then either the intracellular organelles or the cytoskeleton. Thus, for small indentations, the Young's modulus reveals mostly properties of cell membrane tension, while large indentations reveal properties of the cytoskeleton and intracellular organelles.



## **V.2.3. Experimental conditions for cell elasticity and topography measurements**

### **V.2.3.1. AFM imaging of cells**

In this work AFM contact mode was used to characterize mechanical properties and to visualize nano-scale structures on the surface of living melanoma cells before after exposure to ROS.

To visualize the cell surface, the deflection image (based on the recording of the error signal) was used. By this method the cell surface structures are clearly visible; however, this does not provide a quantitative description. The error signal is the input to a feedback system, whose output (after amplification) serves to drive the  $z$ -scanner, which moves either the sample or the probe in the  $z$ -direction. This signal can be recorded simultaneously with a topography image. Since its action is similar to that of the edge filter, it is possible to observe subsurface structures more clearly than in topography. However, it is only from topography that the actual structure heights are obtained. If the feedback is optimized, the deflection image is the first derivative of the topography image.

**Figure 12** shows a 15  $\mu\text{m}$  fragment of a cell surface (Lu1205 melanoma adhered to a glass coverslip) measured using AFM working in contact mode. Two types of images are presented: deflection [**Fig. 12a**] and topography [**Fig. 12b**]. This well-spread cell exhibits many cable-like structures running along the entire cell. The cable-like structures detected by AFM are projections of actin bundles of stress fibers.

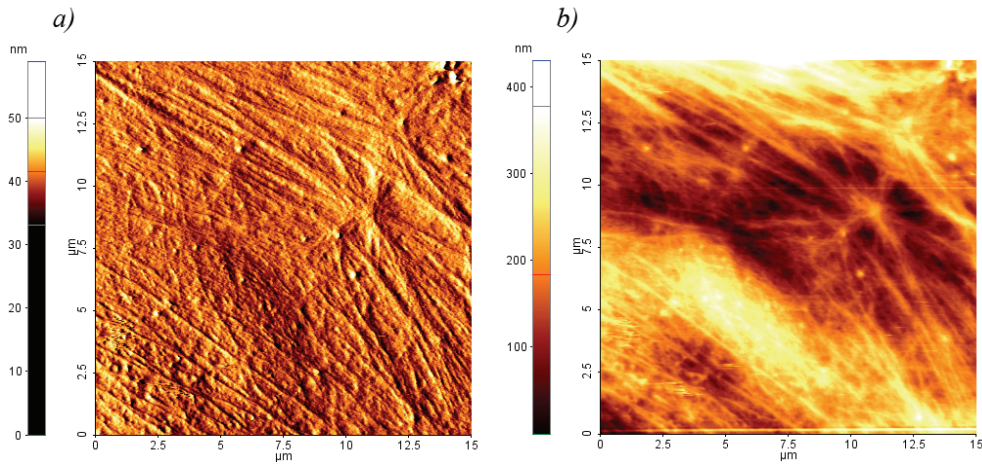


**Figure 12.** Surface of the living 1205Lu cell: (a) deflection and (b) topography images. Images were recorded by applying the force of 0.87 nN (set point) and scan speed of 0.87 Hz.

The cytoskeletal filaments are stiffer than the surrounding cytosol, the liquid composed of water, ions, proteins, and other small molecules. By applying sufficiently high load force acting perpendicularly to the cell surface, it is possible to distinguish between softer and stiffer parts of the cell surface due to the high spatial resolution in AFM elasticity measurements. The softer parts of the cell will be compressed more as compared to the stiffer ones. In such a manner, it is possible to sense the underlying stiff cytoskeletal structures (Henderson et al., 1992; Rotsch et al., 2000), which will then be the most prominent features in standard topographic AFM images [Fig. 13].

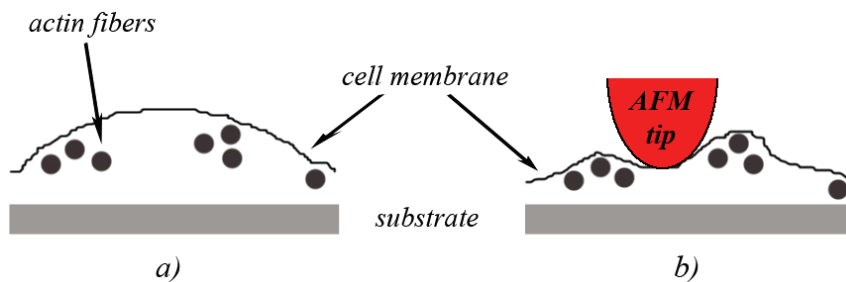


**Figure 13.** In AFM contact mode imaging, cytoskeletal structures lying beneath the cell membrane can be sensed by applying sufficiently high load forces (high set point). The softer regions located between cytoskeleton fibers (black dots denoting cross section) are more compressed enabling visualization of actin fibers.

There is also a more general influence on imaging, since the resolution of images will be a function of load force, tip shape, and elastic properties of the sample. Since a soft sample can be indented several hundred nanometers by the AFM tip, the contact area between the tip and the sample might be large. Thus, the imaging resolution will depend on this contact area.

### V.2.4. Single-cell-level AFM study of cellular response to ROS formed in the presence of TiO<sub>2</sub> nanoparticles and nanowires

The atomic force microscope (Park Systems, Model Xe-120) was equipped with a liquid cell, enabling measurements in conditions mimicking natural ones. It was used for both surface topography imaging and force spectroscopy on living cells. All measurements were performed in either PBS buffer or RPMI culture medium at room temperature. The force spectroscopy was performed using commercially available silicon nitride cantilevers with a nominal spring constant of 0.01 N/m and a tip radius of 50 nm (MLCT-AUHW, Veeco). Force curves were recorded at approach and retraction velocities of 5  $\mu\text{m/s}$ . For the Young's modulus determination, each recorded force curve was converted into a force-indentation relation. Next, for each such relation, the Hertz model was fit assuming a conical shape of the AFM tip [Fig. 14].

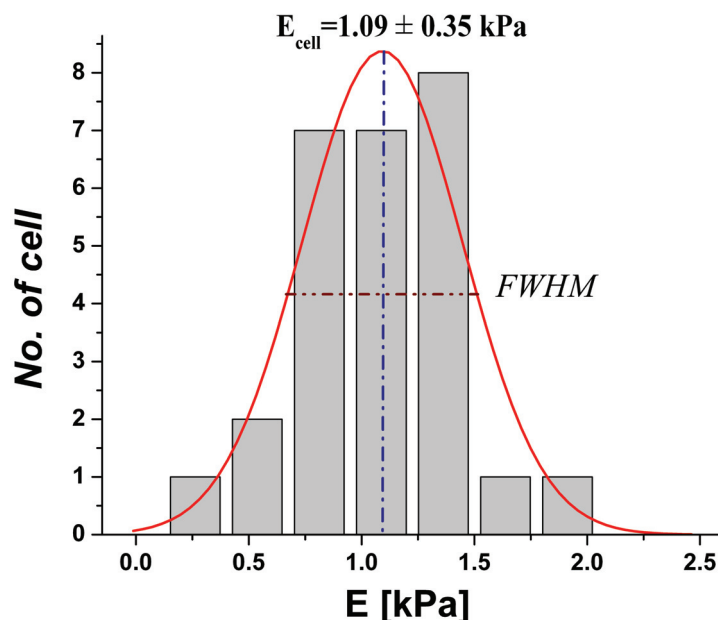


**Figure. 14.** Gaussian distribution (line) fitted to a histogram of the estimated Young's modulus values. The histogram was obtained for 27 cells (16 curves were collected for each cell).

The final, average value of Young's modulus was determined by fitting a Gaussian distribution to the histogram of the values obtained from each curve, following a method described elsewhere (Lekka et al., 1999).

### **V.3. Techniques used for TiO<sub>2</sub> characterization**

Since the nanoTiO<sub>2</sub> particles used in this thesis were obtained from different sources, it was necessary to employ several techniques for their thorough characterization. These techniques were: transmission electron microscopy (TEM) - applied to visualize the size of nanostructures, X-ray powder diffraction (XRD) - enabling characterization of the crystallographic structure, chemical composition, and dimensions and morphologies of the materials, and dynamic light scattering (DLS) - used to measure the hydrodynamic size of the aggregates.

#### **V.3.1. Transmission electron microscopy**

**Transmission electron microscopy (TEM)** is a technique which measures the transmission of an electron beam through an ultra thin specimen. For TEM characterization small amounts of nanoTiO<sub>2</sub> nanoparticles and nanowires were dispersed in ethanol using an ultrasound bath for 40 minutes. Next, the suspension was dropped onto a holey carbon film deposited on a 300-nm mesh copper grid (Plano GmbH S147-3). After drying in air, the specimens were observed by TEM (model Phillips, CM20) at an accelerating voltage of 200 kV.

### **V.3.2. X-ray powder diffraction**

**X-ray powder diffraction (XRD).** The XRD technique is based on observation of the scattered intensity of an X-ray beam as a function of incident and scattered angles. The powder X-ray diffraction patterns were recorded using Cu K $\alpha$  radiation using a powder diffractometer, XRD (Rigaku D/max-2400).

### **V.3.3. Dynamic light scattering**

**Dynamic light scattering (DLS)** is a technique which is used to determine the size distribution profile of small particles in suspension or polymers in solution. The Brownian motion of the particles causes the intensity of the scattered light to vary in time. This fluctuation in intensity is related to the size of the particles; smaller particles move more quickly than larger particles. Analyzing the intensity fluctuations yields diffusion coefficients and particle sizes (*via* the Stokes-Einstein exchange relation).

A Malvern Instruments Zetasizer was used to measure the hydrodynamic size of the aggregates in the culture media RPMI 1640 (pH 7.4, Sigma) supplemented with 10% of FBS.

## **V.4. Techniques used for cell characterization**

Although the AFM technique was used as a major tool to detect the response of living cells exposed to ROS in this thesis, several other methods were also implemented to enhance the overall information. In particular, cell viability assay, selective staining of actin and optical microscopy were used.

The cell viability assay delivers information on the condition of cells, in particular on the presence of necrotic cells. Optical microscopy enabled observation of the morphology of single cells exposed to oxidative stress. More detailed information on actin filament organization was obtained using fluorescent microscopy on cells stained with fluorescently labeled phalloidin.

### **V.4.1. Visualization of actin filaments**

To visualize the actin filaments, cells were fluorescently labeled with Fluorescein Isothiocyanate (phalloidin-FITC, Sigma) using the following protocol: cells were cultured on glass cover slips and after formation of a semi-confluent layer they were exposed to the photo-oxidative stress (460 seconds of UVA irradiation of 1 mW/cm<sup>2</sup> for nanoTiO<sub>2</sub>). After exposure, cells were fixed using 4% formaldehyde solution in PBS for 15 minutes, followed by rinsing in PBS buffer. Next, they were permeabilized with a 0.2% solution of Triton X-100 for 5 minutes at 4 degrees, and washed with PBS buffer. Actin filaments were labeled with phalloidin-FITC solution (300 units/ml of PBS) for 30 minutes at room temperature. Samples were imaged using a fluorescent microscope with a blue light halogen source ( $\lambda = 450$  nm) exciting the characteristic green fluorescence ( $\lambda = 550$  nm) of the phalloidin-FITC (MEIJI TECHNO TC5600 Inverted Biological Microscope, MA865 Blue Excitation Filter).

### **V.4.2. Cell viability assay**

To assess the effect of the various polymorphs of nanoTiO<sub>2</sub>, *i.e.* nanowires and nanoparticles, on Lu1205 and WM793 cells, a viability assay implementing propidium iodide was performed using a NucleoCounter® device (Chemometec, Denmark). This is a compact fluorescence microscope with a green LED light ( $\lambda = 550$  nm) exciting the characteristic red fluorescence ( $\lambda = 650$  nm) of propidium iodide (PI) [Fig. 15].

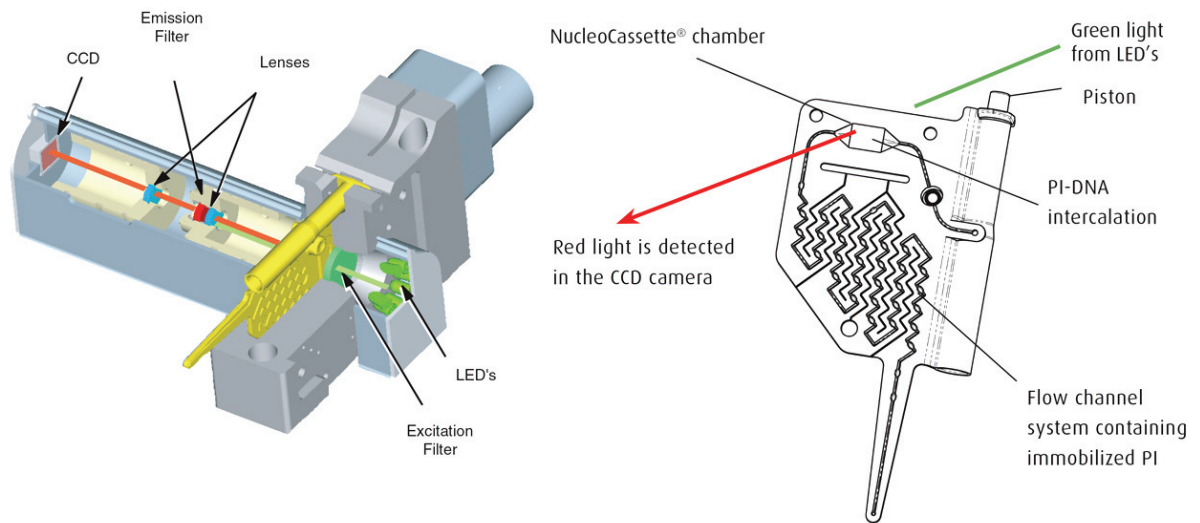


**Figure 15.** NucleoCounter® - the integrated fluorescence microscope [Taken from ChemoMetec, The NucleoCounter® information brochure]

The CCD camera registers the red light and the signal is automatically correlated to the cell count. Cell viability is calculated using the following formula:

$$V = \frac{C_t - C_{nv}}{C_t}, \quad (10)$$

where  $V$  is the cell viability denoting the number of living cells,  $C_t$  is the total count in the sample, and  $C_{nv}$  is the number of non-viable cells.

The viability test carried out with PI is illustrated conceptually in **Figure 16**.

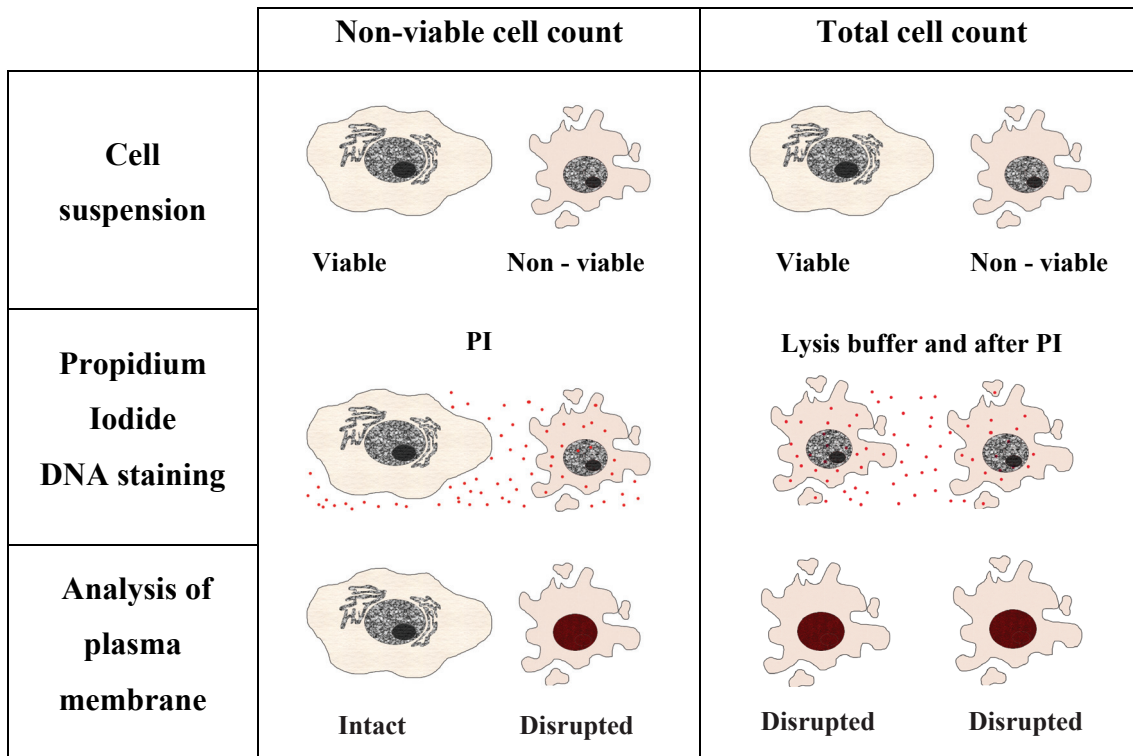


Figure 16. Propidium Iodide staining cellular DNA.

For viability tests, cells were cultured in Petri dishes and after formation of a semi-confluent layer they were exposed to the photo-oxidative stress (230 seconds of UVA irradiation of  $1\text{mW}/\text{cm}^2$  for  $\text{nanoTiO}_2$ ). After exposure, cells were detached using a cell scraper and sucked into the NucleoCassette flow channel system containing immobilized PI. Next, the NucleoCassette was inserted into the excitation chamber and after 10 seconds, staining results were observed. For total cell count, control cells were subjected to lysis and a similar procedure as used for cells exposed to photo-oxidative stress was applied.



### **V.4.3. Cell morphology**

Cell morphology was observed using optical microscopy (MEIJI TECHNO TC5600 Inverted Biological Microscope). They were exposed to photo-oxidative stress in the same way as for fluorescent and atomic force microscopy, and then fixed with 4% formaldehyde for 15 minutes.

### **V.4.4. NBT staining**

Superoxide anions may be detected by histochemical staining, which is based on the ability of cells to reduce nitroblue tetrazolium (NBT). NBT specifically reacts with superoxide radicals and forms a purple / blue formazan precipitate. Similarly as for phalloidin staining, cells were cultured on glass cover slips and after the formation of a semi-confluent layer they were incubated with nanoTiO<sub>2</sub> for 30 min. Afterwards, cells were washed with HBSS medium and incubated with NBT (1.6 mg/mL) in HBSS at 37°C for 60 min. Subsequently, they were exposed to the photo-oxidative stress in the presence of nanoTiO<sub>2</sub> (at the concentration of 2 µg/mL) for 460 seconds of UV-A illumination (1 mW/cm<sup>2</sup>). They were then washed with HBSS and incubated with NBT. After staining, cells were fixed with 4% formaldehyde for 15 minutes and analyzed using optical microscopy (MEIJI TECHNO TC5600 Inverted Biological Microscope).

## **VI. Experimental results**

## VI.1. Characterization of TiO<sub>2</sub> nanoparticles and nanofilaments

Owing to their superior photocatalytic properties, nanoparticulate titania and nano-filamentous forms of titania (TiO<sub>2</sub>-based nanowires and nanotubes) have attracted tremendous scientific interest. Each year, more than 10,000 publications are devoted to titanium dioxide (TiO<sub>2</sub>), with more than 500 dealing with nanoparticulate and nanostructural aspects of this material. Issues of toxicity, workplace safety, and environmental impact as a function of the size and shape of nanoTiO<sub>2</sub> have also been of concern (Colvin, 2003; Sayes, 2006).

At the industrial level, nanoTiO<sub>2</sub> has already found numerous environmental and energy applications, including photocatalysis, advanced oxidation processes (AOPs), self-cleaning coatings, water-splitting, and photo-voltaic conversion.

A considerable body of published research points to the importance of finding correlations between the basic physico-chemical parameters of nanoTiO<sub>2</sub> and its photocatalytic efficiency (Testino et al., 2007). Despite the wide industrial use of this material and common consciousness of the related environmental and health risks, systematic studies oriented towards correlations between toxicity of nanoTiO<sub>2</sub> and its critical parameters, such as crystalline phase (anatase or rutile), size, shape and aspect ratio of individual nanoparticles, are largely missing. Furthermore, there is no consensus on the primary mechanisms which are responsible for cellular damage induced by photo-oxidative processes in the presence of nanoTiO<sub>2</sub>.

Therefore, in the next sections of this chapter, we present a systematic approach to:

- characterize, by a variety of physical methods, a wide range of anatase nanoTiO<sub>2</sub> (3.8 – 150 nm) particles, rutile nanoTiO<sub>2</sub> (5 - 215 nm) particles and anatase-based TiO<sub>2</sub> nanowires (diameter of 35 nm and 0.5 – 1 μm length);
- find correlations between their physico-chemical properties and their ROS formation efficiencies;
- verify the response of living human cells to the nanoTiO<sub>2</sub>-related stress.

### **VI.1.1. ROS generation by TiO<sub>2</sub>-based nanoparticles**

One of the goals of this work was to better understand the mode of action of nanoTiO<sub>2</sub> on biological targets, including living cells. Beyond any doubt, nanoTiO<sub>2</sub>, with its two principal crystalline phases of anatase and rutile, is the most common industrial nanomaterial, with vast applications which affect our daily lives. In this thesis we identify how the crystalline form and particle size can affect the photo-catalytic efficacy and toxicity.

The properties of anatase and rutile nanoTiO<sub>2</sub> are discussed and categorized in terms of the primary particle size. Eleven commercial anatase nanoTiO<sub>2</sub> powders with the primary grain sizes in the range of 3.8 to 150 nm were chosen for this study. The anatase nanoTiO<sub>2</sub> powders were obtained from the following sources:

- (i) Tayca Co., Japan, primary grain sizes: TKP101 – 3.8 nm, AMT100 -5.3 nm, AMT600 – 27nm, JA-1 -105 nm;
- (ii) Millennium Chemicals Inc., USA, primary grain sizes: PC500 – 4.5 nm, PC100 – 14.5 nm, PC105 – 22 nm, PC50 – 25 nm;
- (iii) Fluka GmbH, Switzerland, primary grain size: Fluka - 150 nm;
- (iv)Huntsman Advanced Materials GmbH, Switzerland, primary grain size: A-HR – 75 nm;
- (v) Sigma Aldrich, Switzerland, primary grain size: 110 nm.

Three commercial rutile nanoTiO<sub>2</sub> powders with the primary grain sizes in the range of 5 to 215 nm were selected. These samples were obtained from the following sources:

- (i) Kemira Oyj, Finland, primary grain size: S230 – 5 nm;
- (ii) Sachtleben Chemie GmbH, Germany, primary grain size: Eusolex T-2000 – 26 nm;
- (iii) Huntsman Advanced Materials GmbH, Switzerland, primary grain size: R-HD2 – 215 nm.

The commonly known industrial standard, Degussa P25 formulation (20% rutile and 80% anatase, average grain size of 26 nm) from Degussa GmbH, Germany, was used as a material of reference.

To obtain one missing size within the 3.8 to 150 nm range for anatase nanoTiO<sub>2</sub> powders, one of the commercial anatase powders, AMT600-Tayca, was annealed at 800<sup>0</sup>C for 1 hour in oxygen atmosphere. This process increased the original primary grain size from ~ 27 nm to ~ 42 nm. The XRD assay after the annealing revealed that the obtained nanoTiO<sub>2</sub> powder conserved its crystalline phase (anatase).

The particle primary sizes and grain size distributions were evaluated from TEM bright-field images. The example TEM images collected for several nanoTiO<sub>2</sub> powders selected for this study are shown in **Figure 1**.

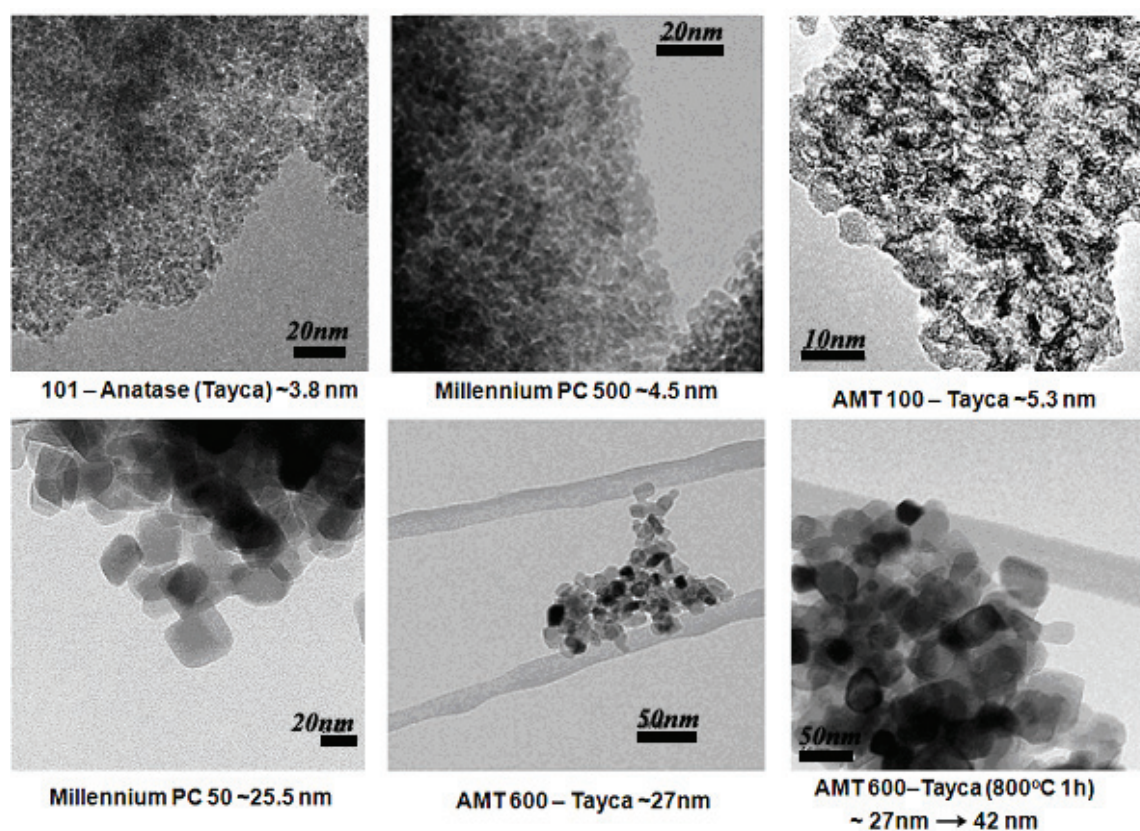


**Figure 1.** Evaluation of the primary particle size using TEM for various commercial and custom-modified\* nano-particulate TiO<sub>2</sub>. The TEM data, collected for selected nanoTiO<sub>2</sub> powders, are shown as a function of increasing particle size. \* The commercial material AMT600-Tayca (lower panel, third picture to the right) was modified by annealing at 800<sup>0</sup>C for 1 hour in oxygen atmosphere, which resulted in growth of the primary grain size from ~27 nm to ~42 nm.

Overall, the TEM results concerning the primary grain sizes for commercial anatase and rutile nanoTiO<sub>2</sub> powders are in good agreement with the manufacturer specification data sheets.

Electron spin resonance (ESR) studies were performed to determine whether differences in crystalline structure and the primary grain size, for anatase and rutile, are related to the efficiency of ROS formation, and thereby to the ability of different forms of nanoTiO<sub>2</sub> to induce oxidative stress.

As mentioned in Chapter V.1.2, we employed the common spin-trap DMPO to measure the photo-catalytic efficiency of ROS formation for various forms of nanoTiO<sub>2</sub>.

The EPR trace of the paramagnetic DMPO-OH adduct consists of four spectral lines with the intensity ratio 1:2:2:1. This characteristic ESR trace results from the partial overlap of the hyperfine and superhyperfine spectral structures. The hyperfine and superhyperfine resonant features are due to the interaction of the unpaired electron (located at the –NO<sup>•</sup> moiety of DMPO-OH) with the nuclear moments of nitrogen and hydrogen nuclei. Thus, in this spectrum, the ESR signal from one unpaired electron is primarily split into three signals due to the hyperfine coupling with the nuclear moment of nitrogen ( $I_N = 1$ ). Furthermore, each of these gives rise to two further lines from superhyperfine coupling originating from interaction with the closest hydrogen (nuclear spin  $I_H = 1/2$ ). These interactions are characterized by the two hyperfine parameters  $a_N$  and  $a_H$ , having the same value of 14.95 G. An example evolution of the ESR traces of the paramagnetic DMPO-OH spin adduct as a function of illumination time is shown in **Figure 2**. UV-A light ( $\lambda = 365$  nm, 10 mW/cm<sup>2</sup>) was used to excite the nanoTiO<sub>2</sub> particles suspended in PBS. To prevent particle agglomeration during illumination, the PBS suspensions were vigorously stirred with a PTFE-coated magnetic stirrer.

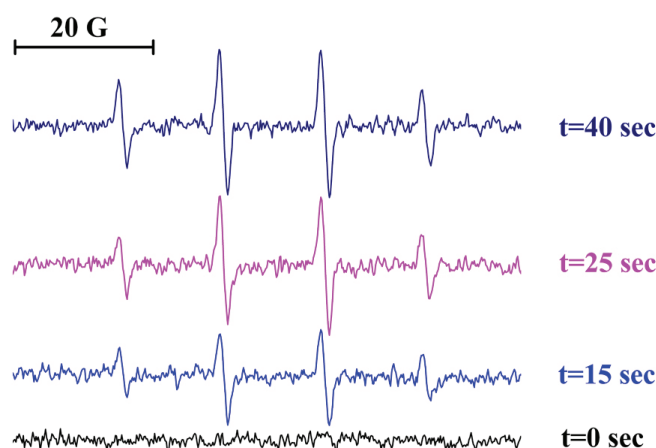


**Figure 2.** An example evolution of the ESR traces of the paramagnetic DMPO-OH spin adduct as a function of illumination time for Tayca AMT100 (5.3 nm grain size).

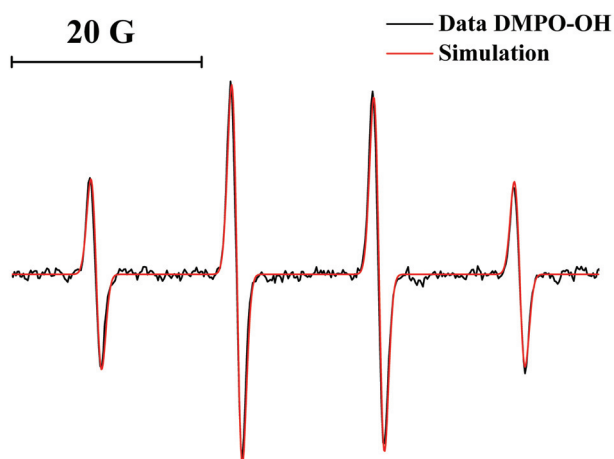


**Figure 3.** An example experimental ESR trace of DMPO-OH and its simulation. The ESR spectrum was obtained for 30 sec of illumination of a PBS suspension of P25 Degussa.

Since the signal-to-noise ratio (S/N) of the ESR spectra acquired in this experiment was typically rather low (see **Figure 2**), all of the experimental ESR traces were carefully analyzed by performing spectral simulation with the commercial software, Mathcad 2001 Professional. An example experimental ESR trace of DMPO-OH and its simulation is shown in **Figure 3**. This ESR spectrum was obtained for 30 sec of illumination of a PBS suspension of P25 Degussa. The following spectroscopic parameters were used to simulate the characteristic 1:2:2:1 quartet of the ESR signal of DMPO-OH: the spectroscopic  $g$ -factor was 2.0058 and the hyperfine and superhyperfine parameters were  $a_N = a_H = 14.95$  G (Buettner, 1987; Arya et al., 1992; Singh et al., 1998; Laachir et al., 2005).

To obtain the actual concentrations of the paramagnetic product, DMPO-OH, the simulated ESR traces were double-integrated using the data analysis and graphing software, Origin 7.5 (OriginLab). The time evolution of the double integrals of the simulated ESR traces of DMPO-OH yielded a family of ROS formation kinetics, some examples of which are shown for anatase and rutile in **Figure 4**. The slopes of these pseudo-zeroth-order kinetics report on the photocatalytic efficacy of nanoTiO<sub>2</sub>. As can be seen in **Figure 4**, the anatase nanoTiO<sub>2</sub> reveals higher efficiency of ROS formation than rutile nanoTiO<sub>2</sub>. The highest efficiency of ROS formation was found for the material of reference, the P25 Degussa formulation from Degussa.

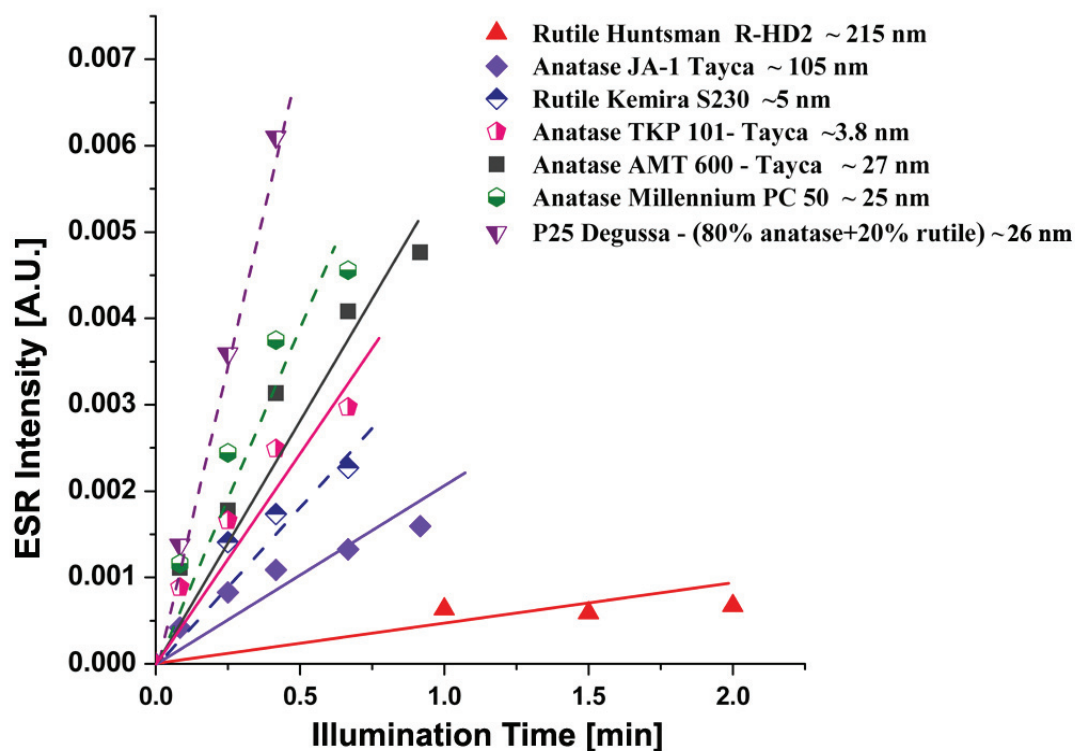


**Figure 4.** Example kinetics of ROS formation in aqueous suspensions of selected nanoparticulate anatase and rutile samples. For all the materials studied, the concentration of nanoTiO<sub>2</sub> in PBS suspensions was of 32 mg/100 mL.

Overall, these results are in good agreement with numerous previously published data, which, in the great majority, point to the superiority of nanoparticulate anatase over rutile in photocatalytic formation of ROS, as well as to the excellent photocatalytic properties of P25 Degussa (Sayes, 2006). The summary of ROS generation efficiencies for the studied nanoparticulate anatase and rutile samples is shown in **Table 1**. The relative quantum yields, QY, were derived from the kinetic slopes of acquired for all the studied materials.



**Table 1.** ROS generation efficiencies for nanoparticulate anatase and rutile samples.

NAME	Primary Particle Size [nm]	QY*	% of QY of P25
P25 Degussa – (80% anatase+20% rutile)	26	0.02714	100
<b>ANATASE</b>			
TKP 101- Tayca	3.8	0.00552	20.34
Millennium PC 500	4.5	0.00438	16.14
AMT 100 - Tayca	5.3	0.00521	19.2
Millennium PC 100	14.5	0.00684	25.20
Millennium PC 105	22	0.00704	25.94
Millennium PC 50	25	0.0086	31.69
AMT 600 - Tayca	27	0.00757	27.89
AMT 600 (800°C, 1h)	42	0.00658	24.25
Huntsman – Tioxide A-HR	75	0.00341	12.56
JA-1 Tayca	105	0.00272	10.02
Sigma	110	0.00179	6.6
FULKA	150	0.00168	6.19
<b>RUTILE</b>			
Kemira S230 rutile	5	0.00413	15.22
Euolex T-2000,Sachtleben	26	0.00128	4.72
Huntsman R-HD2	215	0.000504	1.86

\* QY – relative quantum yield of photocatalytic efficiency of titanium nanoparticles

The photocatalytic efficiencies of anatase and rutile nanoTiO<sub>2</sub> powders were derived from the slopes as a function of the primary particle size (determined on TEM images), as shown in **Figure 5a**. For anatase nanoTiO<sub>2</sub> the photocatalytic efficiency of ROS formation reveals a bell-shaped dependence as a function of the primary particle size. The maximum of this distribution lies in the range of 25 nm to ca. 30 nm. This result is in good agreement with data reported by Daimon and Nosaka for the photocatalytic singlet oxygen generation efficiency in air of various types of commercial nanoTiO<sub>2</sub> [**Fig. 5b**] (Daimon and Nosaka, 2007). The mechanism of formation of singlet oxygen in this work was proposed to proceed *via* collision and subsequent oxidation reaction of two

superoxide radical molecules ( $O_2^{\bullet-}$ ) at the nanoTiO<sub>2</sub> particle surface. Although singlet oxygen generation is not the major ROS generation pathway for nanoTiO<sub>2</sub> under UV illumination, the results of Daimon and Nosaka corroborate well with the efficiencies of hydroxyl and superoxide radicals formation established in this work.

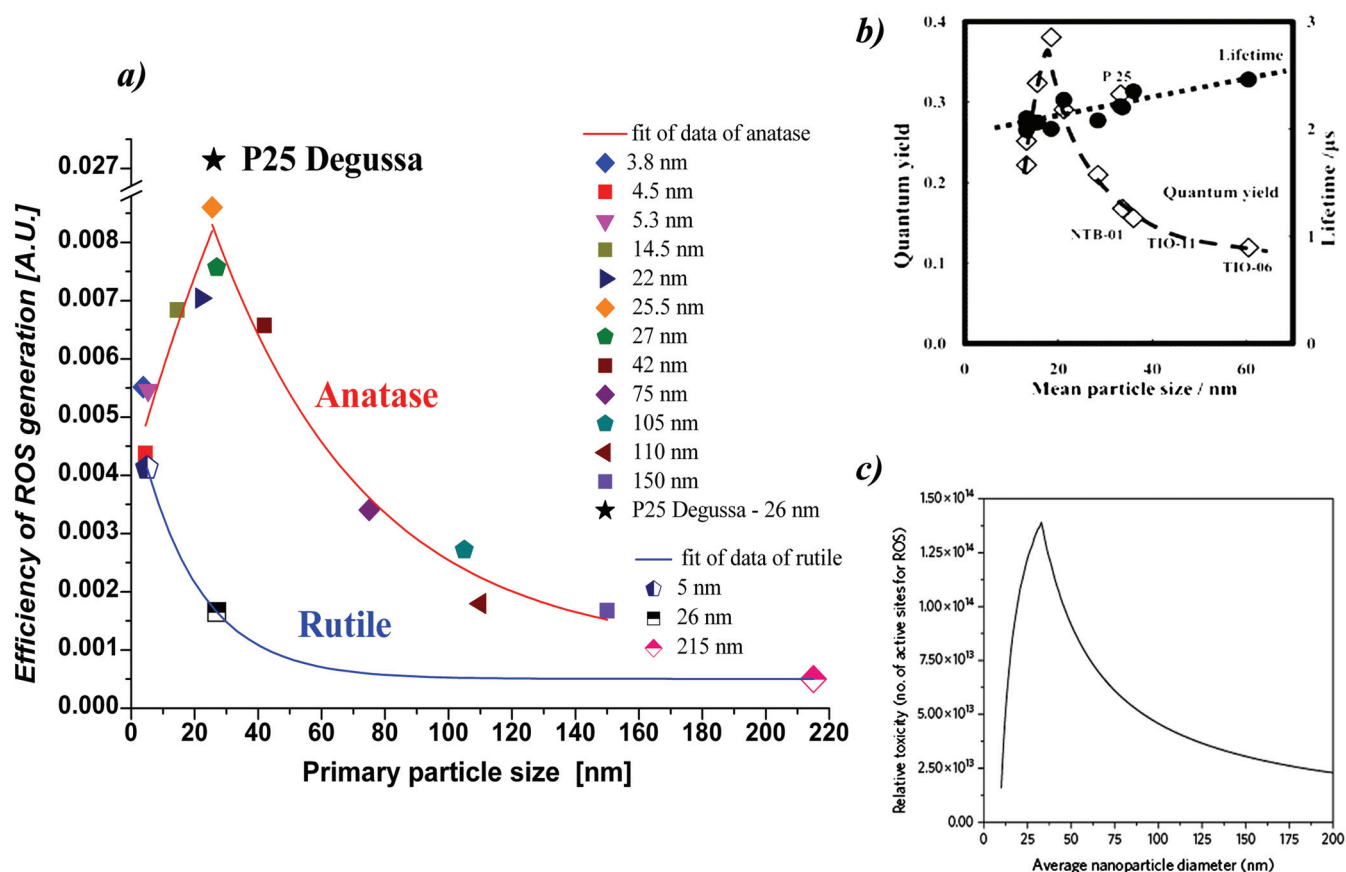


**Figure 5.** a) The ESR-derived efficiency of the photo-production of ROS for anatase and rutile nanoTiO<sub>2</sub> in PBS suspensions illuminated with UV-A light as a function of the primary particle size (Pierzchala - to be published), b) UV-light induced singlet oxygen generation by surfaces covered with anatase nanoTiO<sub>2</sub> (detection in air, at 1270 nm) as a function of primary particle size (Daimon and Nosaka, 2007), c) Prediction of the potential for generation of ROS as a function of nanoparticle size. Maximum number of ROS generated by TiO<sub>2</sub> nanoparticles at a particle loading of  $50 \times 10^9$  nanoparticles per unit volume, under ambient temperature and pressure, and with equilibrium surface chemistry (Barnard, 2010).

Our results, which point to a strong dependence on primary grain size of ROS photo-catalytic efficiency of nanoTiO<sub>2</sub>, are also in good agreement with data obtained by Almquist and Biswas for the photo-catalytic decomposition of phenol in water (Almquist and Biswas, 2002) and the very recent findings of Koci et al. (2009) for the photo-catalytic decomposition of CO<sub>2</sub> in the presence of nanoTiO<sub>2</sub> (Koci et al., 2009).

Recently, in a theoretical study, Barnard showed a very similar dependence of ROS generation by anatase nanoTiO<sub>2</sub> as a function of primary grain sizes (Barnard, 2010). In particular, the theoretical prediction points to an increase in ROS generation up to a size of 33 nm, and then 1/R (R-particle radius) decreases for larger sizes [see Fig. 5]. The decaying slopes of singlet oxygen generation efficiency in the experiment of Daimon and Nosaka and in our ESR measurements of ROS formation can be understood in terms of the specific surface area, which decreases with the increasing particle size. Particularly, the decrease of the quantum yield of singlet oxygen formation may be explained as the decrease in the amount of adsorbed molecular oxygen. On the other hand, nanoTiO<sub>2</sub> photocatalysts smaller than 20 nm show a lower quantum yield owing, presumably, to the enhanced recombination of electron-holes pairs. This is due to decreasing crystallinity of nanoTiO<sub>2</sub> with smaller particle sizes (Daimon and Nosaka, 2007). This seems to be consistent with the results of Almquist and Biswas, who found the optimum size for light induced ROS formation to be in the range of 25-40 nm (Almquist and Biswas 2002).

### **VI.1.2. ROS generation by anatase-based TiO<sub>2</sub> nanowires**

In the following section, we will present a thorough characterization of custom made anatase-based TiO<sub>2</sub> nanowires and their comparison with two selected commercial nanoparticulate TiO<sub>2</sub>: anatase AMT100 and the industrial standard, P25 Degussa.

TiO<sub>2</sub>-based nanowires have recently been synthesized in our laboratory by hydrothermal treatment of anatase in the highly concentrated NaOH solutions. This protocol yielded a large quantity of nano-filaments with Na<sub>x</sub>H<sub>y</sub>TiO<sub>2+δ</sub> composition, as suggested in the original report by Armstrong et al. (Armstrong et al., 2004, 2005). The synthesized nanowires have the Ti-O skeleton of the layered structure, which consists of edge sharing TiO<sub>6</sub> octahedra. Subsequent washing of the Na<sub>x</sub>H<sub>y</sub>TiO<sub>2+δ</sub> material with hydrochloric acid promotes the complete exchange of Na<sup>+</sup> by H<sup>+</sup>, thus yielding H<sub>x+y</sub>TiO<sub>2+δ</sub> nanowires, without drastic modification of their morphological characteristics. Further heat treatment of the H<sub>x+y</sub>TiO<sub>2+δ</sub> materials leads to formation of TiO<sub>2</sub> nanowires with different crystal structures depending on the preparation conditions

(Armstrong et al., 2004; Armstrong et al., 2005). Either nanowires or nanotubes can be obtained by tuning the growth conditions (*i.e.* the temperature and composition of the starting mixture Ti/Na ratio).

The crystallinity and physico-chemical properties of the TiO<sub>2</sub>-based nanowires were determined using X-ray powder diffraction technique (XRD), transmission electron microscopy (TEM), dynamic light scattering (DLS), and electron spin resonance (ESR).

**Figure 6a** presents a typical TEM image of the TiO<sub>2</sub> nanowires, with an average diameter of  $35 \pm 5$  nm and length of 0.5 – 1.0  $\mu$ m. For comparison, images of two commercial nanoTiO<sub>2</sub> materials are shown in **Figure 6b and c**.

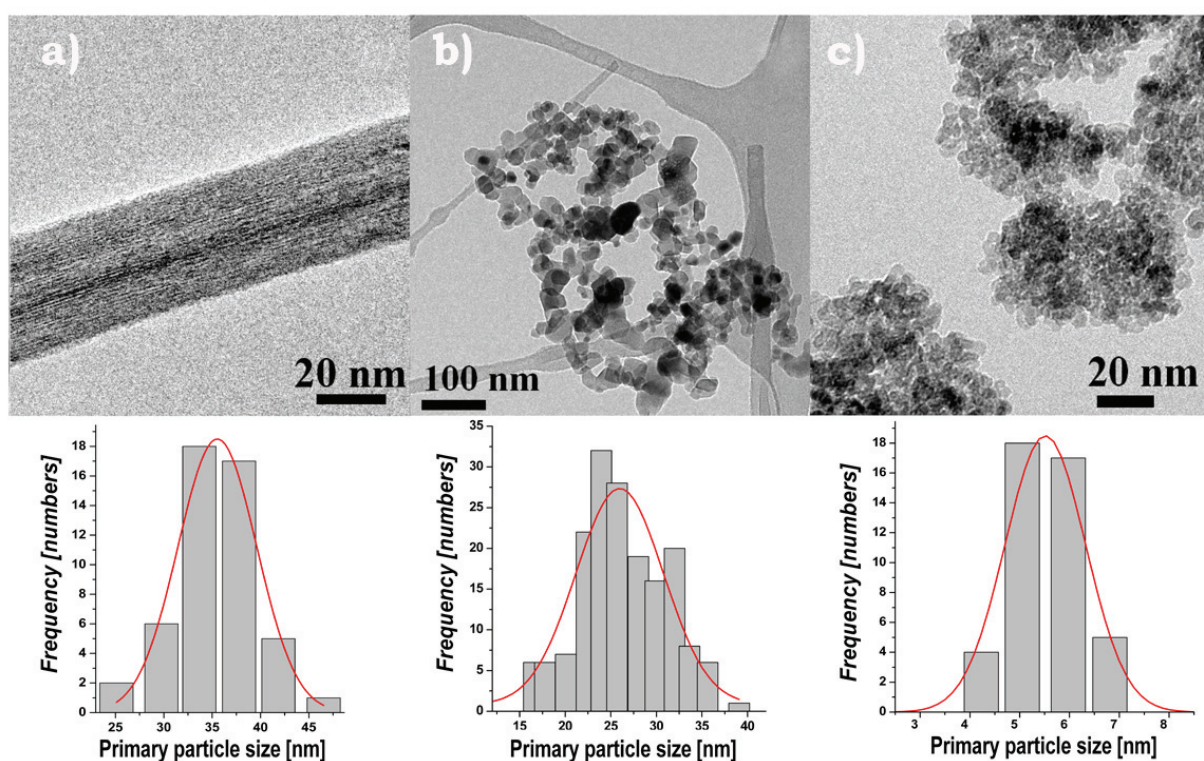


**Figure 6.** A comparison of TEM images and size distributions for anatase-based TiO<sub>2</sub> nanowires, P25 Degussa, and anatase AMT100 nanoparticles: a) anatase-based TiO<sub>2</sub> nanowires, b) nanoparticles of P25 Degussa (particle size of  $26 \pm 1$  nm), and c) anatase AMT 100 nanoparticles (particle size of  $5.3 \pm 1.0$  nm).

To verify the form of the synthesized anatase-based TiO<sub>2</sub> nanowires, XRD measurements were performed [**Fig. 7**].

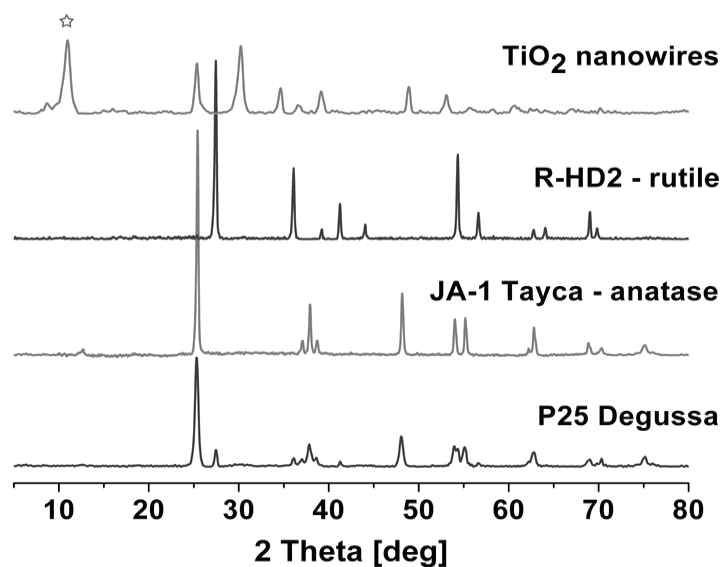


**Figure 7.** A comparison of XRD patterns for anatase-based  $\text{TiO}_2$  nanowires and commercial nano $\text{TiO}_2$  (JA-1 Tayca - anatase, R-HD2 Huntsman - rutile and Degussa P25).

As can be seen in **Figure 7**, the custom-made anatase-based  $\text{TiO}_2$  nanowires show a distinct XRD pattern as compared to those acquired for commercial anatase nano $\text{TiO}_2$ . In particular, the XRD patterns of rutile and anatase nano $\text{TiO}_2$  shown in **Figure 7** exhibit strong diffraction peaks at  $2\theta = 27^\circ$ ,  $36^\circ$  and  $55^\circ$  and  $25^\circ$  and  $48^\circ$ , indicating the rutile and anatase phases, respectively. The XRD spectrum collected for the custom made anatase-based  $\text{TiO}_2$  nanowires shows no phase transformation from the starting material (anatase). Moreover, an additional peak at  $\sim 10^\circ$  was observed. It was identified by Chen and co-workers as the (200) peak of the titanate phase,  $\text{H}_2\text{Ti}_3\text{O}_7$  (Chen et al., 2002). Based on this observation, we concluded that the synthesized nanowires are of the Natitanate structure rather than anatase.

Similarly to the measurements performed for nanoparticulate  $\text{TiO}_2$  (see VI.1.1), an ESR spin-trapping assay with DMPO was used to verify the photocatalytic properties of anatase-based  $\text{TiO}_2$  nanowires. The summary of the ESR results is shown in **Figure 8**.

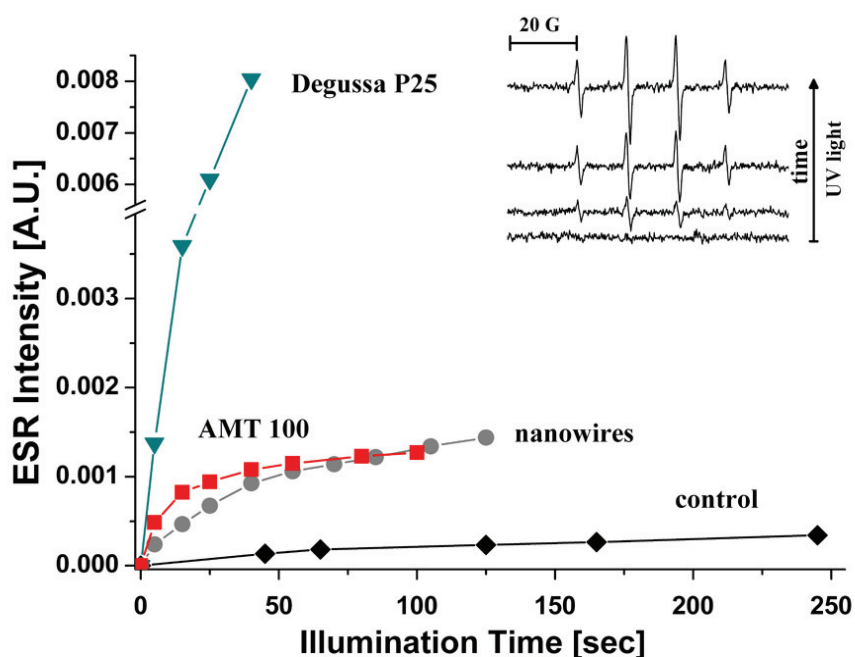


**Figure 8.** The ESR-derived efficiency of the photo-production of ROS for anatase-based  $\text{TiO}_2$  nanowires, P25 Degussa and anatase AMT100 nanoparticles. All particles were suspended in PBS buffer at the concentration 32mg/100ml and 50  $\mu\text{M}$  of DMPO and illuminated with UV-A light ( $\lambda = 365 \text{ nm}$ , 10  $\text{mW}/\text{cm}^2$ ). Control: the ESR signal intensity of DMPO-OH as a function of illumination time in the absence of nanomaterials. **Inset:** typical evolution of ESR traces of the paramagnetic product DMPO-OH as a function of illumination time.

In **Figure 8**, the ESR signal intensity plots are shown as a function of illumination time (DMPO-OH spin adduct), representing the efficiency of ROS generation for anatase-based  $\text{TiO}_2$  nanowires, P25 Degussa and anatase AMT100 nanoparticles. These results point to a rather similar photocatalytic efficiency of anatase-based  $\text{TiO}_2$  nanowires compared with that of anatase AMT100 nanoparticles. The summary of ESR-measured ROS generation efficiencies for the anatase-based  $\text{TiO}_2$  nanowires is shown in **Table 2**.

**Table 2.** ROS generation efficiencies for anatase-based TiO<sub>2</sub> nanowires, P25 Degussa and anatase AMT100 nanoparticles.

NAME	Primary Particle Size	DLS Size [ $\mu\text{m}$ ] *	QY* *	% of QY of P25
P25 Degussa	26 nm	3.435	0.02714	100
AMT 100	5.3 nm	2.116	0.00521	19.2
TiO <sub>2</sub> NW	35 nm $\times$ 0.5 -1 $\mu\text{m}$	0.8	0.0041	15.12

\* Size distribution profile of small particles in suspension.

\*\* QY - quantum yield - photocatalytic efficiency of titanium nanoparticles.

The relative ROS generation efficiency (QY) shown in **Table 2** was calculated taking as a reference material the widely-adopted commercial standard, P25 Degussa.

To check the photocatalytic efficiency of anatase-based TiO<sub>2</sub> nanowires, we also performed an ESR experiment, where the stable, water-soluble nitroxide radical, TEMPOL, was used as a molecular target for the photocatalytically-induced ROS. An example time evolution of the ESR signal of TEMPOL during the process of its photocatalytic degradation in the presence of nanoTiO<sub>2</sub> AMT100 is shown in **Figure 9**.

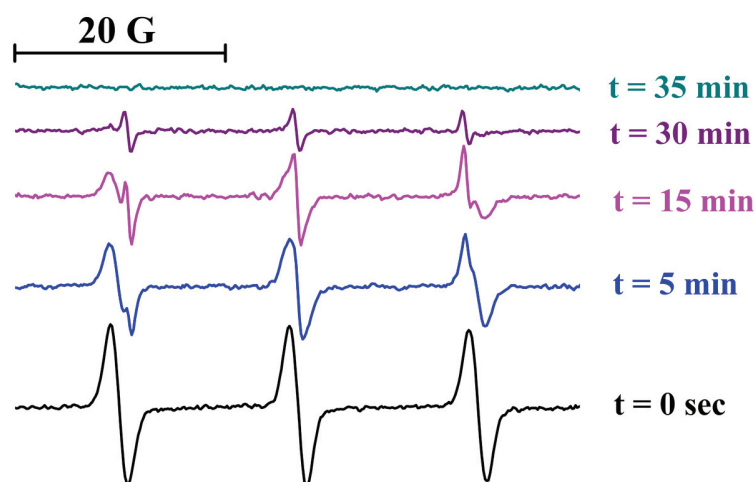


**Figure 9.** An example evolution of the ESR traces of the stable nitroxide radical, TEMPOL, as a function of illumination time with UV-A light in the presence of Tayca AMT100 (5.3 nm grain size). TEMPOL, at the concentration of 50  $\mu\text{M}$  was used as a molecular target for ROS generated by the photocatalytic action of nanoTiO<sub>2</sub> (Tayca AMT100).

As can be seen in **Figure 9**, the ESR signal of TEMPOL decays with illumination time. In addition, the initial ESR triplet of TEMPOL gets distorted by the presence of a new signal, which also consists of three ESR lines. The ESR features belonging to this new

signal are substantially narrower than those of the original TEMPOL signal. The new signal can be attributed to formation of another stable nitroxide radical, TEMPON. TEMPON is generated by ROS attack on TEMPOL (Saito et al., 2002). To better distinguish the complex kinetics of TEMPOL decay and TEMPON formation during the photocatalytic degradation of TEMPOL in the presence of nanoTiO<sub>2</sub>, we simulated the spectra with Mathcad 2001 Professional. Typical experimental ESR traces and spectral simulations are shown in **Figure 10**. The following spectral parameters were used to simulate the characteristic 1:1:1 triplets of ESR signals:  $\Delta H=0.47$  G,  $a_N =15.9$  G,  $g=2.0065$  and  $\Delta H=1.58$  G,  $a_N =16.9$  G,  $g=2.0066$ , for TEMPON and TEMPOL, respectively.

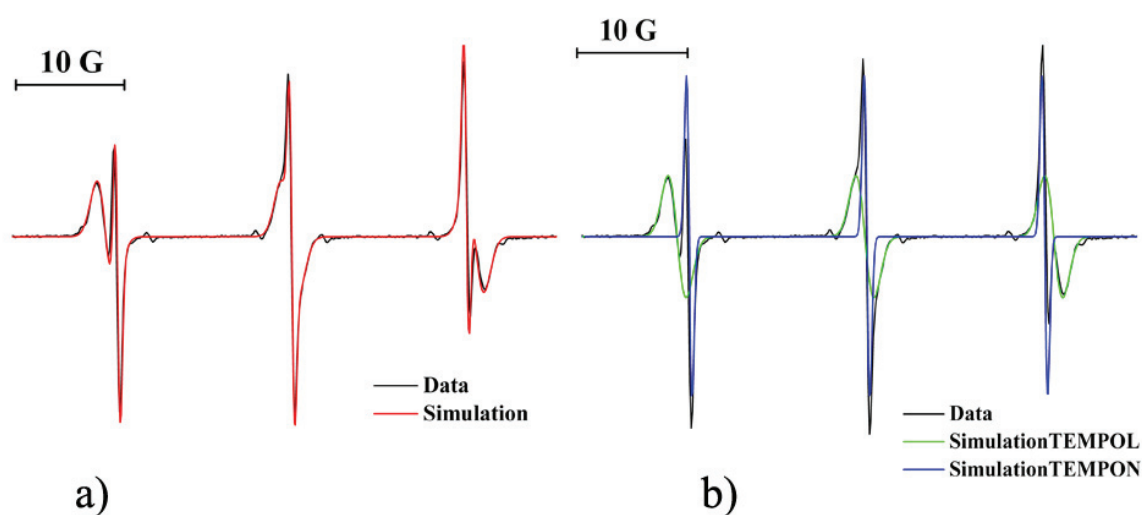


**Figure 10.** The experimental ESR traces and spectral simulations for the photocatalytic degradation of TEMPOL in the presence of P25 Degussa after 3 min of illumination with UV-A. a) The total overlapped experimental and simulated ESR spectra. b) The experimental ESR trace overlapped with the decomposed signals of TEMPOL and TEMPON.

The spectral simulation allowed for derivation of the final kinetics of decay and formation for both components of the complex ESR signal. The double-integration of the simulated individual ESR signals yielded the respective ESR signal intensities of TEMPOL and TEMPON. The corresponding kinetics of decay/formation are shown in **Figure 11**. It can be seen that the photocatalytic decay of TEMPOL is the fastest in the presence of P25 Degussa. Similarly to the previous results of ROS spin-trapping with DMPO, this experiment also confirmed the comparable ROS generation capacities of the custom made anatase-based TiO<sub>2</sub> nanowires and commercial anatase nanoTiO<sub>2</sub>, AMT 100.



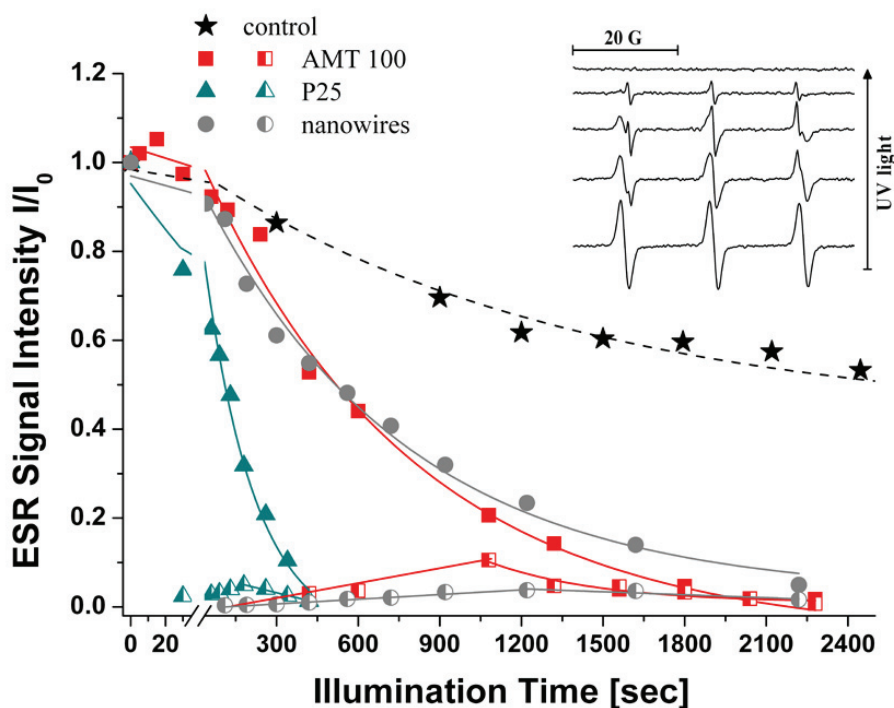
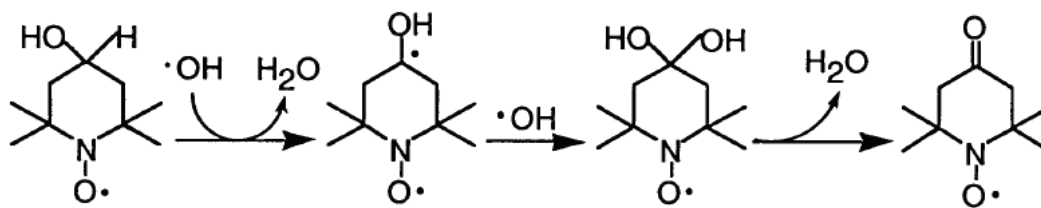


**Figure 11.** Photocatalytic degradation of the water-soluble nitroxide radical TEMPOL (50  $\mu\text{M}$ ) in the presence of anatase-based  $\text{TiO}_2$  nanowires, AMT 100 and P25 Degussa. Full symbols correspond to the degradation of TEMPOL. Half-filled symbols correspond to kinetics of formation and degradation of TEMPON. Control kinetics corresponds to the decomposition of TEMPOL under UV-A light illumination in the absence of nano $\text{TiO}_2$ . The lines are a guide to the eye. **Inset:** typical ESR trace of decay of the paramagnetic spin label TEMPOL.

In conclusion, both ESR assays, i.e. spin trapping with DMPO and photocatalytic degradation of TEMPOL, point to a rather high photocatalytic efficiency of ROS generation by anatase-based  $\text{TiO}_2$  nanowires, which is comparable to that of the commercial anatase nano $\text{TiO}_2$ , AMT100 (5.3 nm). The formation of the paramagnetic spin adduct, DMPO-OH, observed in ROS spin-trapping with DMPO, testifies for marked generation of both superoxide ( $\text{O}_2^{\bullet-}$ ) and hydroxyl ( $\text{OH}^{\bullet}$ ) radicals. Additionally, the spectral analysis of the ESR traces acquired during the photocatalytic degradation of TEMPOL, confirm the formation of hydroxyl ( $\text{OH}^{\bullet}$ ) radicals. The involvement of  $\text{OH}^{\bullet}$  radicals in the destruction of TEMPOL and formation of the ESR signal of TEMPON can be schematically explained by the following reaction (Saito et al., 2002).



It has to be stressed, however, that the process shown in this scheme represents only a small fraction of the overall reaction leading to the degradation of TEMPOL. This can be seen from the relative ESR signal intensities of TEMPOL and TEMPON in **Figure 11**. It is customarily accepted that the major degradation mechanisms originated by the superoxide ( $\text{O}_2^{\cdot-}$ ) and hydroxyl ( $\text{OH}^{\cdot}$ ) radicals might occur without paramagnetic ‘finger-prints’.

Based on the above results, we chose anatase-based  $\text{TiO}_2$  nanowires and AMT100 as well as P25 Degussa as representative materials for the further investigations of the interactions of nano $\text{TiO}_2$  with living human cells. The commercial anatase AMT100 was chosen as a material of reference since, in our previous studies, its ROS generation efficiency was found to be similar to that of anatase-based  $\text{TiO}_2$  nanowires (their relative quantum yields, QYs, were of ca. 20%). P25 Degussa was also included in this study as a commonly used and very efficient photo-catalyst.

## VI.2. ESR *ex vivo* detection of ROS generation in cells in the presence of nanoTiO<sub>2</sub>

To determine the redox status in human melanoma cells after incubation with nanoparticulate TiO<sub>2</sub> (AMT100 and P25 Degussa) and anatase-based TiO<sub>2</sub> nanowires in the dark at 37°C, we performed an ESR experiment using the ACP spin-trap. Although the ACP spin trap is considered to be specific to intracellular O<sub>2</sub><sup>•-</sup>, it has also been shown to react with other ROS (Itoh et al., 2000). Therefore, the ACP spin-trap can be considered as an intracellular reporter of ROS. Moreover, the ACP spin-trap remains inactive (ESR silent) outside the cell, since its ROS-active site is acyl-protected. In contrast, in cytosol, the acyl-protected hydroxylamine site can be de-protected with cellular esterases to yield hydroxylamine, which, in turn, serves as a target for ROS. This latter process yields ESR-detectable nitroxide radicals.

It is worth noting that already at the start of incubation of cells with the ACP spin-trap, we observed a very weak ESR signal due to the presence of a small fraction of de-protected and oxidized ACP. This weak ESR signal agrees with the spectrum of a commonly used nitroxide, carbamoyl PROXYL (3-carbamoyl-2,2,5,5-tetramethylpyrrolidine-N-oxyl) (Yokoyama et al., 2000). The signal markedly increases in the presence of the intracellular ROS (Serrander et al., 2007). An example ESR trace of the oxidized ACP spin-trap detected in Lu1205 melanoma cells incubated for 90 min with ACP in the presence of nanoTiO<sub>2</sub>, AMT100, is shown in **Figure 12**. Thus, ACP is thought to be an appropriate spin-trap agent for measuring the intracellular O<sub>2</sub><sup>•-</sup> generation (Itoh et al., 2000).

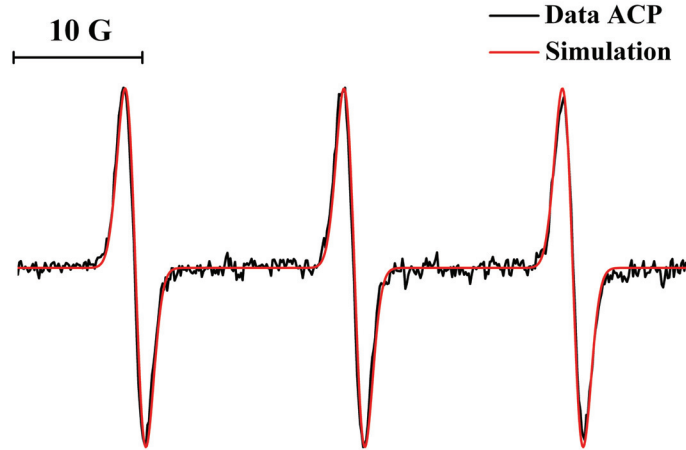


**Figure 12.** An example ESR trace of the intracellular spin-trap ACP for Lu1205 melanoma cells incubated for 90 min with ACP in the presence of nanoTiO<sub>2</sub>, AMT100. The experimentally acquired ESR spectrum is marked in black and its simulation is depicted in red.

The double-integration of the simulated best fits of experimental ESR traces yielded the total ESR signal intensities of the paramagnetic, i.e. oxidized form, of the ACP spin-trap. Subsequently, the actual intracellular concentrations of the ACP-related signals were calculated using the following formula:

$$C_{\text{ACP}(90\text{min})} = C_{\text{TEMPOL}(50\mu\text{M})} \times I_{\text{TEMPOL}(50\mu\text{M})} / I_{\text{ACP}(90\text{min})}$$

where  $C_{\text{ACP}(90\text{min})}$  is the molar concentration of the oxidized form of ACP after 90 min of incubation in cells,  $C_{\text{TEMPOL}(50\mu\text{M})}$  is 50- $\mu\text{M}$  concentration of TEMPOL reference sample,  $I_{\text{TEMPOL}(50\mu\text{M})}$  is the ESR signal intensity of TEMPOL reference sample, and  $I_{\text{ACP}(90\text{min})}$  is the ESR signal intensity for the oxidized form of ACP after 90 min.

The concentrations of the oxidized form of the ACP spin-trap obtained for Lu1205 and WM793 cells exposed to nanoparticular TiO<sub>2</sub> (AMT100 and P25 Degussa) and anatase-based TiO<sub>2</sub> nanowires at concentrations of 2  $\mu\text{g}/\text{mL}$  are presented in **Figure 13**. The columns ‘a’ and ‘b’ in Figure 13 correspond to control measurements. The control ‘a’ was performed for the ACP spin-trap alone incubated for 90 min at 37°C, in the dark. The control ‘b’ was performed for the ACP spin-trap incubated with cells for 90 min at 37°C, in the dark. The remaining columns, ‘c’, ‘d’, and ‘e’ correspond to cells pre-incubated with nanoTiO<sub>2</sub> for 30 minutes in the dark at 37°C, which was followed by incubation with the ACP spin-trap for 90 minutes at 37°C in the dark.

As can be seen in **Figure 13**, the ESR signal intensities of the oxidized ACP spin-trap for the cells exposed to nanoTiO<sub>2</sub> were significantly larger than those obtained in the

control measurements. Depending on the type of nanoTiO<sub>2</sub>, marked differences in intracellular ROS production were observed. For Lu1205 cells, the highest level of detected ROS formation were found for anatase-based TiO<sub>2</sub> nanowires (column ‘e’ in **Fig. 13A**). In contrast, AMT100 induced a ca. 50% lower level of intracellular ROS. The material of reference, P25 Degussa, induced ca. 40% less intracellular ROS as compared to anatase-based TiO<sub>2</sub> nanowires. For WM793 cells, we observed a different dependence as a function of the type of nanoTiO<sub>2</sub>. In this system, all types of nanoTiO<sub>2</sub> produced similar levels of intracellular ROS. The highest level was observed for the material of reference, P25 Degussa. Anatase-based TiO<sub>2</sub> nanowires generated ca. 11% lower ROS, whereas AMT100 resulted in ca. 25% lower ROS.

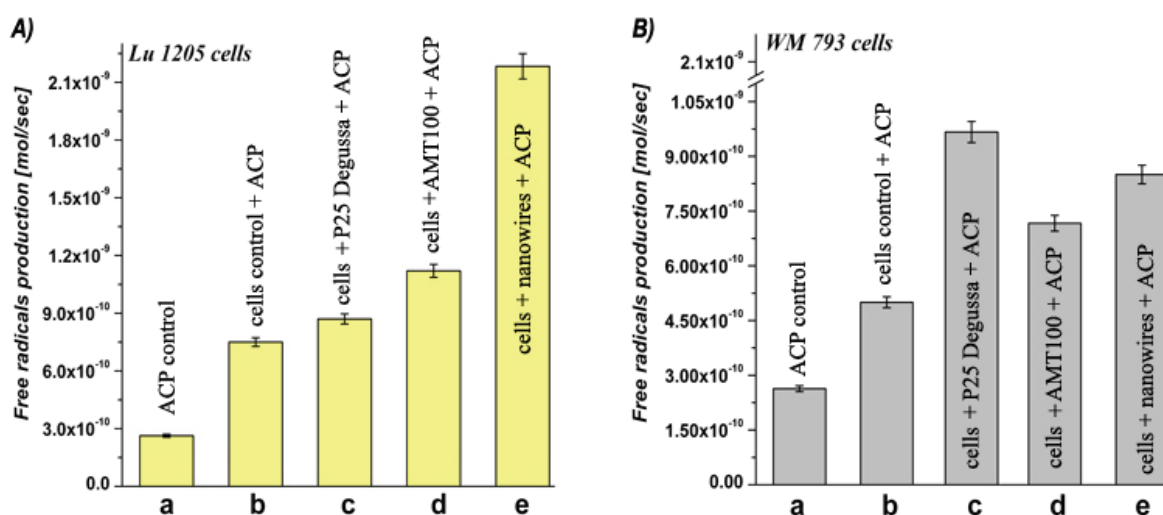


**Figure 13.** Average values of the ESR-derived efficiency of the intracellular production of ROS in the presence of anatase-based TiO<sub>2</sub> nanowires, AMT 100 and P25 Degussa at 2 μg/mL concentrations for Lu1205 cells (A) and WM793 cells (B). Columns: ‘a’ control measurement for ACP spin-trap alone incubated for 90 min at 37°C, in the dark; ‘b’ control measurement for ACP spin-trap incubated with cells for 90 min at 37°C, in the dark; ‘c’, ‘d’, and ‘e’ measurements for cells pre-incubated with nanoTiO<sub>2</sub> for 30 min in the dark at 37°C, which was followed by incubation with the ACP spin-trap for 90 min at 37°C in the dark.

In conclusion, significant amounts of intracellular ROS were generated in cells incubated in the presence of nanoTiO<sub>2</sub> in the dark. Incubation of both Lu1205 and WM793 cells in the dark with nanoTiO<sub>2</sub> resulted in an increase in the concentrations of intracellular ROS depending on the type of nanomaterials used.

### VI.3. Detection of intracellular ROS - NBT staining

One of the oldest and most established methods used for the detection of extra and intracellular ROS, in particular the superoxide radical  $O_2^{\bullet-}$ , is the reduction of nitroblue tetrazolium (NBT), a water-soluble yellow nitro-substituted aromatic tetrazolium. The reduction product is formazan derivative, a dark blue precipitate that can be monitored spectrophotometrically (Baehner et al, 1976; Armstrong et al, 2002). As NBT needs to be reduced, only the superoxide radical  $O_2^{\bullet-}$  is capable of reacting with NBT; it may act both as electron donor and acceptor, whereas  $H_2O_2$  is exclusively an oxidizing agent. Thus, NBT staining indirectly reflects the ROS-generating activity of living cells, and therefore can help to determine the redox status of cells. As such, NBT staining was used in the context of melanoma cells (Lu1205 and WM793) exposed to the presence of nanoTiO<sub>2</sub>. An example optical microscopy image for NBT staining of WM973 cells incubated with AMT100 for 30 min in the dark at 37°C is shown in **Figure 14**. In this figure the black arrows point to the cells with gradually decreasing positive NBT staining.

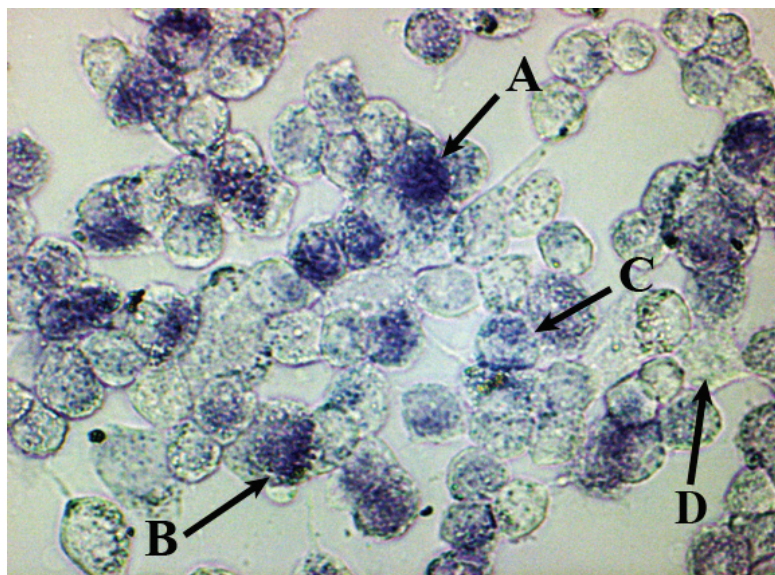


**Figure 14.** An example optical microscopy image for NBT staining of WM973 cells incubated with AMT100 for 30 min in the dark at 37°C. The black arrows point to the cells with gradually decreasing positive NBT staining: **A** - cells filled with formazan (+ + +), **B** - intermediate intensity (+ +), **C** - scattered formazan deposits (+), **D** - no detectable formazan (-).

The optical microscopy images of NBT-stained Lu1205 and WM793 cells exposed to nanoTiO<sub>2</sub> and UV-A induced photo-oxidative stress are shown in **Figures 15** and **16**.

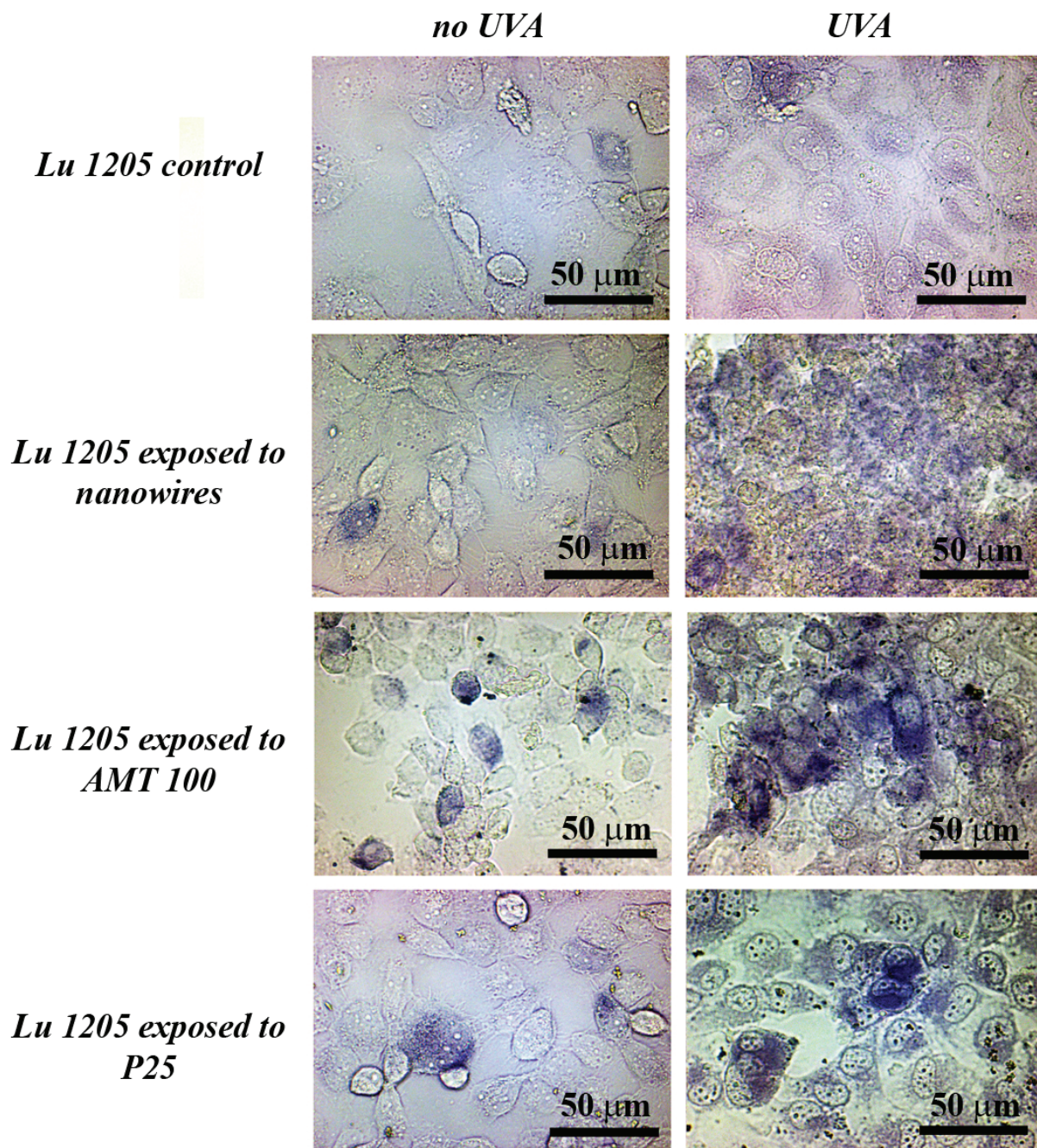


**Figure 15.** ROS detection with NBT staining in metastatic melanoma Lu 1205 cells. Left panel: non-treated (control) cells and cells incubated with: anatase-based TiO<sub>2</sub> nanowires, AMT100 and P25 for 0.5 h at 37° in the dark. Right panel: cells exposed to photo-oxidative stress for 240 sec (UV- A light, 1 mW/cm<sup>2</sup>). Scale bar 50 μm.

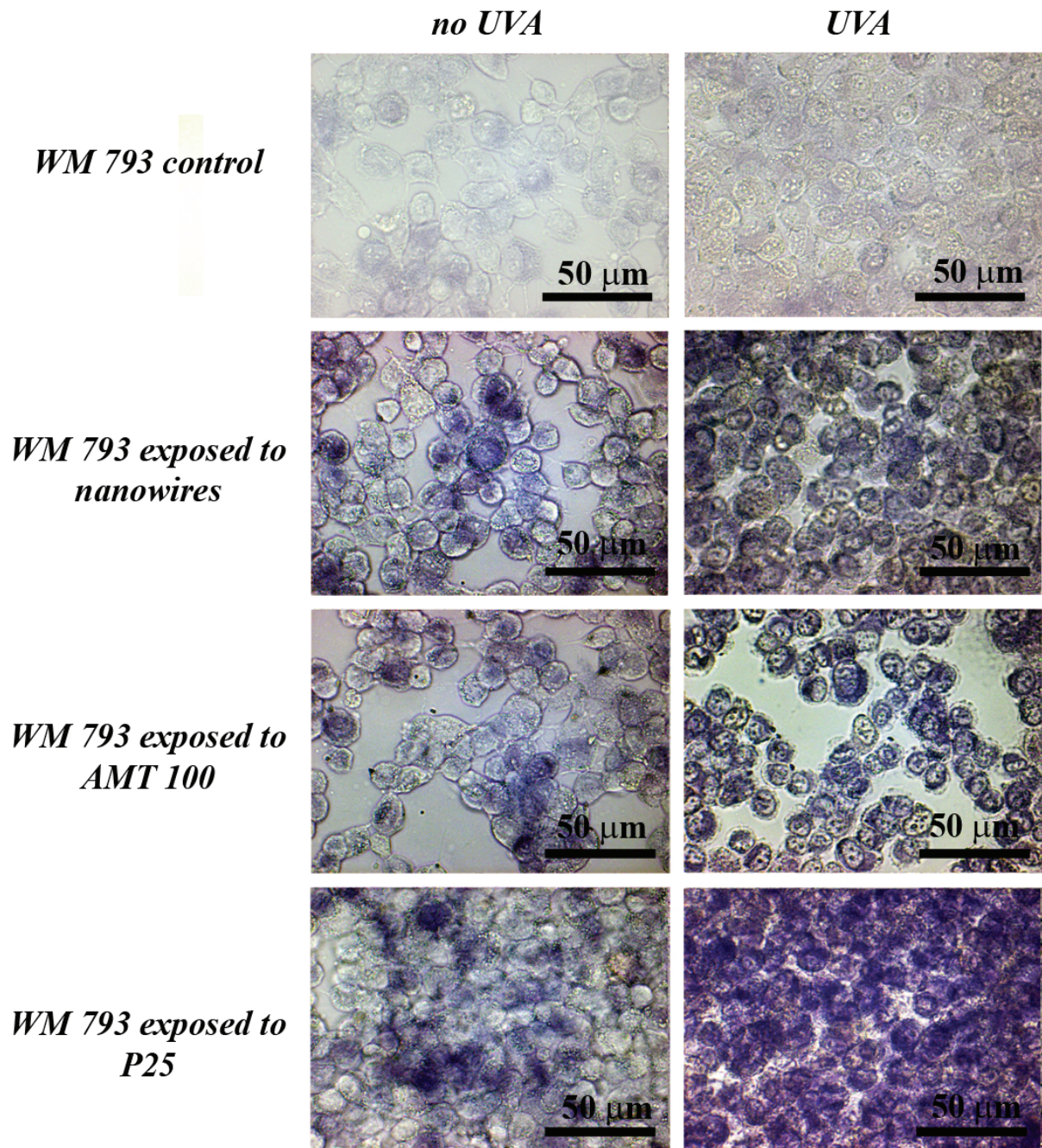


**Figure 16.** ROS detection with NBT staining in metastatic melanoma WM793 cells. Left panel: non-treated (control) cells and cells incubated with: anatase-based  $\text{TiO}_2$  nanowires, AMT100 and P25 for 0.5 h at  $37^\circ$  in the dark. Right panel: cells exposed to photo-oxidative stress for 240 sec (UV- A light,  $1 \text{ mW}/\text{cm}^2$ ). Scale bar 50  $\mu\text{m}$ .



## VI. Experimental results

The results of NBT staining for Lu 1205 and WM 793 cells exposed to the presence of nanoTiO<sub>2</sub> in the dark and under UV-A illumination are summarized in **Tables 3** and **4**. The numerical results shown in these **Tables** indicate the percentage of cells corresponding to the four categories of scoring defined in **Figure 14**.

**Table 3.** NBT staining-derived levels of ROS in Lu 1205 melanoma cells exposed to nanoTiO<sub>2</sub> and UV-A radiation (scored according to **Fig. 14**).

	<i>no UVA</i>				<i>240 sec of UVA (1 mW/cm<sup>2</sup>)</i>			
	-	+	++	+++	-	+	++	+++
<i>Lu 1205 control</i>	92%	8%	-	-	81%	17.2%	1.72%	-
<i>Lu 1205 exposed to NW</i>	85.6%	14.4%	-	-	24.4%	47.5%	28.12%	-
<i>Lu 1205 exposed to AMT 100</i>	81.7%	18.3%	-	-	50.44%	34.76%	12.6%	3.2%
<i>Lu 1205 exposed to P25</i>	82%	18%	-	-	19%	68%	9%	4%

**Table 4.** NBT staining-derived levels of ROS in WM 793 melanoma cells exposed to nanoTiO<sub>2</sub> and UV-A radiation (scored according to **Fig. 14**).

	<i>no UVA</i>				<i>240 sec of UVA (1 mW/cm<sup>2</sup>)</i>			
	-	+	++	+++	-	+	++	+++
<i>WM 793 control</i>	55.5%	44.5%	-	-	23.2%	55.7%	21.1%	-
<i>WM 793 exposed to NW</i>	45.4%	40.4%	14.2%	-	5.2%	19.4%	35.4%	40%
<i>WM 793 exposed to AMT 100</i>	51.7%	44.1%	4.2%	-	2.81%	78.3%	13.3%	5.5%
<i>WM 793 exposed to P25</i>	10.4%	31.6%	34.6%	17.2%	-	-	26.1%	73.9%

Overall, the number of NBT-stained cells increased for cells incubated in the presence of nanoTiO<sub>2</sub>. The populations of NBT-stained cells were even more pronounced after exposure to UV-A for 240 sec (1 mW/cm<sup>2</sup>). For Lu1205 cells incubated in the dark, there were no significant material-related differences. After illumination with UV-A the most numerous NBT-stained Lu1205 cells were observed for anatase-based TiO<sub>2</sub> nanowires. For WM793 cells the most numerous populations of NBT-stained cells was observed for cells incubated in the dark with P25 Degussa. This tendency was conserved for the UV-A exposed cells. Similarly to Lu1205 cells, WM793 cells exposed to UV-A

showed a relatively strong NBT staining for cells pre-incubated with anatase-based TiO<sub>2</sub> nanowires. The localization of the formazan precipitations observed in optical microscopy images of NBT-stained Lu1205 and WM793 cells exposed to nanoTiO<sub>2</sub> suggests that ROS are generated mostly inside cells. This result is also in agreement with ESR spin-trapping study of ROS generation in cells exposed to nanoTiO<sub>2</sub> (see VI.2).

### VI.4. Cell viability

It is known that titania nanoparticles are toxic for living cells if large concentrations are applied (Sayes et al., 2006). Therefore, in this work, there was a need to verify their toxicity, even though substantially lower concentrations of nanoTiO<sub>2</sub> were used. To this end, cell viability tests were carried out to estimate the cytotoxic action of the studied nanoTiO<sub>2</sub> materials. The results are presented in **Figure 17a** and **b**. The graphs in **Figure 17** depict the percentage of living cells, whereas the images show dead cells, stained with Propidium Iodide.

As can be seen in Figure 17, the cell survival rate depends on the type of nanoTiO<sub>2</sub> applied to the living cells. After incubation with nanoTiO<sub>2</sub>, these were exposed for 230 seconds to UV-A light. The fraction of surviving cells in the controls (non-treated cells in culture medium without exposure to UV-A light and to nanoTiO<sub>2</sub>) was 90% for both cells lines. This corresponds to the natural (normal) level of dead cells in a population.

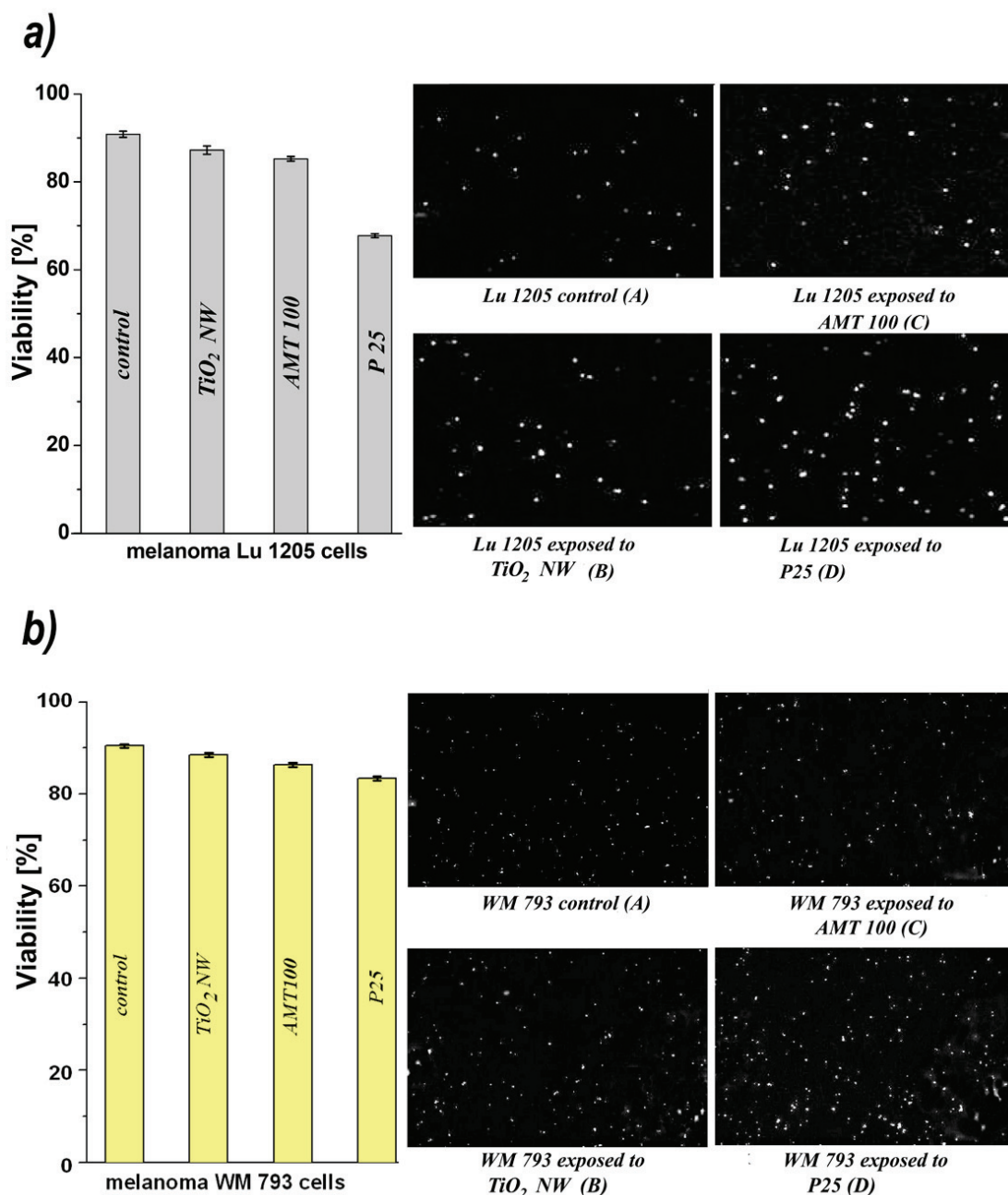


**Figure 17.** Toxic effects of nanoTiO<sub>2</sub> on Lu 1205 (a) and WM793 (b) melanoma cells exposed for 230 sec to UV-A light ( $\lambda = 365\text{nm}$ ) carried out using the Propidium Iodide Luminescent Cell Viability Assay. Test was performed for untreated cells (A), and those incubated with anatase-based TiO<sub>2</sub> nanowires (B), ATM100 (C), and P25 Degussa (D).

Once anatase-based TiO<sub>2</sub> nanowires were added and UV-A exposure was performed, a certain fraction of cells was killed. Out of all types of nanoTiO<sub>2</sub> studied in this work, the most toxic was P25 Degussa for which 23% and 7% of Lu1205 and WM793 cells, respectively, were killed (**Figure 17a** and **b**, image D). In the presence of AMT100, 5.5% and 4% of Lu1205 and WM793 cells, respectively, were found dead

(Figure 17a and b, image C). Finally, the anatase-based TiO<sub>2</sub> nanowires promoted cellular death at the levels of 4% and 2.5% for Lu1205 and WM793 cells, respectively (Figure 17a and b, image B). These results indicate direct proportionality between the efficiency of the ROS generation by nanoTiO<sub>2</sub>, measured by ESR *in vitro*, and the observed cytotoxic effect.

As was shown in Chapter VI.1.2 Figure 8, the ESR-measured ROS generation *in vitro* revealed increasing photocatalytic activity as follows: P25 Degussa > AMT100 > NWs. Similarly, the cell viability tests based on Propidium Iodide staining pointed to the highest phototoxicity for P25 Degussa and correspondingly lower phototoxicities of AMT100 and NWs.

## VI.5. Morphology of melanoma cells exposed to photo-oxidative stress

The morphology of cells can be important in many contexts. In a cell culture, the morphology indicates the status of the cells in terms of their health. In this study, optical microscopy confirmed the appearance of changes in cell morphology for cells exposed to nanoTiO<sub>2</sub> and UV-A light. These changes in cell morphology were independent of the studied cell type. For long exposure times, at least 460 seconds, we observed significant changes in cell morphology, regardless of the type of applied nanoTiO<sub>2</sub>. These results are shown in Figures 18 and 19, for Lu1205 and WM793, respectively. Non-treated melanoma cells were spread on a glass coverslip, while they were illuminated by UV-A in the presence of nanoTiO<sub>2</sub>.

The changes in cellular morphology, depicted in Figures 18 and 19, point to damages in the cell outer- and inner-membranes. Cells tend to shrink in volume, which is accompanied by the occurrence of blebs at the cell edges. The blebs form large three-dimensional structures. The appearance of cell blebbing can be associated with early degradation of the intracellular matrix and changes in the cellular biomechanical properties. These damages can be associated with nanoTiO<sub>2</sub>-induced photo-oxidative stress.

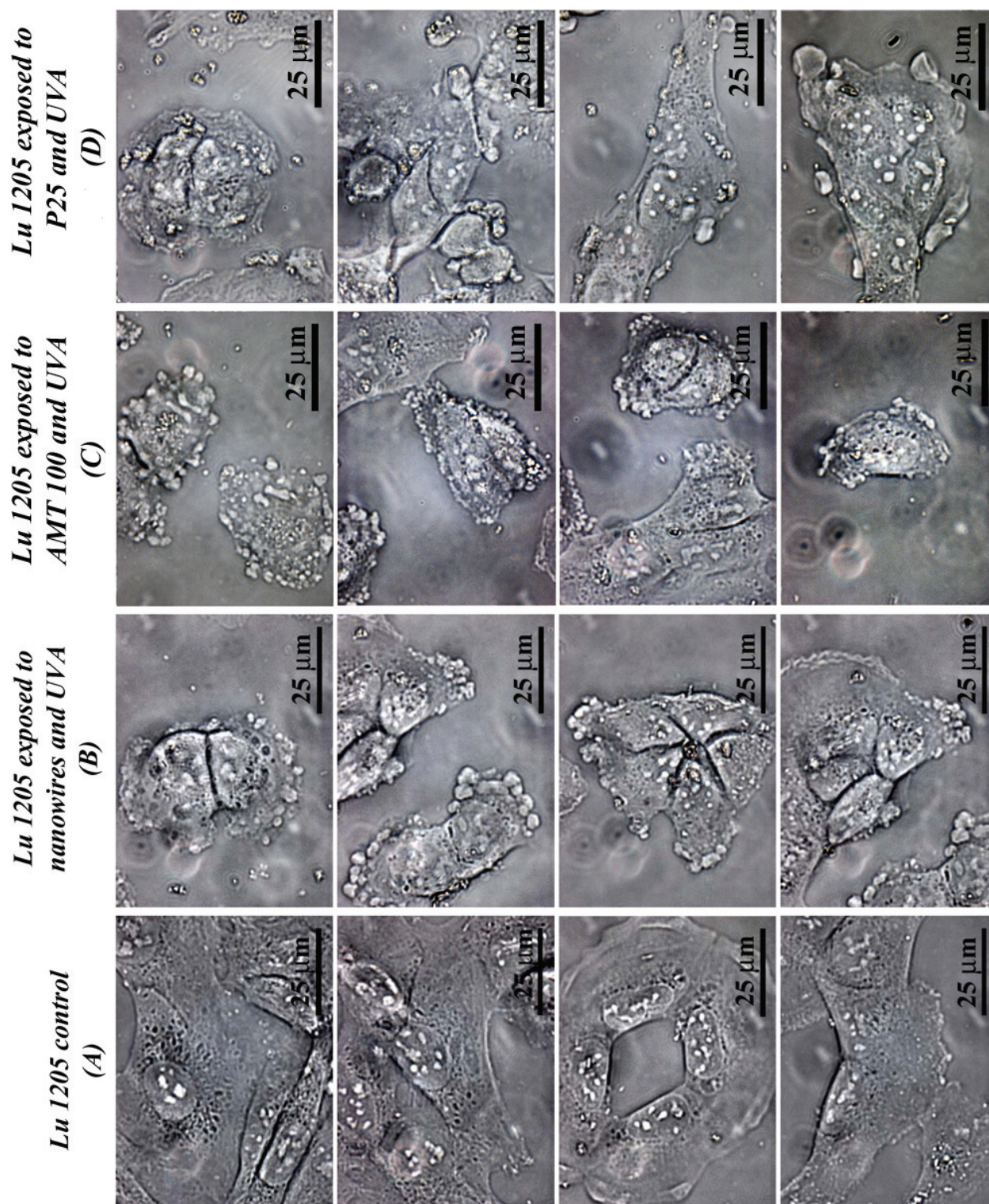


**Figure 18.** Optical images of the metastatic melanoma Lu1205 cells exposed to nanoTiO<sub>2</sub>-induced photo-oxidative stress. Control - non-treated cells (A). Cells incubated for 0.5 h with nanoTiO<sub>2</sub> and illuminated with UV-A for 460 sec (1 mW/cm<sup>2</sup>): anatase-based TiO<sub>2</sub> nanowires (B), AMT100 (C), and P25 Degussa (D).

The depicted changes in cell morphology, including appearance of blebs and modifications of cell edges are typical for cells before and after exposure to the photo-oxidative stress. Scale bar 25μm.

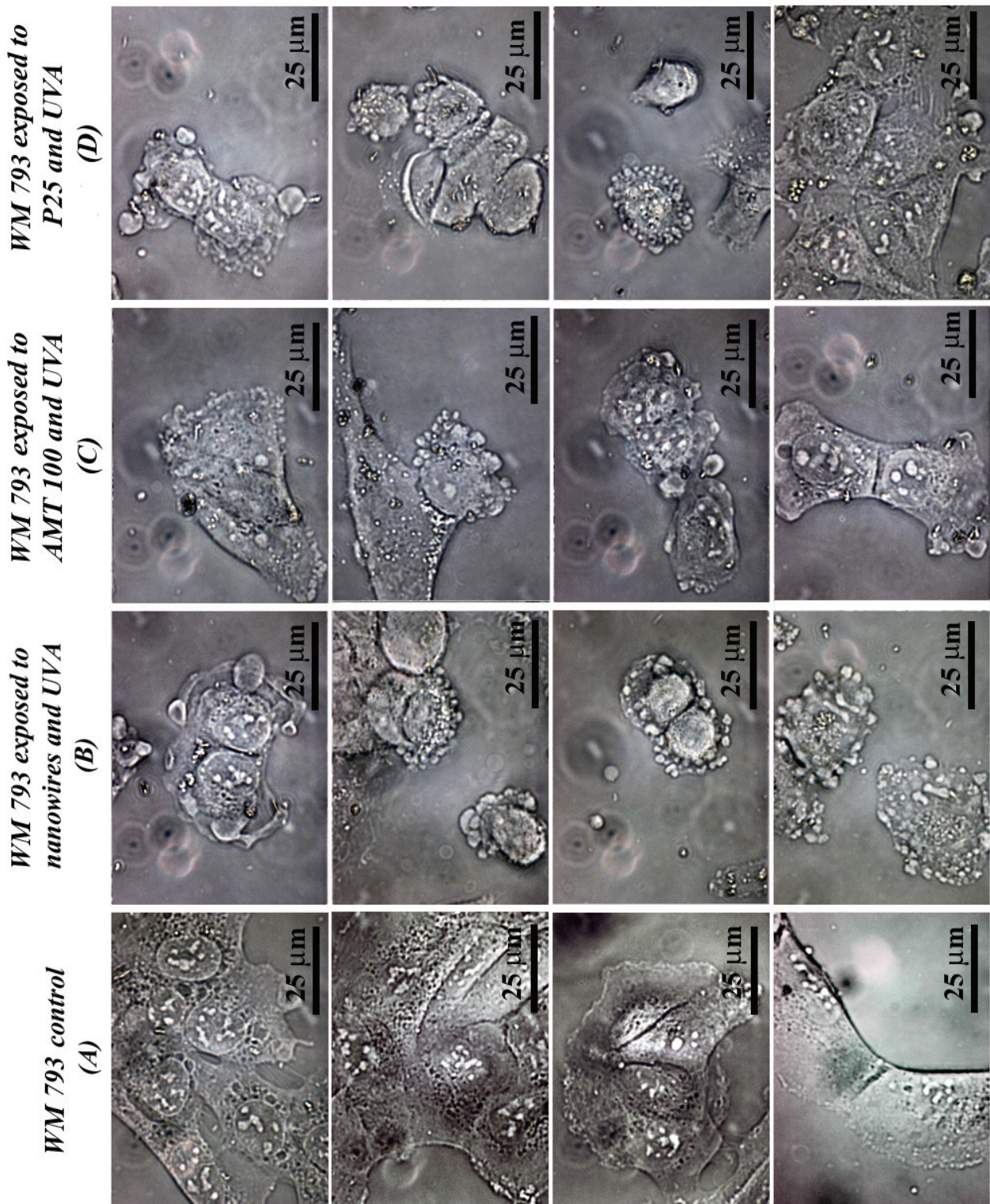


**Figure 19.** Optical images of the metastatic melanoma WM793 cells exposed to nanoTiO<sub>2</sub>-induced photo-oxidative stress. Control - non-treated cells (A). Cells incubated for 0.5 h with nanoTiO<sub>2</sub> and illuminated with UV-A for 460 sec (1 mW/cm<sup>2</sup>): anatase-based TiO<sub>2</sub> nanowires (B), AMT100 (C), and P25 Degussa (D).

The depicted changes in cell morphology, including appearance of blebs and modifications of cell edges are typical for cells before and after exposure to the photo-oxidative stress. Scale bar 25μm.

The changes in cell morphology and underlying associated changes in the cytoskeletal organization considerably alter the cellular mechano-transduction pathways, which are essential for the health and homeostasis. These findings corroborate the results of the cell viability study (see VI.4).

### **VI.5.1. Cell cytoskeleton studies using fluorescence microscopy**

To get insight into the cytoskeleton organization changes in cells exposed to the presence of nanoTiO<sub>2</sub> in the dark and under illumination with UV-A, we performed optical microscopy studies targeting selected cytoskeleton components. We associated the morphological changes observed with standard optical microscopy with perturbation of the actin-based network (actin cortex) in the stress-exposed cells. The protein actin occurs in the cytosol in two forms: G- and F-actin. G-actin is the non-polymerized form, whereas F-actin is polymerized and a constituent of actin fibers.

To characterize the distribution of F-actin *in vivo*, a fluorescent probe (FITC - conjugated phalloidin, Sigma), specifically binding to F-actin, was used. Although there were subtle differences in the observed cytoskeletal structure in the different cell types (Lu1205 and WM793), the phalloidin-FITC staining revealed well-organized networks of linear fibers throughout the cytoplasm, forming a mostly parallel arrangement for control cells. The fluorescence microscopy images of control cells are shown in left panels of **Fig. 20-22**. The phalloidin-FITC stained long filaments seen in **Fig. 20-22** are actin stress fibers, consisting of bunches of single actin filaments (the diameter of a single actin filament is ca. 5-9 nm (Milligan et al., 1990)). The short filaments extend into lamellipodia, which are prominent during cell migration (Cooper et al., 1991). The actin stress fibers are anchored in cellular membranes to focal adhesions that provide necessary attachment to the substratum (Luna et al., 1992). After 30 minutes of incubation with anatase-based TiO<sub>2</sub> nanowires in the dark, the organization of actin filaments remained similar to that of untreated cells, independent of the studied cell type (Lu1205 or WM793) [see **Fig. 20**, middle panel: “Nanowires no UVA”].

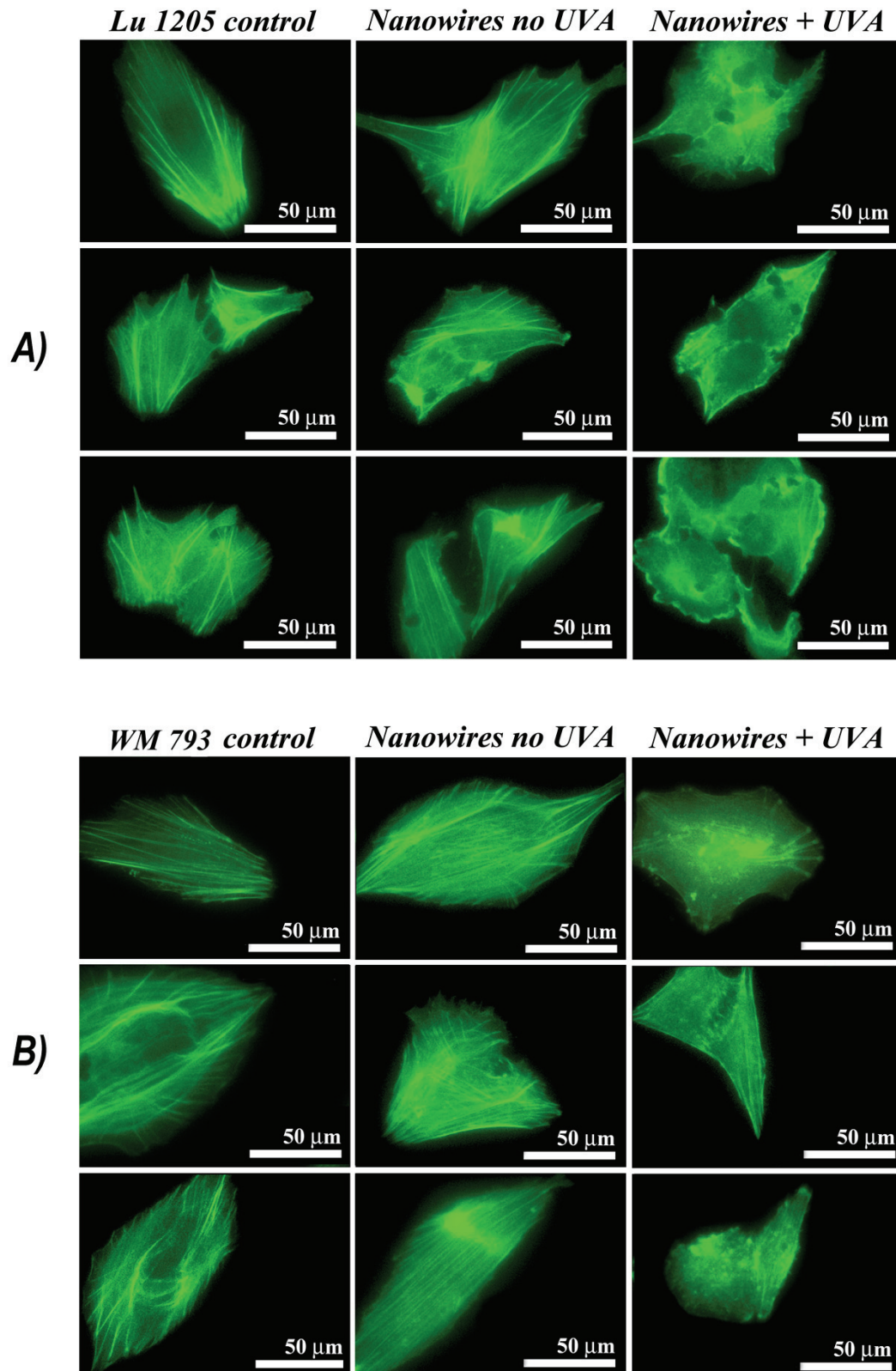


**Figure 20.** Optical microscopy fluorescent images of actin filaments stained using FITC-phalloidin revealing changes in cytoskeleton morphology for Lu1205 (A) and WM793 (B). Left panel – control (non-treated cells), middle panel - cells after 0.5 h incubation with anatase-based TiO<sub>2</sub> nanowires in the dark, and right panel - cells exposed to the photo-oxidative stress for 230 sec (UV– A light exposure, 1 mW/cm<sup>2</sup>) in the presence of anatase-based TiO<sub>2</sub> nanowires.



To compare the effect of ROS generation in the presence of anatase-based TiO<sub>2</sub> nanowires with other nanoTiO<sub>2</sub>, similar experiments were performed for two types of nanoparticles: anatase AMT100 [Fig. 21] and Degussa P25 (80% anatase / 20% rutile) [Fig.22]. Regardless of the type of nanoTiO<sub>2</sub>, once UV-A was applied to the Lu1205 or WM793 cells to generate the photo-oxidative stress (exposure for 230 seconds), changes in the cell shape were observed. These changes were accompanied by a distinct reorganization of stress fibers. As can be seen in **Figures 20 – 22**, the parallel order of the stress fibers was lost [right panel of **Fig. 20**, “Nanowires + UVA”, and right panels of **Fig. 21** and **22**, for anatase AMT100 and P25 Degussa, respectively]. Treatment of Lu 1205 or WM 793 cells with nanoTiO<sub>2</sub> and UV-A induced disruption of the linear arrangement of F-actin fibers, loss of fibers, and a perinuclear or speckled accumulation of stained actin. Cells appeared to lose their characteristic shapes and assumed more rounded morphologies as the F-actin network was disrupted. Stress fibers were lost and the majority of stained F-actin was localized to the plasma membrane, which became wavy and almost ruffled as compared to the control cells.

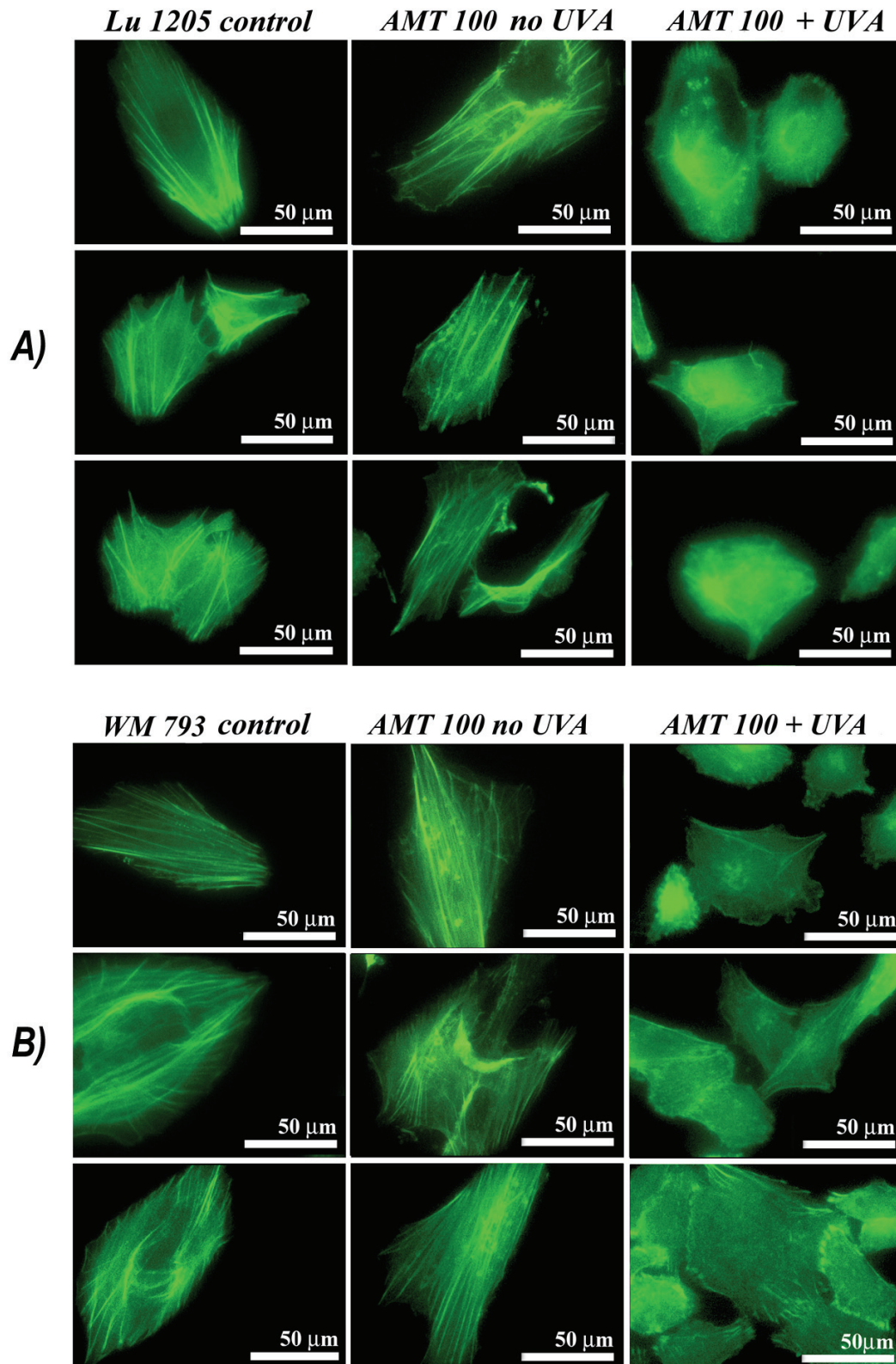


**Figure 21.** Optical microscopy fluorescent images of actin filaments stained using FITC-phalloidin revealing changes in cytoskeleton morphology for Lu1205 (A) and WM793 (B). Left panel – control (non-treated cells), middle panel - cells after 0.5 h incubation with anatase AMT100 in the dark, and right panel - cells exposed to the photo-oxidative stress for 230 sec (UV- A light exposure,  $1 \text{ mW/cm}^2$ ) in the presence of anatase AMT100.

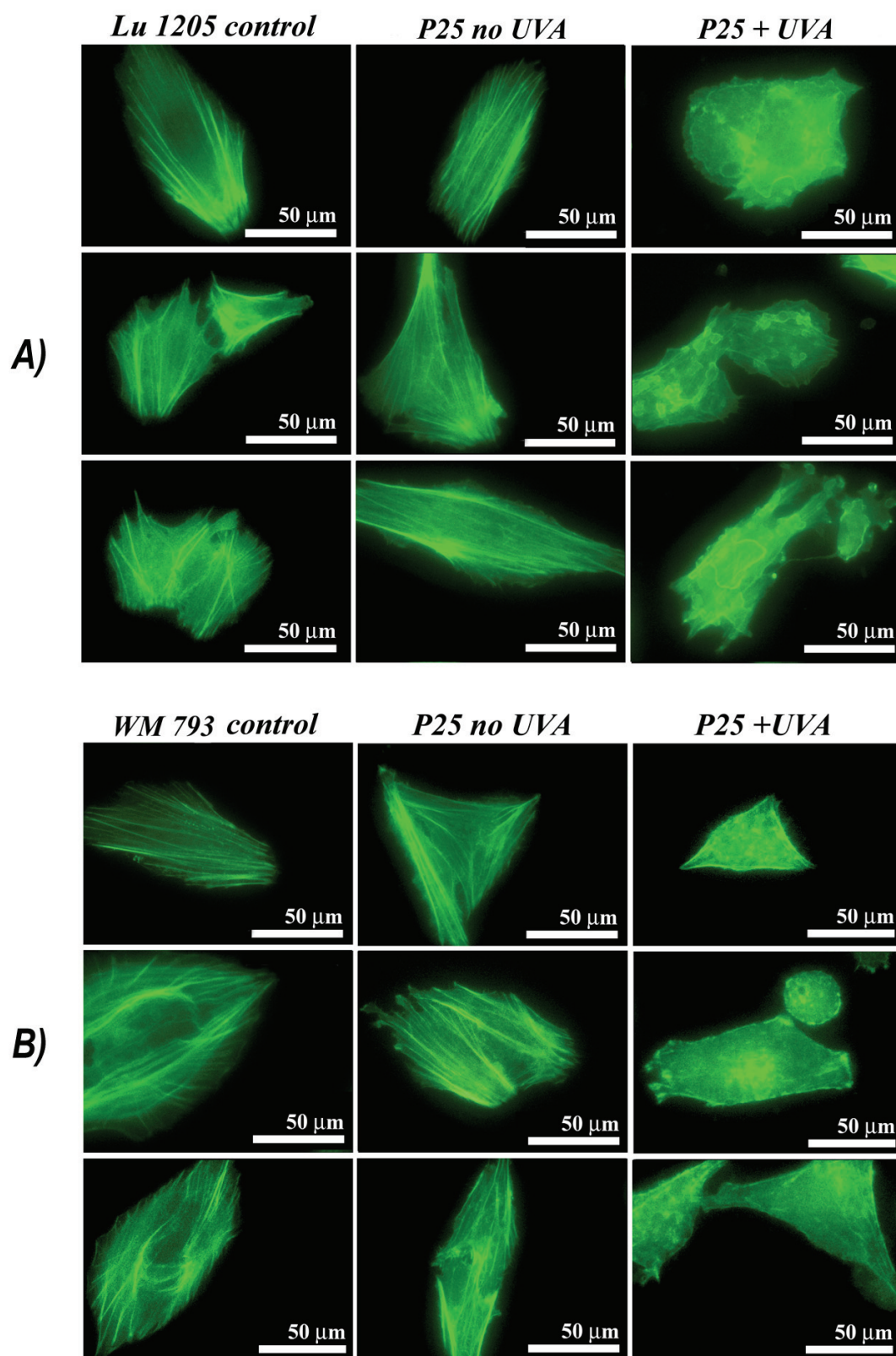


**Figure 22.** Optical microscopy fluorescent images of actin filaments stained using FITC-phalloidin revealing changes in cytoskeleton morphology for Lu1205 (A) and WM793 (B). Left panel – control (non-treated cells), middle panel - cells after 0.5 h incubation with P25 Degussa in the dark, and right panel - cells exposed to the photo-oxidative stress for 230 sec (UV- A light exposure,  $1 \text{ mW/cm}^2$ ) in the presence of P25 Degussa.

Incubation of both Lu1205 and WM793 cells with low concentrations of nanoTiO<sub>2</sub> (2 µg/mL), followed by exposure to UV-A radiation, resulted in a marked change in the actin network. This network consists of actin filaments (F-actin) that can be bundled or cross-linked by several actin binding proteins (ABP). The actin filaments form dynamic structures which can be elongated or shortened by polymerization or dissociation of monomers at the filament ends (Alberts et al., 1994). Thus, the integrity of the actin network can be influenced by either activating or deactivating the ABPs or by changing the accessibility of the filament ends to actin monomers. The released ROS might cause depolymerization of actin filaments, thus leading to the collapse of actin cytoskeleton and changes of the cellular shape.

In conclusion, depolymerization of the actin cytoskeleton appeared in the presence of all kinds of nanoTiO<sub>2</sub> and exposure to UV-A radiation. However, the strongest and the fastest changes were observed in the presence of P25 Degussa. This finding is in good agreement with ESR-measured ROS generation rates (P25 Degussa was found to be the most efficient photocatalyst – see chapter VI.1.2)

### **VI.5.2 High resolution AFM imaging of cells**

In culture conditions and without any applied external stress, melanoma Lu1205 and WM793 cells form a semi-confluent layer, composed of spread, flat cells. The actin network is organized into contractile bundles that form parallel or perpendicular to the cell edge. Contractile F-actin bundles cause contraction of lamellar networks, which constantly assemble and disassemble (Verkhovsky and Borisy, 1993; Verkhovsky et al., 1995; Naumanen et al., 2008). The filamentous network at the cell cortex is organized as a complex polygonal mesh.

An example high-resolution deflection AFM image of a WM793 cell is shown in **Figure 23**. We used AFM deflection imaging, since details of the membrane surface are more easily visualized, as suggested by Putman et al. (Putman et al., 1992). In **Figure 23**, the actin network mesh appears to be structured on two length scales, one on the order of a few hundred nanometers and the other on the order of a few micrometers. The larger mesh is composed of prominent and hence relatively stiff features, with a wide range of forms. The fine mesh is composed of thin filaments yielding a weak contrast,

and can typically be seen inside the large mesh elements. The fine mesh elements are more uniform in appearance, and have areas  $\sim 0.07 - 0.9 \mu\text{m}^2$ . The cell cortex can be described as a coarse mesh intertwined with a fine one. The diameter of the observed fibers was in the range of 50 – 660 nm as determined from the AFM image, taking into account the convolution effect of sample topography and tip shape (Engel et al., 1997).

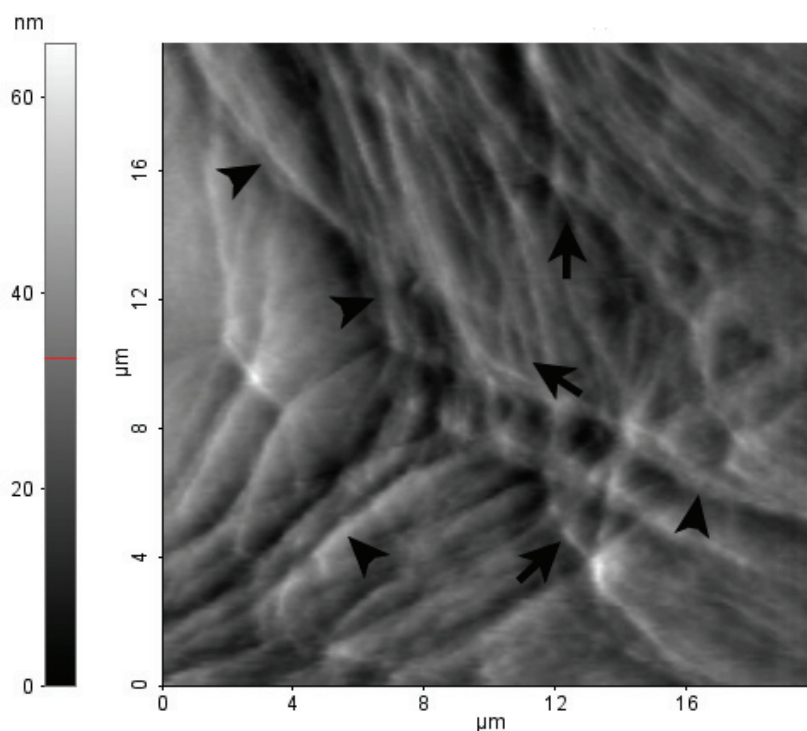


**Figure 23.** High-resolution AFM deflection image of a living WM793 cell acquired in HBSS medium. The filamentous mesh is organized on two length scales: with coarse (*arrowheads*) and fine mesh filaments (*arrows*). The coarse mesh forms larger elements and is easier to identify, whereas the fine mesh elements have much smaller dimensions. These two meshes are likely intertwined; although, it is possible that the fine mesh is layered over the coarse mesh.

Since high-resolution AFM imaging of cells yields information concerning the cytoskeleton organization, we performed this type of imaging to study the potential changes in the actin filament network. The results of surface topography, recorded for Lu1205 and WM793 melanoma cells, are shown in **Figure 24** and **Figure 25**, respectively.

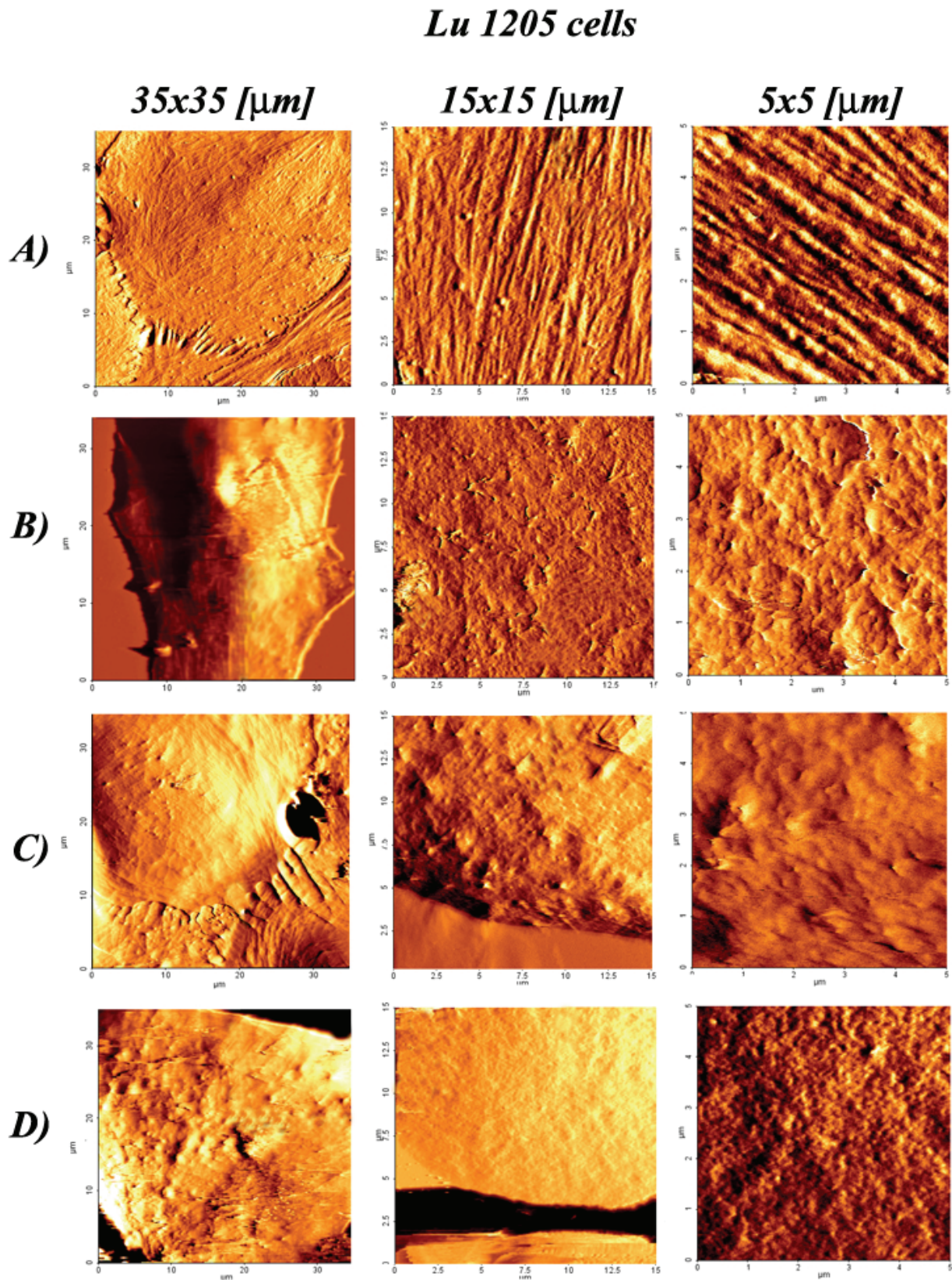


**Figure 24.** High-resolution AFM deflection images of the metastatic melanoma Lu1205 cells. (A) Non-treated (control) cells; (B) Cells after 0.5 h incubation with anatase-based TiO<sub>2</sub> nanowires, (C) Cells after 0.5 h incubation with AMT100 and (D) Cells after 0.5 h incubation with P25 Degussa, which was then followed by 230 sec exposure to UV-A light (1 mW/cm<sup>2</sup>).

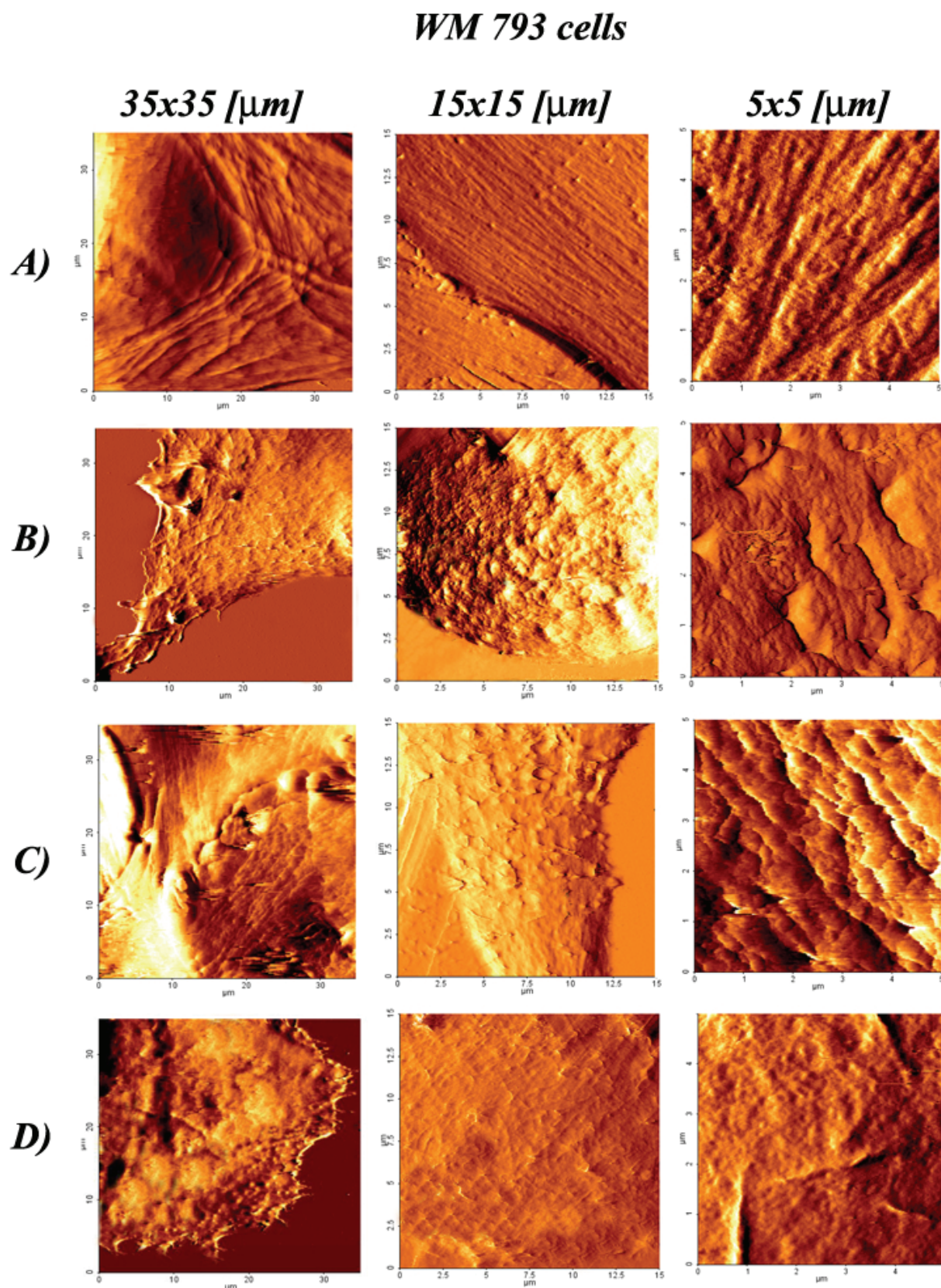


**Figure 25.** High-resolution AFM deflection images of the metastatic melanoma WM793 cells. (A) Non-treated (control) cells; (B) Cells after 0.5 h incubation with anatase-based  $\text{TiO}_2$  nanowires, (C) Cells after 0.5 h incubation with AMT100 and (D) Cells after 0.5 h incubation with P25 Degussa, which was then followed by 230 sec exposure to UV-A light ( $1 \text{ mW}/\text{cm}^2$ ).

The presence of the bundles of stress fibers can clearly be seen in the topological images shown in **Figure 24A** and **25A**. Reducing the scan size from 35x35  $\mu\text{m}$  to 15x15  $\mu\text{m}$  and next to 5x5  $\mu\text{m}$  allowed for acquisition of high resolution surface images. At these magnifications, the images revealed the presence of filamentous structures for the untreated control cells [**Figure 24A** and **25A**]. After treatment with nanoTiO<sub>2</sub> and UV-A light, the prominent actin fibers networks were no longer extended to the cell surface for both Lu1205 and WM793 cells. The AFM-visualized projections of stress fibers are similar to those observed in optical microscopy fluorescent images of cells with FITC-phalloidin stained actin filaments. The cells have retracted and become rounder, the actin fibers are reduced and blebs have started to form on the surface [**Figure 24B-D** and **25B-D**].

Analysis of AFM-visualized cell topography revealed that the cell body increased in height. The AFM images were analyzed using the XEI software provided by the AFM manufacturer, Park Systems Inc.. A line cross-section through the cell apex was then used to calculate the cell height [**Fig. 26, 27**]. When the height difference with respect to the reference point 1, located at  $L_1$ , to the left of the apex is  $H_1$  and the height difference with respect to the reference point 2, located at  $L_2$ , to the right of the apex is  $H_2$ , the weighted average of the cell height becomes  $(L_1 \times H_1 + L_2 \times H_2) / (L_1 + L_2)$ . This method was found to be more precise than using a single reference point, as thermal drift and the sample slope are compensated for (Lee, PhD Thesis, EPFL, 2008).

As can be seen in **Figures 26** and **27**, the average height of non-treated Lu1205 and WM793 cells (control) varied between 2 – 2.5  $\mu\text{m}$ , whereas after exposure to the photo-oxidative stress it increased to 3 – 6  $\mu\text{m}$ . Thus, one can conclude that the photo-oxidative stress induces large changes in the organization of actin filaments.



*Lu 1205 control*

*Lu 1205 exposed to  
NW and UVA*

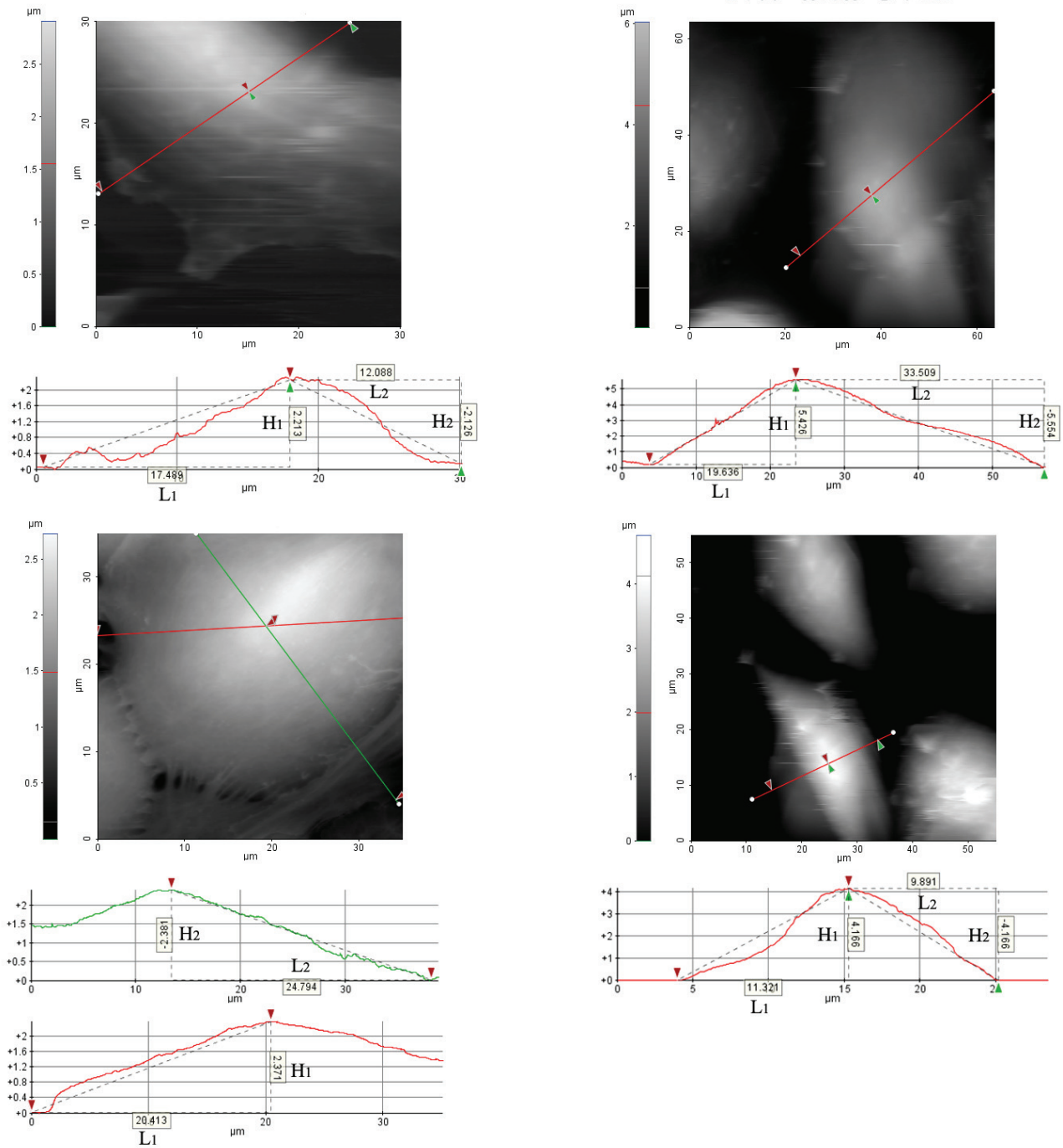


**Figure 26.** Topography and the cross-sections of Lu1205 cells exposed to anatase-based TiO<sub>2</sub> nanowires and UVA irradiation. Control (non-treated) cells are shown in the left panel. Using two reference points, the height of a cell body was determined.

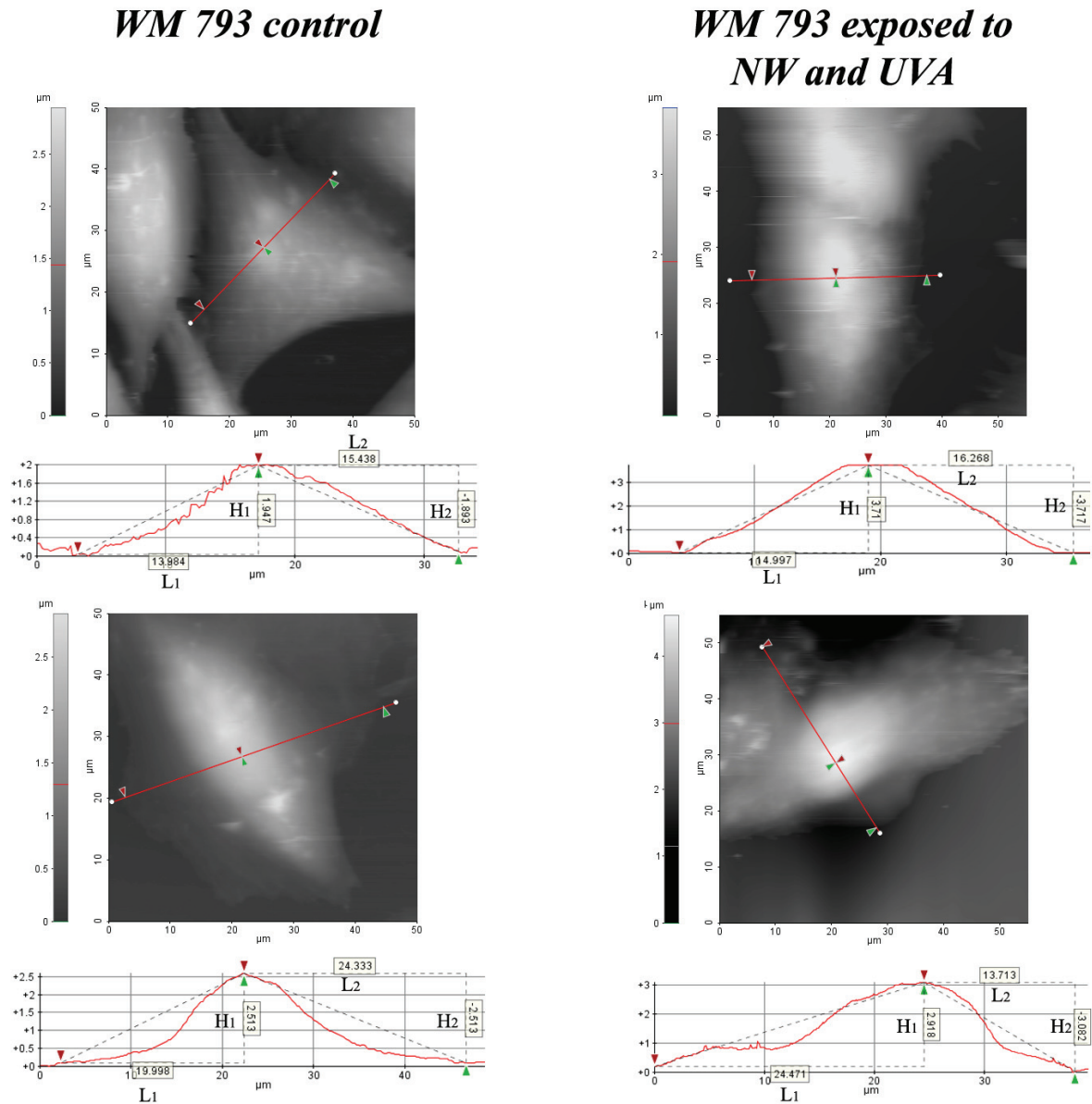


**Figure 27.** Topography and the cross sections of WM 793 cells exposed to nanowires and UVA irradiation. On the left, control i.e. non-treated cells are shown. Using two reference points, the height of a cell body was determined.

In conclusion, the oxidative stress induces different effects both on organization of actin cytoskeleton and on cellular shape, as well as on membrane surface morphology. Combining different optical imaging techniques with AFM for studying cell morphology and cell responses widens the range of information that can be gathered about the cell structure and function.

## VI.6. AFM - determination of the Young's modulus

In 2006 Vileno *et. al.* reported that cell damage induced by photo-oxidative stress could be quantitatively estimated *via* determination of the Young's modulus. The relative changes of the cell elastic properties as a function of UV-A exposure time for all studied nanoTiO<sub>2</sub> are shown in **Figures 28A** and **29A**. Non-dividing, inter-phase cells were chosen for analysis. For control (non-treated) cells [column 'a' in **Figures 28A** and **29A**], the Young's modulus value was of  $1.02 \pm 0.20$  kPa and  $1.12 \pm 0.38$  kPa, for Lu1205 and WM793, respectively. To quantify the relative change in cell stiffness all data were normalized to this value.

Melanoma cells, incubated for 30 minutes with nanoTiO<sub>2</sub> (P25 Degussa, AMT100 nanoparticles and anatase-based TiO<sub>2</sub> nanowires) in the dark, appeared more rigid as compared to control cells. The effect was more pronounced for anatase-based TiO<sub>2</sub> nanowires and AMT100 than for P25 Degussa nanoparticles. For Lu1205 cells, the Young's modulus values increased by ~75%, 115%, 50%, for anatase-based TiO<sub>2</sub> nanowires, AMT100 and P25 Degussa nanoparticles, respectively [**Fig. 28**]. Similarly, for WM793 cells, the growth of the Young's modulus was of ~26%, 34% and 8%, for anatase-based TiO<sub>2</sub> nanowires, AMT100 and P25 Degussa nanoparticles, respectively [**Fig. 29**]. This increase in cellular stiffness can be explained by a considerable rate of nanoTiO<sub>2</sub> uptake and the possible presence of nanoparticles in the cell interior after 30 minutes of incubation. The growth of the Young's modulus values can also be associated with modification of the rate and extent of microtubule assembly/disassembly processes in the presence of nanoTiO<sub>2</sub> (Gheshlaghi *et al.*, 2008). When UV-A irradiation was applied to induce the generation of ROS, the Young's modulus for cells treated with anatase-based TiO<sub>2</sub> nanowires dropped significantly only after 460 seconds of irradiation.

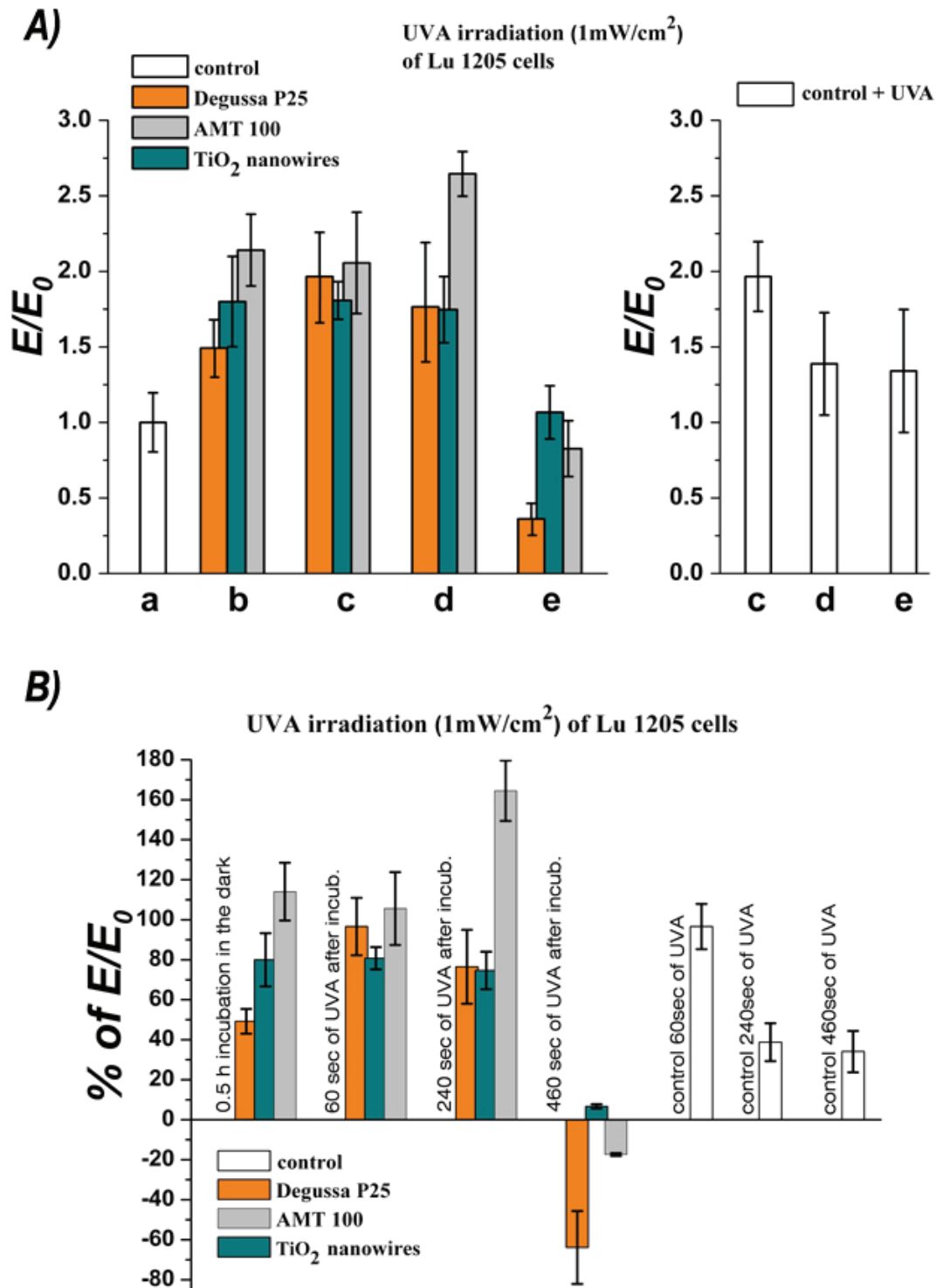


**Figure 28.** Relative (A) and percentage (B) changes of the Young's modulus values for Lu1205 cells determined from AFM measurements.

A) Control (non-treated) cells (a); Cells after 0.5 h of incubation with anatase-based  $\text{TiO}_2$  nanowires, AMT100 and P25 Degussa, in the dark (b). Cells after 0.5 h incubation in the dark with anatase-based  $\text{TiO}_2$  nanowires, AMT100 and P25 Degussa, and then exposed to UV-A light ( $1\text{ mW}/\text{cm}^2$ ) for: 60 sec (c), 240 sec (d), and 460 sec (e).

B) Percentage changes were calculated as reference to the Young's modulus values of control (non-treated) cells.

All results were normalized to the value obtained for control cells ( $1.02 \pm 0.2\text{ kPa}$ ).

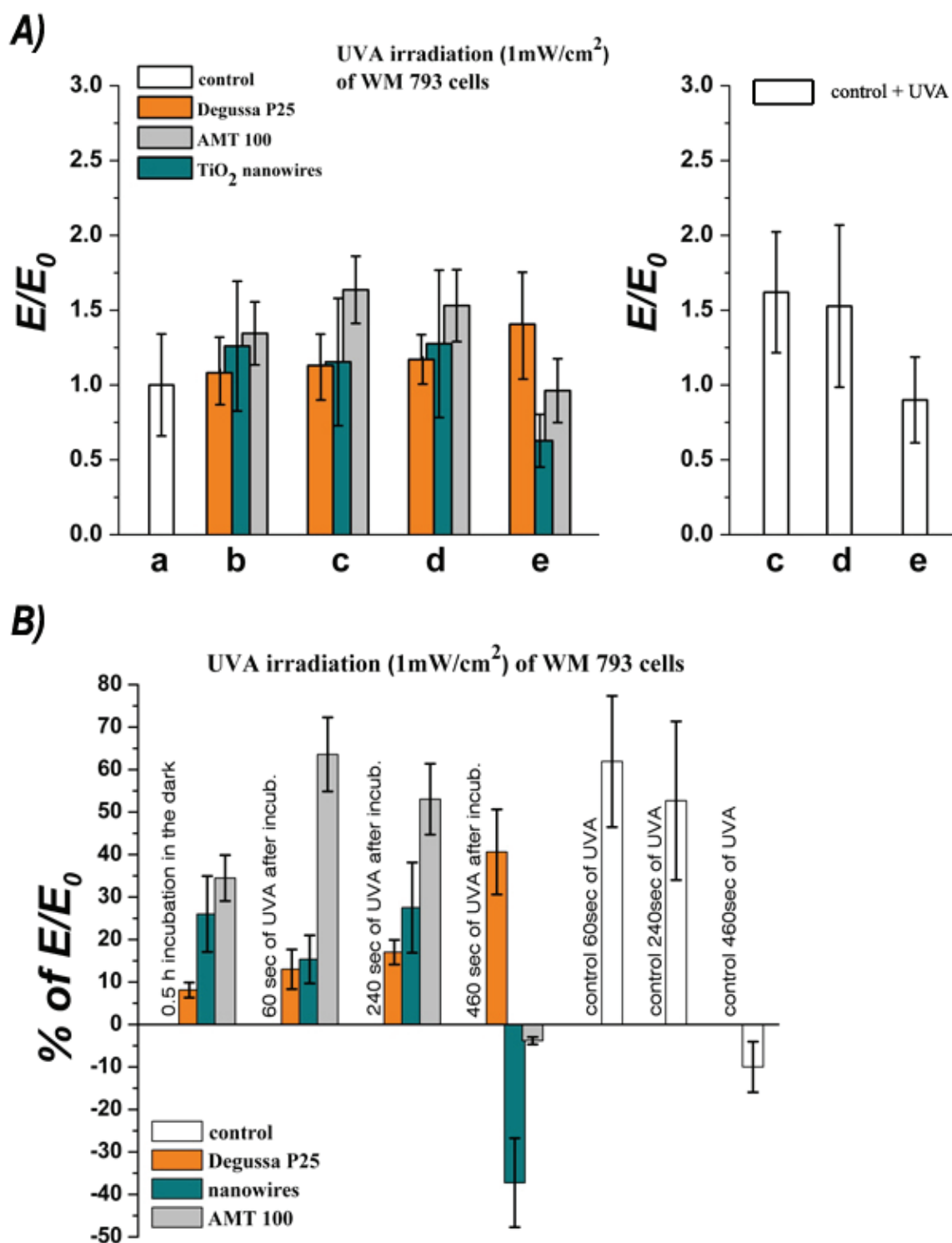


**Figure 29.** Relative (A) and percentage (B) changes of the Young's modulus values for WM793 cells determined from AFM measurements.

A) Control (non-treated) cells (a); Cells after 0.5 h of incubation with anatase-based TiO<sub>2</sub> nanowires, AMT100 and P25 Degussa, in the dark (b). Cells after 0.5 h incubation in the dark with anatase-based TiO<sub>2</sub> nanowires, AMT100 and P25 Degussa, and then exposed to UV-A light ( $1\text{ mW}/\text{cm}^2$ ) for: 60 sec (c), 240 sec (d), and 460 sec (e).

B) Percentage changes were calculated as reference to the Young's modulus values of control (non-treated) cells.

All results were normalized to the value obtained for control cells ( $1.12 \pm 0.38\text{ kPa}$ ).

Shorter exposures to UV-A (60 sec) resulted in no sufficient ROS production that could induce cell softening. This is why the cellular stiffness remained similar to that of the cells incubated with nanoTiO<sub>2</sub> in the dark. The cell stiffness continued to grow up to 240 sec of UV-A illumination. The cell stiffness increased almost twofold as compared to the control, which can be associated with first signs of early apoptosis (Pelling et al., 2009). As could be seen in **Figures 18 and 19**, Chapter **VI.5**, cells treated with nanoTiO<sub>2</sub> and exposed to photo-oxidative stress, displayed membrane blebbing, a common feature of apoptosis. The membrane blebbing has already been associated with the increase of cellular stiffness (Lu et al., 2008). An increase by 60% in cell stiffness was observed for cell intentionally treated with blebbistatin (apoptosis simulation).

For longer exposures to UV-A (460 sec), the Young's modulus dropped significantly. The observed decrease was in the range of 70-130% for Lu1205 and 45-80% for WM793 cells, as compared to cells incubated with nanoTiO<sub>2</sub> without UV illumination. Only in one case, that of WM793 cells exposed to P25 Degussa and 460 sec of UV-A, did the Young's modulus remain high. This can be explained by the loss of the cell's continuum and a more pronounced contribution of the glass substrate to AFM-measured stiffness. At this time, the effect of UV-A alone was also observed [**Fig. 28 and 29**], but the UV-A influence on melanoma cells was smaller and differentiated: the stiffness of Lu1205 control cells increased by ~20%, whereas the stiffness of WM793 cells decreased by ~13%.

Summarizing, for cells incubated with nanoTiO<sub>2</sub> and exposed to photo-oxidative stress for longer times (460 sec of UV-A), the Young's modulus markedly decayed, pointing to a breakdown of intracellular structures.

# Discussion

Epidemiological studies contain evidence indicating that exposure to nanoparticles has toxicological effects on human health. Thus, it is of crucial importance to evaluate not only short term effects, like transient inflammation, but also long term ones which could lead to specific diseases such as pneumoconiosis, fibrosis, and cardiovascular disease. There is an increasing concern that various nanoengineered particles can be translocated into the brain by the vascular route (crossing the blood-brain barrier), which may lead to neurodegenerative diseases (Oberdörster et al., 2004).

In 2006, the International Agency for Research on Cancer (IARC) classified pigment-grade titanium dioxide as a possible carcinogen. The Organization for Economic Co-operation and Development (OECD) Steering Group for Test Guidelines released the nanoparticles list of high priority, where nanoTiO<sub>2</sub> is included together with fullerenes, single-walled carbon nanotubes (SWCNTs), multi-walled carbon nanotubes (MWCNTs), and silver nanoparticles as potentially toxic materials.

In the context of potential health hazards related to nanoengineered materials, this thesis addresses the size- and shape-dependence on the photocatalytic properties of anatase and rutile nanoTiO<sub>2</sub>, as well as demonstrating a multidisciplinary approach to the toxicity of nanoTiO<sub>2</sub> towards human cells.

One of the materials selected for the latter study were anatase-based TiO<sub>2</sub> nanowires (NWs). The motivation for evaluating the photocatalytic and toxic and photo-toxic properties of this type of nanoTiO<sub>2</sub> is driven by an increasing interest in this novel class of nanoparticles, combining a high degree of crystallinity with a high aspect ratio. Anatase-based TiO<sub>2</sub> nanowires are considered as ideal candidates for future efficient photocatalytic and electronic materials, with potential applications in advanced oxidation processes (AOPs), biosensing and photovoltaics. Thus, the study was focused on photocatalytic and toxic properties of custom-made anatase-based TiO<sub>2</sub> nanowires, with a diameter of 35 nm and lengths of 0.5-1 μm. The results obtained from these were compared with two commercial nanoparticulate TiO<sub>2</sub>: AMT100 (5.3 nm grain size) and the well known photocatalyst, P25 Degussa (80% anatase and 20% rutile, with an average grain size of 26 nm).

## **ROS generation by anatase-based TiO<sub>2</sub> nanowires**

ESR spin-trapping with an ROS-scavenger, DMPO, was used to monitor the ROS formation efficiency of eleven anatase and three rutile nanoTiO<sub>2</sub> samples. This research was performed in an unprecedentedly wide range of primary particle sizes, ranging from 3.8 to 150 nm, and 5 to 215 nm for anatase and rutile nanoTiO<sub>2</sub>, respectively. The results point to a strong and non-linear dependence of photocatalytic properties on crystalline phase and primary grain size. In particular, a “bell-shaped” dependence of the photocatalytic ROS efficiency on primary grain size was found for anatase nanoTiO<sub>2</sub>, whereas for rutile nanoTiO<sub>2</sub>, the photocatalytic properties were substantially less particle size-dependent.

For anatase nanoTiO<sub>2</sub>, the efficiency of ROS formation increased with increasing particle size in the range 3.8 – 27 nm. Then, for increasing particle diameters, up to 150 nm, the ROS formation rapidly decreased. The results obtained for anatase nanoTiO<sub>2</sub> are in good agreement with the recent experimental data of Daimon and Nosaka (Daimon and Nosaka, 2007; Daimon et al., 2008), who studied the formation of singlet oxygen on the surface of nanoTiO<sub>2</sub> and observed a steep decrease in the singlet oxygen concentration with increasing TiO<sub>2</sub> particle size in the range 20 to 60 nm. Interestingly, the most recent theoretical model of ROS formation efficiency by nanoTiO<sub>2</sub> claims a very similar dependence on the primary particle size (Barnard, 2010).

The ESR spin-trapping measurements revealed that the photocatalytic efficiency of ROS production of anatase-based TiO<sub>2</sub> nanowires was similar to that of commercially available sample AMT100 (particle size 5.3 nm). This latter commercial anatase sample and the well-known formulation P25 Degussa were chosen as nanomaterials of reference in the toxicity study of nanoTiO<sub>2</sub> towards living human cells.

## **ESR *ex vivo* detection of ROS generation in cells in the presence of nanoTiO<sub>2</sub>**

ESR spin-trapping with the intracellular ROS scavenger ACP revealed the formation of ROS upon incubation of cells with low concentrations of nanoTiO<sub>2</sub> (2 µg/mL). The ESR-detected concentrations of the paramagnetic ACP spin adduct rose with the incubation time and was also material- and cell-type dependent. For Lu1205 cells, after 90 min of incubation in the dark, the highest concentration of the intracellular



ROS was detected for anatase-based TiO<sub>2</sub> nanowires. In contrast, for WM793 cell, the highest concentration of intracellular ROS was found for P25 Degussa.

### **Detection of intracellular ROS - NBT staining**

Since ESR spin-trapping of intracellular ROS formation upon incubation with nanoTiO<sub>2</sub> yielded inconsistent results, a more conventional assay of NBT staining for ROS detection was applied. In the dark, NBT staining revealed the highest levels of ROS for P25 Degussa in Lu1205 and WM793 cells. Anatase-based TiO<sub>2</sub> nanowires and AMT100 resulted in similar levels of detected ROS. Much higher ROS levels were observed for cells incubated with nanoTiO<sub>2</sub> and exposed to UV-A illumination for 230 sec (1mW/cm<sup>2</sup>). Under illumination with UV-A, the highest levels of intracellular ROS were observed for P25 Degussa.

Overall, the detection of intracellular ROS with NBT staining followed a similar dependence to that revealed by ESR spin-trapping with DMPO *in vitro*.

### **Cell viability**

In addition to spectroscopic studies of ROS formation in the presence nanoTiO<sub>2</sub>, cell viability tests were performed. Staining of cells illuminated with UV-A (230 sec, 1 mW/cm<sup>2</sup>) with Propidium Iodide, which detects necrotic cells, pointed to P25 Degussa as having the highest phototoxicity. This result is similar to the one obtained with NBT staining. The cellular toxicity of anatase-based TiO<sub>2</sub> nanowires was lower, being also similar to that of the commercial anatase nanoTiO<sub>2</sub>, AMT100.

### **Morphology, actin selective staining and high resolution AFM imaging of cells**

Membrane blebs are another characteristic feature of cells exposed to stress. Such changes in the cell morphology were observed in optical microscopy images of Lu1205 and WM793 melanoma cells exposed to photo-oxidative stress in the presence of nanoTiO<sub>2</sub> by both optical and atomic force microscopies. The presence of membrane blebs might be explained by the altered expression of the actin-binding family of proteins (ABP), as earlier shown by Cunningham and coworkers (Cunningham, 1995; Cunningham et al., 1992). It is customarily accepted that the loss of this abundant cytoplasmic protein indicates initiation of apoptosis (Kwiatkowski, 1999). Lower

expression of ABP has also been associated with reduced cellular stiffness (Gardel et al., 2006).

AFM imaging of cell surfaces revealed the presence of membrane blebs, which were also accompanied by disappearance of the actin cortex stress fibers. The alterations induced by photooxidative stress were visible on the cell surface already after ca. 4 min. In addition, fluorescence microscopy images of selectively stained actin showed features that corroborated those observed in AFM topography and optical microscopy images. Exposure to various nanoTiO<sub>2</sub> and UV-A radiation causes dramatic effects - the filamentous network disappears, cells lose their mechanical strength and shape, and finally, their structural integrity.

Overall, the cell morphology changes for cells exposed to photo-oxidative stress were similar for all nanoTiO<sub>2</sub> used in this study. Once again, however, the most pronounced changes in cell morphology were induced by P25 Degussa.

### **AFM - determination of the Young's modulus**

The AFM elasticity measurements can detect early changes in cytoskeleton organization in living cells exposed to external stimuli (Lekka et al., 1999, 2001). It is already known that the ability of a cell to deform depends on its internal structure – a filamentous network composed of three types of elements i.e. actin filaments, microtubules, and intermediate filaments. The contribution of these elements to the AFM-determined mechanical properties was discussed in several studies where the importance of both the structural proteins of cytoskeleton and cytoskeleton associated proteins was demonstrated (Janmey, 1998; Janmey, 1995; Thoumine and Ott, 1997; Yamazaki et al., 2005). The results have shown that for small indentations (up to 500–1000 nm), the actin filaments are mostly responsible for the mechanical properties of cells (Wakatsuki et al., 2001).

The AFM elasticity measurements performed in this work revealed that the Young's modulus values increased for cells incubated for 0.5 h with nanoTiO<sub>2</sub> in the dark. The observed increase in cellular stiffness was of 50% – 115% and 8% to 34% for Lu1205 and WM793, respectively. For cells incubated for 0.5 h with nanoTiO<sub>2</sub> in the dark and subsequently exposed to UV-A for a short time (60 sec and 240 sec), the observed Young's modulus values were similar to those measured for cells exposed to nanoTiO<sub>2</sub> in the dark. Thus, in this work, the evolution of cell stiffness was found to be

similar to that observed for glioblastoma cells incubated with low concentrations (147  $\mu\text{M}$ ) of fullerols in the dark (Vileno et al., 2006). Similar increase of the cell stiffness was observed by Lu *et al.* (Lu et al., 2008) for blebbistatin-treated cells.

The observed increase of the Young's modulus values for cells incubated with nanoTiO<sub>2</sub> in the dark and followed by short time exposures to UV-A light are intriguing. However, the increase in cellular stiffness could be associated with mechanisms related to early apoptosis. In particular, during this transient period, the nucleus and microtubules govern an increase in the cortical Young modulus (Pelling et al., 2009).

In contrast with the above results, the cell stiffness dramatically decreased for longer exposures to UV-A (460 sec). The mechanical dynamics of apoptotic/necrotic cells are highly controlled by the cyto-architecture. The actin network appears to govern the cellular stiffness and the cortical Young's modulus measured by AFM. As the cell continues through the apoptotic progression, the Young's modulus values decrease, as the internal cyto-architecture is broken down.

In the experiments reported in this thesis, cells were adhered to glass coverslips, which were placed at the bottom of Petri dishes, and were therefore also exposed to particle diffusion and/or sediments of aggregates of nanoTiO<sub>2</sub>. NanoTiO<sub>2</sub>, when suspended in a culture medium (RPMI 1640 supplemented with 10% bovine serum albumin), tend to aggregate. This leads to an increase in their diameter. DLS measurements revealed the hydrodynamic radii of the studied nanoTiO<sub>2</sub> to be within the range  $\sim 0.8 - 3.5 \mu\text{m}$ . It is probable that during the relatively long incubation times (30 minutes prior to UV-A illumination), such large structures can enter the cell interior (Singh et al., 2007). These conditions could result in higher particle availability to cells than that determined from the concentration in buffer (Limbach et al., 2005).

The ability of different particles to penetrate cells can explain some differences in their toxicity. The most likely mechanism for cellular uptake of particles is endocytosis, foremost pinocytosis, where endocytic vesicles are formed (Singh et al., 2007). The results of this thesis may at least partly be explained by the fact that both nanowires and nanoparticles migrate inside cells using different pathways, and hence are more or less available depending on whether they are in vesicles or free in the cytoplasm. The measurements of cell stiffness of living human melanoma cells (Lu1205 and WM793) revealed that incubation with different nanoTiO<sub>2</sub> affects the organization of the actin filament network, as shown in **Figures 20-22**, chapter **VI.5.1**. Since cell stiffness reveals

properties of the cytoskeleton, the large observed changes may be explained by damages induced by ROS in close proximity to the cell surface. The potential targets for such attack are membrane lipids, transmembrane proteins, or focal adhesion points, which provide anchoring sites for the cytoskeleton (Conlon et al., 2002). The damages induced in these structures would lead to alterations of cell cytoskeleton organization, and thus, would lead to changes in cell elasticity.

Hydroxyl radicals are highly reactive and therefore short-lived (nanoseconds). Superoxide ions are more long-lived (millisecond to seconds). However, due to their negative charge, superoxide ions cannot penetrate the cell membrane (Korshunov and Imlay, 2002). Compared with hydroxyl radicals and superoxide ions, hydrogen peroxide ( $\text{H}_2\text{O}_2$ ) is less detrimental. However, it can enter the cell and be activated by Fe(II) ions *via* the Fenton reaction. Iron levels on the cell surface, in the periplasmic space or inside the cell are significant and can serve as a source of Fe(II) ions. In cells, iron occurs either as iron clusters or in iron storage proteins (such as ferritin).

While the nanoTiO<sub>2</sub> is being illuminated to produce  $\text{H}_2\text{O}_2$ , the Fenton reaction may take place and produce the more damaging hydroxyl radicals (Borg et al., 1988; Gutteridge J.C., 1988). When the light is turned off, any residual hydrogen peroxide would continue to interact with the iron species and generate additional hydroxyl radicals through the Fenton reaction. When both  $\text{H}_2\text{O}_2$  and superoxide ions are present, the iron-catalyzed Haber-Weiss reaction (Reactions 1 and 2 below) can provide a secondary pathway to forming additional hydroxyl radicals. The Haber-Weiss reaction and the spontaneous (i.e. non-catalysed) dismutation of  $\text{O}_2^{\bullet-}$  have been proposed as possible mechanisms for the generation of  $^1\Delta_g$  (Youngman, 1984).



The photooxidative stress-induced alterations to cellular and subcellular structures generated in the presence of nanoTiO<sub>2</sub> can be monitored by measurements of cell stiffness, which is related to changes in cytoskeleton. Thus, hydroxyl and/or superoxide radicals are linked with initiation of the cascade of events leading to actin filament reorganization.

To conclude, our results show that anatase-based TiO<sub>2</sub> nanowires can produce ROS in aqueous suspensions, which was confirmed by ESR measurements *in vitro*. During the process of illumination, two radicals are generated: OH• and O<sub>2</sub>•<sup>-</sup>.

The photocatalytic efficiency of anatase-based TiO<sub>2</sub> nanowires was compared with commercial nanoTiO<sub>2</sub>, anatase AMT100 and P25 Degussa. Interestingly, the photocatalytic efficiency of nanowires was remarkably smaller, reaching only ~30% of the most efficient pure anatase sample (AMT600 with grain sizes of 27 nm) and only ~20% when compared to the photocatalytic efficiency of P25 Degussa.

The concentrations of photo-produced ROS in the presence of the variants of nanoTiO<sub>2</sub> selected for this study were sufficiently high to cause adverse effects on living melanoma cells. The viability test, NBT staining, ACP intracellular free radical trapping and AFM measurements delivered evidences of ROS presence and action. The irradiation of cells with UV-A in the presence of nanoTiO<sub>2</sub>, resulted in cell softening, observed clearly for longer illumination times (460 sec). The altered mechanical properties of cells were interpreted as early apoptotic events leading to changes in the cellular structures. Marked changes in the cell shape and disorganization of the actin cytoskeleton were observed for cells exposed to photo-oxidative stress in the presence of nanoTiO<sub>2</sub>.

## Concluding remarks and outlook

This thesis presents a study on the photocatalytic properties and toxicity of custom-made anatase-based TiO<sub>2</sub> nanowires (NWs), which have recently been synthesized in our laboratory. Anatase-based TiO<sub>2</sub> NWs, *i.e.* nanoparticles having a high aspect ratio, have generated much interest as possible electronic and photocatalytic materials, with potential applications including biosensors, photovoltaic devices, bio-compatible scaffolds for tissue engineering, medical implants, etc.

The photocatalytic and toxic properties of anatase-based TiO<sub>2</sub> nanowires were compared with two commercial nanoTiO<sub>2</sub> materials: anatase AMT100 (primary grain size of 5.3 nm) from Tayca Inc. and P25 Degussa, a well known photocatalytic formulation consisting of 80% anatase and 20% rutile (primary grain sizes of 26 nm). The selection of nanoTiO<sub>2</sub> materials for this comparative study was made through a thorough characterization of the photocatalytic properties of eleven anatase and three rutile nanoTiO<sub>2</sub> samples. The primary grain sizes varied in the range from 3.8 to 150 nm, and 5 to 215 nm for anatase and rutile nanoTiO<sub>2</sub>, respectively. The ESR spin-trapping technique was used to monitor ROS formation efficiency of nanoTiO<sub>2</sub>, revealing that the UV-light induced photocatalytic action was strongly material- and size-dependent. For anatase nanoTiO<sub>2</sub> samples, a nonlinear ROS generation efficiency, achieving its maximum for particle diameter around 25-30 nm, was found as a function of particle size. The best photocatalytic properties were obtained for anatase nanoTiO<sub>2</sub>, AMT600, with a particle size of 27 nm. In contrast, for rutile nanoTiO<sub>2</sub>, the photocatalytic efficiency was markedly weaker, and with a less pronounced size-dependence. The reference material in this study, P25 Degussa (average particle size 26 nm) revealed ca. 3 times higher photocatalytic efficiency than the best anatase nanoTiO<sub>2</sub>, AMT600.

The results obtained for ROS formation efficiency for pure anatase nanoTiO<sub>2</sub> are in excellent agreement with the recent theoretical prediction by Barnard (Barnard, 2010).

In parallel, the custom made anatase-based TiO<sub>2</sub> nanowires (35 nm diameter – 0.5-1 μm length) were characterized, resulting in the observation that their photocatalytic efficiency for ROS production was similar to that of a commercial variant of nanoTiO<sub>2</sub>, AMT100 (particle size 5.3 nm).

Then, for the selected nanoTiO<sub>2</sub> materials, the focus of study was shifted to toxicity towards living human melanoma cells (Lu1205 and WM793) *ex vivo*. The

comparative study of their nanotoxicity was performed using very low concentrations of nanoTiO<sub>2</sub>, 2 – 2.5 µg/mL, considerably lower than that applied in the majority of previous *ex vivo* assays.

Although the *in vitro* ESR studies confirmed a very high photocatalytic efficiency of ROS formation of P25 Degussa as compared to the studied nanoTiO<sub>2</sub> (AMT100 and custom-made anatase-based TiO<sub>2</sub> nanowires), the *ex vivo* assays revealed much smaller differences in adverse effects of these variants of nanoTiO<sub>2</sub> towards living cells. The cell toxicity studies were performed both in the dark and under exposure to weak UV-A illumination (1 mW/cm<sup>2</sup>). The dark toxicity studies were performed using various experimental techniques and revealed marked nanotoxicity, which was both material- and cell-type dependent. For WM793 cells, ESR intracellular spin-trapping and NBT staining revealed increasing nanotoxicity as follows: P25 Degussa > NWs > AMT100. In contrast, for Lu1207 cells, these assays revealed no significant correlations relating to the type of material used. For cells exposed to UV-A illumination, the toxic effects were also material- and cell-type dependent. For WM793 cells, force spectroscopy AFM and NBT staining revealed increasing nanotoxicity from P25 Degussa to NWs to AMT100, similar to the result obtained for the dark studies. For Lu1207 cells, both assays revealed the strongest phototoxic effects in the presence of P25 Degussa.

Thus, two of the applied *ex vivo* techniques, *i.e.* ESR spin-trapping and NBT staining, point to enhanced intracellular ROS generation for cells incubated in the presence of nanoTiO<sub>2</sub>. This toxic action was also detected by force microscopy AFM, which revealed an increase in the cellular stiffness of cells exposed to nanoTiO<sub>2</sub>. Moreover, strong correlations were found between the AFM-measured topography and optical microscopy images of selectively stained actin stress fibers. The AFM topography revealed progressive decay of the projections of stress fibers, whereas FITC-phalloidin selective staining pointed to marked disintegration of the actin stress fibers.

Overall, this study points to ROS-mediated processes strongly contributing to the toxicity of nanomaterials in living cells. Moreover, the results indicate a lack of direct and simple correlations between the nanoparticles size, aspect ratio, and aggregation state. This is in contrast with numerous published data suggesting possible correlations between the primary grain sizes and cellular toxicity (Obersdorfer, 1992, 2004). In this context, the results of this work are in good agreement with several seminal studies by

Warheit (Warheit et al., 2006, 2007) and Sayes (Sayes et al. 2006), who found no straightforward correlation between nanotoxicity and particle physical parameters.

In summary, this thesis addresses the size and shape dependence on photocatalytic properties of anatase and rutile nanoTiO<sub>2</sub> in aqueous suspensions. The results indicate that the photocatalytic capability of ROS formation for anatase nanoTiO<sub>2</sub> *in vitro* is highly dependent on the primary particle size, achieving its maximum for particle diameter around 25-30 nm. This finding is in excellent agreement with the recent theoretical prediction by Barnard (Barnard, 2010). In contrast, the toxicity *ex vivo* studies performed on two human melanoma cell lines did not reveal direct and simple correlations between the adverse effects of nanoTiO<sub>2</sub> and sizes, aspect ratio and aggregation state of nanoparticles.

***The most important achievements of this thesis are listed below:***

- (i) Demonstration, for the first time, with the use of ESR spin-trapping technique, the photo-catalytic activity of the custom-made TiO<sub>2</sub>-based nanowires. Their photo-catalytic ROS formation efficiency *in vitro* was found to be similar to that of the commercial anatase nanoTiO<sub>2</sub>, AMT100 (primary particle size 5.3 nm).
- (ii) Finding of the non-linear, 'bell-shaped' type dependence of ROS generation efficiency as a function of the primary particle sizes for anatase nanoTiO<sub>2</sub>. This dependence was measured in the very large range of the particle primary sizes of 3.8 nm to 150 nm and revealed maximum of ROS formation efficacy for particle sizes around 25 - 30 nm.
- (iii) Finding of the lack of direct correlations between the cell morphology changes and ROS generation efficiency measured *in vitro* for the three selected classes of nanoTiO<sub>2</sub> materials, *i.e.* for the commercial anatase nanoTiO<sub>2</sub>, AMT100, well-known industrial photo-catalytic standard P25 Degussa and custom-made TiO<sub>2</sub>-based nanowires.
- (iv) Demonstration, *via* intracellular ESR spin trapping, of enhanced concentrations of intracellular ROS for cells incubated with nanoTiO<sub>2</sub> in the dark.



- (v) Obtaining excellent high-resolution AFM images of the cell surface for cells exposed to the oxidative stress. These high-resolution cell topography images clearly point to the potential of the AFM technique for tracking changes in the organization of actin network of living cells exposed to different kind of stressors, including the photo-oxidative stress generated in the presence of nanoTiO<sub>2</sub>.
- (vi) While using a very wide palette of experimental techniques, including optical microscopy, actin selective staining and high-resolution AFM imaging of cells, finding of the particularly good correlations for cell morphology changes for cells exposed to photo-oxidative stress in the presence of nanoTiO<sub>2</sub>. Interestingly, all these methods, which are sensitive to probe the actin fiber network, pointed to early changes in the organization of actin fibers in cells exposed to the photo-oxidative stress in the presence of nanoTiO<sub>2</sub>.
- (vii) Innovative use of the AFM force spectroscopy for tracking early changes in cellular and sub-cellular structures in living cells incubated in the presence of very low concentrations of nanoTiO<sub>2</sub> (2 – 2.5 µg/mL), and subsequently exposed to the photo-oxidative stress under UV-A light illumination. In particular, the increase of cell stiffness for cells incubated with nanoTiO<sub>2</sub> in the dark was associated with rearrangement of microtubules and related to the early apoptotic mechanisms. In contrast, the decrease of cell stiffness under the subsequent exposure to the photo-oxidative stress corroborates well with the changes in the cellular actin cortex.

Thus, this thesis contributes to a better understanding of cellular toxicity mechanisms of various forms of nanoTiO<sub>2</sub>, including its novel form, *i.e.* of TiO<sub>2</sub>-based nanowires.

## **Outlook**

Thus far, most reported nanotoxicity studies have focused on *ex vivo* cell culture studies. Generally, in these studies hazard identification has generally been achieved by ‘*case-by-case*’ approaches. As a consequence, it has been difficult to establish nanomaterial-related risk assessment frameworks. Moreover, data obtained from such studies may not correspond to the *in vivo* toxic effects of nano-engineered materials (Sayes et al., 2007). Therefore, in the future, full *in vivo* ‘life cycle’ characterization

schemes and protocols must be formulated. Systematic evaluation of the size, shape, and surface chemistry of nanostructures *in vitro*, and their correlation to *in vivo* behavior should be obtained. This will finally enable an unraveling of the pathways, fate, kinetics, clearance, metabolism, immune response and toxicity of nanostructures, as well as a correlation of these behaviors with the nanostructure's physical properties. It is also clear that a broad, interdisciplinary approach, including materials science, medicine, molecular biology, and toxicology, is mandatory for nanotoxicology research to arrive at an appropriate risk assessment. Such a multidisciplinary approach might be able to elucidate the whole cascade of mechanisms underlying nanotoxicity, by identifying nano-biomolecular interactions, *in vitro* and *ex vivo* cytotoxicity, and shed light on nanotoxicity in *in vivo* animal models. This, in turn, might result in a more general approach to nanotoxicity, which would replace today's 'case-by-case' approach for identification of nano-engineered materials-related hazard.

# References

- Abraham A. and Bleaney B.** (1973) “Electron Paramagnetic Resonance of Transition Metal Ions”, Oxford Press, London.
- Arya P., J.C. Stephens, D. Griller, S. Pou, C.L. Ramos, W.S. Pou, G.M. Rosen, J.** *Org. Chem.* 57 (1992) 2297.
- Alberts B., D. Barry, J. Lewis, M. Raff, K. Roberts, J.D. Watson,** (1994), “Molecular Biology of The Cell”, Third Edition, *Garland Publishing Inc, New York*.
- Almquist CB, Biswas P.** (2002). “Role of synthesis method and particle size of nanostructured TiO<sub>2</sub> on its photoactivity”. *J Catal* 212:145-156.
- Anderson MW, Hewitt JP, Spruce SR:** Broad spectrum physical sunscreens: titanium dioxide and zinc oxide; (1997) in *Lowe NJ, Shaath NA, Pathak MA (eds): Sunscreens: Development, Evaluation and Regulatory Aspects. New York, Dekker,* pp 353–397.
- Armstrong A. R., Armstrong J., Canales J. and Bruce P. G.** (2004). “TiO<sub>2</sub>-B nanowires”. *Angewandte Chemie International Edition* 43, 2286-2288.
- Armstrong G., Armstrong A. R., Canales J. and Bruce P. G.** (2005). “Nanotubes with the TiO<sub>2</sub>-B structures”. *Chemical Communications* 19, 2454-2456.
- Armstrong J.S., Bivalacqua T.J., Chamulitrat W., Sikka S., Hellstrom W.J.,** (2002) “A comparison of the NADPH oxidase in human sperm and white blood cells”. *Int J Androl.*; 25:223–229.
- Band R.P., Burton A.C.,** (1964). “Mechanical properties of the red cell membrane. I. Membrane stiffness and intracellular pressure”. *Biophysical Journal* 4, 115.
- Baehner R.L., Boxer L.A., Davis J.,** (1976), “The biochemical basis of nitroblue tetrazolium reduction in normal human and chronic granulomatous disease polymorphonuclear leukocytes”. *Blood.*;48:309–313.
- Barnard A.S.** (2010). “One-to-one comparison of sunscreen efficacy, aesthetics and potential nanotoxicity”. *Nature Nanotechnology*, 271 – 274.
- Bermudez E., Mangum J.B., Asgharian B., Wong B.A., Reverdy E.E., Janszen D.B., Hext P.M., Warheit D.B., Everitt J.I.,** (2002). Long-term pulmonary responses of three laboratory rodent species to subchronic inhalation of pigmentary titanium dioxide particles. *Toxicol. Sci.* 70, 86–97.

- Bermudez E., Mangum J.B., Wong B.A., Asgharian B., Hext P.M., Warheit D.B., Everitt J.I.**, (2004). Pulmonary responses of mice, rats, and hamsters to subchronic inhalation of ultrafine titanium dioxide particles. *Toxicol. Sci.* 77, 347–357.
- Binnig G., C.F. Quate, and C. Gerber**, (1986). “Atomic Force Microscope”. *Physical Review Letters*, 56(9):930–933.
- Boal, D.** (2002). “Mechanics of the Cell”. *Cambridge University Press, Cambridge, UK.*
- Boey S.K., Boal D.H., Discher D.E.**, (1998). “Simulations of the erythrocyte cytoskeleton at large deformation”. I. Microscopic models. *Biophysical Journal* 75 (3), 1573–1583.
- Borg D.C. and K.M. Schaich.**, (1988), “A Iron and Iron-Derived Radicals”, Augusta, Michigan, April 1987. *Ed. B. Halliwell. Federation of American Societies for Experimental Biology, Bethesda, MD*, pp. 20-6.
- Borm P.J., Schins R.P., Albrecht C.**, (2004). Inhaled particles and lung cancer. *part B: paradigms and risk assessment. Int J Cancer* : 110: 3–14.
- Brown S.B., E.A. Brown, and I. Walker**, (2000), “Photodynamic therapy: a clinical reality in the treatment of cancer”, *The Lancet Oncology* 1 (No. 4), pp. 212-219.
- Boudreau N., Bissell M.J.**, (1998). “ Extracellular matrix signaling: integration of form and function in normal and malignant cells”. *Current Opinion in Cell Biology* 10 (Suppl. 5), 640–646.
- Brunet L., Lyon D. Y., Hotze E. M., Alvarez P. J. J. and Wiesner M. R.** (2009). Comparative Photoactivity and Antibacterial Properties of C60 Fullerenes and Titanium Dioxide Nanoparticles. *Environ. Sci. Technol.* **43**, 4355-4360.
- Buettner G.R.**, *Free Radical Biol. Med.* 3 (1987) 259.
- Cai R., Hashimoto K., Itoh K., Kubota Y., Fujishima A.**, (1991), “Photokilling of malignant cells with ultrafine TiO<sub>2</sub> powder”. *Bull Chem Soc Jpn*, 64: 1268–1273.
- Cai R., Kubota Y., Shuin T., Sakai H., Hashimoto K., Fujishima A.**, (1992), “Induction of cytotoxicity by photoexcited TiO<sub>2</sub> particles”. *Cancer Res*, 52: 2346–2348.
- Cairns J.**, (1975). “*Mutation selection and the natural history of cancer*”. *Nature*, Vol. 255, Issue 5505, pp. 197-200.
- Campbell N.A.**, (1991) *Biology*, Third Edition, *University of California.*
- Chen Q., Du G.G., Zhang S. and Peng L.M.** (2002). “The structure of trititanate nanotubes”. *Acta Cryst. B* 58, 587.
- Chin, L. et al.** (1998). “The INK4a/ARF tumor suppressor: one gene–two products–two pathways.” *Trends Biochem. Sci.* 23, 291–296

- Clark W.H.J.**, (1991), “Tumour progression and the nature of cancer”, *Brit. J. Cancer* 64: 631.
- Conlon K.A., Rosenquist T. and Berrios M.** (2002). Site-directed photochemical disruption of the actin cytoskeleton by actin-binding Rose Bengal-conjugates. *J. Photochem. Photobiol. B.* **68**, 140-146.
- Colton C.A., Gilbert D.L.**, (1987). Production of superoxide anions by a CNS macrophage, the microglia. *FEBS Lett.* 223, 284–288.
- Colvin V.L.**, (2003). The potential environmental impact of engineered nanomaterials. *Nat. Biotechnol.* 21 (10), 1166–1170.
- Cooper J.A.**, (1991), “The role of actin polymerization in cell motility”. *Annu. Rev. Physiol.* 53: 585-605.
- Costa K.D.**, (2003) Single-cell elastography: “Probing for disease with the atomic force microscope”. *Dis. Markers*, 19:139–154.
- Coughlin M.F., Stamenovic D.**, (2003). “A prestressed cable network model of the adherent cell cytoskeleton”. *Biophysical Journal* 84 (2), 1328–1336.
- Crick F.H.C., Hughes A.F.W.**, (1950). “The physical properties of cytoplasm: a study by means of the magnetic particle method”. *Part I. Experimental. Experimental Cell Research* 1, 37–80.
- Cunningham C.C., Gorlin J.B., Kwiatkowski D.J., Hartwig J.H., Janmey P.A., Byers H.R. and Stossel T.P.** (1992). “Actin-binding protein requirement for cortical stability and efficient locomotion”. *Science* 255, 325-327.
- Cunningham C. C.** (1995). “Actin polymerization and intracellular solvent flow in cell surface blebbing”. *J. Cell Biol.* 129, 1589 -1599.
- Daimon T. and Nosaka Y.** (2007). “Formation and Behavior of Singlet Molecular Oxygen in TiO<sub>2</sub> Photocatalysis Studied by Detection of Near-Infrared Phosphorescence”, *J. Phys. Chem. C*, Vol. 111, No. 11.
- Daimon T., T. Hirakawa, M. Kitazawa, J. Suetake, Y. Nosaka**, (2008). “Formation of singlet molecular oxygen associated with the formation of superoxide radicals in aqueous suspensions of TiO<sub>2</sub> photocatalysts”. *Applied Catalysis A: General* 340,169–175.
- Davies M.J.** (2005). The oxidative environment and protein damage. *Biochimica et Biophysica Acta* **1703**, 93-109.

- De Lorenzo A.J.**, (1970). The olfactory neuron and the blood–brain barrier. *In: Wolstenholme, G., Knight, J. (Eds.), Taste and Smell in Vertebrates London. J&A Churchill*, pp. 151–176.
- Dockery D.W., Pope C.A., Xu X., Spengler J.D., Ware J.H., Fay M.E., Ferris B.G., Speizer F.E.** (1993). An association between air pollution and mortality in six US cities. *N Engl J Med* ;329:1753–1759.
- Dolmans D.E.J.G.J, D. Fukumura, and R. K. Jain**, (2003). “Photodynamic therapy for cancer”. *Nature Reviews Cancer*, 3(5):380–387
- Donaldson K. and Tran C.L.**, 2002. “ Inflammation caused by particles and fibers” *Inhal Toxicol* 14: 5-27).
- Donaldson K., Stone V., Tran C.L., Kreyling W., Borm P.J.A.**, (2004). Nanotoxicology: a new frontier in particle toxicology relevant to both the workplace and general environment and to consumer safety. *Occup. Environ. Med.* 61, 727–728.
- Drake B., Prater C.B., Weisenhorn A.L., Gould S.A. C., Albrecht T.R., Quate C.F., Cannell D.S., Hansma H.G., and Hansma P.K.** (1989). “Imaging crystals, polymers and biological processes in water with AFM”. *Science* 243, 1586–1589.
- Douglas H. and Weinberg R.A.**, (2000). “The Hallmarks of Cancer”. *Cell, Vol. 100*, 57–70.
- Dunford R., A. Salinaro, L. Cai, N. Serpone, S. Horikoshi, H. Hidaka, and J. Knowland**, (1997).” Chemical oxidation and DNA damage catalysed by inorganic sunscreen ingredients” *FEBS Letters* 418, 87.
- Duonghong D., J. Ramsden and M. Grätzel**, (1982). “Dynamics of interfacial electron-transfer processes in colloidal semiconductor systems”. *Journal of The American Chemical Society*, 104(11):2977–2985.
- Eaton S. S. and Eaton G. R.** (1998), “EPR imaging,” in ”*Foundations of Modern EPR*” (G. R. Eaton, S. S. Eaton, and K. M. Salikhov, eds.), (Singapore), pp. 684–694, World Scientific Publishing.
- Elson E.L.** (1988). “Cellular mechanics as an indicator of cytoskeletal structure and function”. *Annu. Rev. Biophys. Biophys. Chem.* 17:397–430.
- Encyclopedia Britannica** (2010),”History of optical microscopes”.
- Engel A., Schoenenberger C.A. and Müller D.J.** (1997). “High resolution imaging of native biological sample surfaces using scanning probe microscopy”. *Curr. Opin.Struct. Biol.* 7, 279-284.

- Evans E. A.** (1989). "Structure and deformation properties of red blood cells: concepts and quantitative methods". *Methods Enzymol.* 173:3–35.
- Evans E. and Yeung A.** (1989). "Apparent viscosity and cortical tension of blood granulocytes determined by micropipet aspiration". *Biophys. J.* 56, 151–160.
- Fabry B., Maksym G.N., Butler J.P., Glogauer M., Navajas D., Fredberg J.J.**, 2001. "Scaling the microrheology of living cells". *Physical Review Letters* 87 (14), 148102.
- Fabry B., Maksym G.N., Butler J.P., Glogauer M., Navajas D., Taback N.A., Millet E.J., Fredberg J.J.**, 2003. "Time scale and other invariants of integrative mechanical behavior in living cells". *Physical Review E* 68 (4), 041914.
- Fidler I.J.**, (2003). "The pathogenesis of cancer metastasis: the 'seed and soil' hypothesis revisited". *Nat. Rev. Cancer* 3:453-458.
- Fisher B. and E.R. Fisher.** , (1966) "The interrelationship of hematogenous and lymphatic tumor cell dissemination". *Surg Gynecol Obstet* 122:791.
- Fujishima A. and Honda K.**, (1972). "Electrochemical Photolysis of Water at a Semiconductor Electrode". *Nature* 238, 37-38.
- Fujishima A. and K. Honda**, (1971). "Studies on photosensitive electrode reactions .3. Electrochemical evidence for mechanism of primary stage of photosynthesis". *Bulletin of The Chemical Society of Japan*, 44(4):1148.
- Fujishima A., Rao T.N. and Tryk D.A.** (2000). "Titanium dioxide photocatalysis". *J.Photochem.Photobiol. C: Photochemistry Reviews* 1, 1-21.
- Fritz M., Radmacher M., and Gaub H.E.** (1994). "Granula motion and membrane spreading during activation of human platelets imaged by atomic force microscopy". *Biophys. J.* 66(5), 1328–1334.
- Galimzyanovich S.R., L.I. Larina, T. Il'inichna, J.R. Harbour, V. Chow, and J.R. Bolton**, (1974). "Electron-spin resonance study of spin adducts of OH and HO<sub>2</sub> radicals with nitrones in ultraviolet photolysis of aqueous hydrogen-peroxide solutions. *Canadian Journal of Chemistry-Revue Canadienne De Chimie*, 52(20):3549–3553.
- Gardel M.L., F. Nakamura, J.H. Hartwig, J.C. Crocker, T.P. Stossel and D.A. Weitz** (2006). "Prestressed F-actin networks cross-linked by hinged filamins replicate mechanical properties of cells". *PNAS* vol. 103, 1762–1767.
- Geerts H., De Brabander M., Nuydens R., Geuens S., Moeremans M., De Mey J., Hollenbeck P.**, (1987). "Nanovid tracking: a new automatic method for the study of mobility in living cells based on colloidal gold and video microscopy". *Biophysical Journal* 52 (5), 775–782.

- Geiser M., Casaulta M., Kupferschmid B., Schulz H., Semmler-Behnke M., Kreyling W.,** (2008). The Role of Macrophages in the Clearance of Inhaled Ultrafine Titanium Dioxide Particles. *AJRCMB*, vol. 38.
- Gehr P., Bachofen M., Weibel E.R.,** (1978) “The normal human lung: ultrastructure and morphometric estimation of diffusion capacity”. *Respir Physiol*, 32:121-140.
- Gheshlaghi Z.N., G.H. Riazi, S. Ahmadian, M. Ghafari and R. Mahinpour,** (2008), “Toxicity and interaction of titanium dioxide nanoparticles with microtubule protein”, *Acta Biochim Biophys Sin*: 777-782.
- Gilchrest B.A.,** (1999). “The pathogenesis of melanoma induced by ultraviolet radiation.” *N. Engl. J. Med.* 340, 1341–1348.
- Gogniat G., Thyssen M., Denis M., Pulgarin C. and Dukan S.** (2006). The bactericidal effect of TiO<sub>2</sub> photocatalysis involves adsorption onto catalyst and the loss of membrane integrity. *FEMS Microbiol. Lett.* **258**, 18-24.
- Gould S.A. C., B. Drake, C.B. Prater, A.L. Weisenhorn, S. Manne, H.G. Hansma, P.K. Hansma, J. Massie, M. Longmire, V. Elings, B.D. Northern, B. Mukerjee, C.M. Peterson, W. Stoeckenius, T.R. Albrecht, and C.F. Quate,** (1990). “From atoms to integrated-circuit chips, blood-cells, and bacteria with the Atomic Force Microscope”. *Journal of Vacuum Science & Technology A - Vacuum Surfaces and Films*, 8(1):369–373.
- Gulak F., Tedrow J.R., Burgkart R.,** (2000). “Viscoelastic properties of the cell nucleus”. *Biochemical and Biophysical Research Communications* 269 (3), 781–786.
- Gutteridge J.C.,** (1988), “A Lipid Peroxidation Some Problems and Concepts”, Augusta, Michigan, April 1987. *Ed. B. Halliwell. Federation of American Societies for Experimental Biology, Bethesda, MD.* pp. 9-19.
- Hartwig J.H., and Kwiatkowski D.J.** (1991). „Actin-binding proteins”. *Curr. Op. Cell Biol.* 3, 87–97.
- Henderson E., Haydon P.G., and Sakaguchi D.S.** (1992). “Actin filament dynamics in living glial cells imaged by atomic force microscopy”. *Science* 257, 1944–1946.
- Henon S., Lenormand G., Richert A., Gallet F.,** (1999). „A new determination of the shear modulus of the human erythrocyte membrane using optical tweezers”. *Biophysical Journal* 76 (2), 1145–1151.
- Herlyn D., Iliopoulos D., Jensen P.J., Parmiter A., Baird. J., Holla H., Adachi K., Ross A.H., Jambrosic J., Koprowski H., and Herlyn M.,** (1990). “In vitro properties of human melanoma cells metastatic in nude mice.” *Cancer Res.*, 50: 2296-2302.



- Herlyn, D.** et al. (1991). "Growth Factors, Metastases, and Antigens." *In: L. Nathanson (ed.) Melanoma Research: Genetics*, p. 105. Boston, MA: Kluwer Academic Publishers.
- Herlyn M., Thurin J., Balaban G., Bennicelli J.L., Herlyn D., Elder D.E., Bondi E., Guerry D., Nowell P., Clark W.H., Koprowski H.**, (1985). "Characteristics of Cultured Human Melanocytes Isolated from Different Stages of Tumor Progression", *Cancer Res.* 45: 5670.
- Hersey P. and Zhang X.D.**, (2001)." How melanoma cells evade trailinduced apoptosis." *Nat. Rev. Cancer* 1, 142–150.
- Hertz H.** (1882). Ueber die berührung fester elastischer körper. *Journal für die reine und eingewandte Mathematik*, 92:156–1711.
- Hirakawa T., Kominami H., Ohtani B. and Nosaka Y.** (2001). Mechanism of Photocatalytic Production of Active Oxygens on Highly Crystalline TiO<sub>2</sub> Particles by Means of Chemiluminescence Probing and ESR Spectroscopy. *J. Phys. Chem. B* 105, 6993-6999.
- Hirakawa T. and Nosaka Y.** (2002). Properties of O<sub>2</sub><sup>•-</sup> and OH<sup>•</sup> Formed in TiO<sub>2</sub> Aqueous Suspensions by Photocatalytic Reaction and the Influence of H<sub>2</sub>O<sub>2</sub> and Some Ions. *Langmuir* 18, 3247-3254.
- Hochmuth, R.M.** (2000). "Micropipette aspiration of living cells". *J. Biomech.* 33, 15–22
- Hoffmann M.R, Martin S.T, Choi W., Bahnemann D.W.** (1995)."Environmental applications of semiconductor photocatalysis". *Chem Rev*, 95: 69–96.
- Hoh J.H., Schoenenberger C.A.**, (1994). „Surface morphology and mechanical properties of MDCK monolayers by atomic force microscopy". *Journal of Cell Science* 107 (5), 1105–1114.
- Howard J.** (2001). "Mechanics of Motor Proteins and the Cytoskeleton". *Sinauer Press, Sunderland, MA*.
- Huang S., Ingber D.E.**, (1999). "The structural and mechanical complexity of cell-growth control". *Nature Cell Biology* 1 (5), E131–E138.
- Itoh O., M. Aoyama, H. Yokoyama, H. Obara, H. Ohya, and H. Kamada**, (2000). "Sensitive ESR Determination of Intracellular Oxidative Stress by Using Acyl-Protected Hydroxylamines as New Spin Reagents". *Chemistry Letters*, CL-991067.
- Janmey P.** (1998). "The cytoskeleton and cell signaling: component localisation and mechanical coupling". *Physiological Reviews* 78, 763-781.

- Janmey P., Chaponnier Ch.**, (1995). “Medical aspects of the actin cytoskeleton”. *Current Opinion in Cell Biology* 7, 111-117.
- Janssen K.P., L. Eichinger, P.A. Janmey, A.A. Noegel, M. Schliwa, W. Witke, and M. Schleicher**, (1996). “Viscoelastic properties of F-actin solutions in the presence of normal and mutated actin-binding proteins”. *Arch. Biochem. Biophys.* 325:183–189.
- Jen C.J., Jhiang S.J., Chen H.I.**, (2000). “Cellular responses to mechanical stress: invited review: effects of flow on vascular endothelial intracellular calcium signaling of rat aortas ex vivo.” *Journal of Applied Physiology* 89 (4), 1657–1662.
- Jeong H., Tombor B., Albert R., Oltvai Z.N., Barabasi A.L.**, 2000. “The large-scale organization of metabolic networks”. *Nature* 407 (6804), 651–654.
- Jiang J., G. Oberdörster, A. Elder, R. Gelein, P. Mercer and P. Biswas**, (2008). “Does nanoparticle activity depend upon size and crystal phase?”. *Nanotoxicology*, 2(1): 33-42
- Kamat P.V.** (2008). Quantum Dot Solar Cells. Semiconductor Nanocrystals as Light Harvesters. *J. Phys. Chem. C* 112, 18737-18753.
- Karp G.**, “Cell and Molecular Biology: concepts and experiments”, 2<sup>nd</sup> edition.
- Khan A.U. and M. Kasha**, (1963). “Red chemiluminescence of molecular oxygen in aqueous solution”. *Journal of Chemical Physics*, 39(8):2105–&.
- Kim S., Lim Y.T., Soltesz E.G., De Grand A.M., Lee J., Nakayama A., Parker J.A., Mihaljevic T., Laurence R.G., Dor D.M., Cohn L.H., Bawendi M.G., Frangioni J.V.** (2004): Near-infrared fluorescent type II quantum dots for sentinel lymph node mapping. *Nat Biotechnol*; 22: 93–97.
- Kochelaev B.I. and Yablokov Y.V.** (1995), “The Beginning of Paramagnetic Resonance”. *World Scientific, Singapore*, (Engl. transl. of **Zavoisky, E.**, *J. Phys. USSR*, 9 (1945) 245.).
- Koci K., L. Obalova L. Matejova D. Placha, Z. Lacny, J. Jirkovsky, O. Solcova**, (2009). "Effect of TiO<sub>2</sub> particle size on the photocatalytic reduction of CO<sub>2</sub>", *Applied Catalysis B: Environmental*.
- Kolmakov A. and Moskovits M.**, (2004). Chemical Sensing and Catalysis by One-dimensional Metal-oxide Nanostructures. *Annu. Rev. Mater. Res.* **34**, 151-180.
- Konstantinou I.K., and T.A. Albanis**, (2004), *Appl. Catal. B* 49, pp. 1–14.
- Limbach L. K., Li Y., Grass R.N., Brunner T.J., Hintermann M.A., Muller M., Gunther, D. and Stark, W.J.** (2005). “Nanoparticle uptake in human lung fibroblasts:

effects of particle size, agglomeration, and diffusion at low concentrations”. *Environ. Sci. Technol.* 39, 9370-9376.

**Korshunov S.S. and Imlay J.A.** (2002), “A potential role for periplasmic superoxide dismutase in blocking the penetration of external superoxide into the cytosol of Gram-negative bacteria”. *Molecular Microbiology* 43(1), 95–106

**Kuchan M.J., Frangos J.A.**, (1993). “Shear stress regulates endothelin-1 release via protein kinase C and cGMP in cultured endothelial cells.” *American Journal of Physiology—Heart and Circulatory Physiology* 264 (1), H150–H156.

**Kwiatkowski D.J.**, (1999). “Function of gelsolin: motility, signaling, apoptosis, cancer”, *Curr. Opin. Cell Biol.*,11:103-108.

**Laachir S., M. Moussetad, R. Adhiri, A. Fahli**, *Electron. J. Theor.Phys.* 5 (2005) 12.

**Langer M. G., A. Koitschev, H. Haase, U. Rexhausen, J.K.H. Horber, and J.P. Ruppertsberg**, (2000). „Mechanical stimulation of individual stereocilia of living cochlear hair cells by Atomic Force Microscopy”. *Ultramicroscopy*, 82(1-4):269–278. 259(3):645–650, 1999.

**Lee K.**, PhD Thesis, EPFL, 2008, “Surface-Bound Nanostructures: Mechanical and Metrological”

**Lekka M., Laidler P., Gil D., Lekki J., Stachura Z. and Hryniewicz A.Z.** (1999).”Elasticity of normal and cancerous human bladder cells studied by scanning force microscopy”. *Eur. Biophys. J.* 28, 312-316.

**Lekka M., P. Laidler, J. Ignacak, M. Labedz, J. Lekki, H. Struszczyk, Z. Stachura, and A.Z. Hryniewicz**, (2001) The effect of chitosan on stiffness and glycolytic activity of human bladder cells. *Biochimica et Biophysica Acta-Molecular Cell Research*, 1540(2):127–136.

**Leterrier J.F.**, (2001). “Water and the cytoskeleton”. *Cell and Molecular Biology* 47 (5), 901–923.

**Levchenko A.A., Li G., Boerio-Goates J., Woodfield B.F., Navrotsky A.**, (2006). “TiO<sub>2</sub> Stability Landscape: Polymorphism, Surface Energy, and Bound Water Energetics”. *Chem. Mater.*, 18, 6324–6332.

**Li, J., Dao, M., Lim, C.T., Suresh, S.**, (2005). “Spectrin-level modeling of the cytoskeleton and optical tweezers stretching of the erythrocyte”. *Biophysical Journal*, Volume 88, Issue 5, Pages 3707-3719.

- Li S.Q., R.R. Zhu, H. Zhu, M. Xue, X.Y. Sun, S.D. Yao, S.L. Wang,** (2008). “Nanotoxicity of TiO<sub>2</sub> nanoparticles to erythrocyte in vitro”, *Food and Chemical Toxicology* 46, 3626–3631.
- Liao D.L., Badour C.A. and Liao B.Q.** (2008). Preparation of nanosized TiO<sub>2</sub>/ZnO composite catalyst and its photocatalytic activity for degradation of methyl orange. *J. Photochem. Photobiol. A, Chem.* 194, 11-19.
- Lim C.T., E.H. Zhou, S.T. Quek,** (2006), “Mechanical models for living cells—a review”. *Journal of Biomechanics* 39, 195–216
- Lo C.M., Glogauer M., Rossi M., Ferrier J.,** (1998). “Cell–substrate separation: effect of applied force and temperature”. *European Biophysical Journal* 27 (1), 9–17.
- Long T.C., Saleh N., Tilton R.D., Lowry G., Veronesi B.,** (2006). Titanium dioxide (P25) produces reactive oxygen species in immortalized brain microglia (BV2): implications for nanoparticle neurotoxicity. *Environ. Sci. Technol.* 40, 4346– 4352.
- Long T.C., J. Tajuba, P. Sama, N. Saleh, C. Swartz, J. Parker, S. Hester, G.V. Lowry, and B. Veronesi,** (2007). Nanosize Titanium Dioxide Stimulates Reactive Oxygen Species in Brain Microglia and Damages Neurons in Vitro. *Environmental Health Perspectives* Volume 115, Number 11.
- Lu L., et al.,** (2008). “Mechanical properties of actin stress fibers in living cells”. *Biophys. J.* 95 (12), 6060–6071.
- Luch A.** “Nature and nurture-lessons from chemical carcinogenesis”. *Nat Rev Cancer* 2005; 5: 113–25.
- Luna, E.J., and A.L. Hitt,** (1992). “Cytoskeleton-plasma membrane interactions”. *Science Wash. DC* 258: 955-964.
- Maksym G.N., Fabry B., Butler J.P., Navajas D., Tschumperlin D.J., Laporte J.D., Fredberg J.J.,** (2000). “Mechanical properties of cultured human airway smooth muscle cells from 0.05 to 0.4 Hz”. *Journal of Applied Physiology* 89 (4), 1619–1632.
- Masters J.R.W and B. Palsson,** (1999), “Human Cell Culture” *Vol. 1*, 259–274. © 1999 *Kluwer Academic Publishers. Printed in Great Britain.*
- Masters J.R.W.,** (2000). “ Human cancer cell lines: fact and fantasy.” *Nat. Rev.* 1, 233–236.
- McBride H.M., M. Neuspiel, S. Wasiak,** (2006). “Mitochondria: more than just a powerhouse”. *Curr. Biol.* 16 (14): R551
- Merlino G. and F.P. Noonan,** (2003). “Modeling gene-environment interactions in malignant melanoma”. *Trends Mol Med* 9:102

- Mitchison J.M., Swann M.M.**, (1954). “The mechanical properties of the cell surface I”. *The cell elastimeter. Journal of Experimental Biology* 31, 443–460.
- Miyazaki H., Hasegawa Y., Hayashi K.**, (2000). “A newly designed tensile tester for cells and its application to fibroblasts”. *Journal of Biomechanics* 33 (1), 97–104.
- Meyer E., R. Overney, D. Brodbeck, L. Howald, R. Lüthi, J. Frommer, and H.J. Güntherodt** , (1992). Friction and wear of Langmuir-Blodgett films observed by friction force microscopy. *Physical Review Letters*, 69(12):1777–1780.
- Mills A. and Wang J.** (1999a). *Photochem. Photobiol. A, Chem.* 127, 123-134.
- Mills A. and Wang J.** (1999b). “Photobleaching of Methylene Blue Sensitised By TiO<sub>2</sub>: An Ambiguous System?” *Photochem. Photobiol. A, Chem.* 127, 123-134.
- Milligan R. A., Whittaker M. and Safer D.** (1990). Molecular structure of F-actin and location of surface binding sites. *Nature* 348, 217-221.
- Moan J.; Boye E.**, (1981), “Photodynamic effect on DNA and cell survival of human cells sensitized by hematoporphyrin” *Photobiochem. Photobiophys* 2, 301.
- Mogyorósi B., N. K. Srankó, D. F. Pallagi, A. Alapi, T. Oszkó, A. Dombi, A. Sipos, P.**, “The Effect of Particle Shape on the Activity of Monocrystalline TiO<sub>2</sub> Photocatalysts in Phenol Decomposition”. *Appl. Catal., B*, doi:10.1016/j.apcatb.2008.
- Mor G.K., Carvalho M.A., Varghese O.K., Pishko M. V. and Grimes C.A.** (2004). A room-temperature TiO<sub>2</sub>-nanotube hydrogen sensor able to self-clean photoactively from environmental contamination. *J. Mater. Res.* 19, 628-634.
- Morganti P.**, (2010) “Use and potential of nanotechnology in cosmetic Dermatology” *Clinical, Cosmetic and Investigational Dermatology* 3, pp. 5-13.
- Mühlfeld C., Geiser M., Kapp N., Gehr P., Rothen-Rutishauser B.** (2007), “Re-evaluation of pulmonary titanium dioxide nanoparticle distribution using the “relative deposition index”: evidence for clearance through microvasculature”. *Part Fibre Toxicol*, 4: 7.
- Muscat J., Swamy V., Harrison N.M.**,( 2002). “First-Principles Calculations of the Phase Stability of TiO<sub>2</sub>”. *Phys. Rev. B*, 65, 224112–224126.
- Naumanen P., Lappalainen P., Hotulainen P.**, (2008). “Mechanisms of actin stress fibre assembly”. *J. Microsc.* 231 (3), 446–454.
- Nel A., T. Xia, L. Madler, and N. Liet**, (2006), "Toxic potential of materials at the nanolevel", *Science* 311, 622–667.

- Niedre M., Patterson M.S., Wilson B.C.,** (2002), “Direct near-infrared luminescence of singlet oxygen generated by photodynamic therapy in cells in vitro and tissues in vivo”. *Photochem. Photobiol.* 75, 382.
- Oberdörster G., Z. Sharp, V. Atudorei, A. Elder, R. Gelein, W. Kreyling and C. Cox** (2004). Translocation of Inhaled Ultrafine Particles to the Brain. *Inhalation Toxicology*, 16:437–445.
- Oberdörster G., Ferin, J., Gelein R., Soderholm S.C., Finkelstein J.,** (1992). Role of the alveolar macrophage in lung injury: studies with ultrafine particles. *Environ. Health Perspect.* 97, 193–199.
- Oberdörster G., Oberdörster E., Oberdörster J.,** (2005). “Nanotechnology: an emerging discipline evolving from studies of ultrafine particles”. *Environ Health Perspect*, 113: 823–839.
- Ophus E.M., Rode L.E., Gylseth B., Nicholson G., Saeed K.,** (1979), “Analysis of titanium pigments in human lung tissue.” *Scand J Work Environ Health*, 5: 290–296.
- Park J., Bauer S., von der Mark K. and Schmuki P.** (2007). “Nanosize and Vitality: TiO<sub>2</sub> Nanotube Diameter Directs Cell Fate”. *Nano Letters* 7, 16860-1691.
- Pelling A.E., F.S. Veraitch, C.P.K. Chu, Ch. Mason, and M.A. Horton,** (2009). “Mechanical Dynamics of Single Cells During Early Apoptosis”. *Cell Motility and the Cytoskeleton* 66: 409–422.
- Petersen N.O., McConnaughey W.B., Elson E.L.,** (1982). “Dependence of locally measured cellular deformability on position on the cell, temperature, and cytochalasin B”. *PNAS* 79 (17), 5327–5331.
- Pesen D. and Hoh J.H.,** (2005). “Micromechanical Architecture of the Endothelial Cell Cortex”, *Biophysical Journal* Volume 88.
- Pollard T.D., L. Blanchoin, and R.D. Mullins.,** (2000). “Molecular mechanisms controlling actin filament dynamics in nonmuscle cells.” *Annu. Rev. Biophys. Biomol. Struct.* 29:545–576.
- Pollard T.D., and G.G. Borisy.,** (2003). “Cellular motility driven by assembly and disassembly of actin filaments”. *Cell* 112:453–465.
- Puccetti G., F. Lahjomri, and R.M. Leblanc.,** (1997). “Pulsed photoacoustic spectroscopy applied to the diffusion of sunscreen chromophores in human skin: the weakly absorbent regime.” *J. Photochem. Photobiol.* B 39, 110.

- Putman C.A., K.O. van der Werf B.G. de Grooth, N.F. van Hulst, J.Greve, and P. K. Hansma.** (1992). "A new imaging mode in atomic force microscopy based on the error signal". *Proc. Soc. Photo-Opt. Instrum. Eng.* 1639:198–204.
- Raab O.,** (1900) "Über die Wirkung, fluorescirender Stoffe auf infusorien". *Z. Biol.* 39, 524-546.
- Radmacher M.,** (1997), "Measuring the elastic properties of biological samples with the afm". *IEEE Engineering In Medicine And Biology Magazine*, 16(2):47–57.
- Ruddon R.W., M.D., Ph.D.** (2007). "Cancer Biology". *University of Michigan Medical School Ann Arbor, Michigan, Copyright © 2007 by Oxford University Press, Inc.*
- Rahman Q., Lohani M., Dopp E., Pemsel H., Jonas L., Weiss D.G., Schiffmann D.**(2002), "Evidence that ultrafine titanium dioxide induces micronuclei and apoptosis in Syrian hamster embryo fibroblasts". *Environ Health Perspect*, 110: 797–800.
- Radmacher, M., Fritz, M., and Hansma, P.K.** (1995). "Imaging soft samples with the atomic force microscope: Gelatin in water and propanol". *Biophys. J.* 69(7), 264–270.
- Redmond, R. W. and Kochevar, I. E.** (2006). Spatially Resolved Cellular Responses to Singlet Oxygen. *Photochem. Photobiol. B* 82, 1178-1186.
- Rengifo-Herrera J.A., K. Pierzchała, A. Sienkiewicz, L. Forró, J. Kiwi, J.E. Moser, and C. Pulgarin,** (2010) "Synthesis, Characterization, and Photocatalytic Activities of Nanoparticulate N, S-Codoped TiO<sub>2</sub> Having Different Surface-to-Volume Ratios", *J. Phys. Chem. C* 114, pp. 2717–2723.
- Rothen-Rutishauser B., Mühlfeld C., Blank F., Musso C., Gehr P.,** (2007). "Translocation of particles and inflammatory responses after exposure to fine particles and nanoparticles in an epithelial airway model". *Part Fibre Toxicol*, 4: 9.
- Rotsch C., Jacobson K., and Radmacher M.,** (1999). "The dynamics of active and stable edges in motile fibroblasts investigated by atomic force microscopy". *Proc. Natl. Acad. Sci. U.S.A.* 96, 921–926.
- Rotsch C., and M. Radmacher.** (2000). "Drug-induced changes of cytoskeletal structure and mechanics in fibroblasts: an atomic force microscopy study". *Biophys. J.* 78:520–535.
- Rotsch C., Jacobson K., and Radmacher M.** (2000b). "Investigating living cells with the atomic force microscope". *Scanning Microsc. in press.*
- Roy S.C., Paulose M. and Grimes C.A.** (2007). The effect of TiO<sub>2</sub> nanotubes in the enhancement of blood clotting for the control of hemorrhage. *Biomaterials* 28, 4667-4672.

- Rus G. and J.García-Martínez,** (2007). *Ultrasonic tissue characterization for monitoring nanostructured TiO<sub>2</sub>-induced bone growth* Phys. Med. Biol. **52** (2007) 3531–3547.
- Saito T., Iwase T., Horie J. and Morioka T.** (1992). Mode of photocatalytic bactericidal action of powdered semiconductor TiO<sub>2</sub> on mutants streptococci. *J. Photochem. Photobiol. B.* 14, 369–379.
- Sakai H., Ito E., Cai R. X., Yoshioka T., Kubota Y., Hashimoto K. and Fujishima A.,** (1994). Intracellular Ca<sup>2+</sup> concentration change of T24 cell under irradiation in the presence of TiO<sub>2</sub> ultrafine particles. *Biochim. Biophys. Acta* 1201, 259–265.
- Saran M., Beck-Speier I., Fellerhoff B., Bauer G.,** (1999). “Phagocytic killing of microorganisms by radical processes: consequences of the reaction of hydroxyl radicals with chloride yielding chlorine atoms”. *Free Radic Biol Med.*;26:482–490.
- Satcher Jr. R.L., Dewey Jr. C.F.,** (1996). “Theoretical estimates of mechanical properties of the endothelial cell cytoskeleton”. *Biophysical Journal* 71 (1), 109–118.
- Sato M., Levesque M.J., Nerem R.M.,** (1987). “Micropipette aspiration of cultured bovine aortic endothelial cells exposed to shear stress.”, *Arteriosclerosis* 7 (3), 276–286.
- Sayes, C.M., Wahi R., Kurian P.A., Liu Y., West J.L., Ausman K.D., Warheit D.B. and Colvin V.L.** (2006). Correlating Nanoscale Titania Structure with Toxicity: A Cytotoxicity and Inflammatory Response Study with Human Dermal Fibroblasts and Human Lung Epithelial Cells. *Toxicol. Sci.* 92, 174-185.
- Sayes C.M., Reed K.L., Warheit D.B.,** (2007) “Assessing toxicology of fine and nanoparticles: comparing in vitro measurements to *in vivo* pulmonary toxicity profiles”. *Toxicol Sci*, 97:163-180.
- Swartz H. M. and Berliner L. J.,** (1998), “In-vivo EPR,” in “*Foundations of Modern EPR*” (G. R. Eaton, S. S. Eaton, and K. M. Salikhov, eds.), (Singapore), pp. 361–378, World Scientific Publishing.
- Scotti R., Morazzoni F.,** (2007). “Optimizing the Photocatalytic Properties of Hydrothermal TiO<sub>2</sub> by the Control of Phase Composition and Particle Morphology”. *A Systematic Approach. J. Am. Chem. Soc.*, 129, 3564–3575.
- Scown T.M., R. van Aerle, B.D. Johnston, S. Cumberland, J.R. Lead, R.Owen, and Ch.R. Tyler** (2009). “High Doses of Intravenously Administered Titanium Dioxide Nanoparticles Accumulate in the Kidneys of Rainbow Trout but with no Observable Impairment of Renal Function.”, *TOXICOLOGICAL SCIENCES* 109(2), 372–380.



**Serrander L., Cartier L., Bedard K., Banfi B., Lardy B., Plastre O., Sienkiewicz A., Fórró L., Schlegel W., Krause K.H., (2007),**“NOX4 activity is determined by mRNA levels and reveals a unique pattern of ROS generation”. *The Biochemical journal*; 406(1):105-14.

**Shieh A.C., Athanasiou K.A., (2002).** “Biomechanics of single chondrocytes and osteoarthritis”. *Critical Reviews in Biomedical Engineering* 30 (4–6), 307–343.

**Shieh A.C., Athanasiou K.A., (2003).** “Principles of cell mechanics for cartilage tissue engineering”. *Annals of Biomedical Engineering* 31 (1), 1–11.

**Shin D., Athanasiou K., (1999).** “Cytoindentation for obtaining cell biomechanical properties”. *Journal of Orthopaedic Research* 17 (6), 880–890.

**Sienkiewicz A., S. Garaj, E. Bialkowska-Jarowska, and L. Forró, (2000).** „Singlet oxygen generation by C60 and C70 - An ESR study”. In *Eds Kuzmany/Finck/Mehring, editor, Winterschool on Electronic Properties of Novel Materials*, vol. 544 of AIP Conference Proceedings, pages 63–66. Melville New-York.

**Singh S., Shi T., Duffin R., Albrecht C., van Berlo D., Hohn D., Fubini B., Martra G., Fenoglio I., Borm P.J., (2007).** “Endocytosis, oxidative stress and IL-8 expression in human lung epithelial cells upon treatment with fine and ultrafine TiO<sub>2</sub>: role of the specific surface area and of surface methylation of the particles”. *Toxicol. Appl. Pharmacol.* 222, 141-151.

**Sies H. (1993).** "Strategies of antioxidant defense". *European Journal of Biochemistry* 215 (2): 213–219.

**Singh R.J., H. Karoui, M.R. Gunther, J.S. Beckman, R.P. Mason, B. Kalyanaraman, Proc. Natl. Acad. Sci. USA 95 (1998) 6675.**

**Sneddon I.N., (1965).** “The relation between load and penetration in the axisymmetric boussinesq problem for a punch or arbitrary profile”. *Int. J. Engng. Sci.*, 3:47–57.

**Soengas M.S. et al. (2001).** “ Inactivation of the apoptosis effector Apaf-1 in malignant melanoma.” *Nature* 409, 207–211.

**Sollich P., (1998).** “Rheological constitutive equation for a model of soft glassy materials”. *Physical Review E* 58 (1), 738–759.

**Sopyan I., Watanabe M., Murasawa S., Hashimoto K., Fujishima A., (1996).** *J. Photochem. Photobiol. A, Chem.* 98, 79.

**Stadtman E.R., (1990).** “Metal ion-catalyzed oxidation of proteins: Biochemical mechanism and biological consequences”. *Free Radical Biology & Medicine*, Vol. 9, pp. 315-325.

- Stamenovic D., Ingber D.E.,** (2002). „Models of cytoskeletal mechanics of adherent cells”. *Biomechanics and Modeling in Mechanobiology* 1 (1), 95–108.
- Stamenovic D., Fredberg J.J., Wang N., Butler J.P., Ingber D.E.,** (1996). “A microstructural approach to cytoskeletal mechanics based on tensegrity”. *Journal of Theoretical Biology* 181 (2), 125–136.
- Stamenovic D., Suki B., Fabry B., Wang N., Fredberg J.J.,** (2004). “Rheology of airway smooth muscle cells is associated with cytoskeletal contractile stress”. *Journal of Applied Physiology* 96 (5), 1600–1605.
- Stearns R.C., Paulauskis J.D., Godleski J.J.,** (2001), “Endocytosis of ultrafine particles by A549 cells”. *Am J Respir Cell Mol Biol*, 24: 108–115.
- Tachikawa T., Fujitsuka M. and Majima T.J.** (2007). *J. Phys. Chem. C* 111, 5259-5275.
- Tan M.H., C.A. Commens, L. Burnett, and P.J. Snitch.,** (1996), “A pilot study on the percutaneous absorption of microfine titanium for sunscreens “*J. Dermatol.* 37, 185.
- Testino A., Bellobono I. R., Buscaglia V., Canevali C., D’Arienzo M., Polizzi S., Rajh T., Nedeljkovic J.M., Chen L.C., Poluektov O., Thurnauer M.C.,** (1999) “Improving Optical and Charge Separation Properties of Nanocrystalline TiO<sub>2</sub> by Surface Modification with Vitamin C”. *J. Phys. Chem. B*, 103, 3515–3519.
- Testino A., Bellobono I.R., Buscaglia V., Canevali C., D’Arienzo M., Polizzi S., Scotti R., Morazzoni F.,** (2007). “Optimizing the Photocatalytic Properties of Hydrothermal TiO<sub>2</sub> by the Control of Phase Composition and Particle Morphology. A Systematic Approach”. *J. Am. Chem. Soc.*, 129, 3564–3575.
- Thevenot P.,** (2008). *Nanomedicine: Nanotechnology, Biology, and Medicine* 4, 226-236.
- Thoumine O. and Ott A.** (1997). Comparison of the mechanical properties of normal and transformed fibroblasts. *Biorheology* 34, 309-326.
- Thoumine O. and Ott, A.,** (1997). “Time scale dependent viscoelastic and contractile regimes in fibroblasts probed by microplate manipulation”. *Journal of Cell Science* 110 (17), 2109–2116.
- Treloar L.R.** (1975). “The Physics of Rubber Elasticity.” *Clarendon Press, Oxford.*
- Vakul’skaya M. and Grigor’evich V.,** (2002), “Electron Paramagnetic Resonance in Biochemistry and Medicine”, *Kluwer Academic Publishers New York, Boston, Dordrecht, London, Moscow.*

- Verkhovsky A.B., Borisy G.G.,** (1993). “Non-sarcomeric mode of myosin II organization in the fibroblast lamellum”. *J. Cell Biol.* 123 (3), 637–652.
- Verkhovsky A.B., Svitkina T.M., Borisy G.G.,** (1995). “Myosin II filament assemblies in the active lamella of fibroblasts: their morphogenesis and role in the formation of actin filament bundles”. *J. Cell Biol.* 131 (4), 989–1002.
- Vileno B., Marcoux P. R., Lekka M., Sienkiewicz A., Fehér T. and Forró L.,** (2006). “Spectroscopic and Photophysical Properties of a Highly Derivatized C60 Fullerol”. *Adv. Funct. Mater.* 16, 120-128.
- Wakatsuki T., Schwab B., Thompson N.C. and Elson E.L.,** (2001). “Effects of cytochalasin D and latrunculin B on mechanical properties of cells.” *J. Cell Sci.* 114, 1025-1036.
- Wang J., G. Zhoua, Ch. Chena, H.Yu, T. Wang, Y. Mad, G. Jia, Y. Gaoa, B. Li, J. Suna, Y. Li, F. Jiao, Y. Zhaoa, Z. Chai,** (2007). “Acute toxicity and biodistribution of different sized titanium dioxide particles in mice after oral administration”, *Toxicology Letters* 168, 176–185
- Wang J.X., C.Y. Chen, H.W. Yu, J. Sun, B. Li, Y.F. Li, Y.X. Gao, W. He, Y.Y. Huang, Z.F. Chai, Y.L. Zhao, X.Y. Deng, H.F. Sun,** (2007). “Distribution of TiO<sub>2</sub> particles in the olfactory bulb of mice after nasal inhalation using microbeam SRXRF mapping techniques.” *Journal of Radioanalytical and Nuclear Chemistry*, Vol. 272, No.3, 527–531
- Wang J., Ch. Chen, Y. Liu, F.Jiao, W. Li, F. Lao, Y. Li, B. Li, C. Ge, G. Zhou, Y. Gao, Y. Zhao, Z. Chai,** (2008). “Potential neurological lesion after nasal instillation of TiO<sub>2</sub> nanoparticles in the anatase and rutile crystal phases.” *Toxicology Letters* 18, 72–80.
- Wang N., Butler J.P., Ingber D.E.,** (1993). „Mechanotransduction across the cell surface and through the cytoskeleton”. *Science* 260 (5111), 1124–1127.
- Warheit D.B., Webb T.R., Sayes C.M., Colvin V.L. and Reed K.L.,** (2006). “Pulmonary instillation studies with nanoscale TiO<sub>2</sub> rods and dots in rats: toxicity is not dependent upon particle size and surface area”. *Toxicol. Sci.* 91, 227-236.
- Warheit D.B., Webb T.R., Colvin V.L., Reed K.L., and Sayes C.M.,** (2007). “Pulmonary bioassay studies with nanoscale and fine-quartz particles in rats: toxicity is not dependent upon particle size but surface characteristic”. *Toxicol. Sci.* 95, 270-280.
- Wardman P. and L.P. Candeias,** (1996). “Fenton chemistry: An introduction.” *Radiation Research*, 145(5):523–531.

- Weber I., J. Niewohner, and J. Faix,** (1999). "Cytoskeletal protein mutations and cell motility in Dictyostelium". *Biochem. Soc. Symp.* 65:245–265.
- Weinberg R.A.,** (2007). "Biology of Cancer" © 2007 by *Garland Science, Taylor & Francis Group, LLC.*
- Weisenhorn A.L., Hansma P.K., Albrecht T.R., and Quate C.F.** (1989). "Forces in atomic force microscopy in air and water", *Appl. Phys. Lett.* 54, 2651–2653.
- Weisenhorn A.L., Khorsandi M., Kasas S., Gotozos V., Celio M.R., and Butt H.J.,** (1993). "Deformation and height anomaly of soft surfaces studied with the AFM". *Nanotechnology* 4, 106–113.
- Wu J., W. Liub, Ch. Xueb, S. Zhoua, F. Lana, L. Bia, H. Xub, X. Yangb, F.D. Zeng,** (2009): Toxicity and penetration of TiO<sub>2</sub> nanoparticles in hairless mice and porcine skin after subchronic dermal exposure. *Toxicol. Lett.*, doi:10.1016/j.toxlet.2009.05.020.
- Yamada S., D. Wirtz and S. C. Kuo,** (2000). "Mechanics of living cells measured by laser tracking microrheology". *Biophys. J.* 78:1736–1747.
- Yamadori I., Ohsumi S., Taguchi K.,** (1986). Titanium dioxide deposition and adenocarcinoma of the lung. *Acta Pathol. Jpn.* 36 (5), 783–790.
- Yamazaki D., Kurisu S. and Takenawa T.** (2005). *Cancer Sci.* 7, 379.
- Yokoyama H., Itoh O., Aoyama M., Obara H., Ohya H. and Kamada H.** (2000), "In vivo EPR imaging by using an acyl-protected hydroxylamine to analyze intracerebral oxidative stress in rats after epileptic seizures". *Magn. Reson. Imaging* 18, 875–879.
- Youngman R.J.,** (1984). "Oxygen activation: is the hydroxyl radical always biologically relevant?", *Trends in Biochemical Sciences*, 9, 280.
- Zavoisky E. K.,** (1945a), "Paramagnetic relaxation of liquid solutions for perpendicular fields," *Journal of Physics-USSR*, vol. 9, pp. 211–216.
- Zavoisky E.K.,** (1945b), "Spin magnetic resonance in paramagnets," *Journal of Physics-USSR*, vol. 9, pp. 245–249.
- Zhang A.P. and Sun Y.P.,**( 2004), "Photocatalytic killing effect of TiO<sub>2</sub> nanoparticles on Ls-174-t human colon carcinoma cells". *World J Gastroenterol*, 21: 3191–3193.
- Zvyagin A.V., X. Zhao, A. Gierden, W. Sanchez, J.A. Ross, and M.S. Roberts,** (2008). "Imaging of zinc oxide nanoparticle penetration in human skin in vitro and in vivo", *Journal of Biomedical Optics* Vol. 13, No. 6, pp. 064031-9.

# List of Figures

## I. Introduction

**Figure 1.** The size of various familiar objects on a logarithmic scale ..... 7

## II. Health effects of Titanium Dioxide

**Figure 1.** Localization of ultrafine TiO<sub>2</sub> particles in ultrathin sections of BAL–macrophages. Micrographs with uppercase letters show the cellular localization of the particles at a magnification of 36,300 while those with lowercase letters show the individual particles at a magnification of 325,000. (A, a). Ultrafine TiO<sub>2</sub> particle contained in a vesicle with gray, homogenous matter. (B, b) Multiple ultrafine particles in one macrophage profile; (b) shows the two particles located in the elongated vesicle. (C, c) Particle located in a phagolysosome containing surfactant. (Taken from Geiser et al., 2008) ..... 13

**Figure 2.** Suggested neuronal translocation pathways in humans for solid nanosized particles and for soluble components of larger particles. These include uptake into nerve endings embedded in mucosa of nasal (a, olfactory; b, trigeminal nerves) and tracheobronchial (c, afferent vagal nerves) region. The biological/toxicological importance of these pathways and their contribution to particle clearance vis-a-vis the classical clearance pathways of mucociliary and phagocytic cell transport, dissolution, diffusion, and protein binding remain to be determined. Taken from Oberdörster et al., 2004 ..... 14

**Figure 3.** Distribution of titanium in olfactory bulb of mice in the different experimental groups analyzed by SR-XRF (Taken from Wang et al., 2007, 2008). The greyscale shows the nanoparticle concentration, from white (no particles observed) to black (high concentration of nanoparticles) ..... 15

**Figure 4.** Morphological changes of neurons in the Nissl stained brain tissue sections of (A&B) control group, (C) 80 nm group and (D) 155 nm group. Note that apparently scattered Nissl body, large cell somata (arrows) and an irregular appearance were found especially in the CA1 region of hippocampus in the exposed mice. Image magnification: 100× (B–D); 40× (A). E represents the comparison of cell numbers in the CA1 region of the hippocampus (number/mm<sup>2</sup>) of mice 30 days after treatment with different TiO<sub>2</sub> nanoparticles. (Taken from Wang et al., 2007, 2008). .15

**Figure 5.** TEM of P25 (20 ppm, 3 hr) treated N27 neurons showed numerous membrane-bound aggregates. An amorphous substance was seen within the vacuoles (insert). In addition, individual nanosize P25 particles (circle) were noted throughout the cytoplasm. Mitochondria in nearby proximity showed no evidence of disruption or swelling. (Taken from Long, 2007) . . . **16**

**Figure 6.** The structure of skin (<http://faculty.irsc.edu/FACULTY/TFischer/AP1/skin.jpg>). . . **17**

**Figure 7.** Section of skin showing large numbers of dendritic (Langerhans) cells in the epidermis. *M. ulcerans* infection, S100 immunoperoxidase stain. (Taken from Kim et al.,2004). . . . . **18**

**Figure 8.** Histopathological evaluation of the organ of hairless mice after dermal exposure to different sized TiO<sub>2</sub> nanoparticles for 60 days. Samples were stained with hematoxin and eosin (H&E) and observed at 100×. The arrows points at pathological changes in various tissue sections (Taken from Wu et al., 2009). The marked histopathological changes corresponding to focal necrosis are visible for the tissues exposed to 25 and 60 nm particles, and for P25 Degussa. In contrast, liquefaction necrosis was observed for 10 nm sized TiO<sub>2</sub> . . . . . **19**

**Figure 9.** (A) Overview (20× magnification) of the 8 h control (i) and 24 h control (ii). Perinuclear localization highlighted by magnified inset. Minimal presence of QD can be seen even in the lower stratum corneum layers. (B) Example slices of the 24 h UV radiation exposed mouse skin with high penetration areas in the dermis highlighted by magnified insets. (Taken from Luke et al., 2008) . . . . . **20**

**Figure 10.** TEM images of 24 h UV radiation exposed mouse skin sections. (A) The penetration pathway through the skin can be clearly seen and is shown in more detail in B with the large dark spots being the NP's. (C) Another section of skin demonstrating the penetration pathway and with an example silver enhanced QD present in the epidermal layer. (D) The negative control (no QD, glycerol only) of silver enhanced mouse skin 24 h UV radiation exposure. (Taken from Luke et al., 2008) . . . . . **21**

**Figure 11.** Titanium levels in the kidney, liver, and blood of trout at sampling time points from 6 h to 90 days after intravenous injection of nanoTiO<sub>2</sub> (34.2 nm). Data are means ± SE. \*Significantly different from 6, 12, and 504 h. (Taken from Scown et al., 2009) Long-term accumulation of nanoTiO<sub>2</sub> over a period of 90 days was observed in liver and kidney . . . . . **22**

**Figure 12.** TEM images of kidney tissues dissected from rainbow trout 3 weeks after intravenous injection of 1 ml of trout perfusion ringer (A) or 100 µg TiO<sub>2</sub> nanoparticles (34.2 nm) in 1 ml of trout ringer (B–D). (B, C) Clusters of nanoparticles, indicated by arrows, are visible in tissue surrounding the kidney tubule T. (D) A cluster of nanoparticles in a membrane-bound vesicle. (Taken from Scown et al., 2009) . . . . . **23**

**Figure 13.** Ultra-thin section of erythrocyte under exposure to nanoTiO<sub>2</sub> analyzed by TEM. (a) Erythrocyte + PBS, (b) erythrocyte + nanoTiO<sub>2</sub> (100 µg/ml, 20 nm in diameter), (c) erythrocyte + microTiO<sub>2</sub> (100 µg/ml, 200 nm in diameter), (d, e, f, and g) erythrocyte + nanoTiO<sub>2</sub> (100 µg/ml) at higher magnification. NanoTiO<sub>2</sub> aggregate was found to be attached along the membrane of erythrocyte (Fig. 13b), with only a few within the erythrocyte (black arrow, Fig. 13f). MicroTiO<sub>2</sub> can be seen as small dark spots close to the erythrocyte membranes (Fig. 13c). At higher magnification, the nanoTiO<sub>2</sub> was seen to insert into the membrane (Fig. 13e). Ghost cells (Fig. 13f, g) were found in erythrocytes exposed to nanoTiO<sub>2</sub>. (Taken from Li et al., 2008) . . . . . **24**

**Figure 14.** Erythrocyte morphology after exposure to TiO<sub>2</sub> particles. (a) erythrocyte + PBS, (b) erythrocyte + nanoTiO<sub>2</sub> (100µg/ml, 20 nm in diameter), (c) erythrocyte+microTiO<sub>2</sub> (100µg/ml, 200 nm in diameter). NanoTiO<sub>2</sub> attachment-deformed erythrocytes with surface herniations (Fig. 14b). The effect is more pronounced than for microTiO<sub>2</sub> (Fig. 14c). (Taken from Li et al., 2008). . . . . **24**

**Figure 15.** Histopathology of brain tissue (100×) in female mice 2 weeks post-exposure to different sized TiO<sub>2</sub> particles by a single oral administration of control group (only exposure to 0.5% HPMC) (A), 80 nm group (B), and fine (155 nm) group (C). Arrows indicate the fatty degeneration of hippocampus in the brain tissue. (Taken from Wang et al., 2007) . . . . . **26**

**Figure 16.** Histopathology of kidney tissue (100×) in female mice 2 weeks post-exposure to different sized TiO<sub>2</sub> particles by a single oral administration of control group (only exposure to 0.5% HPMC) (A), 80 nm group (B), and fine (155 nm) group (C). Circles indicate the proteinic liquid in the renal tubule; arrows indicate the swelling in the renal glomerulus. (Taken from Wang et al., 2007) . . . . . **26**

**Figure 17.** Histopathology of liver tissue (100×) in female mice 2 weeks post-exposure to different sized TiO<sub>2</sub> particles by a single oral administration of control group (only exposure to 0.5% HPMC) (A), 80 nm group (B), and fine (155 nm) group (C). Circles indicate the hydropic degeneration around the central vein; Arrows indicate the spotty necrosis of hepatocytes. (Taken from Wang et al., 2007) . . . . . **27**

**Figure 18.** Histopathology of stomach tissue (100× for A and B; 40× for C) in female mice 2 weeks post-exposure to different sized TiO<sub>2</sub> particles by a single oral administration of control group (only exposure to 0.5% HPMC) (A), 80 nm group (B), and fine (155 nm) group (C). Arrows indicate the inflammation cells. (Taken from Wang et al., 2007) . . . . . 27

### III. The cell

**Figure 1.** Eukaryotic cell. ([http://www.malebolge.net16.net/science10/animal\\_cell.gif](http://www.malebolge.net16.net/science10/animal_cell.gif)). . . . . 30

**Figure 2.** Plasma membrane – a continuous sheet of bilayer of phospholipid molecules, about 4 - 5 nm thick, with various proteins embedded. (Taken from <http://www.britannica.com/EBchecked/topic-art/463558/45550/A-molecular-view-of-the-cell-membrane> Intrinsic-proteins-penetrate) . . . . . 31

**Figure 3.** Phospholipid molecule (Bruce Alberts et al., 1994) . . . . . 31

**Figure 4.** Electron micrograph of a thin section of the nucleus of a human cell, showing the nuclear envelope and nucleolus. (Taken from E.G. Jordan and J. McGovern) . . . . . 32

**Figure 5.** The cytoskeleton – a complex network of intermediate filaments, actin, and microtubules, all of them stained with Coomassie Blue. (Taken from Weinberg, 2007) . . . . . 33

**Figure 6.** The structure and function of the cytoskeleton . . . . . 34

**Figure 7.** The main steps in formation of metastasis – the metastasis cascade. (Adapted from Fidler, 2003) . . . . . 36

**Figure 8.** Physical shielding of keratinocyte nuclei from UV radiation. The white arrows indicate agglomerations of melanin on the surface of keratinocytes. (Taken from Weinberg, 2007) . . 41

**Figure 9.** An overview of the mechanical models for living cells (Taken from Lim, Zhou, Quek, 2006). . . . . 47

### IV. Principle action of photosensitizers

**Figure 1.** Excitation energy and orbital occupancy of the lowest singlet excited states of molecular oxygen (<sup>1</sup>Δ<sub>g</sub> and <sup>1</sup>Σ<sub>g</sub>). . . . . 51



**Figure 2.** Diagram of the electron transport chain in the mitochondrial intermembrane space. (This image has been released into the public domain by its author, LadyofHats, who grants anyone the right to use this work for any purpose, without any conditions.) . . . . . **52**

**Figure 3.** Partial reduction products of dioxygen (black) and electronic excitation (red) . . . . . **52**

**Figure 4.** Jabłoński - Kasha diagram showing ROS generation via Type I or II photoreaction mechanisms. The light-induced excitation populates the short-lived singlet excited states ( $^1S_n^*$ ) of the PS. The process then proceeds by a rapid internal conversion (IC) to the lowest singlet excited state ( $^1S_1^*$ ). Then, the majority of the captured energy of  $^1S_1^*$  is transferred via an efficient inter system crossing mechanism (ISC) to a long-lived excited triplet state ( $^3S^*$ ). Subsequently, for Type I processes, electron or hydrogen transfer leads to free radical generation, whereas for type II processes, molecular oxygen in its triplet ground state ( $^3\Sigma_g$ ) effectively quenches the PS triplet state ( $^3S^*$ ), through a resonant energy transfer (RET), which results in singlet oxygen ( $^1\Delta_g$ ) generation . . . . . **55**

**Figure 4.** Crystal structure of anatase (a), and rutile (b), anatase nanoTiO<sub>2</sub>-based custom-made nanowires (c). (Made using the free software VESTA - 3D visualization program) . . . . . **59**

**Figure 5.** Schematic representation of the mechanisms involved in the generation of an electron/hole pair ( $e_{cb}^-/h_{vb}^+$ ) and primary radicals formation for a TiO<sub>2</sub> anatase particle upon UV irradiation . . . . . **60**

## **V. Sample characterization techniques**

**Figure 1.** Precession of the spin vector  $\vec{S}$  about the magnetic field  $\vec{B}$  in the z direction . . . . . **64**

**Figure 2.** Electron-Zeeman splitting as a function of the strength,  $B$ , of the magnetic field and the resonance condition (a), the application of a low-amplitude magnetic field modulation and *lock-in* detection converts the absorption curve into a first derivative (b) . . . . . **65**

**Figure 3.** Mechanism of DMPO-OH generation resulting from the DMPO spin-trapping of hydroxyl and superoxide radicals (a), splitting diagram and corresponding ESR spectrum ( $d\chi''/dH$ ) of the resonant transitions of the DMPO-OH spin-adduct in H<sub>2</sub>O at ambient conditions (b) . . . . . **68**

**Figure 4.** Reactive mechanism of TEMPOL degradation to the diamagnetic hydroxyl amine (a), splitting diagram and corresponding ESR spectrum ( $d\chi''/dH$ ) of the resonant transitions of a  $\sim 0.2$  mM TEMPOL solution in  $H_2O$  at ambient conditions (b) . . . . . **69**

**Figure 5.** Metabolism of ACP in living cells (a), splitting diagram and corresponding ESR spectrum ( $d\chi''/dH$ ) of the resonant transitions of a  $\sim 0.26$  nM CP in HBSS medium at ambient conditions (b) . . . . . **70**

**Figure 6.** The UV-A light generator consisting of the Hamamatsu Lightingcure lamp, quartz light-guide and Delrin-made adapter, which accommodates the light-guide and a 5-mL glass beaker. This setup enables one to mix the aqueous suspensions during illumination as well as to exchange gases (e.g.,  $N_2$  and  $O_2$ ). Before illumination (a), and during illumination of  $TiO_2$  (b). **72**

**Figure 7.** Schematic diagram of the atomic force microscope . . . . . **75**

**Figure 8.** Scanning electron microscope images of different cantilevers (a) microfabricated at the edge of a chip. Probing tips (b) are placed at the free ends and have shape of four-sided pyramid. (c) Scheme presenting the dimensions for a cantilever, Veeco Microlever D. (Adapted from Veeco Instruments) . . . . . **76**

**Figure 9.** Lennard-Jones potential describing the dependence of interatomic forces on tip-sample distance and the resulting modes of AFM operation. Three AFM operating modes are located by black dots in the diagram showing the interaction force between tip and sample. In the tapping and resonant modes, the cantilever vibrates close to its resonance frequency, whereas the contact mode is quasi-static . . . . . **78**

**Figure 10.** Force curve between the end of the AFM tip and the hard surface . . . . . **80**

**Figure 11.** The concept of the elasticity measurement in an AFM experiment. The concept of the elasticity measurement in an AFM experiment. The blue line corresponds to the force curve acquired for the stiff substrate, whereas the red line corresponds to the soft specimen. . . . . **81**

**Figure 12.** Surface of the living 1205Lu cell: (a) deflection and (b) topography images. Images were recorded by applying the force of 0.87 nN (set point) and scan speed of 0.87 Hz . . . . . **84**

**Figure 13.** In AFM contact mode imaging, cytoskeletal structures lying beneath the cell membrane can be sensed by applying sufficiently high load forces (high set point). The softer regions located between cytoskeleton fibers (black dots denoting cross section) are more compressed enabling visualization of actin fibers. . . . . **84**

**Figure. 14.** Gaussian distribution (line) fitted to a histogram of the estimated Young's modulus values. The histogram was obtained for 27 cells (16 curves were collected for each cell) . . . . **85**

**Figure 15.** NucleoCounter® - the integrated fluorescence microscope [Taken from ChemoMetec, The NucleoCounter® information brochure] . . . . . **89**

**Figure 16.** Propidium Iodide staining cellular DNA . . . . . **90**

## **VI. Experimental results**

**Figure 1.** Evaluation of the primary particle size using TEM for various commercial and custom-modified\*) nano-particulate TiO<sub>2</sub>. The TEM data, collected for selected nanoTiO<sub>2</sub> powders, are shown as a function of increasing particle size. \*) The commercial material AMT600-Tayca (lower panel, third picture to the right) was modified by annealing at 800<sup>0</sup>C for 1 hour in oxygen atmosphere, which resulted in growth of the primary grain size from ~27 nm to ~42 nm . . . . . **95**

**Figure 2.** An example evolution of the ESR traces of the paramagnetic DMPO-OH spin adduct as a function of illumination time for Tayca AMT100 (5.3 nm grain size). . . . . **96**

**Figure 3.** An example experimental ESR trace of DMPO-OH and its simulation. The ESR spectrum was obtained for 30 sec of illumination of a PBS suspension of P25 Degussa. . . . . **97**

**Figure 4.** Example kinetics of ROS formation in aqueous suspensions of selected nanoparticulate anatase and rutile samples. For all the materials studied, the concentration of nanoTiO<sub>2</sub> in PBS suspensions was of 32 mg/100 mL . . . . . **98**

**Figure 5.** a) The ESR-derived efficiency of the photo-production of ROS for anatase and rutile nanoTiO<sub>2</sub> in PBS suspensions illuminated with UV-A light as a function of the primary particle size (Pierzchala - to be published), b) UV-light induced singlet oxygen generation by surfaces covered with anatase nanoTiO<sub>2</sub> (detection in air, at 1270 nm) as a function of primary particle size (Daimon and Nosaka, 2007), c) Prediction of the potential for generation of ROS as a

function of nanoparticle size. Maximum number of ROS generated by TiO<sub>2</sub> nanoparticles at a particle loading of  $50 \times 10^9$  nanoparticles per unit volume, under ambient temperature and pressure, and with equilibrium surface chemistry (Barnard, 2010) . . . . . **100**

**Figure 6.** A comparison of TEM images and size distributions for anatase-based TiO<sub>2</sub> nanowires, P25 Degussa, and anatase AMT100 nanoparticles: a) anatase-based TiO<sub>2</sub> nanowires, b) nanoparticles of P25 Degussa (particle size of  $26 \pm 1$  nm), and c) anatase AMT 100 nanoparticles (particle size of  $5.3 \pm 1.0$  nm) . . . . . **102**

**Figure 7.** A comparison of XRD patterns for anatase-based TiO<sub>2</sub> nanowires and commercial nanoTiO<sub>2</sub> (JA-1 Tayca - anatase, R-HD2 Huntsman - rutile and Degussa P25). . . . . **103**

**Figure 8.** The ESR-derived efficiency of the photo-production of ROS for anatase-based TiO<sub>2</sub> nanowires, P25 Degussa and anatase AMT100 nanoparticles. All particles were suspended in PBS buffer at the concentration 32mg/100ml and 50  $\mu$ M of DMPO and illuminated with UV-A light ( $\lambda = 365$  nm, 10 mW/cm<sup>2</sup>). Control: the ESR signal intensity of DMPO-OH as a function of illumination time in the absence of nanomaterials. **Inset:** typical evolution of ESR traces of the paramagnetic product DMPO-OH as a function of illumination time . . . . . **104**

**Figure 9.** An example evolution of the ESR traces of the stable nitroxide radical, TEMPOL, as a function of illumination time with UV-A light in the presence of Tayca AMT100 (5.3 nm grain size). TEMPOL, at the concentration of 50  $\mu$ M was used as a molecular target for ROS generated by the photocatalytic action of nanoTiO<sub>2</sub> (Tayca AMT100) . . . . . **105**

**Figure 10.** The experimental ESR traces and spectral simulations for the photocatalytic degradation of TEMPOL in the presence of P25 Degussa after 3 min of illumination with UV-A. a) The total overlapped experimental and simulated ESR spectra. b) The experimental ESR trace overlapped with the decomposed signals of TEMPOL and TEMPON . . . . . **106**

**Figure 11.** Photocatalytic degradation of the water-soluble nitroxide radical TEMPOL (50  $\mu$ M) in the presence of anatase-based TiO<sub>2</sub> nanowires, AMT 100 and P25 Degussa. Full symbols correspond to the degradation of TEMPOL. Half-filled symbols correspond to kinetics of formation and degradation of TEMPON. Control kinetics corresponds to the decomposition of TEMPOL under UV-A light illumination in the absence of nanoTiO<sub>2</sub>. The lines are a guide to the eye. **Inset:** typical ESR trace of decay of the paramagnetic spin label TEMPOL . . . . . **107**

**Figure 12.** An example ESR trace of the intracellular spin-trap ACP for Lu1205 melanoma cells incubated for 90 min with ACP in the presence of nanoTiO<sub>2</sub>, AMT100. The experimentally acquired ESR spectrum is marked in black and its simulation is depicted in red . . . . . **110**

**Figure 13.** Average values of the ESR-derived efficiency of the intracellular production of ROS in the presence of anatase-based TiO<sub>2</sub> nanowires, AMT 100 and P25 Degussa at 2 µg/mL concentrations for Lu1205 cells (A) and WM793 cells (B). Columns: ‘a’ control measurement for ACP spin-trap alone incubated for 90 min at 37°C, in the dark; ‘b’ control measurement for ACP spin-trap incubated with cells for 90 min at 37°C, in the dark; ‘c’, ‘d’, and ‘e’ measurements for cells pre-incubated with nanoTiO<sub>2</sub> for 30 min in the dark at 37°C, which was followed by incubation with the ACP spin-trap for 90 min at 37°C in the dark . . . . . **111**

**Figure 14.** An example optical microscopy image for NBT staining of WM973 cells incubated with AMT100 for 30 min in the dark at 37°C. The black arrows point to the cells with gradually decreasing positive NBT staining: **A** - cells filled with formazan (+ + +), **B** - intermediate intensity (+ +), **C** - scattered formazan deposits (+), **D** - no detectable formazan (-). . . . . **112**

**Figure 15.** ROS detection with NBT staining in metastatic melanoma Lu 1205 cells. Left panel: non-treated (control) cells and cells incubated with: anatase-based TiO<sub>2</sub> nanowires, AMT100 and P25 for 0.5 h at 37° in the dark. Right panel: cells exposed to photo-oxidative stress for 240 sec (UV– A light, 1 mW/cm<sup>2</sup>). Scale bar 50 µm. . . . . **113**

**Figure 16.** ROS detection with NBT staining in metastatic melanoma WM793 cells. Left panel: non-treated (control) cells and cells incubated with: anatase-based TiO<sub>2</sub> nanowires, AMT100 and P25 for 0.5 h at 37° in the dark. Right panel: cells exposed to photo-oxidative stress for 240 sec (UV– A light, 1 mW/cm<sup>2</sup>). Scale bar 50 µm. . . . . **114**

**Figure 17.** Toxic effects of nanoTiO<sub>2</sub> on Lu 1205 (a) and WM793 (b) melanoma cells exposed for 230 sec to UV-A light (λ = 365nm) carried out using the Propidium Iodide Luminescent Cell Viability Assay. Test was performed for untreated cells (A), and those incubated with anatase-based TiO<sub>2</sub> nanowires (B), ATM100 (C), and P25 Degussa (D) . . . . . **117**

**Figure 18.** Optical images of the metastatic melanoma Lu1205 cells exposed to nanoTiO<sub>2</sub>-induced photo-oxidative stress. Control - non-treated cells (A). Cells incubated for 0.5 h with nanoTiO<sub>2</sub> and illuminated with UV-A for 460 sec (1 mW/cm<sup>2</sup>): anatase-based TiO<sub>2</sub> nanowires (B), AMT100 (C), and P25 Degussa (D). The depicted changes in cell morphology, including

appearance of blebs and modifications of cell edges are typical for cells before and after exposure to the photo-oxidative stress. Scale bar 25 $\mu$ m. . . . . 119

**Figure 19.** Optical images of the metastatic melanoma WM793 cells exposed to nanoTiO<sub>2</sub>-induced photo-oxidative stress. Control - non-treated cells (A). Cells incubated for 0.5 h with nanoTiO<sub>2</sub> and illuminated with UV-A for 460 sec (1 mW/cm<sup>2</sup>): anatase-based TiO<sub>2</sub> nanowires (B), AMT100 (C), and P25 Degussa (D). The depicted changes in cell morphology, including appearance of blebs and modifications of cell edges are typical for cells before and after exposure to the photo-oxidative stress. Scale bar 25 $\mu$ m. . . . . 120

**Figure 20.** Optical microscopy fluorescent images of actin filaments stained using FITC-phalloidin revealing changes in cytoskeleton morphology for Lu1205 (A) and WM793 (B). Left panel – control (non-treated cells), middle panel - cells after 0.5 h incubation with anatase-based TiO<sub>2</sub> nanowires in the dark, and right panel - cells exposed to the photo-oxidative stress for 230 sec (UV– A light exposure, 1 mW/cm<sup>2</sup>) in the presence of anatase-based TiO<sub>2</sub> nanowires. . . . 122

**Figure 21.** Optical microscopy fluorescent images of actin filaments stained using FITC-phalloidin revealing changes in cytoskeleton morphology for Lu1205 (A) and WM793 (B). Left panel – control (non-treated cells), middle panel - cells after 0.5 h incubation with anatase AMT100 in the dark, and right panel - cells exposed to the photo-oxidative stress for 230 sec (UV– A light exposure, 1 mW/cm<sup>2</sup>) in the presence of anatase AMT100. . . . . 124

**Figure 22.** Optical microscopy fluorescent images of actin filaments stained using FITC-phalloidin revealing changes in cytoskeleton morphology for Lu1205 (A) and WM793 (B). Left panel – control (non-treated cells), middle panel - cells after 0.5 h incubation with P25 Degussa in the dark, and right panel - cells exposed to the photo-oxidative stress for 230 sec (UV– A light exposure, 1 mW/cm<sup>2</sup>) in the presence of P25 Degussa. . . . . 125

**Figure 23.** High-resolution AFM deflection image of a living WM793 cell acquired in HBSS medium. The filamentous mesh is organized on two length scales: with coarse (*arrowheads*) and fine mesh filaments (*arrows*). The coarse mesh forms larger elements and is easier to identify, whereas the fine mesh elements have much smaller dimensions. These two meshes are likely intertwined; although, it is possible that the fine mesh is layered over the coarse mesh . . . . . 127

**Figure 24.** High-resolution AFM deflection images of the metastatic melanoma Lu1205 cells. (A) Non-treated (control) cells; (B) Cells after 0.5 h incubation with anatase-based TiO<sub>2</sub> nanowires, (C) Cells after 0.5 h incubation with AMT100 and (D) Cells after 0.5 h

incubation with P25 Degussa, which was then followed by 230 sec exposure to UV–A light (1 mW/cm<sup>2</sup>) . . . . . **128**

**Figure 25.** High-resolution AFM deflection images of the metastatic melanoma WM793 cells. (A) Non-treated (control) cells; (B) Cells after 0.5 h incubation with anatase-based TiO<sub>2</sub> nanowires, (C) Cells after 0.5 h incubation with AMT100 and (D) Cells after 0.5 h incubation with P25 Degussa, which was then followed by 230 sec exposure to UV–A light (1 mW/cm<sup>2</sup>) . . . . . **129**

**Figure 26.** Topography and the cross-sections of Lu1205 cells exposed to anatase-based TiO<sub>2</sub> nanowires and UVA irradiation. Control (non-treated) cells are shown in the left panel. Using two reference points, the height of a cell body was determined . . . . . **131**

**Figure 27.** Topography and the cross sections of WM 793 cells exposed to nanowires and UVA irradiation. On the left, control i.e. non-treated cells are shown. Using two reference points, the height of a cell body was determined . . . . . **132**

**Figure 28.** Relative (A) and percentage (B) changes of the Young’s modulus values for Lu1205 cells determined from AFM measurements. A) Control (non-treated) cells (a); Cells after 0.5 h of incubation with anatase-based TiO<sub>2</sub> nanowires, AMT100 and P25 Degussa, in the dark (b). Cells after 0.5 h incubation in the dark with anatase-based TiO<sub>2</sub> nanowires, AMT100 and P25 Degussa, and then exposed to UV–A light (1 mW/cm<sup>2</sup>) for: 60 sec (c), 240 sec (d), and 460 sec (e). B) Percentage changes were calculated as reference to the Young’s modulus values of control (non-treated) cells. All results were normalized to the value obtained for control cells (1.02 +/- 0.2 kPa) . . . . . **134**

**Figure 29.** Relative (A) and percentage (B) changes of the Young’s modulus values for WM793 cells determined from AFM measurements. A) Control (non-treated) cells (a); Cells after 0.5 h of incubation with anatase-based TiO<sub>2</sub> nanowires, AMT100 and P25 Degussa, in the dark (b). Cells after 0.5 h incubation in the dark with anatase-based TiO<sub>2</sub> nanowires, AMT100 and P25 Degussa, and then exposed to UV–A light (1 mW/cm<sup>2</sup>) for: 60 sec (c), 240 sec (d), and 460 sec (e). B) Percentage changes were calculated as reference to the Young’s modulus values of control (non-treated) cells. All results were normalized to the value obtained for control cells (1.12 +/- 0.38 kPa) . . . . . **135**

# List of Tables

## III. The cell

**Table 1.** US Mortality Data in 2006. (Source: National Center for Health Statistics, Centers for Disease Control and Prevention, 2009) ..... **37**

**Table 2.** Ten leading cancer types for estimated new cancer cases and deaths, grouped by sex, in United States in 2009 (Source: American Cancer Society, 2009) ..... **38**

**Table 3.** Locations of melanoma secondary sites. (Source: Meyers ML, Balch CM. “Diagnosis and Treatment of Metastatic Melanoma.” Cutaneous Melanoma. Balch CM, Houghton AN, Sober AJ, Soong S-J (Eds): St. Louis: Quality Medical Publishing, Inc. 1998:329) ..... **42**

**Table 4.** Experimental techniques and mechanical models of a cell ..... **46**

## V. Sample characterization techniques

**Table 1.** Typical cantilever characteristics ..... **76**

## VI. Experimental results

**Table 1.** ROS generation efficiencies for nanoparticulate anatase and rutile samples ..... **99**

**Table 2.** ROS generation efficiencies for anatase-based TiO<sub>2</sub> nanowires, P25 Degussa and anatase AMT100 nanoparticles ..... **105**

**Table 3.** NBT staining-derived levels of ROS in Lu 1205 melanoma cells exposed to nanoTiO<sub>2</sub> and UV-A radiation (scored according to **Fig. 14**) ..... **115**

**Table 4.** NBT staining-derived levels of ROS in WM 793 melanoma cells exposed to nanoTiO<sub>2</sub> and UV-A radiation (scored according to **Fig. 14**) ..... **115**



# Curriculum Vitae



Katarzyna Pierzchała

**Born:** October 7, 1981, Oświęcim, Poland

**Citizenship:** Polish

**e-mail:** pierzchala.katarzyna@gmail.com

- **Employment:**

- **Aug. 2006 –14<sup>th</sup> Aug. 2010** - Ecole Polytechnique Fédérale de Lausanne Institute of Physics of Complex Matter
- **Aug. 2004 – Dec. 2006** – medical physicist in the Oświęcim Hospital - collaboration in testing of medical equipment
- **October 2004 – February 2005** - teacher of physics in the Oświęcim High School

- **Education:**

- **Aug. 2006 –14<sup>th</sup> Aug. 2010** - postgraduate (Ph.D.) studies - Ecole Polytechnique Fédérale de Lausanne Institute of Physics of Complex Matter
- **Jan. 2006 – Aug. 2006** - postgraduate (Ph.D.) studies - Institute of Physics, Polish Academy of Sciences, Warsaw, Poland
- **2003 - 2005** - graduate studies - Department of Physics, Division of Nuclear Physics and Its Applications, University of Silesia, Katowice, Poland
- **2005 – M.Sc. degree, thesis:** “*Examination of the Natural Radioactivity Background in the Underground Laboratory for Particle Physics and Nuclear Astrophysics - Water Tests from LNGS/INFN Gran Sasso Italy, December 2004*”

**Thesis’ Director:** Prof. Jan Kisiel (University of Silesia)

- **2000-2003** - undergraduate studies - Department of Physics, Division of Medical Physics, University of Silesia and Department of Radiodiagnostic and Nuclear Medicine, Central Clinical Hospital, Medical Academy of Silesia, Katowice, Poland

-**2003** – **B.Sc. degree, interim thesis:** “*Design of the Scintillating Detector-based System for Monitoring of I-131 in the Thyroid Gland in a Wide Range of Radiation Dose (1-1000MBq)*”

**Thesis’ Director:** Dr. Krystian Rudzki (Medical University of Silesia)

- **Professional Competences:**

- Electron Spin Resonance
- Atomic Force Microscopy
- Optical and fluorescence microscopy
- Cell culture
- Spectrophotometry
- Scintillation Spectroscopy
- Computer Tomography

- **Research interests:**

- Oxidative Stress
- Molecular and cell (cancer) biophysics
- Medical techniques and their applications

- **Professional Activities:**

- **2006-2010** - Teaching: Travaux Pratiques de Physique – 2nd year of Physic Section, EPFL. Awarded for teaching performance in academic year 2008/2009, Faculty of Basic Science, EPFL.

- **9-12 March, 2010 CHUV, Lausanne** - 2nd NanoImpactNet Conference

- **January 2009** - Education and training of Persons Conducting Animal Experiments

- **June 12<sup>th</sup> 2008** - **Collaboration with Nestle:** Antioxidant potential of Nescafe Alta Rica, ESR training at the EPFL for Nestle stuff

- **Basel, May 19-21, 2008** – 1<sup>st</sup> European Conference for Clinical Nanomedicine

- **March 6, 2008** - Nano Eco Workhop Monte Verita, Switzerland
- **USGEB-2008: Biology Meets Engineering:EPFL, Lausanne**
- **Sept. 5 – 7, 2007** - Bio-Imaging & Optics Platform BI-Op Inauguration EPFL, Lausanne
- **May 2006** - Workshop on the Structure and Function of Biomolecules II – conference organization
- **Sept. 5 – 7, 2007** - Bio-Imaging & Optics Platform BI-Op Inauguration EPFL, Lausanne
- **July - August 2002** - workshop practice in the Oświęcim Hospital

- **Languages:**

*Polish, English*

- **Other:**

Interest in medicine, fine arts, and sports.

- **Publications and presentations:**

***Poster presentations:***

[1] Bertrand Vilen, Katarzyna Pierzchała, Mariusz Czuba, Pierre Marcoux, Alfreda Graczyk, Piotr G. Fajer, Andrzej Sienkiewicz, and László Forró, “*Oxidative stress-mediated protein conformation changes: ESR study of spin labeled Staphylococcal nuclease*”, Workshop on the Structure and Function of Biomolecules II, May 10–13 May, 2006, Bedlewo, Poland.

[2] A. Sienkiewicz, B. Vilen, K. Pierzchała, M. Czuba, A. Graczyk, P. Marcoux, P.G. Fajer, and L. Forro, “*Oxidative stress-mediated protein conformation changes: ESR study of spin labeled Staphylococcal nuclease*”, Gordon Conference Series - NOX FAMILY NADPH OXIDASES - LES DIABLERETS CONFERENCE CENTER, OCTOBER 15-20, 2006, Les Diablerets, Switzerland.

[3] K. Pierzchała, M. Lekka, B. Vilen, A. Sienkiewicz, and L. Forró, “*Imaging and elasticity measurements of living fibroblasts exposed to the photo-oxidative stress in the presence of nanoTiO<sub>2</sub>: ESR and AFM studies*”, EPFL, Sept. 5 – 7, 2007: “Bio-Imaging & Optics” Platform BI-Op Inauguration <http://biopsymposia.epfl.ch/>, EPFL School of Life Sciences - BioImaging and Optics, Lausanne, Switzerland.

[4] K. Pierzchała, A. Sienkiewicz, B. Vilen, M. Lekka, P.R. Marcoux, A. Magrez, and L. Forró, “*Photo-cytotoxicity of nanostructured materials: in vitro ESR and AFM assays*”, USGEB-2008: Biology Meets Engineering:EPFL, Lausanne, Switzerland.

[5] K. Pierzchała, A. Sienkiewicz, M. Lekka, B. Vilenó, A.J. Kulik, P.R. Marcoux, A. Magrez, and L. Forró, “Photo-toxicity of water-soluble C60 derivatives and nanoTiO<sub>2</sub>: *in vitro* ESR and *single-cell-level* AFM assays”, March 6, 2008 - Nano Eco Workhop Monte Verita, Switzerland.

[6] K. Pierzchała, B. Vilenó, A. Magrez, M. Lekka, A.J. Kulik, P.R. Marcoux, A.Sienkiewicz, and L. Forró, “*Nano-engineered TiO<sub>2</sub>- and C60-based Materials for Performing Bio-oxidations: ESR, NIR and Single-cell-level AFM Assays* ”, Basel, May 19-21, 2008 – 1<sup>st</sup> European Conference for Clinical Nanomedicine, Switzerland.

[7] K. Pierzchała, A. Sienkiewicz, L. Forró, I. Milosevic, S. Guillot, M.-L. Saboungi, J.-P. Salvétat, “*ESR Characterization of Iron Oxide Nanomagnets in Aqueous Media*”, Basel, May 19-21, 2008 – 1<sup>st</sup> European Conference for Clinical Nanomedicine, Switzerland.

### ***Publications:***

[1]. Inactivation of MS2 coliphage in Fenton and Fenton-like systems: role of transition metals, hydrogen peroxide and sunlight. Jessica I. Nieto-Juarez, Katarzyna Pierzchała, Andrzej Sienkiewicz and Tamar Kohn, *Environ. Sci. Technol.*, 44 (9), pp. 3351–3356, 2010

[2]. Synthesis, Characterization, and Photocatalytic Activities of Nanoparticulate N, S-Codoped TiO<sub>2</sub> Having Different Surface-to-Volume Ratios. Author(s): Rengifo-Herrera, JA; Pierzchała, K; Sienkiewicz, A, et al. Source: *JOURNAL OF PHYSICAL CHEMISTRY C* Volume: 114 Issue: 6, pp. 2717-2723, 2010

[3]. CVD Synthesis of Shape and Size Controlled ZnO Nanoparticles for Application as UV Filters. Revathi Bacsa, Andrzej Sienkiewicz, Katarzyna Pierzchała, Jeannette Dexpert-Ghys, László Forró and Philippe Serp 216th *IEEE ECS Transactions* Volume 25 (8), pp. 11601-11607, 2009

[4]. Transfer Radical Addition Reactions Catalyzed by RuCp\* Complexes: A Mechanistic Study. Author(s): FERNANDEZ-ZUMEL Mariano A.; THOMMES Katrin ; KIEFER Gregor ; SIENKIEWICZ Andrzej ; PIERZCHAŁA Katarzyna ; SEVERIN Kay. Source: *CHEMISTRY-A EUROPEAN JOURNAL* Volume: 15 Issue: 43, pp. 11601-11607, 2009

[5]. Abatement of organics and Escherichia coli by N, S co-doped TiO<sub>2</sub> under UV and visible light. Implications of the formation of singlet oxygen (O-1(2)) under visible light Author(s): Rengifo-Herrera, JA; Pierzchała, K; Sienkiewicz, A, et al. Source: *APPLIED CATALYSIS B-ENVIRONMENTAL* Volume: 88 Issue: 3-4, pp. 398-406, 2009

[6]. La@C-82 as a spin-active filling of SWCNTs: ESR study of magnetic and photophysical properties. Author(s): Ciric, L; Pierzchała, K; Sienkiewicz, A, et al. Source: *PHYSICA STATUS SOLIDI B-BASIC SOLID STATE PHYSICS* Volume: 245 Issue: 10, pp. 2042-2046, 2008

[7]. Oxidative stress-mediated protein conformation changes: ESR study of spin-labelled staphylococcal nuclease. Author(s): Sienkiewicz, A; Vilenó, B; Pierzchała, K, et

al.Conference Information: Workshop on Structure and Function of Biomolecules II, Date: MAY 11-13, 2006 Bedlewo POLAND Source: *JOURNAL OF PHYSICS-CONDENSED MATTER* Volume: 19 Issue: 28 Article Number: 285201, pp. 1-13, 2007

***Publications in preparation:***

- [1] Katarzyna Pierzchała, Małgorzata Lekka, Arnaud Magrez, Andrzej J. Kulik, Piotr Laidler, László Forró, and Andrzej Sienkiewicz, “Photocatalytic and phototoxic properties of TiO<sub>2</sub>-based nanofilaments: ESR and AFM assays”, to be published in *Nanotoxicology*.
- [2] Katarzyna Pierzchała, Arnaud Magrez, László Forró and Andrzej Sienkiewicz, “UV-A light induced ROS generation the presence of nano-TiO<sub>2</sub> -crystalline phase and primary particle size dependence - and ESR spin trapping study”, to be published in *Journal of Photochemistry and Photobiology B: Chemistry*.
- [3] Katarzyna Pierzchała, Arnaud Magrez, László Forró, and Andrzej Sienkiewicz, ”Photocatalytic decay of TEMPOL in the presence of nano-TiO<sub>2</sub>: evidence of OH<sup>•</sup> and O<sub>2</sub><sup>-</sup> formation”, to be published in *Environm. Sci. & Technol.*